Universitat Autònoma de Barcelona

Study of structural changes in Zr-based bulk metallic glasses upon annealing and deformation treatments

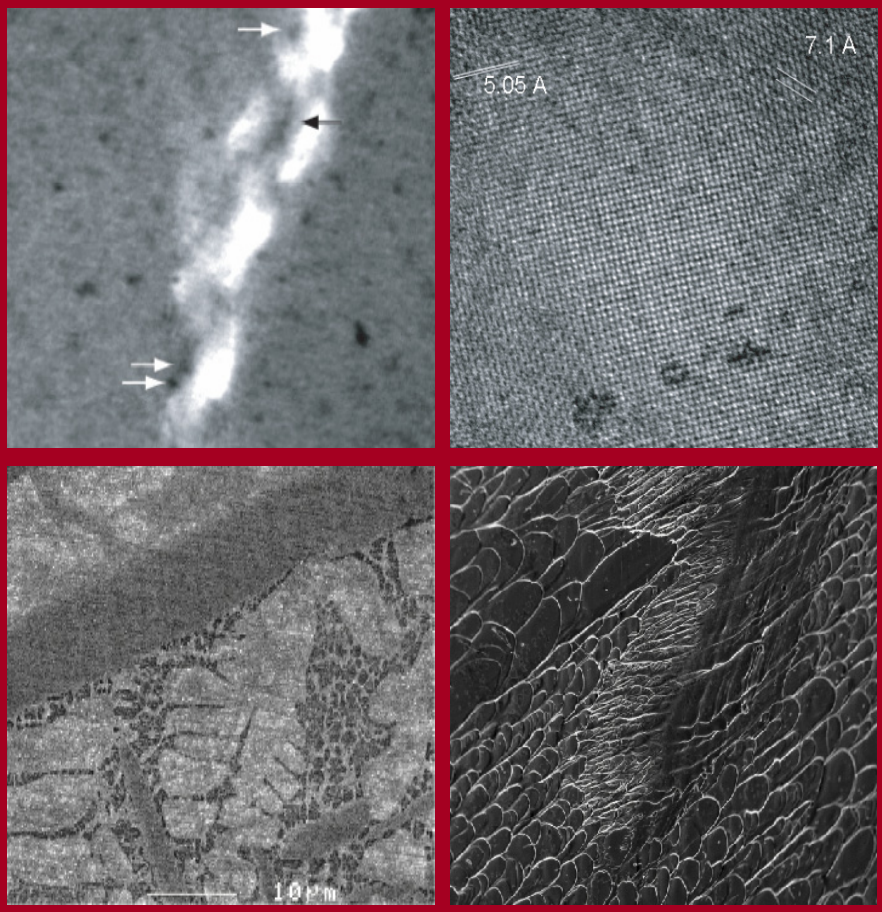

Doctoral thesis presented by

Nele Van Steenberge

Bellaterra, April 2008

Study of structural changes of Zr-based bulk metallic glasses upon annealing and deformation treatments

Doctoral thesis presented by
Nele Van Steenberge

Bellaterra, April 2008
Departament de Física
Facultat de Ciències

Els Doctors **Maria Dolors Baró Mariné** i **Jordi Sort Viñas** , directors de la tesi doctoral realitzada per Nele Van Steenberge, i que porta per títol "**Study of structural changes of Zr-based bulk metallic glasses upon annealing and deformation treatments**",

FAN CONTESTAR

Que l'aportació del doctorand al treball que es presenta ha estat fonamental tant pel que fa al disseny experimental, com a l'obtenció de les mostres, la realització dels experiments, l'anàlisi de les dades i la discussió i elaboració dels articles presentats.

I perquè així consti, a petició de l'interessat i als efectes oportuns, ho signem a Bellaterra, el 15 d' abril de 2008.

Dra. Maria Dolors Baró

Dr. Jordi Sort

ACKNOWLEDGEMENTS

During the course of this research work, a lot of people have lent me their helping hands and therefore I would like to take the opportunity to acknowledge them.

First and foremost, I would like to thank my supervisors Prof. Maria Dolors Baró and Dr. Jordi Sort for giving me the opportunity to work in their group and for their support and advice, not only about research but also on non-scientific matter, and especially for their confidence in me. A special thanks in particular to Dr. Amadeu Concustell, for sharing his knowledge and experience on bulk metallic glasses. His enlightening discussions have been a great help for the realization of this thesis. I also owe thanks to Prof. Santiago Suriñach for his help with experimental set-ups and technical assistance.

Furthermore, I may certainly not forget to thank my other colleagues from the group "Física dels Materials II": Germán, Enric, Jordina, Sebastiano, Pau, Alberto, Eva, Josep and Véronique for giving me a hearty welcome and making me feel like at home, just as much at work as well as beyond. To the technicians Jordi López, Manel Garcia and Rafael Moraira, thank you for your help on the reparation of small and bigger technical issues. Moltes gracies!

It was very interesting to participate in the European Research Training Network on "Ductilisation by length-scale control of Bulk Metallic Glasses and Bulk Metallic Glass Composites". It gave me the opportunity to meet and discuss with some very specialized scientists on the topic. Special thanks to Prof. Jürgen Eckert, Dr. Annett Gebert and Dr. Jayanta Das from the IFW Dresden (Germany), for their input and advice as well as for the practical help during my stays in their institute. Thanks also to Dr. Tanya Baser (University of Torino) for the interesting talks we had during our stay in Dresden, as well as for her efforts on the modulated DSC.

Besides, I am indebted to the people of the Microscopy Service, in particular Dr. Emma Rossinyol and Onofre Castells for their permanent assistance in the

TEM experiments, as well as to the people from the X-ray diffraction Service at the UAB for their help. Dr. Oriol Ossó from Matgas and Dr. Jaume Caro from the CTM Manresa for their collaboration on the nanoindentation experiments.

I am grateful for the technical support on in-situ TEM and high-resolution TEM by Dr Frédéric Mompiou and Florent Houdellier during my stays at the CEMES in Toulouse within the framework of the ESTEEM project.

This work would not have been possible without the financial and partial financial support of three European projects: "Ductilisation by length-scale control of Bulk Metallic Glasses and Bulk Metallic Glass Composites" (MRTN-CT-2003-504692), the special support action "Strengthening the role of women scientists in nano-science" and ESTEEM (Enabling Science and Technology through European Electron Microscopy) project (026019).

Thank you Stella, Fran, Cassie, Peca, Claire and all the others for making this time here in Barcelona just unforgettable!

Dani, thank you for your infinite support, patience and encouragement.

En het laatste woordje van dank gaat naar mijn ouders, mijn broer en zus en vrienden in België - bedankt voor jullie steun, woorden van moed, de bezoekjes en zoveel meer. Een heel dikke merci!

TABLE OF CONTENTS

Acknowledgements . . . iii

Table of Contents . . . v

Preface . . . ix

1. Introduction . . . 1
1.1 Bulk metallic glasses - state of the art . . . 1
1.2 Glass formation . . . 2
1.2.1 Definition of a glass - glass transition . . . 2
1.2.2 Classical crystallization theory . . . 3
1.2.3 Glass forming ability . . . 5
1.2.4 Application of classical nucleation theory for metallic glass 6
1.2.5 Glass forming systems . . . 8
1.3 Structural Aspects of Metallic glasses . . . 9
1.3.1 Short- and medium-range order - theoretical aspects . . . 9
1.3.2 Medium-range order - experimental observation . . . 12
1.3.3 Free volume . . . 12
1.4 Mechanical behavior of metallic glasses . . . 14
1.4.1 Introduction . . . 14
1.4.2 Atomic-level mechanisms . . . 16
1.4.3 Elastic deformation - mechanical strength - elastic constants 17
1.4.4 Plastic deformation - Catastrophic failure . . . 18
1.4.5 Possible mechanisms to improve plasticity - overview of literature data . . . 20
1.5 Possible applications . . . 29

2. Experimental techniques . . . 33
2.1 Preparation techniques . . . 33
2.1.1 Arc-melting . . . 33
2.1.2 Cu mold casting . . . 34
2.1.3 Experimental procedure . . . 35
2.2 Treatments . . . 36
2.2.1 Annealing treatment . . . 37
2.2.2 Heavy deformation - high pressure torsion . . . 37

2.3 Characterization techniques . . . 39
2.3.1 Thermal characterization . . . 39
2.3.2 Microstructural characterization - X-ray diffraction . . . 51
2.3.3 Microstructural characterization: Electron Microscopy . . . 59
2.3.4 Mechanical characterization . . . 89

3. Indentation size effect . . . 103
3.1 Introduction . . . 103
3.2 Experimental conditions . . . 105
3.3 Thermal characterization . . . 105
3.4 Nanoindentation results . . . 106
3.5 Discussion . . . 109
3.6 Summary . . . 119

4. Characterization of $Zr_{55}Cu_{30}Al_{10}Ni_5$ *after annealing treatments* . . . 121
4.1 Introduction . . . 121
4.2 Thermal characterization of $Zr_{55}Cu_{30}Al_{10}Ni_5$ . . . 122
4.3 Microstructural characterization of $Zr_{55}Cu_{30}Al_{10}Ni_5$ . . . 124
4.3.1 X-ray diffraction . . . 124
4.3.2 Transmission electron microscopy . . . 126
4.3.3 Discussion . . . 134
4.4 Mechanical characterization . . . 135
4.4.1 Compression tests . . . 135
4.4.2 Nanoindentation . . . 140
4.4.3 Acoustic measurements of elastic constants . . . 148
4.4.4 Discussion . . . 149
4.5 Summary . . . 151

5. Characterization of $Zr_{55}Cu_{30+x}Al_{10}Ni_{5-x}$ *(x=-2, 0, 2)* . . . 153
5.1 Thermal characterization . . . 153
5.2 Microstructural characterization - Crystallization products . . . 157
5.2.1 Introduction - literature review . . . 157
5.2.2 Results . . . 158
5.2.3 Discussion . . . 174
5.3 Mechanical and thermo-mechanical characterization . . . 178
5.3.1 Viscosity measurements . . . 178
5.3.2 Compression tests . . . 178

6. Characterization of $Zr_{55}Cu_{30}Al_{10}Ni_5$ *after severe deformation* . . . 183
6.1 Introduction . . . 183
6.2 Thermal characterization: DSC . . . 186
6.3 Microstructural characterization . . . 187
6.3.1 X-ray diffraction . . . 187
6.3.2 Transmission electron microscopy . . . 188

6.4 Mechanical characterization - Nanoindentation 190
6.4.1 Introduction 190
6.4.2 Experimental conditions nanoindentation 193
6.4.3 Results and discussion 193
6.5 Summary 197

7. Conclusions 199
7.1 Indentation size effect 199
7.2 Study of changes on medium range order upon annealing 200
7.3 Study of changes on medium range order upon deformation 201
7.4 Suggestions for future research 201
7.5 Articles 202

Bibliography 204

Appendix 221

A. Electron diffraction . . . . . A
A.1 The reciprocal lattice . . . . . A
A.2 The reflecting sphere . . . . . B
A.3 The structure factor C

B. Stereographic projection . . . . . E

PREFACE

Metallic glasses have been the subject of widespread research since the 1950's with significant progress in the understanding in their behavior. As the name suggests, they are amorphous metallic alloys, i.e. with the absence of long-range order. This lack of long-range order offers them unique physical, chemical and mechanical properties compared to conventional metallic materials.

However, the early glassy systems were obtained typically by rapid quenching techniques, with critical cooling rates up to 10^6 K s^{-1}, resulting typically in ribbons or thin foils with a thickness limited to a few tens of micrometer. About thirty to forty years later, the first so-called *bulk* metallic glass (BMG) was born, based on Pd, and after extensive work, a large range of multicomponent alloys was developed which required significant lower critical cooling rates and could thus be processed by conventional casting techniques. Among these multicomponent systems, Zr-based alloys have been key players with outstanding glass forming ability, which has made them to model alloys for the study of fundamental properties and characteristic behaviors.

The exceptionally high yield strength, close to the theoretical limit, and yield strain of these amorphous metallic systems in bulk offer them potential for structural applications. However, plastic deformation at room temperature occurs in a highly localized manner by the formation of a few shear bands. Instead of work-hardening, metallic glasses soften upon deformation, which prevents stable plastic elongation. Although BMGs possess a high fracture strength, once yielding has set in, early failure after a small percentage of macroscopic deformation appears, often along one single shear band. This inhomogeneous deformation mechanism at ambient temperature still limits the reliability of BMGs for structural applications. Logically, the enhancement of ductility of this type of materials has been the subject of many research works in the last decade.

It was found that when increased plasticity levels were obtained, it involved al-

ways multiplication of shear bands, indicating that this multiplication is a powerful toughening mechanism in metallic glasses, regardless of how it is accomplished. Probably the most explored concept to avoid catastrophic failure has been the development of a heterogeneous microstructure, with a second phase on different length scales, both crystalline and amorphous. Various routes have been tried out to obtain this second phase in the amorphous matrix: physically adding a reinforcing phase to the melt, by direct precipitation from the melt of a properly designed composition or by (partial) nano-crystallization of the glass after casting.

Upon annealing below the glass transition, changes in both topological and chemical short range order have been reported. The former is believed to deteriorate plasticity due to structural relaxation of the amorphous structure, reducing its "free volume", necessary for local shear transformations, and redistribution of local stresses frozen in during rapid quenching. The latter effect, changes on chemical short/medium range order, has hardly been studied into detail. Besides annealing, deformation has been reported to induce structural and microstructural changes.

These (micro)structural changes, induced by annealing and deformation, form the main topic of the work presented in this thesis. Various techniques have been applied to observe/visualize in the first place possible changes. In a next step, their influence on thermal behavior and mechanical behavior will be exposed.

Furthermore, depth-sensing techniques have become widely used for the mechanical characterization of solid materials since they allow the evaluation of the mechanical properties from a relatively small volume of material. In particular, indentation techniques permitted the determination of the mechanical properties of thin ribbons of metallic glasses. They are becoming to be of inestimable value in the study of the mechanical behavior of metallic glasses, due to their resolution down to the nanometric scale. However, in a first part of this thesis, it will be shown that one should be aware when applying this technique, of the existence of a so-called size-effect, directly linked with the structural changes upon deformation.

Below follows the subdivision of this thesis with a brief description of the main objective of each chapter:

Chapter 1 introduces some general aspects on the theory of metallic glasses and glass formation. A special emphasis is put on the structural aspects of

metallic glasses. A brief discussion is given on the basics of mechanical properties of this new class of materials and the different routes to improve plasticity. The chapter is concluded with some possible applications, where this limited plasticity can be avoided.

Chapter 2 describes the experimental techniques used, divided into preparation techniques (casting, annealing and deformation) and characterization techniques of the thermal behavior, microstructure and mechanical properties. Further, the experimental procedure of each technique is briefly explained. Different aspects related with transmission electron microscopy will appear to be one of the key techniques used in this work. However, sample preparation for this technique of these metastable materials is far from trivial - therefore, an overview of problems encountered and possible solutions is described into detail in this chapter as well.

Chapter 3 deals with the abovementioned indentation size effect and correlates it with the dynamical mechanical softening occurring during deformation, a softening effect which is reduced after previous relaxation annealing treatments.

Chapter 4 studies the changes on compositional short/medium range order upon annealing, both ex- and in-situ and reports on the significant influence of these changes on the mechanical behavior.

Chapter 5 deepens the results of the previous chapter, by studying the observed alteration in thermal/crystallization behavior. Alloys with small variations in the overall composition were explored, in order to help to understand better the thermal and mechanical behavior observed upon annealing.

Chapter 6 discusses briefly the influence of deformation as an alternative treatment to annealing with possible similar results on the microstructure.

Chapter 7 presents the main conclusions and possible future research to be developed.

1. INTRODUCTION

1.1 Bulk metallic glasses - state of the art

Glass is a solid which does not crystallize upon cooling from the melt. It is an amorphous solid body in which the structure from the liquid has been *frozen*. In principle, glasses can be found with all atomic bondings: ionic, covalent, Van der Waals and metallic. However, due to the non-directional nature of the metallic bond, metallic glasses are the most difficult ones to manufacture: only by the application of very high cooling rates (10^6 K s^{-1}), it was possible to obtain metallic glasses, with the first amorphous alloy observed in 1960 in the Au-Si system [1]. As a consequence of these very high cooling rates required, metallic glasses could initially only be produced under the form of thin ribbons (around 50 μm), by melt spinning or splat quenching.

In fact, it was long doubted whether metallic glasses could be manufactured in *bulk form*, which would require significantly lower cooling rates. It was only in the 1990's that a number of complex metallic alloys were found which have a critical cooling rate for solidification without crystallization below 100 K s^{-1}, and allow the use of conventional casting techniques [2], [3], [4]. In these systems, the critical condition for glass formation is not the cooling rate, but the level of undercooling that can be achieved in the metastable liquid state. More details regarding the theory of glass formation and glass forming alloys are highlighted in section 1.2.

The discovery of this new class of alloys gave a new boost to scientific interest of the material's science community in metallic glasses. After all, these materials offer attractive qualities, combining some of the desirable properties of conventional crystalline metals and the formability of conventional oxide glasses. The absence of grain boundaries and dislocations in glassy alloys contributes to the exceptional combination of mechanical, magnetic, chemical and tribological properties. For example, metallic glasses possess a room-temperature strength much

closer to the theoretical strength than their crystalline counterparts due to the absence of dislocations. Likewise, the lack of magnetocrystalline anisotropy provides metallic glasses with excellent soft-magnetic properties [5], [6]. Section 1.4 deals in further details with the exceptional mechanical (elastic) properties and gives a extended discussion on the plastic deformation behavior and the limited plasticity, up to date the major drawback of bulk metallic glasses. In section 1.5, a brief overview of possible applications is illustrated.

1.2 Glass formation

1.2.1 Definition of a glass - glass transition

A perfect crystalline solid has a completely ordered arrangement of its constituents, while real solids have imperfections of many kinds. However, when the order present is marginally greater than for liquids, but considerably less than in a perfect crystal, the substance is referred to as a *non-crystalline solid*.

In general, when a liquid is *cooled*, its free volume decreases, and the amount of short range order increases. As a result the mobility in the liquid decreases, measurable through reduced values for diffusion constants and increased values of viscosity. The time scale for relaxation of the liquid becomes longer. At a certain point, the relaxation times become too large and equilibrium cannot be maintained any longer. In fact, this time scale exceeds the time scale of the experiment and the material behaves more like a solid than like a liquid. This transition, where the equilibrium configuration become inaccessible, is called the *glass transition*. A glass is then defined as a liquid cooled below its glass transition temperature . Similarly, upon *annealing*, glasses typically do not melt at a sharply-defined temperature, but soften over a temperature interval, the glass transition . Above the glass transition region, it becomes a supercooled liquid, metastable with respect to crystallization, but in thermal equilibrium and still in the amorphous state.

This glass transition effect is a purely kinetic phenomenon, only observable due to the finite heating rate of the experiment during which it is measured [7]. The glass transition temperature itself is not a constant of the materials, but is a function of the experimental conditions. Slower cooling rates will move the glass transition temperature to lower temperatures and vice versa. At each cooling rate,

the glass will thus freeze in a different state of internal energy. The ideal glass transition temperature would only occur upon infinitely slow cooling [8], [9], [10].

1.2.2 Classical crystallization theory

Crystallization of conventional metals from the melt occurs through two processes: *nucleation* of stable seeds and *growth* of these seeds to grains. Lowering the solidifying system's free energy ΔG is the driving force for the whole solidification process [11, 12].

However, the formation of small particles of the new phase involves the creation of an interface, and thus an increase of the free energy of the system:

$$\Delta G* = -\frac{4\pi}{3} r^3 \Delta g_v + 4\pi r^2 \gamma_{sl}. \tag{1.1}$$

Growth will only lead to a decrease of the free energy, once the nucleus has grown to a critical size $r = \frac{2\gamma_{sl}}{\Delta g_v}$ for which $\Delta G*$ in Eq. (1.1) becomes maximum. In the above equations, Δg_v is the difference in free energy between volume units of the crystal and the liquid and γ_{sl} is the interfacial energy between the crystal and the liquid.

Eq. (1.1) described above is strictly valid only in case of *homogeneous* nucleation, where nucleation occurs throughout the volume of liquid without an association with any catalytic nucleation sites. For the majority of processing conditions, nucleation is initiated with a lower activation energy at certain nucleation sites, e.g. at the surface with the mold or at impurities distributed within the bulk volume of the liquid. The activation free energy for this *heterogeneous* nucleation $\Delta G*$ is lowered with a factor $f(\theta) = \frac{(2+\cos\theta)(1-\cos\theta)^2}{4}$.

A general expression for the steady state nucleation rate, assuming that it follows an Arrhenius law, can be expressed as:

$$I_n = \Omega e^{-\frac{\Delta G*}{kT}} \tag{1.2}$$

where the increase of the nuclei density is considered independent on the size of the respective nuclei. The kinetic prefactor Ω takes into account the number of potential sites for heterogeneous or homogeneous nucleation, as well as the temperature dependence of the mobility in the liquid [11]. Assuming that the mobility for nucleation is proportional to the fluidity of the liquid, the temperature

dependence of the kinetic prefactor Ω in eq. (1.2) is usually described by the Vogel-Fulcher equation for viscosity:

$$\Omega(T) = \Omega'(T)/\eta \tag{1.3}$$

with

$$\Omega'(T) = \frac{Nk_BT}{3\pi r_{at}^3} \tag{1.4}$$

where N is the number of potential nucleation sites and $r_{at}^3$is the atomic radius, and $\eta = \eta_\infty \exp(\frac{DT_{VF}}{T-T_{VF}})$ where η_∞ is the high temperature limit of the viscosity, D is the fragility index, and T_{VF} is the Vogel-Fulcher temperature.

In case of continuous cooling, Eq. (1.2) requires some modification: the total number of nuclei N formed during cooling from T_M to T_N at a constant cooling rate β becomes

$$N = \frac{1}{\beta}\int_{T_N}^{T_M} I_n(T)dT. \tag{1.5}$$

The formation of a stable nucleus is followed by their subsequent *growth*. The velocity of this growth is determined by the balance between the frequency of adhesion of atoms to the growing crystal and the dissolution of atoms into the remaining disordered phase, leaving the crystal.

In the general *kinetic* theory of growth, two main types of thermally activated growth are recognized: interface controlled and diffusion controlled.

Interface growth is controlled by processes in the immediate vicinity of the boundary. This means that there is continuous growth at all points of the boundary or the interface is stepped on an atomic scale, and atoms are transferred from one phase to the other only at these steps. When crystals grow by interface control, the growth rate u can be written [12]

$$u = (\frac{fD_c}{\lambda})(1 - e^{-\frac{\Delta G_v}{kT}}) \tag{1.6}$$

where D_c is the kinetic coefficient governing the rate of transport at the crystal/liquid interface, f is the interface site factor that expresses the fraction of sites on the interface to which an atom can attach. The quantity $(1 - e^{-\frac{\Delta G_v}{kT}})$ is the thermodynamic factor determining the probability that an atom on the crystal surface will remain there, rather than jumping back into the liquid.

Diffusion controls the growth when the nuclei are richer in solute atoms than

the liquid (or vice versa). This can lead to the presence of a region depleted (or enriched) in solute atoms formed around the crystals as growth proceeds. The continual growth of the particles requires chemical diffusion, and as the particle increases in size, the effective distances over which diffusion takes place may also increase. Therefore, grain radius R of a crystal growing by a diffusion controlled process, as a function of time t is given by [13]:

$$R(t) = \lambda_s \sqrt{D_s(t - t_s)}, \tag{1.7}$$

with λ_s a parameter determined by the solubility of solute elements in both the liquid and the solid phase, D_s the diffusion coefficient of the solute element in the liquid phase and t_s the moment of nucleation.

1.2.3 Glass forming ability

A glass completely free of any crystallinity would require the absence of any nucleation during cooling from the melt until the glass transition temperature. Calculations in conventional (non-metallic) glasses predicted that to fulfill this rigorous definition e.g. As_2O_3 would have to be quenched at 10^7 K/s, which is inconsistent with experimental observations for that particular alloy [14]. In practice, it is not necessary to avoid any nucleation.

Equations (1.2)- (1.4) demonstrate that the nucleation rate itself for metallic glasses shows already a strong temperature dependence. This temperature dependence originates both from thermodynamic as well as from kinetic factors, expressed by the prefactor. Above the liquidus temperature, the liquid is thermodynamically stable, so no crystals can form and the nucleation rate is zero. The higher the undercooling below the liquidus temperature, the larger becomes the thermodynamic driving force for crystallization, which would increase the nucleation rate. However, concurrently, at lower temperature, the mobility within the liquid decreases (expressed by the lower kinetic prefactor in case of the nucleation rate), resulting in an optimum temperature for nucleation. Plotting Eq. (1.2) and (1.6) versus temperature (Fig. 1.1), one can easily see that the maximum rate for growth kinetics typically occurs at higher temperatures while nucleation is favored at lower temperatures. In the limit, a system will be able to form a glass when a temperature range exist where nucleation and growth rates do not overlap. It

may be virtually impossible to avoid forming a nucleus, but those nuclei that do form, will probably not be able to grow to a meaningful size, detectable by most experimental techniques [8], [15].

For a long time, it was generally assumed that good glass formers would be characterized by large critical nuclei, or large values of interfacial energy between crystal/(supercooled) liquid. However, recent work on a variety of Zr-based glass forming systems revealed that the best glass formers surprisingly showed a low value for this parameter [16]. This result indicates that the main determining parameter in glass forming systems is in fact the viscosity.

Since both I and u vary with η^{-1}, glass forming ability is usually expressed through the reduced glass transition temperature $T_{r,g} = \frac{T_g}{T_m}$. On the other hand, once a glass is formed, its stability against crystallization can be expressed by $\Delta T_x = T_x - T_g$, with T_g, T_x and T_m the glass transition, crystallization and melting temperatures respectively [10].

1.2.4 Application of classical nucleation theory for metallic glass

Classical nucleation theory ignores several important aspects of nucleation in bulk metallic glass forming liquids. For example, it is questionable whether a description of the steady state nucleation rate is applicable to the instantaneous nucleation rate during continuous cooling. In addition, the use of the Vogel-Fulcher theory to describe the kinetic effects on the nucleation rate might not be correct. Viscous flow in bulk glass forming liquids involves cooperative motion of a large number of atoms [17]. Crystal nucleation involves local rearrangements of atoms with respect to their nearest neighbors. It has been shown that at low temperatures the diffusivity of small atoms may be orders of magnitude faster than predicted on the basis of viscosity [18]. Conversely, at high temperature the cooperative motion required for viscous flow may be hindered in the vicinity of a crystal, so that the mobility may be lower than expected on the basis of viscosity [8].

Nonetheless, classical nucleation theory provides a simplistic description of the complex process of nucleation in bulk metallic glass forming liquids. Nucleation rate varies over many orders of magnitude between the liquidus temperature and the glass transition temperature, and classical nucleation theory does capture the essential features of this temperature dependence. As a liquid is cooled from the

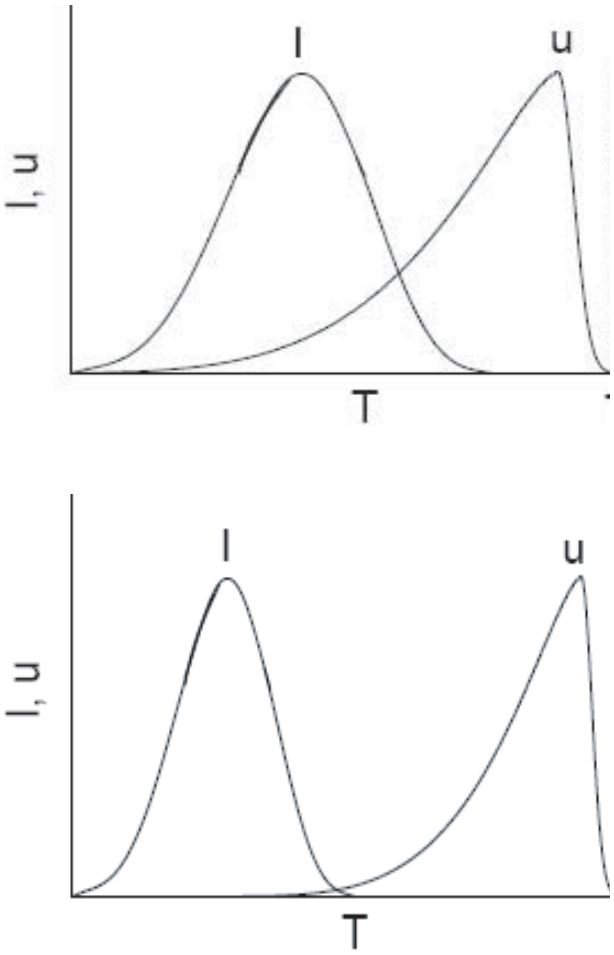

Fig. 1.1: Schematic representation of nucleation and growth. In the limit, when no overlap occurs (bottom part), a glass is obtained.

melt, the nucleation rate initially increases with increased undercooling below the liquidus temperature and then decreases again as the mobility in the liquid decreases. This is in agreement with experimentally determined TTT-diagrams.

1.2.5 Glass forming systems

Glass formation requires the stabilization of the amorphous structure and suppression of crystallization.

Applying extremely *high cooling rates* ($10^5 - 10^6$K/s) was one the most straightforward methods to obtain such glassy structures. However, this requires special casting techniques and limits the sample size on the micrometer scale to thin ribbons.

To increase size to the mm- (and even cm-) range and thus to produce so-called "bulk" metallic glasses was to frustrate the process of crystallization by introducing *"chemical" disorder*. This is done by making a *multicomponent* alloy, composed moreover of atoms of different sizes and valences. Such a multicomponent alloy with chemically different elements forms a dense "random-packed" structure [1], which limits strongly the atomic mobility, necessary for crystallization [19]. However, it is not only kinetics that are suppressed in this way. Thermodynamically, this difference in size and valence introduces local atomic-level strains, which are more easily accommodated by the liquid phase, due to its configurational entropy, than is done by the crystalline phase [20], [21]. Besides this size and valence difference, a negative enthalpy of mixing between the various elements has often been reported to be a necessary condition to obtain a glass [19]. However, recently, systems with at least one pair of elements with a positive heat of mixing have been reported, leading to two-phase amorphous systems [22].

The process of making metallic glasses is illustrated schematically in Fig. 1.2. Where initially the "nose" of a time - temperature - transformation (TTT) diagram of a certain system had to be avoided to exclude crystallization by applying very fast quenching rates, this is now overcome by moving the nose (and the TTT-curve) itself towards longer transformation (crystallization) times, by changing the composition and introducing chemical disorder.

Finally, glass forming ability implies external parameters as well such as the

[1] Note that in metallic glasses no "random-packed" structure is presented, but a certain degree of short- and even medium range order is present, as is explained in the next section.

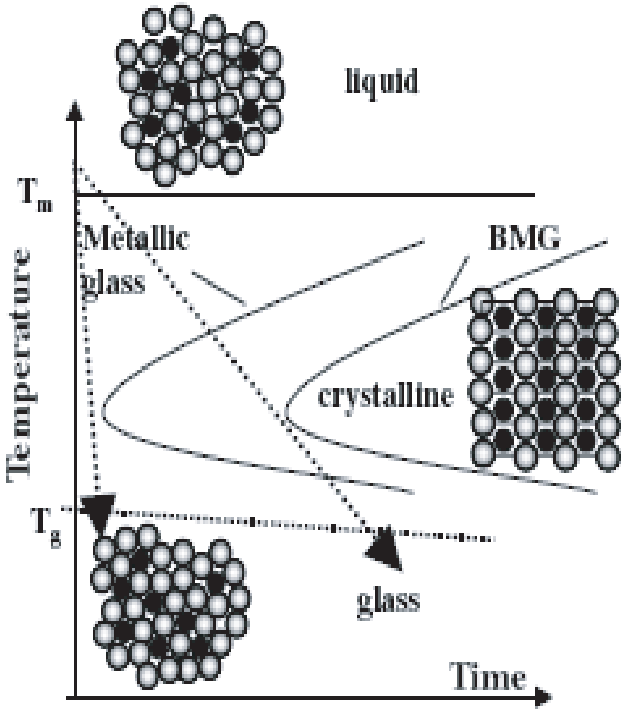

Fig. 1.2: Schematic time temperature - transformation diagram of glass formation during quenching from the melt. Comparison between metallic glass (ribbon) and bulk metallic glass [23].

cooling rate above mentioned. Further, purity plays an even important role; this purity applies both to the environment (high level vacuum upon casting) as to the elements of the alloy to suppress heterogeneous nucleation. This purity can be improved by e.g. fluxing techniques [24] or electrochemical deoxidation of the melt [25].

These bulk glassy samples can now be produced by conventional metallurgical casting methods, which will be explained in section 2.1.

1.3 Structural Aspects of Metallic glasses

1.3.1 Short- and medium-range order - theoretical aspects

Like normal glass, metallic glasses lack long-range order. This lack is signalled by the absence of sharp Bragg peaks - features characteristic of a periodically structured material - in the angular distribution of diffracted beams used to probe

them.

These missing peaks and the fact that glasses are in fact supercooled liquids led early researchers to consider atomic packing in metallic glasses to be similar to the "dense random packing of hard spheres" in conventional liquids [26]. In this theory, the larger atoms are randomly, but densely distributed, with the smaller (solute) atoms jammed into cavities left available by the geometry of this packing. However, these so-called Bernal holes are too few and too small to host solutes in metallic glasses. Another model, the stereochemically defined model, which is used for oxide glasses, was able to reproduce a short-range order structure, observed in compositionally similar crystalline metallic alloys [27].

However, these models failed to give an unmistakable explanation why in metallic glasses atomic sizes have to be significantly different, as discussed above - the dense random packing was also found in systems of equally sized spheres [26]. Neither do they provide a simple, general description for the medium-range order (order on the range of 1-1.5 nm) later established in metallic glasses [28], [29].

Nonetheless, a significant *short-range order* (SRO) should exist, consistent with low entropy [30], large negative heat of mixing [19] and the density of the glass that is only marginally ($\leq 0.5\%$) lower than the same alloy in the crystalline state [31].

The principle of efficient filling of space, an important principle behind the dense random packing and stereochemically defined models, remains the inspiration of the currently generally accepted model of *efficient packing of clusters* (ECP), which describes a new way to achieve dense atomic packing. *Solute-centered clusters* with mostly solvent atoms in the first coordination shell give efficient local atomic packing when the solutes have particular radius ratios relative to the solvent, and form the local representative structural elements of metallic glasses [28]. The precise form/size of such a cluster depends on the ratio of the effective sizes of solute and solvent atoms, which also determines the competition between several types of solute-centered clusters in multi-component alloys [32], although other sources attribute this competition to the heat of mixing between the various elements [33].

The nature and degree of short-range order depends on topology, electronic structure and can be sensitive to composition, even to very small changes of this composition [34].

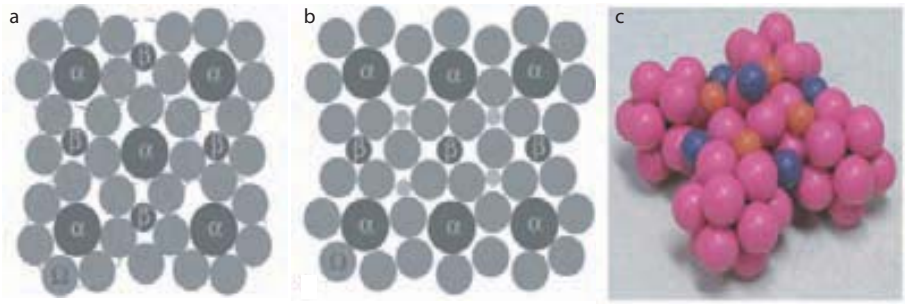

Fig. 1.3: (a)Two-dimensional schematic representation of the efficient cluster packing model: efficiently packed solute-centered (α, β) clusters, organized with cubic-like (fcc) packing over a restricted length scale, with overlapping nearest-neighbor clusters, sharing solvent atoms (Ω). (b) Cavities exist even in this efficiently packing of clusters, into which additional solute species (of suitable size) can be introduced. (c) Three dimensional representation of a cubic packing of icosahedral clusters. [32]

Besides this short-range order, a surprisingly *medium-range order* (MRO), i.e. order up to the 1 nm range (typical atom diameter is about 0.3 nm [29]) was established in metallic glasses.

This can be explained by the spatial organization of the above described solute-centered clusters, which is driven by a solute-solute avoidance. This avoidance leads to an efficient packing even beyond the nearest-neighbor shell.

A first proposal to describe this medium-range order was a dense packing of overlapping atomic clusters into an arbitrary 'face-centered cubic'-like lattice (note that the fcc lattice is the densest possible cubic packing), as illustrated in Fig 1.3a. To maintain long-range disorder, i.e. to keep the material glassy, a strain factor was introduced to limit coherence of such a lattice to the 1-1.5 nm scale. This results in a lack of orientational order between the clusters and randomly placed solvent atoms [28], [32].

Besides this cubic-like medium-range order of solute-centered clusters for a length-scale of a few cluster diameters, others have suggested icosahedral cluster packing on the medium range order [29], [35], independent whether the clusters themselves are icosahedral or cubic in nature. Both possibilities are currently being considered, and could be even essentially equivalent [28]. Note that both models lead to an effective packing of various clusters but generate interstitials between the various clusters, as shown in Fig. 1.3b. Inside these open spaces, other solute atoms, if available and of the right size, can be placed, improving

packing and thus glass forming ability.

1.3.2 Medium-range order - experimental observation

Whereas much information came from simulations in the past, current experimental techniques show to be promising to resolve further questions on medium-range order. For example, the ability to deconvolute the total diffraction signal into separate signals of each pair of atomic constituents gives a powerful tool for exploring the structure of metallic glasses [23], [36]. One of these experimental observations is that BMGs have a high degree of short- and medium-range order already in the melt. Glasses are indeed supercooled liquids, but the metallic glass forming liquids already show a high degree of the short- and medium-range order described above. The different kinds of atoms form complex clusters in the melt with a well defined short-range order. These structural results are in accordance with measurements of the viscosity of the melt, which is found to be three orders of magnitude higher for bulk glass-forming alloys compared to that of simple metals [23]. Furthermore, by suited conditions in transmission electron microscope, it has been possible to image selectively atomic clusters in an amorphous matrix as high-contrast lattice fringes. Under suited defocus, bcc atomic clusters in an amorphous $Fe_{84}B_{16}$ [37] and fcc-clusters in amorphous $Pd_{77.5}Cu_6Si_{16.5}$ [38] and $Pd_{82}Si_{18}$ [39] were observed, already in the 1980s and 1990s. Finally, three-dimensional atom probe and fluctuation electron microscopy (FEM) give chemical information with near-atomic spatial resolution across meaningful length scales. FEM has been successfully applied to probe MRO in amorphous materials [40].

Short- and medium-range order control glass formation and stability, e.g. crystallization products will show similar local order, different structural order is difficult. Furthermore, they influence physical properties of the glass and recently, it is suggested that already the short/medium range order may influence the mechanical behavior of metallic glasses [28], [41], [42].

1.3.3 Free volume

1.3.3.1 Theory

When a metallic glass is quenched from the liquid state through the glass transition, an amorphous structure results with a specific volume dependent on the

cooling rate.

The concept of free volume was initially developed by Cohen and Turnbull for liquids [43] and was later extended by Spaepen for metallic glasses [44]. According to Cohen and Turnbull, free volume in an amorphous structure is defined as excess volume, retained within the disordered state of the atomic configuration. A site in the structure where the free volume exceeds a certain critical value comprises a defect wherein the atomic mobility is enhanced locally. The enhanced atomic mobility at the defect sites would make them preferred facilitators of diffusion and plastic flow.

According to the free volume model, the probability for an atom to have a free volume with a size between ν and $\nu + d\nu$ is

$$p(\nu)d\nu = \frac{\nu_f}{\gamma} \exp(-\frac{\gamma\nu}{\nu_f}). \tag{1.8}$$

γ is a constant of the order of unity that takes into account overlap of free volume between neighboring atoms and ν_f is the average free-volume per atom. The total probability, c_f, that a free volume fluctuation is formed with a minimum size $\nu*$ which makes a diffusional jump possible, is given by:

$$c_f = \int_{\nu*}^{\infty} p(\nu)d\nu = \exp(-\frac{\gamma\nu*}{\nu_f}) = \exp(-\frac{1}{x}), \tag{1.9}$$

with x the reduced free volume. The diffusivity in this context is given by:

$$D = ak\lambda^2 c_f, \tag{1.10}$$

with a a geometric factor, k the atomic jump frequency and λ the average jump distance. This equation gives rise to the Vogel-Fulcher law for viscosity in liquids.

When a liquid is rapidly cooled, the system freezes and the value of ν_f remains high. If the rapidly cooled glass is annealed, structural relaxation takes place and ν_f decreases.

1.3.3.2 Experimental evidence versus limitations of the theory

Although the free volume theory has some limitations and is in fact not quantitative valid for metallic glasses, experimental evidence of certain open spaces and its changes upon annealing have been reported in literature, by means of in-situ synchrotron diffraction [45], [46], by a combination of density measure-

ments and differential scanning calorimetry [47] and by positron annihilation spectroscopy [48], [49].

A first limitation is that the original theory was developed based on dense packing of hard spheres, which is clearly not valid in metallic glasses. However, the ECP theory described above also leads to the generation of open spaces (Fig. 1.3) and density fluctuations between the clusters, and thus the free volume stated in these research works could still be interpreted in this context.

Secondly, molecular dynamics simulations of diffusion in glasses revealed that diffusion does not occur by a single atom jump, as assumed in the free volume theory, but rather by a collective process, where chain actions occur [17].

Furthermore, the quantifications deduced from the free volume theory use only one macroscopic average, while a distribution in sizes of open volume was observed by positron annihilation spectroscopy, and this distribution seemed to depend also on the atom type [48]. Most recent results [49] suggested the existence of three types of open spaces. A first type would be the interstitials described above, similar to interstitial positions in crystals. Surprisingly, also vacancy-like defects as described originally in the theory of Spaepen [44] were detected, but they only constitute less than 1% of the total open volume. Finally, a third type with intermediate, though relatively long, lifetime, composes about 15% of the total open volume, and was interpreted as a *distribution* of open spaces, in agreement with the observed chain-like diffusion mechanism . Note that such a distribution was already suggested by Argon [50]. Thus rather than existing as distinct, concentrated vacancies, the open volume regions are most likely distributed arrangements of microscopic free volume sites. These entities do not only play a dominant role in diffusion processes, but form also the basis for deformation in metallic glasses at the atomic level. In this context, they are referred to as flow defects or shear transformation zones [28]. The deformation behavior of metallic glasses forms the topic of the following section.

1.4 Mechanical behavior of metallic glasses

1.4.1 Introduction

Fig. 1.4 compares the (uni-axial) mechanical properties of a typical bulk metallic glass and a typical high-strength steel (HSLA - high strength low alloying), in

compression. A detail of the elastic region is shown in the inset.

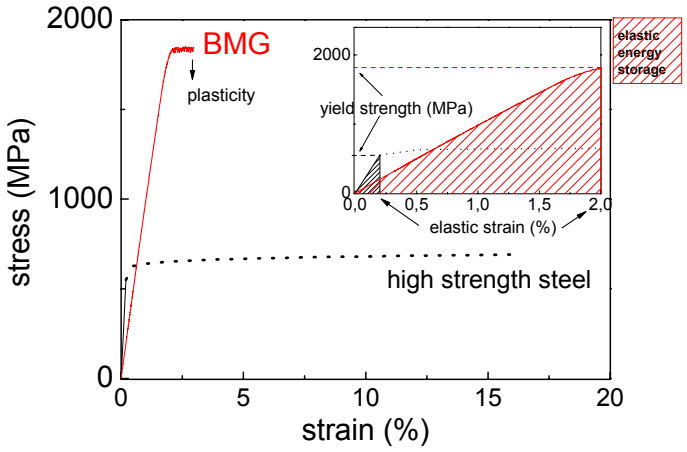

Fig. 1.4: Comparison of the mechanical properties of a typical BMG (in compression) and a typical high strength steel (HSLA) (in tension). Data of the latter were obtained from [51]. A detail of the elastic region is given in the inset.

Although a HSLA steel has one of the highest limits of elastic strength among conventional metallic alloys, it can be easily seen that the elastic strength of a BMG is much larger than the value of the HSLA steel. On the other hand, the elastic modulus can typically be up to 30% lower than the one of corresponding crystalline structures. Metallic glasses do not possess slip systems and lattice dislocations as in crystalline materials [52], which allow changes in the atomic neighborhood at low energies or stresses in crystalline materials. Local arrangement of atoms in metallic glasses is a relatively high-energy or high-stress process. Due to the combination of this high stress and a relatively low elastic modulus, they manifest elastic deformation of more than 2% before yielding - in conventional metallic alloys this is about 10 times lower. Similarly, metallic glasses can absorb up to 30 times more elastic energy, which is represented by the surface area under the curve in the elastic region (Fig. 1.4 inset), offering them possibilities for mechanical energy storage for example.

Despite their exceptional elastic properties, a large amount of BMGs lack plasticity: the BMG shown in Fig. 1.4 fails almost immediately once plastic deformation set in, while a typical high strength steel can take up to 20% of plastic

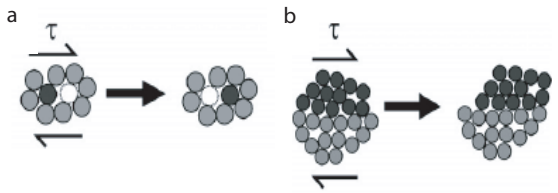

Fig. 1.5: Two-dimensional schematics of the atomistic deformation mechanisms proposed for amorphous metals. (a) local atomic jump - free volume model (b) shear transformation zone. [54]

deformation in tension and over 70% in compression.

1.4.2 Atomic-level mechanisms

It is generally accepted that the fundamental unit process of deformation involves a local rearrangement of atoms that can accommodate shear strain. A first viewpoint on the mechanism of plastic flow was given by the classical "free-volume" model. This model views deformation as a series of discrete atomic jumps in the glass, as illustrated in Fig. 1.5 a, at sites where the excess free volume is large enough, which in fact is a diffusion-like process. However, strictly spoken, volume should not be affected by shear, only by purely hydrostatic stresses. Egami calculated further that a dilatation of less than 10% was sufficient to change the atomic environment [53], instead of the 80% critical free volume suggested by the free volume model. Furthermore, the amount of free volume necessary for atoms to move in local shear transformations appears to be much smaller than the amount of free volume for diffusion [53].

Therefore, a second type of deformation unit, developed by Argon in 1979 [50] and meanwhile confirmed by simulation studies [17], is referred to a shear transformation zone. The STZ is essentially a local cluster of atoms that undergoes an inelastic shear distortion from one relatively low energy configuration to a second low energy configuration, crossing an activated configuration of higher energy and volume. In contrast to the free volume model, where atomic rearrangement occurs highly localized, the activation of a STZ involves a subtle redistribution of many atoms over a diffuse volume (Fig. 1.5). These clusters comprise a few to sometimes around 100 atoms, depending on glass composition, as commonly observed by simulations [55]. The STZ that is activated first from among the

different potential sites, depends on energetic changes, correlated with the local atomic arrangements.

Although the classical free volume theory fails to explain certain aspects of *metallic* glass deformation, it offers an intuitive and easy representation of several aspects in metallic glass science and a simple mechanism to describe deformation. In fact, despite the differences between the two models described above, they share several common features, crucial to the understanding of macroscopic deformation response of metallic glasses. Deformation involves thermal activation and dilatation. For example, the local distribution of free volume is widely believed to control deformation of metallic glasses, where sites with a higher amount of free volume will accommodate local shear more easily and STZs will be activated more rapidly at those sites. However, other variables, like topological and chemical short range order are expected to influence local shearing as well, as suggested by atomistic simulations [54], [56].

The atomic level mechanisms that were described here qualitatively form the basis for the understanding of metallic glass deformation, both elastic and plastic deformation.

1.4.3 Elastic deformation - mechanical strength - elastic constants

Because the bonding in amorphous alloys is of primarily metallic character, strain can be readily accommodated at the atomic level through changes in the neighborhood: atomic bonds can be broken and reformed at the atomic scale without substantial concern for e.g. the rigidity of the bond angles as in a covalent solid or the balance of charges as in an ionic solid. This explains the relatively low elastic modulus [54]. However, due to the absence of dislocations, local arrangements require a much larger energy than in crystalline materials.

From a fundamental point of view, however, it is useful to consider the bulk modulus ($K = \frac{E}{3(1-2\nu)}$) and shear modulus ($\mu = \frac{E}{2(1+\nu)}$), instead of the elastic modulus E and the Poisson ratio ν. These constants represent the response to pure hydrostatic stresses (K) and pure shear stresses (μ). The former involves bond stretching/compression only while shear stresses cause bond distortion.

The bulk modulus of amorphous alloys is typically only 6% smaller than for crystalline alloys of similar composition. The short-range order and thus the cohesive forces between crystalline and amorphous metallic structures can be assumed

to be equal. On the other hand, metallic glasses are slightly less dense $(0.5-2\%)$ and thus have a larger atomic separation than their crystalline counterpart, which explains this small difference in bulk modulus.

In contrast, the response of metallic glasses to shear stresses is significantly different from that of crystals, illustrated by their smaller values of shear and elastic moduli. The difference of about 30% is too large to be adequately explained by a change in atomic spacing alone. In a crystal, each atom experiences a displacement that is defined by the macroscopic strain. An unrelaxed glass has a wider range of different atomic environments (distribution of sites with different amounts of free volume), allowing local atomic displacements that differ from those prescribed by the macroscopic strain. These internal rearrangements reduce the shear modulus by about 30%, as evidenced by simulations, in agreement with the experimental observations [54].

1.4.4 Plastic deformation - Catastrophic failure

Plastic deformation in metallic glasses on the macroscopic scale is essentially an interplay between an accumulation of local strains, caused by the operation of STZs and the redistribution of free volume.

Whereas at high temperature, activation of STZs and deformation occur homogeneously distributed all over the sample, at low temperatures (typically $T/T_g < 0.9$) deformation occurs *localized*. When the yield strength is exceeded, only few energetic favorable STZs (locally perturbated region) are activated.

For an individual STZ with a volume Ω_0 which sustains a shear strain γ_0, Argon calculated the (Helmholtz) free energy required to operate a single STZ, in terms of the elastic properties of the glass as:

$$\Delta F_0 = (\frac{7-5\nu}{30(1-\nu)} + \frac{2(1+\nu)}{9(1-\nu)}\beta^2 + \frac{1}{2\gamma_0}\frac{\tau_0}{\mu(T)})\mu(T)\gamma_0^2\Omega_0 \tag{1.11}$$

where $\mu(T)$ and ν are the temperature-dependent shear modulus and Poisson's ratio of the glass, respectively, and τ_0 is the ideal shear strength of the STZ, i.e., the athermal stress required to activate the shear transformation. The parameter β is a numerical constant that describes the volumetric dilatation of the STZ relative to its shear distortion, and is about equal to unity for amorphous metals [50].

Johnson and Samwer developed a cooperative shear model to describe the *activation* of plastic *yielding* of metallic glasses in the glassy state below T_g [57]. They related the barrier for shear flow W to a universal critical yield strain γ_C, the shear modulus μ and the effective volume of shear transformation zones $\Omega_{eff} = \zeta\Omega$ by:

$$W = (\frac{8}{\pi^2})\mu\gamma_C^2\zeta\Omega. \tag{1.12}$$

The core volume of a STZ is Ω and ζ is a correction factor, taking into account the confinement by the matrix, with a value roughly between 2 and 4. The relation predicts that the barrier height for shear flow for a given configuration is proportional to μ and depends on the size of a STZ. The characteristic strain (γ_C) or "configurational displacement" separating neighboring configurations will increase in small STZ volumes. On the other hand, the total barrier W will increase with increasing STZ volume Ω. Therefore $W \sim \Omega\gamma_C^2$ is expected to have a minimum for some intermediate volume, which they estimated and later confirmed to be on the order of some 100-120 atoms [55]. Yielding occurs when the applied stress causes a critical density of such a "minimum" barrier STZs (thus of suited size) to become unstable [57].

Increasing the applied stress and stress concentrations ahead of the shear front lead to the activation of each time more STZs, along certain preferred directions (i.e. direction of maximum shear stress), leading to the creation of a shear band nucleus [58], [54]. The transition of a nucleus into a real shear band occurs through autocatalytic directed growth, characterized by the partitioning of strain rate from the bulk into the shear band. The more deformation is localized into these shear bands (as compared to the rest of the matrix), all the more the deformation will have an inhomogeneous character and catastrophic failure. This localization is generally believed to be caused by a local change in the state of the glass.

In the free volume model, this localization is the consequence of an increase in free volume, necessary to force the atom into a "vacancy" that is in fact not sufficiently large for the atom to jump into, but is forced into it by external forces [44]. In other models, it is a decrease of the local structural order, caused by the forced breaking up stiff bonds and rearrangement of less stiff atomic bonds [53]. Both excess free volume and/or rearrangements of bonds reduce the viscosity within such a shear band and lead to dilatation.

Furthermore, local temperature rises within a shear band due to the dissipation of elastic energy [59] which on its turn leads again to a strong decrease in viscosity. This shear and thermal softening leads to further localization of plastic flow and additional heating within this same shear band. In such a self-accelerating process, only a few shear bands can be generated in an unconstrained geometry and the specimen fails catastrophically shortly after yielding [54], [60].

1.4.5 Possible mechanisms to improve plasticity - overview of literature data

If shear band propagation is not constrained in some manner, plastic strain accumulates on one dominant shear band which reaches the critical value for shear displacement at which point fracture initiates. Thus, fracture occurs with only limited macroscopic plastic strain. However, if it were possible to limit the propagation of individual shear bands and thus distribute the plastic strain over many bands, then the onset of fracture might be delayed and significant macroscopic plastic strains could be realized. Recently, several BMGs with various compositions showed some surprising extensive plastic deformation in compression or bending.

Different explanations have been given for factors contributing to plasticity of BMGs. Probably the two most explored approaches to distribute shear bands are the *intrinsic* approach, related to the elastic properties of the alloy [61], [62], [63], [64] and the *extrinsic* approach, related to the formation of composite structures on different length scales. The latter group can further be divided in ex-situ and in-situ techniques, depending on how this inhomogeneous composite structure was obtained. Both structural [65], [66] and/or chemical [67] inhomogeneities have been reported to improve plasticity.

In the following sections, these mechanisms proposed/proven to improve plasticity are discussed in further detail.

1.4.5.1 Optimization of elastic constants - Critical Poisson ratio

In 2004, Schroers and Johnson reported for the first time on a *monolithic* BMG with up to 20% plastic strain in unconfined uniaxial compression testing. They attributed this large plasticity to a high value of the Poisson ratio (or low ration of shear to bulk modulus μ/K), in accordance of what is observed in crystalline materials [61].

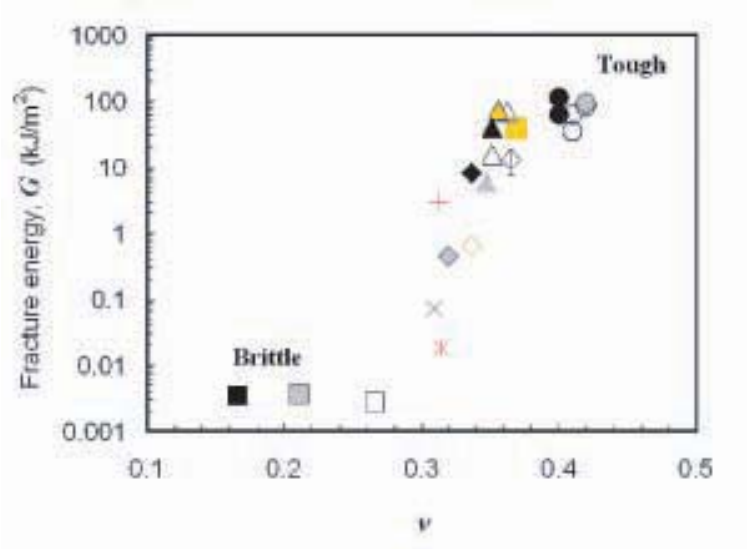

Fig. 1.6: Illustration of the relation between the Poisson's ratio of several metallic and oxide glasses and their fracture energy (toughness) [62]

In 2005, Lewandowski and co-workers found a correlation between the ratio $\mu/K \sim \nu^{-1}$ and fracture energy (alloys with $\mu/K < 0.41$ are tough, alloys with $\mu/K > 0.43$ brittle) for about ten different BMG compositions as well as oxide glasses (Fig. 1.6). They interpreted this in terms of a competition between plastic flow and fracture [62]. Schroers and Johnson rationalized it in terms of a competition between shear and dilatation [61].

A low value of μ implies a weak resistance to plastic deformation in shear, in accordance with Eq. (1.12), while a high value of K implies a strong resistance to dilatation (and thus resistance against strain softening).

Later on, similar results for Fe-based metallic glasses confirmed these findings [63].

An additional useful point about the correlations stated by Lewandowski and co-workers could be that it appears possible, at least approximately, to predict the elastic properties of a metallic glass based on an appropriately weighted average of the properties of its constituents. Or the other way around, it might be possible to design a metallic glass composition, with in the first place good glass forming ability, but in addition with the appropriate elastic constants and thus enhanced plasticity. Very recently, Liu et al. [64], followed this approach by adjusting the

composition of a $Zr_{65}Cu_{15}Ni_{10}Al_{10}$ in such a way to maximize the Poisson number, the resulting BMGs can sustain extremely high deformation (up to 170%) without fracture both in compression and in bending.

1.4.5.2 Microstructural inhomogeneities

In metallic glass composites, a second phase is introduced in the amorphous matrix, with the twin goals of promoting shear band *initiation*, which distributes the plastic strain more broadly instead of the catastrophic localization, and hindering shear band *propagation*.

As stated above, such inhomogeneities exist in many types. First of all, from micrometer-sized dendrites to atomic scale clusters are being reported to improve plasticity. These inhomogeneities can be structurally/topologically different (crystals in an amorphous matrix, or at least with a higher degree of order) but also purely chemically different, two-phase amorphous alloys have been reported. Basically, two main routes can be distinguished. *Ex-situ*, where second phase particles (particles, dendrites, wires, fibers...) are added to the melt before casting [68], [69], [70]. In the *in-situ* approach, the second phase is "created" from the basic alloy itself. This can be done 1) upon casting, by designing a suited composition [22], [58], [65], [67], [71], [72], [73], [74], [75], [76], 2) after casting, upon annealing above T_g [66] or even up to T_x [77], or 3) during deformation [78], [79].

Again, both crystalline and amorphous with different composition than the matrix have been reported, by various methods described above. Mainly the design of glass forming alloys which contain a pair of elements with positive heat of mixing lead to the formation of two-phase amorphous alloys [73], [74], [67], [22]. Furthermore, such a phase separation has also been reported to occur upon deformation [79]. Although some chemically inhomogeneous glasses exhibit increased plasticity [73], [80], others embrittle [81]. The latter could be related to the intrinsic properties of the respective phases, although this requires further investigation [82].

The mechanism how each type of inhomogeneity contributes to plasticity is expected to depend strongly on its size (and morphology), and forms currently still a very active research area in the field of metallic glasses. An overview of several mechanisms suggested in literature is given below, based mainly on the different length-scales of the second phase.

- Large scale inhomogeneities

  Introduction of large-scale (micrometer-sized) particles and dendrites through both extrinsic and intrinsic approaches have proven to be able to improve both compressive and tensile ductility of BMGs [72].

  These micrometer-sized inhomogeneities are believed to improve plasticity through increased shear band initiation at stress concentrations around these structural inhomogeneities, as suggested by finite element simulations [83]. There are three principal contributions to stress concentrations around second phase particles in a composite [54]:

  1. *Residual stresses* can be present in both particles and matrix, due to thermal mismatch strains, developed during processing.
  2. *Difference in elastic properties* between both phases will cause stress concentrations in the matrix during elastic loads.
  3. At higher loads, *plastic misfit* strains will arise. In particular, softer second phase particles will flow before the yield stress of the matrix is reached. However, the stronger amorphous matrix prevents this yielding, leading to stress concentrations around these particles. Note that softer particles are very effective in this way in improving plasticity, but can decrease strength significantly at high volume fractions according to a rule of mixture: $\sigma_{comp} = \sigma_{matrix} * V_{matrix} + \sigma_p * V_p$.

  Due to these stress concentrations, the yield criterion of the matrix may be satisfied locally around the second phase particles, and shear bands in the amorphous matrix will be initiated. However, at that moment, shear bands do not propagate because the yield criterion of the matrix is only satisfied in the region immediately around the particles. At the higher stresses, the yield criterion is satisfied in large regions of the matrix, allowing extensive shear band propagation and significant macroscopic plastic deformation. The distinction between the stress required for localized yielding on the one hand and that required for shear band propagation and large scale plasticity on the other is illustrated in Fig. 1.7.

  Besides improvement of shear band nucleation, propagating shear bands can also be deflected or even stopped by a second phase, due to interaction

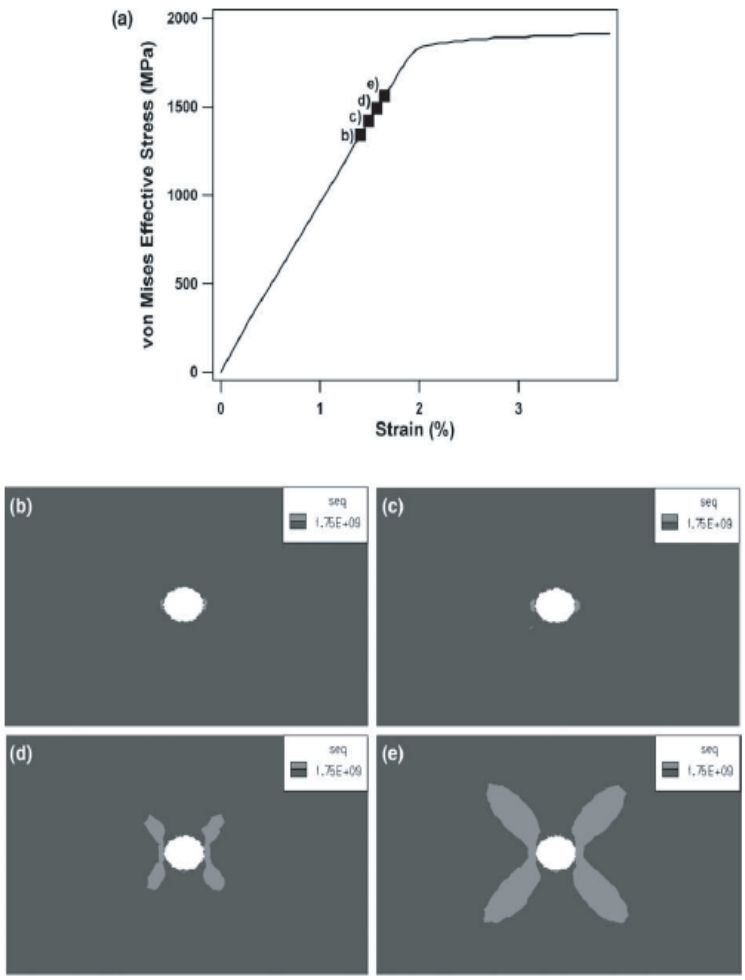

Fig. 1.7: Contour maps of the (von Mises) effective stress around a single particle (white) embedded in an amorphous matrix, obtained by finite element modelling. The images show the results for successive displacement steps increasing from (b) through (e). The light colored areas correspond to regions in the matrix where the von Mises stress is greater than the matrix yield stress. The corresponding stress for the contour maps is noted on the stressstrain curve (a) [83].

between the stress concentrations associated with both the shear front of the shear band and the second phase. This is usually the case for harder second phase particles.

Note that this second phase does not necessarily has to be crystalline. Amorphous regions of different *chemical* compositions may exhibit different critical shear stresses for local yielding, leading to deflection and delocalization. Nanoindentation in such a two-phase amorphous alloy showed clear deflection around globular amorphous regions [22].

- Nanometer scale composites

  Shear bands in metallic glasses have a characteristic thickness of 10 to 30 nm, as revealed both by experimental measurements and atomistic measurements [84]. The discussion above on how a second phase can improve plasticity in metallic glasses is only valid under the assumption that the second phase particles are larger than the characteristic dimensions associated with plasticity in the amorphous matrix. So, the mechanism above is not necessarily true if the second phase is as small as a few nanometer. Nonetheless, nanocrystals/nanocrystalline nuclei as small as 2-5nm have been reported to improve plasticity drastically [66], [85].

  Spatially, the size of the zone under stress concentration due to the presence of a second phase particle scales with the particle size. Even if the magnitude of the stress concentration around the nanocrystal (or nano-sized amorphous region) is large, it might not extend over a region large enough to permit nucleation of a shear band. However, at large volume fractions of nanoparticles, zones around adjacent particles might overlap, so the net effect might still lead to increased shear band initiation [54]. Furthermore, defects, like twins, in such nano-crystals might contribute and extend the stress concentration zones, enhancing shear band nucleation [78].

  Similarly, a single nano-particle has little ability to disrupt shear band propagation. However, collectively, a large volume fraction might affect the rheology of the propagating shear band, taken into account that nanocrystals present in the shear zone before deformation can grow rapidly: the shear zone becomes liquid-like, due to increased free volume and temperature rise,

both reducing strongly the viscosity of a shear band. Active shear bands then constitute of two phases: the glassy phase that behaves in a liquid-like manner and the nanocrystals that are a growing solid phase component. The deformation behaviour is then like that of a semi-solid slurry. Viscosity of such a semi-solid slurry increases with increasing solid fraction, given by

$$\frac{\eta}{\eta_0} = (\frac{1-\Phi_s}{\Phi_c})^{-2.5\Phi_c} \tag{1.13}$$

where η_0 is the viscosity of the liquid phase, Φ_s is the solid fraction of the suspension and Φ_c its maximum fraction of solid component when the remaining liquid is fully trapped (at about 60% solid component). However, major viscosity changes occur already at 10% solidlike volume fraction [66].

- Atomic scale inhomogeneities

  Finally, amorphous structures with improved plasticity have been reported although no clear second phase larger than 2nm could be detected [41], [42]. This improvement was attributed to atomic-scale inhomogeneities, i.e. to the strong short and medium range order clusters that had been observed experimentally by fluctuation electron microscopy [40].

  A special case of such clustered glasses are the so-called M-glasses based on martensitic ingot alloys which exhibit high compressive strength and large plastic deformability [58], [75].

  In extension of the theory described above for nanometersized inhomogeneous glasses, Eckert suggested the following (preliminary) mechanism for deformation in clustered glasses. Glasses with inhomogeneities down to the atomic level can be viewed as a mixture of "solid-like" and "liquid-like" structural entities, where the "liquid-like" entities carry the plasticity. On the other hand, inelastic atomic level structural changes associated with the transformation of liquid-like to solid-like ones (and vice versa) have been reported. Such a transformation of liquid-like to solid-like can be thought to retard the propagation of a shear band drastically and force it to search for other liquid-like regions [58]. In the martensitic glasses in particular, the observed ductility was attributed to a stress induced displacive transformation in the austenite-like clusters to a martensite-like structure, which releases

the stress concentration around STZs and restricts free volume accumulation [75]. Similarly, Sun and co-workers reported on the plasticity improvement in Zr-Cu-Al BMG composites containing martensite phase [76].

However, the role of medium range order on (mechanical) properties and the deformation mechanism is still under investigation.

In addition to the direct effect of second phases, the nucleation "in-situ" of such a second phase can alter the remaining glassy structure which on its turn might affect the mechanical behavior. Very recently, questions rise whether the presence of a second phase itself causes the improved plasticity or whether the change in composition, and thus elastic properties of the remaining matrix might be thought responsible for the improved plasticity. Finally, annealing treatments do not always lead to the expected improvement, due to the occurrence of structural relaxation of the matrix [54].

1.4.5.3 Other parameters affecting plasticity

Macroscopic plasticity and toughness depend on the number of shear bands activated during deformation. Extensive shear-banding has been observed during high-strain rate experiments, both in compression and in tension. At high strain rates, which may even exceed the rate of relaxation by a single shear band, many shear bands are needed to accommodate the imposed strain rate. As a result, multiple shear bands in the entire deformed sample improve plasticity of BMGs [86].

Other experiments suggest that plasticity is strongly affected by the specimen geometry/size, [87], loading conditions (compression/tension/bending/...), surface roughness and (surface) residual stresses, e.g. after shot peening [88]. Constrained deformation methods like nanoindentation, rolling and e.g. the high pressure torsion method allow deformation up to large plastic strains. This can be of technological interest for deformation processing as well as of scientific interest to study the behavior of metallic glasses upon deformation, without early failure [54].

1.4.5.4 Work hardening

In several structurally inhomogeneous BMGs work hardening behavior was observed in the stress-strain curves [75], [89], [90], [91], . The origin of this work hardening behavior, i.e. the requirement of an increase in the applied load/stress

to continue deformation in contrast to the suggested elastic-perfectly plastic or softening behavior, is currently still under discussion. Several explanations have been given to it.

One possible explanation, suggested by Li and co-workers, based on atomistic simulations [92] as well as by Yang and co-workers based on nanoindentation experiments, involves free volume. According to Spaepen's theory, a competition between free volume accumulation due to the applied stress and free volume annihilation by local atom rearrangement occur upon deformation, leading to a net increase of free volume [44]. Therefore, plastic deformation can be considered as a process associated with free volume production, and therefore the energy associated with the plastic deformation under the applied external stress should be related to the formation energy of free volumes. From this argument, Li concluded that work hardening is simply the consequence of the irreversible free volume production under the external stress [92]. Additionally, the increased hardness after each unloading during cyclic nanoindentation experiments [93] was attributed to a net annihilation of free volume upon unloading, causing an arrest of propagating shear bands. Furthermore, the decrease in temperature related to arrested shear bands was thought to play a role in the hardening process as well.

On the other hand, temperature rise at or near the shear bands might lead to the nucleation [78], [90] and/or growth [66] of nanocrystalline nuclei, resulting from an increase in excess free volume and thus atomic mobility. Once grown, these nanocrystals might block propagation of shear bands and cracks [66], [85]. A stress level increase is then necessary to propagate shear which results in work-hardening [82]. A similar explanation was given by Schuh and co-workers. They attributed this apparent "strain-hardening" to the presence of nanocrystals in the shear bands, raising the yield stress of the shear band, preventing its reactivation and forcing initiation of new shear bands elsewhere in the material [54].

However, in the ductile M-glasses, no crystallization of the clusters was observed upon deformation. The stress induced transformation in the austenite-like clusters leads to locally different shear rates inside the shear band, resulting in a wavy (deflected) propagation. An increase in stress is needed to move this slither shear bands, leading to the observed hardening [75].

1.5 Possible applications

From the section above, it is clear that BMGs have outstanding *mechanical*, in particular elastic, properties. The large elastic strain of BMGs enables large reversible deflection and mechanical energy storage. This offers especially good perspectives for applications in sports equipment, pressure gauges, springs with high accuracy,..., if only they are not strained beyond the elastic range where most fail with little macroscopic plasticity. Its high strength and excellent abrasion resistance offer further possibilities for cutting materials with high durability. High strength often allows size (and thus weight) reduction.

Figure 1.8 illustrates two current applications of Zr-based BMG. The first one (top) are diaphragms made of $Zr_{55}Cu_{30}Al_{10}Ni_5$ used for fuel-injection control to lower fuel consumption and thus CO_2 exhaust emissions. They show a greater sensitivity to pressure and strain fluctuations due to their lower E-modulus, while at the same time they have a higher strength than currently used commercial materials. This same combination of properties (high strength, low modulus) allow the production of slimmer and shorter springs (bottom image), which is a hot topic in decreasing the weight of automotive engines by miniaturizing cylinder heads, again leading to a reduction of fuel consumption [94].

Furthermore, the absence of grain boundaries in iron-based compositions leads to excellent soft-*magnetic* properties, like low coercive force and a high permeability, with commercial applications as transformer cores, magnetic read-heads and magnetic shielding [94].

The lack of grain structure and high viscosity offer generally some extra advantages over conventional crystalline materials, making BMGs multifunctional materials with some outstanding properties. For example, it improves the *corrosion* resistance significantly in most common environments [95] as well as cavitation erosion [96]. This on its turn leads to an increased durability of metallic glasses for various applications and can be exploited in particular in corrosion and/or wear resistant coatings, which can often be reduced in thickness as compared to conventional crystalline materials used.

Glasses are structurally very similar to the liquids from which they solidify, leading to low shrinkage upon solidification. This allows near net-shaping, while the absence of grain structure offers a high polish and almost mirror finish directly

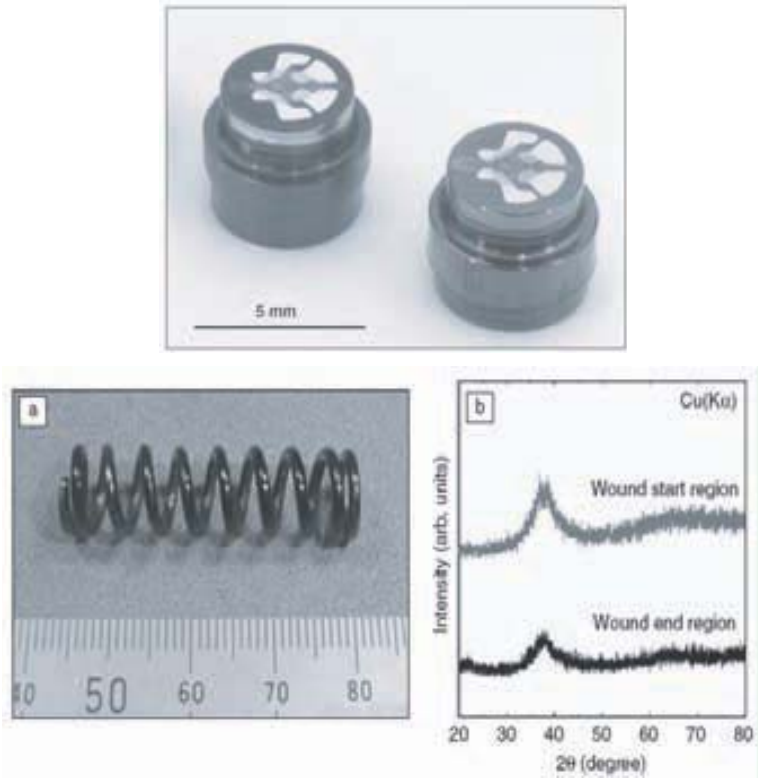

Fig. 1.8: Possible applications for Zr-based BMGs: (up) diaphragms in BMG for fuel injection (under) springs for automotive applications [94].

upon casting, which reduces *processing* costs. Additionally, the large supercooled region allows superplastic forming in that region, without the risk of crystallization. The easy shaping possibility allows the production of complex shapes with high durability, while the surface finish and high hardness offers possibilities e.g. for scratch-free fashion items, like jewelry and casings of mobile devices.

Lack of grain structure and high hardness suggest that features of near-atomic scale could be made, e.g. by molding or etching, without the loss of coherency, with applications as nanowires, tips for AFM, templates for nanoprint lithography... Also micro and nano electro-mechanical systems (MEMS/NEMS) offer outstanding opportunities for the exploitation of metallic glasses. High yield strain, low loss coefficient and good fatigue resistance they require, are perfectly fulfilled by metallic glasses. For all these nanometerscale applications, the lack of ductility is no longer a problem, since the dimension of the application becomes smaller

than the plastic zone around a propagating crack [87].

Nonetheless, the lack of (tensile) ductility for larger dimensions, the cost of the components, the demand of very pure elements, the slow production rate due to vacuum casting techniques and the difficulties of recycling once casted into a product are probably the main drawbacks of this new class of engineering materials [87].

2. EXPERIMENTAL TECHNIQUES

2.1 Preparation techniques

The method used in this work to produce metallic glass is injection casting, which belongs to the broader group of "copper mold casting" techniques (CMC). In fact, this production route usually involves two steps: preparation of a homogeneous pre-alloy or master alloy by arc-melting where the pure elements are mixed together into the desired composition, followed by a second melting and casting into a Cu mold.

2.1.1 Arc-melting

An electric arc furnace is a system that heats charged material by means of an electric arc. Arc furnaces of various capacities exist: units of approximately one ton capacity used in foundries for producing cast iron products, while e.g. in research laboratories units with a capacity as small as around 50 grams are used, as illustrated in Fig 2.1.

The basic set-up of an electric arc furnace consists of a furnace shell with a roof on top. The furnace shell is lined with ceramic bricks insulating the furnace from the liquid metal alloy. On the upper side walls and on the inside of the roof, water cooled elements are used instead of ceramic insulation. These water cooled panels are positioned so there will be no direct contact with the liquid metal. Through the retractable roof, one or more tungsten electrodes enter the furnace. Electrodes may be pyramidal allowing the formation of an electric arc between the material and the electrode. On contact, electrical power is transformed into heat as arcing takes place between the electrodes and the solid feedstock. The material is heated both by current passing through the charge and by the radiant energy evolved by the arc.

The tungsten electrodes can be raised and lowered either manually for small devices or automatically (industrial melters) by a positioning system using electric

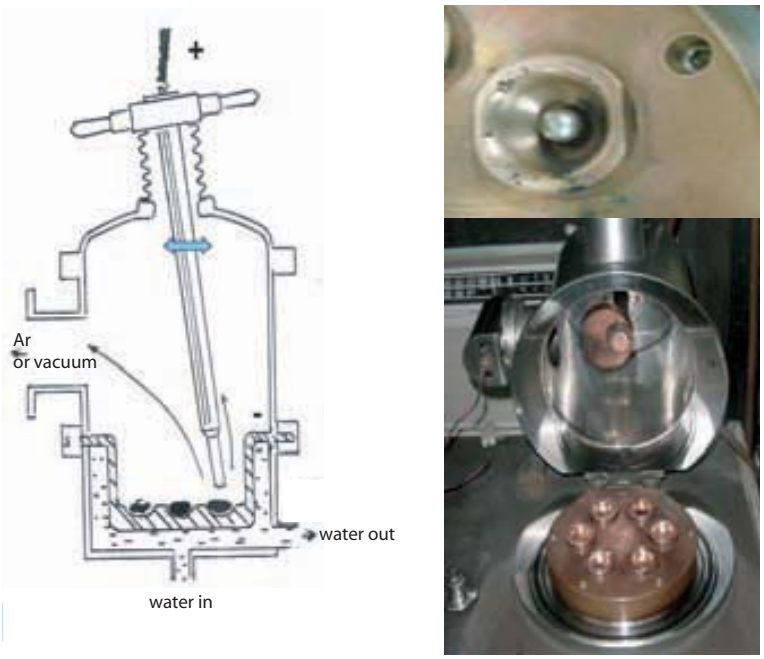

Fig. 2.1: Illustration of the principle of a laboratorium scale arc-melter [97].

winch hoists or hydraulic cylinders. The regulating system maintains an approximately constant current and power input during the melting of the alloy, even though scrap may move under the electrodes while it melts. The arc furnace described above can be used extensively for the preparation of different alloys. This includes systems with high-melting point elements like tungsten, rhenium, and molybdenum. In order to make an alloy melt as homogeneously as possible, generally the samples are remelted numerous times. If the alloys are brittle then the standard procedure is to crush the melt with mortar and pestle and then remelted. If the alloy samples are not brittle they can be machined into chips which then can be remelted. However, quite homogenous melt can be made by simply distributing the constituents in a random manner in the mold and repeating the arc melting several times with successive inversions of the sample [98, 99].

2.1.2 Cu mold casting

Pieces of master alloy are introduced in a crucible (quartz or graphite) where it will be melted by means of an induction furnace. Then, the melt is brought into a copper mold (see Fig. 2.2b-c). This insertion into the Cu mold can occur by

applying an overpressure in the crucible (injection casting) or by the application of a negative pressure at one end of a mobile copper mold, that moves into the molten alloy and sucks the molten alloy into the copper mold (suction casting). A third method, centrifugal casting, consists of casting the liquid alloy into rotating molds under the bearing of the centrifugal force.

Optimization of the casting parameters is an essential work to obtain a metallic glass and to control the quality of the final product. Crucibles and chamber atmosphere depend on the reactivity of the alloy with them. The main parameters controlling the quality of the cast rods are the temperature and pressure of ejection. In case of centrifugal casting, the pressure is determined by the speed of rotation. In fact, both temperature and pressure determine *viscosity* of the molten alloy, which is the most important parameter in glass forming ability [16].

Alloys with a high glass-forming ability typically have high viscosity values, while fragile liquids (alloys with low glass-forming ability) have low viscosities. The first group requires rather high overheating and/or high pressure to ensure a good filling and contact with the mold. However, a too high temperature of ejection may lead to a low cooling rate, providing more time for crystallizaton of the solidifying alloy. For the second group, viscosity should be kept in fact as high as possible, what is obtained with low (over)pressures and/or low overheating.

2.1.3 Experimental procedure

Almost all castings were done by the principles of injection casting, with a Buehler injection casting device located at the IFW Dresden, which is shown in Fig.2.2 a, b and c. Injection temperature was kept as constant as possible, around 1250°C. Since Zr-based BMGs are known as very good glass formers and thus known to possess high viscosities, a high injection pressure of 300 mbar was necessary to fill the mould. Graphite crucibles were used in all cases to limit oxygen contamination. Furthermore, vacuum pressure before casting was brought at least to 10^{-5} mbar and the chamber was flushed before with Ar to minimize oxygen contamination. Rods with a diameter of 3mm and length of 5 cm were obtained (Fig.2.2d). Afterwards, oxygen content was measured with an average of 0.0005 at% $\pm$ 0.00001.

The $Zr_{58.5}Ti_{8.2}Cu_{14.2}Ni_{11.4}Al_{7.7}$-alloy, used to study the indentation size effect, was prepared by suction casting into rods of 2.5 mm diameter and 10 cm length.

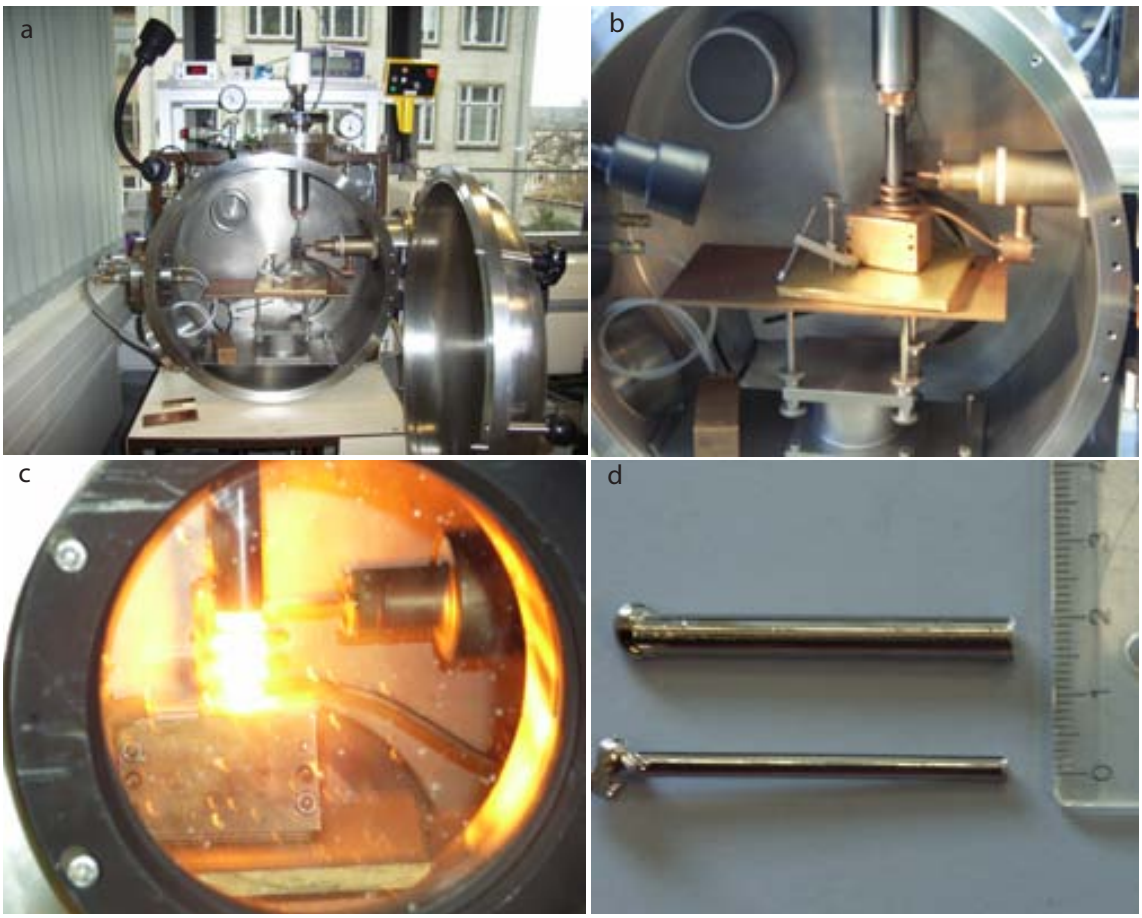

Fig. 2.2: (a) Buehler injection device at the IFW Dresden,(b) Set-up showing the graphite crucible, induction coil for heating and Cu mold,(c) detail of set-up just before injection into the Cu mold (d) rods obtained by injection casting with a diameter of 5 (top) and 3 (bottom) mm.

The cooling rate is expected to be in the order of $2000°C/\mathrm{s}$ [100], [101].

2.2 Treatments

As mentioned in the preface, the objective of this work was to study the influence of various treatments (annealing, heavy deformation and irradiation) on thermal stability and microstructural changes and the influence of the latter on mechanical properties. In this section, an overview of the respective treatments, the theory of the technique applied and the experimental details are highlighted.

2.2.1 Annealing treatment

The annealing treatments, analyzed in chapter 4, were performed in a tubular vacuum furnace with Ti as oxygen-getter. Temperature was measured by a thermocouple placed very close to the sample. Samples were brought into a preheated furnace and taken out immediately when the temperature was reached. The annealing treatments were performed at the *IFW Dresden* (Germany). After annealing, oxygen content was measured carrier gas-hot extraction with a O/N analyzer TC-436/LECO USA. No contamination upon annealing could be detected.

2.2.2 Heavy deformation - high pressure torsion

2.2.2.1 Principles

High pressure torsion straining belongs to the group of severe plastic deformation (SPD). The basic principle of SPD processing is that a bulk material is subjected to a very intense plastic strain, without necessarily introducing significant changes in the overall dimensions of the work-piece.

Two different procedures are generally used in SPD processing. The first one, known as equal-channel angular pressing (ECAP), involves pressing a bar or rod through a die within a channel bent into an L-shaped configuration. In the second technique, high pressure torsion (HPT), a sample in the form of a thin disk is subjected to a high pressure, of several GPa, and a concurrent torsional straining. The principles of HPT processing are schematically illustrated in Fig. 2.3 a. The torsional straining is imposed through rotation of the lower support. The disk deforms by pure shear through the surface frictional forces, under quasi-hydrostatic pressure, which prevents the sample from failing, despite the high strains applied [102].

Fig. 2.3 b depicts the variables used in estimating the strain imposed during HPT. An infinitely small rotation $\mathrm{d}\theta$ leads to an infinitely small displacement $\mathrm{d}l = r\ \mathrm{d}\theta$, with r the disk radius, and an incremental shear strain $\mathrm{d}\gamma$, given by $\mathrm{d}\gamma = \frac{\mathrm{d}l}{h} = \frac{r\mathrm{d}\theta}{h}$, with h the disk thickness.

In the relationship above, the strain value should change linearly from zero in the center to a maximum at the edge. Thickness is assumed to be constant, while the initial thickness of a sample can actually be reduced by approximately a factor two under the high compressive stress. This means that the expression

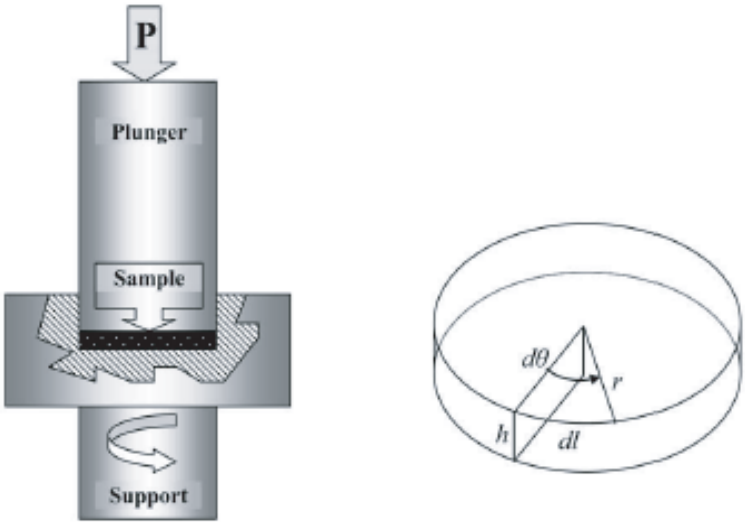

Fig. 2.3: (a) Schematic illustration of HPT processing and (b) parameters used in estimating the total strain in HPT. [102]

given above might underestimate the calculated values as compared to the true value [103].

As a first approach and based on the uncertainties in calculating strain, it is reasonable to suggest that the straining created during HPT, can be realistically expressed by simply specifying the number of revolutions imposed on the sample [102], [104].

A more accurate evolution of total strain stored within the disk during HPT was obtained by finite element simulations [103].

2.2.2.2 Experimental procedure

The high pressure torsion treatments were performed at the *Institute for Physics of Advanced Materials* in Ufa (Russia). Pieces of Cu-mould cast $Zr_{55}Cu_{30}Al_{10}Ni_5$ BMG were subjected to 2 or 5 whole-turn torsion under an applied pressure of 6 GPa, using a modified Bridgemann anvil type device. Disks of approximately 10mm diameter and 0.3 mm thickness were obtained.

2.3 Characterization techniques

This section gives an overview of the different techniques applied to study changes induced in thermal stability and microstructure after the different treatments.

Differential Scanning Calorimetry (DSC) has been used to study the thermal stability and the crystallization kinetics of the metallic glass. The different treatments induce morphological and structural changes in the studied materials, which have been analyzed by means of X-ray diffraction (XRD) and of transmission electron microscopy (TEM). Scanning electron microscopy was mainly used for shear band observation and fracture surface analysis after deformation.

2.3.1 Thermal characterization

2.3.1.1 Definition of thermal analysis

To provide useful qualitative and quantitative information on the effect of heat on materials, experiments should be carefully planned and sophisticated material is often used. The following formal definition of *thermal analysis* was provided by the International Confederation for Thermal Analysis and Calorimetry (ICTAC): *Thermal analysis refers to a group of techniques in which a property of a sample is monitored against time or temperature while the temperature of the sample , in a specified atmosphere, is programmed.* In practice, often only a *change* in a certain property is measured, not the property itself [9]. Furthermore, *absolute* values of the sample property may be recorded (thermal analysis), or the *difference* in the property of the sample, compared to the same property of a reference material may be more convenient to measure. Similarly, the *rate of change* of the sample property with time or temperature may be of interest (*differential thermal analysis*).

All thermal analysis instruments have common features. The sample, contained in a suitable sample pan or crucible, is placed in a furnace and subjected to some desired temperature programme. During this procedure, one or more properties of the sample are monitored by means of suitable transducers for converting the properties to electrical quantities, such as voltages or currents. The variety of techniques to be discussed stems from the variety of physical properties that can be measured and the variety of transducers that can be used. For a detailed overview on this topic, the reader is referred to [9].

2.3.1.2 Principles of differential thermal analysis and differential scanning calorimetry

Differential thermal analysis (DTA) is the simplest and most widely used thermal analysis technique. The difference in temperature between the sample and a reference material is recorded while both are subjected to the same heating programme.

As the specimen is heated or cooled in a controlled manner, its temperature will deviate from the temperature of the reference sample as it undergoes a reaction or a transformation. When for example an endothermic event occurs in the sample, the temperature of the sample will lag behind the temperature of the reference material, which follows the programmed heating. For exothermic processes, the response is would be a faster heating. Furthermore, second order transitions characterized by for example a change in thermal conductivity or heat capacity of the sample, would give rise to a change in slope during thermal analysis and an offset of the baseline in differential thermal analysis.

The use of a reference sample, besides the specimen of interest, is essential in order to eliminate disturbances in the recorded signal resulting from unintended fluctuations in the rate of heating or cooling. This reference sample should be inert during the temperature interval of interest and should have a similar heat capacity. Since both the sample and reference material will react similarly to possible fluctuations, the final effect should be cancelled, leaving the baseline undisturbed.

A typical DTA-curve is the temperature difference between sample and reference monitored against the reference temperature, the actual sample temperature or time. Ideally, the area under the DTA peak should be proportional to the enthalpy of the process that gave rise to the peak. However, changes in thermal transport properties of the system, detector sensitivity,...decrease the response of the DTA device with increasing temperature and are not compensated for in a traditional DTA curve.

Differential scanning calorimetry (DSC) was designed to avoid or compensate for these effects. This technique aims to maintain the sample and the reference material at the same temperature at any time during the experiment, by compensating independently the supplies of power to the sample and reference. Any

difference in these power supplies is recorded against the programmed temperature (or time).

The temperature difference, which should be kept as close to zero as possible, is measured in a DSC by placing a temperature sensor into a bridge circuit. Any imbalance drives a heater to compensate in the appropriate (sample or reference) part of the cell. The power needed to the bridge circuit in balance is proportional to the change in heat capacity or enthalpy. The integral of power over the time of the total event gives the energy difference between sample and reference, which corresponds to the enthalpy difference of the process. A typical DSC-curve is the difference in power supply between sample and reference monitored against the program temperature or time. Thermal events in the sample thus appear as deviations from the DSC baseline, in either an endothermic or exothermic direction, depending upon whether more or less energy has to be supplied to the sample relative to the reference material.

The reference material in most DSC experiments is simply an empty sample pan. Usually, Al sample pans are used at lower temperatures, while for higher temperatures, graphite pans should be applied. The sample holder is purged by a gas, which may be inert or reactive as desired. Samples used should be under the form of discs or dense powders [9].

2.3.1.3 Quantitative aspects of DSC curves

The International Union of Pure and Applied Chemistry, IUPAC, has given precise definitions of the terminology used for the interpretation of DSC curves, as illustrated in Fig.2.4.

Baseline part or parts of the DSC curve in which dQ/dt is nearly zero (lines AB and DE)

Peak part of the curve which initially goes off and later goes back on the baseline (line BCE)

Peak width interval of time or temperature in which the DSC curve goes off the baseline (line B'D')

Peak height distance, perpendicular to the time or temperature axis, between the interpolation of the baseline and the peak vertex (line CF)

Peak area closed area by the peak and the interpolation of the baseline (area enclosed by the lines BC, CD and BD)

Initial temperature of transformation temperature corresponding to the intersection point between the tangent at the the maximum slope point at the beginning of the peak and the interpolation of the baseline point (point G)

Final temperature of transformation temperature corresponding to the intersection point between the tangent at the the maximum slope point at the end of the peak and the interpolation of the baseline point (point H)

The (interpolated) baseline is the line constructed in such a way that it connects the measured curve before and after a peak, as if no peak had developed. However, this baseline is not always easy to distinguish, although the features of interest in both DTA and DSC curves are the deviations of the signal from the baseline. Initial displacements of the baseline itself from zero are possible, as a consequence of mismatching thermal properties of the sample and the reference material and asymmetry in the construction of sample and reference holders. In severe cases, this may cause a sloping baseline, which may require electrical compensation.

Furthermore, after a thermal event, the response will not return to the original baseline if the thermal properties of the high temperature form of the sample are different from those of the low-temperature form. To take this into account, different procedures for baseline construction have been suggested and are often incorporated in the software supplied with the instrument [9].

2.3.1.4 Modulated temperature differential scanning calorimetry

In modulated (temperature) differential scanning calorimetry (mt-DSC), the conventional linear heating programme is modulated by superimposing an alternating fast temperature change, e.g. by means of a sinusoidal or stepped temperature profile. Each cycle involves both heating and cooling portions. The overall trend however, remains a linear change in average temperature with time (Fig. 2.5).

Analysis of the signal requires the separation of the response to the periodic signal from the response to the underlying heating programme. For a sine wave modulated temperature programme $T = (T_0 + \beta t) + A\sin(2\pi f t)$, with T_0 the starting temperature, β the underlying heating rate, A the amplitude of the mod-

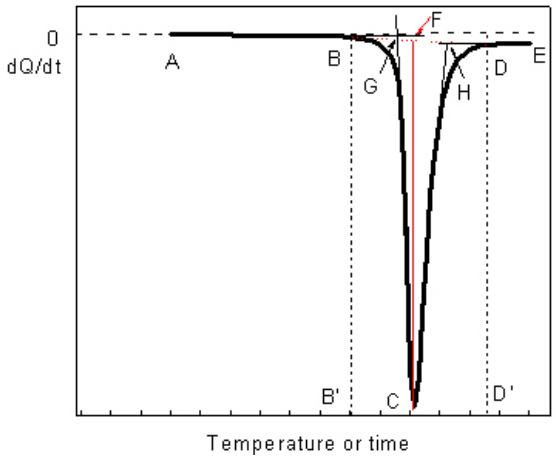

Fig. 2.4: Schematic representation of a DSC curve and its interpretation following the IUPAC rules [105]

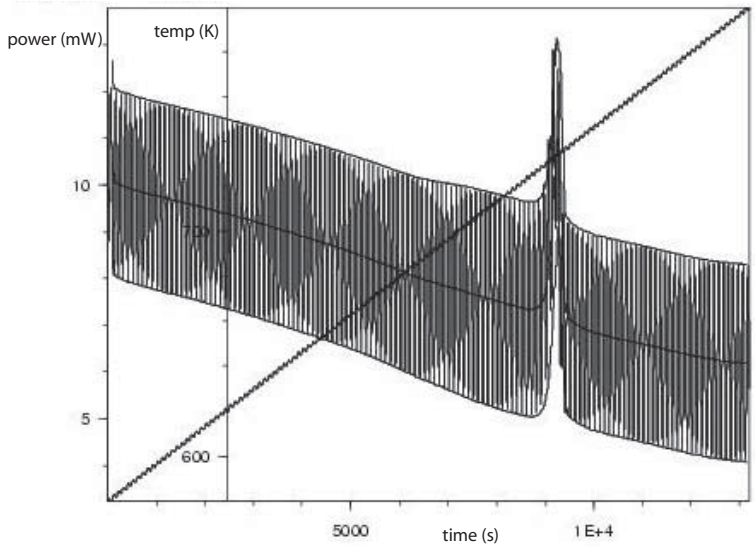

Fig. 2.5: Illustration of the superimposition of a periodic wave on the conventional linear heating programme and its result on the outcoming heat flow. The overall result however remains a linear increase of temperature.

ulation and f the frequency, the resulting heat flow dq/dt can be calculated as following:

$$\frac{dq}{dt} = C_p \frac{dT}{dt} + f(t,T) \tag{2.1}$$

C_p is the heat capacity of the sample and $f(t,T)$ is the heat flow arising as a consequence of a *kinetically hindered* event, which can be different types of processes. Enthalpic relaxation in polymers and metallic glasses is such a kinetically hindered process [106].

Combination of the expression for T and Eq. (2.1) gives:

$$\frac{dq}{dt} = \underbrace{\{\beta C_p + F(t,T)\}}_{} + \underbrace{\{2\pi f C_p A \cos(2\pi f t) + D \sin(2\pi f t)\}}_{}. \tag{2.2}$$

The first part of Eq. (2.2) is the *underlying* signal (equal to the conventional DSC signal). $F(t,T)$ is the average of $f(t,T)$ over at least one interval of modulation. The second part is called the *cyclic* signal, with D the amplitude of the kinetically hindered response to the temperature modulation. Both C_p and D vary very slowly with time and temperature, and can be considered constant over the duration of one modulation. The kinetically hindered event $f(t,T)$ could also give a cosine response, but this is usually made negligible by adjusting the frequency of modulation and a suited heating rate.

One of the strong advantages of using mt-DSC over conventional DSC, is that it allows the separation of *reversing* processes, such as glass transitions, from *non-reversing* processes, such as relaxation endotherms. This is illustrated in Fig. 2.6. The underlying signal, described above, is in fact the sum of the reversing and non-reversing signals. The reversible signal can be calculated, once C_p has been calculated, which can be done from the *in-phase, cyclic signal*, since all the other parameters determining this signal, are known. Diminishing this reversible signal from the underlying finally results in the non-reversible signal.

Further advantages of mt-DSC are that the baseline curvature on the cyclic signal is generally very low, which makes it easier to distinguish between baseline effects and real transitions. The signal-to-noise ratio of the cyclic measurement of heat capacity is generally greater, because all drift or noise at frequencies other than the modulation frequency are ignored by the Fourier transform analysis. Resolution of processes is improved by the use of very low underlying heating

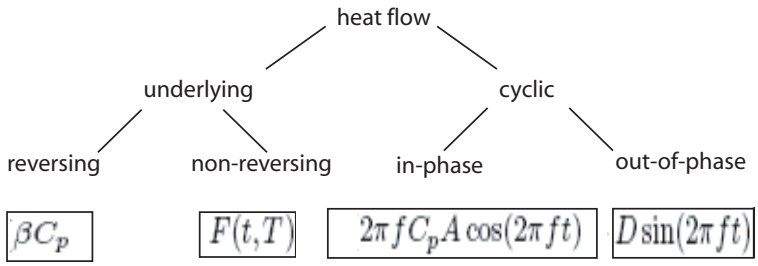

Fig. 2.6: Schematic representation of the signals derived from a modulated DSC experiment.

rates [9].

2.3.1.5 Use of DSC in this work

1. A typical DSC-scan of a metallic glass - below crystallization

   Amorphous metallic alloys obtained from the melt by rapid solidification techniques have a non-equilibrium structure. Heating of these metallic glasses *below crystallization temperature* leads to a transformation of its structure towards a more relaxed (closer to equilibrium) state. This phenomenon is called *structural relaxation* and is manifested by a continuous change in all physical properties. Several models have been developed to describe and explain the structural relaxation of metallic glasses, of which the free volume model is one of the most commonly used.

   The as-quenched metallic glass contains an excess (non-equilibrium) amount of free volume frozen in the material during rapid solidification of the melt. Fig. 2.7 schematically shows the characteristic change in the average free volume per atom, ν_f, upon heating. When the system is heated, atomic mobility increases and the excess free volume is annihilated. This decrease of ν_f with temperature is accompanied by a decrease of enthalpy of the system, which is observed as an exothermic dip in the DSC trace (section AB in Fig. 2.7). At the same time, the equilibrium free volume of the supercooled liquid, $\nu_{f,eq}$, increases approximately linearly with temperature [7], [107]. Thus, once ν_f reaches $\nu_{f,eq}$, the average free volume should begin to increase with temperature. However, in a constant heating rate experiment the kinetics of free volume production are too sluggish to keep up with the constantly

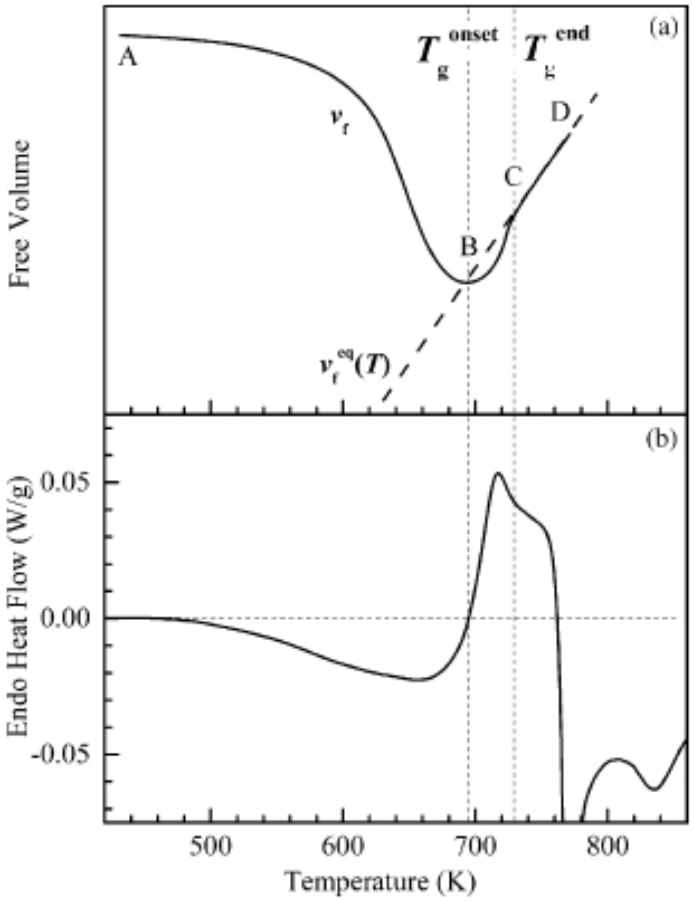

Fig. 2.7: Schematic representation of the interrelation between free volume change (a) and DSC heat flow (b) upon continuous heating of an as-quenched metallic glass. [47]

increasing temperature, and hence ν_f undershoots the equilibrium behavior (section BC). As the temperature continues to increase, atomic mobility increases sufficiently to bring the system back to equilibrium (point C). This rapid production of free volume is observed as an endothermic peak on the DSC trace, and is identified as the glass transition [47], [108].

Van den Beukel and Sietsma [107] stated that the change in free volume $\Delta\nu_f$ is proportional to the energy released during relaxation or required during production, $(\Delta H)_{fv}$:

$$(\Delta H)_{fv} = \alpha\Delta\nu_f, \tag{2.3}$$

with α a constant. Experimental evidence of this assumption was given later by Slipenyuk and Eckert [47]. Note that in the latter article, ν_f stands for the free volume per atomic volume, which is in fact $\sim \gamma x \sim x$ ($\gamma \sim 1$) with x the reduced free volume defined in Eq. (1.9).

To calculate peak areas, as e.g. the peak area of the exothermic event accompanying relaxation, a correct baseline determination is important. Even a small shift in the DSC curve, caused by instrumental error, might result in a drastic change of the integrated area. To correct these possible instrumental errors, Slipenyuk and Eckert described an additional base line correction which should be applied for calculation of free volume changes based on changes in the relaxation enthalpy [47]. The construction of a linear baseline was based on the two following assumptions: at a temperature T_1, sufficiently below T_g or any pre-heating temperature, the heat flow can be assumed to be zero. In the supercooled liquid state, the structure of metallic glass forming alloys should not depend on the thermal history of the material and concomitantly, heat capacity should be the same for all samples of a certain composition in this temperature range. However, often shifts are observed, which concomitantly are due to instrumental error. Baseline heat flow was set equal to the deviation of the measured heat flow from the value averaged over all samples:

$$W_i^{base}(T_{SQL}) \quad = \quad W_i^{exp}(T_{SQL}) - \overline{W^{exp}(T_{SQL})} \tag{2.4}$$

Once corrected, the total enthalpy change ΔH due to structural relaxation can be calculated as the difference between the as-cast and the (thermally) treated sample [47]:

$$\Delta H = \int_{T_1}^{T_{SQL}} \frac{W_i^{exp}(T) - W_i^{base}(T)}{\beta} dT - \int_{T_1}^{T_{SQL}} \frac{W_0^{exp}(T) - W_0^{base}(T)}{\beta} dT, \tag{2.5}$$

with W_0^{exp} and W_0^{base} the experimental and base-line heat flow for the as-cast sample, while the index i indicates the treated sample. β is the applied heating rate.

2. Crystallization - Kissinger method

The most common application of the DSC technique in the study of the crystallization kinetics has been the determination of the activation energy by the Kissinger method [109]. This method originates from the fundamental kinetic equation:

$$\frac{dx}{dt} = K(T)f(x) \tag{2.6}$$

where $\frac{dx}{dt}$ represents the transformation rate of the transformed fraction x, $f(x)$ is a characteristic function of the studied process and $K(T)$ is the rate constant of transformation, which is constant in time and which temperature dependence can be expressed as an Arrhenius type:

$$K(T) = K_0 \exp(\frac{-E_a}{RT}). \tag{2.7}$$

K_0 is a pre-exponential factor, E_a is the activation energy of the process, related with the potential barrier of the process, T is the temperature and R is the universal gas constant.

On the assumption that the transformation rate is maximum in the peak maximum ($(\frac{d^2x}{d^2t})_{T=T_p}$) and that the transformed fraction in this point, x_p is the same for all heating rates β, Eq. (2.6) can be derived as:

$$[\frac{d^2x}{d^2t}]_{x=x_p} = K(T_p)[\frac{df(x)}{dt}]_{x=x_p} + [\frac{dK(T)}{dt}]_{x=x_p} f(x_p) = 0. \tag{2.8}$$

Based on Eq. (2.6) and (2.7), $\frac{df(x)}{dt}$ and $\frac{dK(T)}{dt}$ can be substituted respectively by:

$$\begin{aligned} \frac{df(x)}{dt} &= \frac{df(x)}{dx}\frac{dx}{dt} \\ &= f'(x)K(T)f(x) \end{aligned} \tag{2.9}$$

$$\begin{aligned} \frac{dK(T)}{dt} &= \frac{dK(T)}{dT}\frac{dT}{dt} \\ &= \frac{E_a}{RT^2}K(T)\frac{dT}{dt} \\ &= \frac{E_a}{RT^2}K_0\beta\exp(\frac{-E_a}{RT}), \end{aligned} \tag{2.10}$$

which results in:

$$[\frac{d^2x}{d^2t}]_{x=x_p} = K_0 f'(x_p)\exp(\frac{-E_a}{RT}) + \frac{E_a}{RT^2}\beta. \tag{2.11}$$

This can be rewritten as:

$$\ln(\frac{\beta}{T_p^2}) = \frac{-E_a}{RT_p} + \ln(\frac{RK_0}{E_a}(-f'(x_p))). \tag{2.12}$$

For reactions in the solid state, $\ln(f'(x_p)) \simeq 1$, which is much smaller than the value of $\frac{-E_a}{RT_p}$. Therefore, Eq. (2.12) can be approximated by:

$$\ln(\frac{\beta}{T_p^2}) \simeq \frac{-E_a}{RT_p} + \ln(\frac{RK_0}{E_a}). \tag{2.13}$$

The Kissinger method consists of plotting consists of plotting $\ln(\frac{\beta}{T_p^2})$ versus $1/T_p$ for different heating rates. The activation energy can be calculated from the slope of the linear regression curve to the experimental data.

The Kissinger method to determine the activation energy of a reaction by continuous heating e.g. in DSC, is a very convenient manner, as compared to the time-consuming isothermal analysis. However, this method has its restrictions, specifically those resting on the assumption of first order chemical reaction kinetics [110].

3. Experimental conditions used

   All conventional DSC experiments were performed with a *Perkin Elmer DSC-7* at the Universitat Autònoma and at the IFW Dresden (Germany).

   Since scans up to 923K were made, graphite and alumina crucibles were used, with an empty crucible as a reference sample. For each experiment, two consecutive scans were made: one to let the sample crystallize and measure its thermal properties, and a second scan (with the crystallized sample) was made for baseline correction.

   Usually a heating rate of 40 Kmin^{-1} was used for standard measurements and homogeneity checks. For more detailed studies of the crystallization behaviour and calculations of the activation energy by the Kissinger method, heating rates of 5,10, 20, 40 and 80 Kmin^{-1} were applied.

   mt-DSC experiments were carried out using a *Perkin Elmer DSC-1* by Dr. Ádám Révész at the Materials Physics department of the Eötvös University in Budapest (Hungary). A heating rate of 1K/min was applied, with an amplitude of 1K and a frequency of 1s.

2.3.1.6 Thermomechanical characterization: viscosity measurements

In thermomechanical analysis (TMA), dimensional changes in a sample are measured during heating, cooling or during isothermal experiments.

The sample lies on a support within a furnace. It is brought into contact with a probe to sense changes in length, which are measured by a sensitive position transducer. A thermocouple near the sample indicates its temperature. The probe and support are made of a material with a low, reproducible and accurately known coefficient of thermal expansion, like quartz glass. Furthermore, they should have a low conductivity, to isolate the sensitive transducer from the changing temperatures in the furnace. Usually, there is the possibility to establish a flowing gas atmosphere, to prevent oxidation and to improve heat transfer to the sample.

Using a thermomechanical analyser, it is possible to measure viscosity at any temperature of the undercooled liquid. By measuring the height of the sample in function of time, viscosity η can be calculated as:

$$\eta = \frac{Fh}{3\pi a^2 \frac{dh}{dt}}, \tag{2.14}$$

with F the applied load, a the radius of the sample and h the height of the sample [15], [111].

Viscosity measurements were carried out using a *TMA 7 (Perkin Elmer)* located at the IFW Dresden (Germany). Sample preparation involves polishing them to obtain perfectly parallel, flat and clean faces of around 300μm thickness, to avoid artefacts in the recorded curves.

2.3.2 Microstructural characterization - X-ray diffraction

2.3.2.1 Principles of structure determination by diffraction

When X-rays hit an atom, they make the electronic cloud move as does any electromagnetic wave. The movement of these charges leads to a re-radiation of coherent spherical waves by the vibrating electrons with the same frequency and a low intensity; this phenomenon is known as the Rayleigh or elastic scattering.

At a certain distance from the material, the intensity of the resulting waves is given by the superposition of the contributions of all the atoms and this intensity will show a characteristic pattern, as a consequence of interference between the wave fields. This interference is caused by the existence of specific phase shifts between the waves emitted by the different atoms and this on its turn is a consequence of the specific distances between the atoms. The resulting wave interference pattern is the basis of diffraction analysis [112].

To obtain constructive interference, i.e. diffraction, the phase shift should be proportional to 2π or that the difference in the length of the path for rays reflected from successive planes be equal to an integral number of wavelengths, as illustrated in Fig. 2.8. Thus, the peak of the crystallographic planes characterized by the interplanar distance d will appear in the diffraction pattern if for a certain wavelength λ of the X-ray radiation and a certain incident angle θ Bragg's law is obeyed, given by

$$n\lambda = 2d\sin(\theta) \tag{2.15}$$

The integer n, which gives the number of wavelengths in the difference in path for waves coming from successive planes, is the *order of reflection*.

Both neutron and X-ray wavelengths are comparable with inter-atomic distances ($\sim$ 150 pm) and thus are an excellent probe for this length scale.

The Bragg's law assumes the crystal is ideal (without structural defects) and the incident beam is perfectly monochromatic and collimated. These conditions are however never fulfilled completely. Usually, the particles are found to be composed of several grains, with different orientation and with certain amount of defects. Each of these grains is called a crystallite. Small crystallite sizes and presence of microstrains among others lead to a broadening of the X-ray diffraction peaks.

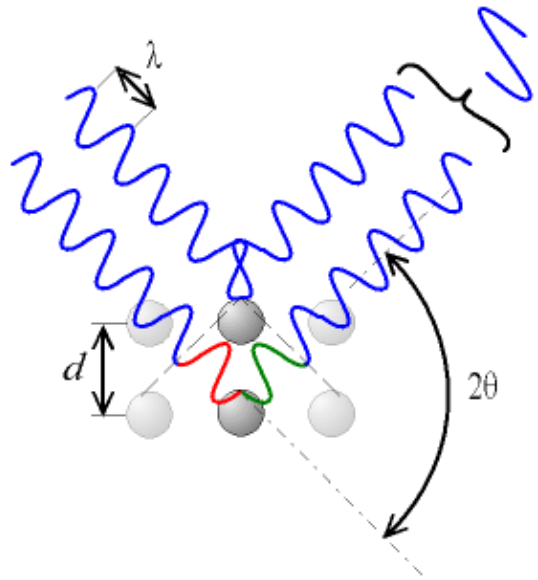

Fig. 2.8: Schematic representation of the conditions for constructive interference, resulting in Bragg's law

The peak shape of conventional materials can usually be fit by a simple Gaussian function:

$$\chi(2\theta_i - 2\theta) = \alpha \exp(\frac{(2\theta_i - 2\theta)^2}{\Gamma_i^2}) \tag{2.16}$$

where Γ_i is the half-width of the i^{th} reflection with center in 2θ, which on its turn can be calculated with the formula of Cagliotti:

$$\Gamma_i^2 = U \tan^2 \theta_i + V \tan \theta_i + W \tag{2.17}$$

with U, V, W the half-width parameters. However, when crystallite size drops below certain values, or large strains are present, a deviation of the shape occurs from pure gaussian to a mixture of a Gaussian and a Lorentzian function, also referred to as a pseudo-Voight function:

$$\chi'(2\theta_i - 2\theta) = \eta L + (1 - \eta) G \tag{2.18}$$

$$\chi'(2\theta_i - 2\theta) = \eta(\beta[1 + \frac{(2\theta_i - 2\theta)^2}{\Gamma_i^2}]^{-1}) + (1 - \eta)(\alpha \exp[\frac{(2\theta_i - 2\theta)^2}{\Gamma_i^2}]) \tag{2.19}$$

The crystallite size can be deduced from the lorentzian contribution, Γ_{fL} to the integral width of the diffraction peak, as given by the Scherrer formula:

$$\delta_{hkl} = k * \frac{\lambda}{\Gamma_{fL} \cos\theta_B} \tag{2.20}$$

where θ_B is the angular position of the peak in radians and λ is the wavelength in Å. k is a parameter whose value is close to unity ($k \approx 0.9$). The value of δ_{hkl}, also measured in Å, represents the average size of a coherent diffraction domain. Analogously, microstrains can be determined from the gaussian contribution, Γ_{fG}, to the integral peak width, using the expression:

$$\langle e \rangle = \frac{\Gamma_{fG}}{4 \tan\theta_B} \tag{2.21}$$

where $\langle e \rangle$ represents the upper limit of the microstrains. However, it is more frequent to use the mean square root of microstrains, $\langle \epsilon^2 \rangle^{\frac{1}{2}}$ (rms strain), which is related to $\langle e \rangle$ as follows: $\langle e \rangle = 1.25 \langle \epsilon^2 \rangle^{\frac{1}{2}}$.

2.3.2.2 *Methods of structure analysis by X-Rays*

- Bragg-diffractometer

  This method is often used for phase-identification and uses monochromatic X-rays. The polycrystalline sample can either be massive or under the form of powder. In the former case, it is essential that the sample is flat.

  The generation of X-rays is based on the impacts between thermo-ionic electrons, emitted from a cathode, and metal atoms (typical Cu, Co, Mo, Cr) in the anode, which results in the emission of electrons of the metal, leaving a large number of holes inside the inner electronic shells. These holes become immediately occupied by electrons from more external shells and the excess of energy is liberated as X-ray radiation, whose energy depends on the energy difference between the energy levels of the electrons and, hence, has discrete values. In order to obtain characteristic radiation, a sufficiently high voltage should be applied in the tube to avoid too much generation of Bremsstrahlung (noise radiation).

  This X-ray tube is equipped with a filter to obtain maximum monochromatisation, by absorbing K_β radiation, and Soller slits, a set of very fine metallic

foils, positioned very close to each other and parallel to the diffraction circle plane. These Soller slits are necessary to make a parallel and collimated beam, since the X-ray source emits in all directions. In front of and behind these Soller slits, divergence slits are present to limit the divergence of the beam to typical limits of $\frac{1}{30}^{\circ}$ to 4°.

The sample, placed in the center of a flat goniometer, rotates with an angle velocity of $\frac{\theta}{\Delta t}$.

The X-ray detector moves around at the circumference of the goniometer with an angular velocity of $\frac{2\theta}{\Delta t}$ and counts the number of photons per second. Since the detector has to follow the diffracted radiation, when the sample rotates at an angular speed θ , the detector has to rotate at 2θ, since the diffracted beam is deviated 2θ with respect to the incident beam. As a consequence, this Bragg-Brentano geometry is also known as "θ - 2θ scan".

Before entering the detector, the diffracted X-rays pass again through Soler and divergence slits, in order to keep the X-rays diffracted by the sample collimated and make them convergent respectively. The width of these slits determines the maximum intensity in the detector.

These different parts of the Bragg diffractometer are illustrated in Fig. 2.9. Note that diffraction of a crystallographic plane (hkl) will only occur when this plane is parallel to the sample surface, so crystallographic texture will have a very strong influence on the intensities of the spectrum.

- Synchrotron

  Synchrotron radiation arises when energetic electrons are accelerated, for example by being forced to travel in a curved path or in a straight path, acted on by special magnetic structures (wigglers and undulators).

  Electrons emitted by an electron gun are first accelerated in a linear accelerator (linac) and then transmitted to a circular accelerator (booster synchrotron) where they are accelerated to reach an energy level on the order of several GeV. These high-energy electrons are then injected into a large storage ring with a circumference around 10^3 m where they circulate in an ultra high vacuum environment at a constant energy for many hours (Fig. 2.10a).

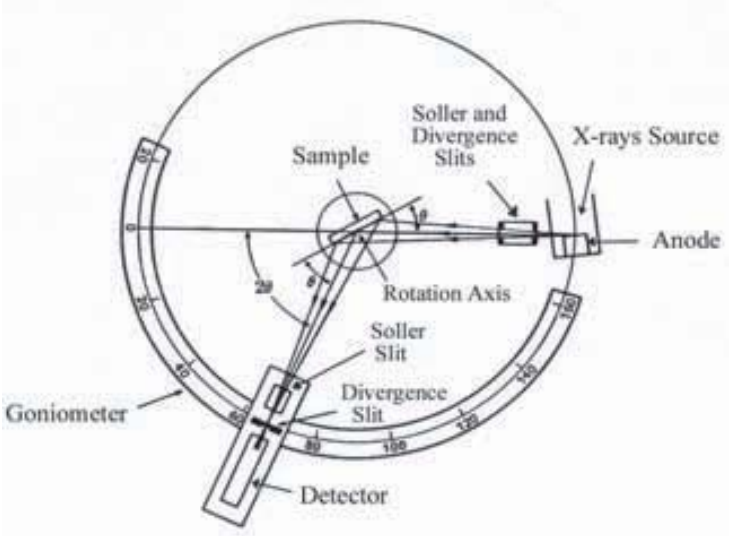

Fig. 2.9: Schematic representation of an X-Ray diffractometer in Bragg-Brentano geometry.

The storage ring includes both straight and curved sections . As they travel around the ring, the electrons pass through different types of magnets: bending magnets, undulators and focusing magnets. When the electrons pass through the bending magnets (wiggler), they are deflected from their straight path by several degrees. This change in direction causes them to emit photons, the synchrotron radiation (Fig. 2.10b). The undulators are magnetic structures, made up of a complex array of small magnets, forcing the electrons to follow an undulating, or wavy, trajectory in the vertical plane. The beams of radiation emitted from the different bends overlap and interfere with each other to generate a much more intense beam of radiation than that generated by the bending magnets.

The focusing magnets, placed in the straight sections of the storage ring, are used to focus the electron beam to keep its diameter small and well-defined. On the other hand, as a consequence of relativity, the radiation pattern is distorted into an extremely forward-pointing cone, making synchrotron radiation sources one of the brightest known sources of X-rays. This brightness is extremely important for the experiments, and is one of the most important advantages of synchrotron radiation over conventional sources.

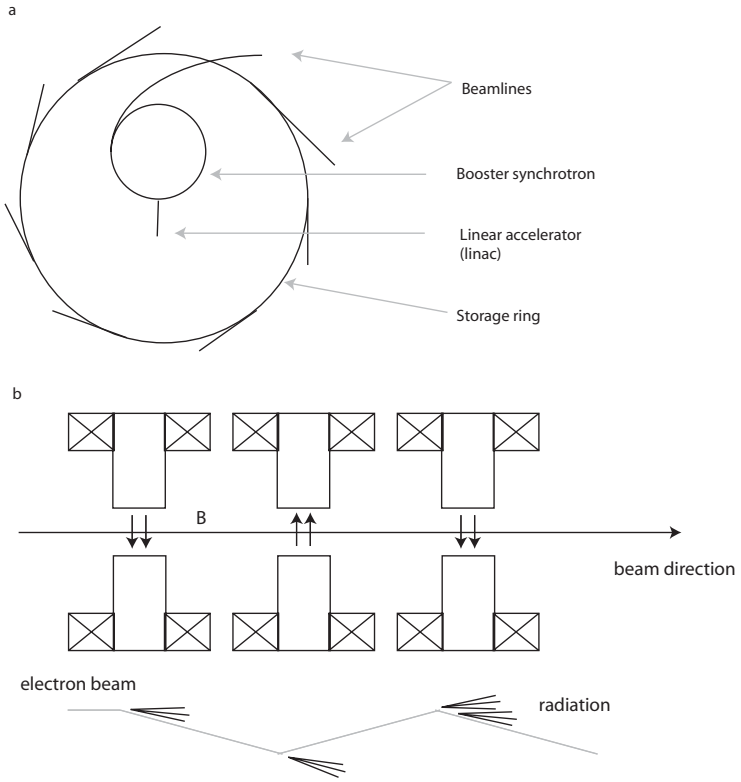

Fig. 2.10: (a) Schematic representation of a synchrotron and its different parts contributing to the production of high energy X-rays. (b)Schematic representation production of synchrotron radiation at wiggler (bending) magnets in an electron synchrotron, mounted in the straight parts of the storage ring.

For example, the high brilliancy and intensity of synchrotron light makes it possible to obtain diffracted intensities, with good resolution in *transmission* geometry within short times. This transmission geometry is with conventional sources only possible with very thin capillaries, due to too high absorption. As a consequence of the possibility to work on very short time scales, nucleation - which is usually completed in less than a minute - can be detected, even in the very first stages [66], where the time resolution of the fastest conventional X-ray geometry is too low. Furthermore, the transmission geometry avoids the detection of nucleation on surfaces as is usually the case in reflection set-up [113].

By the use of high-energy synchrotron radiation, large values for the scattering vector $q = \frac{4\pi \sin\theta}{\lambda} = \frac{2\pi}{d_{hkl}}$ can be reached, increasing significantly the resolution (smaller $d_{hkl}-$values). This allows the direct measurement of the structure factor $S(q)$ and has contributed substantially to the understanding of the atomic structure of disordered solids, like metallic glasses, e.g. study of short and medium range order.

This structure factor for atoms $S(q)$ is obtained by scattering a monochromatic beam from the sample and measuring the intensity, for a given scattering vector q, integrated over the energy loss due to atomic motions. Once $S(q)$ is determined for all scattering vectors, the pair correlation function $g_(r)$ can be calculated from the Fourier transform of the structure factor [36], [114]:

$$4\pi\rho_0(g(r)-1) = \frac{2}{\pi}\int (S(q)-1)q\sin(qr)dq \tag{2.22}$$

where $\rho(r)$ is the atomic pair density distribution function and ρ_0 is the mean atomic density. The $g(r)$ curves exhibit systematic changes for the different compositions. The total atomic pair correlation function $g(r)$ represents the weighted sum of the partial atomic pair correlation functions $g_{ij}(r)$:

$$g(r) = \sum_i \sum_j w_{ij} g_{ij}(r). \tag{2.23}$$

The weight factors $w_{ij} = c_i c_j f_i f_j (\sum_i c_i f_i)^{-2}$ depend on the concentration c_i; the atomic form amplitude f_i is of the i^{th} atom. These partial pair

correlation function $g_{ij}(r)$ express the probability to find the center of an atom i at a given distance r from the center of another atom j.

2.3.2.3 Experimental procedure

X-ray diffraction (XRD) experiments were carried out at the Servei de Difracció at the Universitat Autònoma de Barcelona, using a Phillips X'Pert diffractometer.

The X-ray spectra were obtained in a *step-scan* mode. This means that the sample and the detector rotated in steps instead of in a continuous way. The appropriate step size for each experiment was selected in order to have at least 10 experimental points above the half height width. Therefore, steps of $0.02 - 0.04°$ were chosen. Moreover, the time for step was selected to be relatively long (10 s) in order to reduce the statistical error.

The powder diffractometer used in our study was set up in *Bragg-Brentano geometry*.

Synchrotron measurements and RDF calculations were performed by Dr. Stoica and Dr. Mattern, respectively, from the IFW Dresden at the synchrotron radiation facilities of HASYLAB in Hamburg (beamline BW5 at the storage ring DORIS). The 4.5 GeV storage ring DORIS III at DESY in Hamburg has 9 wiggler/undulator insertion devices and several dipole beamlines. In total there are 36 beamline stations. The stored current is 140 mA of positrons in 5 bunches with a typical lifetime of 10 to 18 hours. The radiation in the extreme ultraviolet and X-ray regime is used in a broad range of applications from biology and chemistry to material science.

2.3.3 Microstructural characterization: Electron Microscopy

The main characteristic of electron microscopes, compared to conventional optical microscopes, is that they use electrons instead of light and electromagnetic lenses instead of glass lenses. Under certain assumptions, electrons can be considered as waves, with wavelengths much smaller than visible light. This allows the observation of very small structures that would remain unobservable using optical microscopes, due to diffraction effects. Basically, it is possible to distinguish between: (i) scanning electron microscopy (SEM), where the electron beam scans over the surface of a *bulky* sample and (ii) transmission electron microscopy (TEM), which uses basically thin *electrotransparent* samples

Similarly as the eye cannot see anything unless it interacts with visible light in some way, e.g. reflection or refraction, we cannot see anything in the electron microscope unless the specimen interacts with the electrons in some way, unless the electrons become *scattered* by matter.

Based on the particle character of electrons, we can divide electron scattering into elastic and inelastic scattering, referring to whether interaction occurred without any loss of energy or with a certain measurable loss of energy respectively. Division of scattering into coherent and incoherent refers to the wave nature of electrons. Elastic coherent scattering occurs at relatively low angles (within 1 to 10°) as compared to the primary beam. At higher angles, elastic scattering becomes incoherent. The higher the angle of scattering of an electron emerging from the specimen, the greater the chance that it will have undergone an inelastic event at some time during its passage through the specimen. Inelastic scattering is almost always incoherent.

During imaging in the TEM, we are usually interested in those electrons that do not deviate far from the incident electron direction ($\lll 90°$), which are basically the result of interaction with the negatively charged electron cloud. The TEM microscope is constructed in such a way to collect primarily these electrons. SEM on the other hand basically collects electrons that are scattered inelastically through large angles ($\ggg 90°$) for imaging purposes. These electrons mainly provide surface-sensitive information, as illustrated in Fig. [115]. Finally, during inelastic scattering, energy is released resulting in certain "signals", which can be used for microanalysis since the energy released is usually characteristic for the

atoms present in the specimen.

The following sections will deal in further detail with the principles of SEM and TEM respectively, highlighting more the specific specimen-beam interactions important for each technique and discussing the set-up of both microscopes. Finally, a last section will deal with TEM sample preparation, which is one of the crucial steps in TEM analyis and which is for metastable materials as metallic glasses even more non-trivial.

2.3.3.1 Scanning electron microscopy: important specimen - beam interactions

Due to consecutive interactions of the incident electrons with both nuclei and electrons of the atoms of the sample, both primary electrons and generated 'signals' will diffuse and the information obtained from the different signals typically comes from a hemisperical interaction volume (Fig. 2.11) that may be up to five times larger than the cross section of the incident beam, depending on the primary energy of the beam and the composition of the sample [116].

When an electron beam penetrates into the sample, part of these *primary* electrons will immediately be reflected back without any significant loss of energy (< 1 eV), only a change in direction occurs due to reaction with the atomic nuclei of the sample. These electrons are called *backscattered* electrons and are a form of elastic incoherent scattering. These backscattered electrons have a typical energy between 15 and 30 keV, depending on the primary beam energy. Electrons with lower energies are likely to be absorbed , while, if they have a too high energy, they will not interact anymore with the nuclei of the atoms of the specimen [116]. Since heavier elements backscatter more, information on composition can be obtained from this signal: elements with a higher atomic number will be seen brighter on the resulting image. Furthermore, these backscatter electrons can also provide information about topographical aspects of the surface, because the intensity of this signal depends on the angle between the primary beam and the surface.

The electrons that are not backscattered immediately will lose their kinetic energy by interaction with the electrons of the atoms of the sample. A primary electron with sufficiently high energy will react with one of the core electrons of the atoms of the sample, providing the latter electron with sufficient energy to

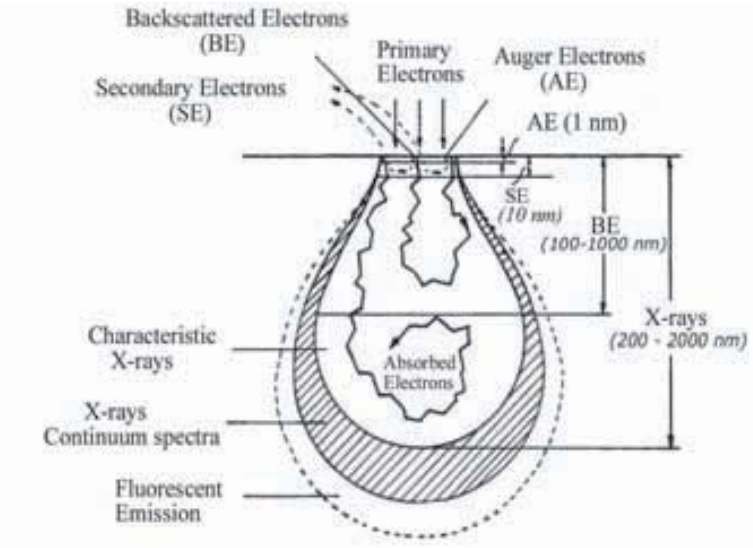

Fig. 2.11: Types of electrons and radiation generated inside the sample in a scanning electron microscope together with the relative depths from where the information is obtained [116].

leave its shell, with a kinetic energy expressed by,

$$\Delta E_{secondary} = E_{primary} - E_{bind,X}, \tag{2.24}$$

with $E_{primary}$ the energy of the incident electron beam and $E_{bind,X}$ the binding energy of the electron at a core shell X. If its kinetic energy $\Delta E_{secondary}$ is high enough, this *secondary* electron can escape from the sample. However, typical values for the energy of secondary electrons is in the order of 0-50 eV, therefore only the secondary electrons created in the surface layer can escape from the sample and thus information is limited to come from a maximum depth of around 10 nm, while the signal of backscattered electrons usually comes from a depth up to 1 μm, as shown in Fig. 2.11.

Due to this "inner-shell ionization", the atom finds itself in a highly unstable state and therefore, the corresponding "hole" is immediately occupied by a third electron, located in a more external electronic shell with lower binding energy. During this relaxation process, an amount of energy is liberated, which can be expressed as

$$\Delta E_{bind} = E_{bind,X} - E_{bind,Y}, \tag{2.25}$$

where $E_{bind,X}$ and $E_{bind,Y}$ are the respective binding energies of the electron of the more inner shell X where the hole was created and the binding energy of the electron at a more outer shell Y that will refill shell X. This "refilling" process has to obey some quantum mechanical rules [116].

The energy released can be used to emit another electron from one of the outer shells, called an *Auger electron*, or can be emitted directly under the form of *X-rays*, both carrying information (energies) characteristic for the atom where they were generated, and thus providing information about the composition of the sample. The probability of emitting an X-ray (instead of an Auger electron) is represented by the fluorescence yield:

$$\omega = \frac{Z^4}{a + Z^4}, \tag{2.26}$$

which shows that this fluorescence is a strong function of the atomic number.

The kinetic energy of the Auger electron is given by $\Delta E_{bind} - E_{bind,Auger}$. This value however is rather low. Therefore, only Auger electrons that are generated in the surface layer of the sample (typically 0.2-5 nm) can escape from the sample, and as a consequence, no information can be obtained from the inner part of the sample (Fig. 2.11).

The direct emission of characteristic X-rays with a wavelength with a wavelength $\nu = h^{-1}\Delta E_{bind}$, provides an information signal that is collected and analyzed by *Energy Dispersive X-ray analysis (EDX)*. If some regions of the sample are scanned selecting the part of the X-ray spectra corresponding to one of the elements in the sample, it is possible to obtain the distribution of this element at the surface. This technique is commonly known as X-ray mapping. Therefore, regions with higher densities of this element will appear as bright in the image, while lack of this element will result in a dark area. Since the energy in this case is higher than in the case of the Auger electrons, information can be obtained from a more inner part of the sample. However, the information obtained from the characteristic X-rays for example comes from a rather large hemisperical volume (Fig. 2.11) which can make it difficult to accurately map very fine compositional structures. Besides, while the emission of Auger electrons results mainly from elements with a low atomic number, X-ray emission is more efficient for higher weight elements [116, 117, 118].

2.3.3.2 Transmission Electron Microscopy - Electron scattering in thin foils

When the penetration depth of the electronic incident beam is larger than the sample thickness, some electrons are able to go through it, i.e. they are transmitted. The *stopping power* of the sample is insufficient for the corresponding electron beam energy, which is the case for very thin samples and high energy (100-300 kV). These electrons can be detected so as to obtain a two-dimensional image of the internal structure of the sample, which is basically the principle for TEM. However, it is important to note that such electrons are not simply *transmitted* in the sense of visible light through window glass. The electrons are *scattered*, elastically or inelastically.

1. *Elastic scattering and resolution*

   Basic TEM (imaging and diffraction) operations use elastically, coherently scattered electrons, i.e. scattered in the forward direction, nearly parallel to the incident beam direction. Modern *analytical* TEM also takes advantage of the inelastically scattered electrons that are generated anyway, e.g. for micro-analysis.

   The contribution of different parameters contributing to this elastic scattering are expressed by the atomic scattering factor $f(\theta)$, which is the measure of the amplitude of an electron wave, scattered from an isolated atom:

   $$f(\theta) = \frac{1 + \frac{E}{E_0}}{8\pi^2 a_0} \left(\frac{\lambda}{\sin\frac{\theta}{2}}\right)^2 (Z - f_x) \tag{2.27}$$

   with θ the angle of scattering, E, E_0 the beam energy (in keV), a_0 the Bohr radius of the scattering atom, λ the wavelength, Z the atomic number and f_x the scattering factor for X-rays.

   Eq.(2.27) shows that elastic scattering increases for heavier elements (large Z) but decreases as θ increases and as λ increases (i.e. as the accelerating voltage increases). Thus, the higher the voltage of a microscope, the lower the contrast obtained with it will be. On the other hand, one of the basic reasons for which the electron microscope is used is its high resolution (as compared e.g. to scanning electron microscopy). This resolution can be expressed by the Rayleigh formula, in a first approximation, which shows

that resolution increases with higher voltage and lower wavelength:

$$R = \frac{0.61\lambda}{\alpha}. \tag{2.28}$$

In Eq. (2.28), R is the size of the resolved object (the smaller R, the higher the resolution), λ is the wavelength and α is the semi-angle of the objective lens aperture. However, the use of larger apertures to increase resolution is limited by several aberration error in the lenses, as will be discussed further. As a result, an optimum aperture equilibrating minimum aberration and maximum resolution exists [115], [119], [120].

2. *Elastic scattering: Imaging.*

Practically, the transmitted and scattered electrons leaving the TEM sample pass through the objective lens (which is placed behind the specimen in contrary to the scanning electron microscope) and a *diffraction spectrum* is formed in the back focal plane of this objective lens (Fig. 2.12 a). Recombination of the diffracted electron waves results in the formation of an *image* on the image plane. To operate in imaging mode, suitably sized objective lens apertures are placed in the back focal plane of the objective lens. In this way, diffracted beams can be deliberately excluded and only the central beam is allowed to pass through. The image built up is called *bright field* image (Fig. 2.12 b). Alternatively, a *dark field* image is formed by excluding all beams, except a particular *diffracted* beam of interest (Fig. 2.12 c) [115], [119], [120].

This dark field image reveals the regions contributing to the diffracted beam intensity selected, which can be useful in the characterization of complex microstructures. In particular for amorphous samples, the dark field technique can be very useful to reveal (or exclude) the presence of nanocrystals. In samples with a certain contrast in bright field imaging but an apparent amorphous diffuse halo in diffraction, dark field imaging by selecting part of the diffuse halo can be useful to give the definite answer.

The most limiting factor for the use of the dark field technique is the confined resolution, caused by spherical aberration. This can be avoided in most modern TEMs by tilting the illumination system so that the chosen

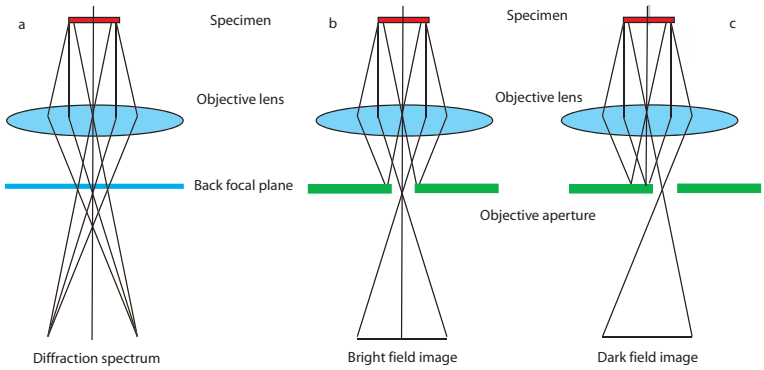

Fig. 2.12: Schematic diagram illustrating the difference between operating in (a) diffraction mode, (b) bright field imaging and (c) (low resolution) dark field imaging [119].

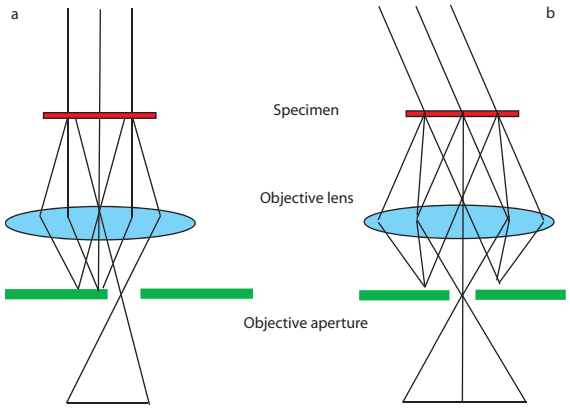

Fig. 2.13: Schematic ray diagrams showing the difference between the formation of (a) a low-resolution, displaced-aperture dark-field image and (b) a high-resolution centered dark field image, where the incident beam is tilted so that the scattered beam remains on axis [119].

diffracted beam is aligned accurately along the objective axis of the microscope, instead of simply positioning an objective aperture around the desired diffracted beam, as illustrated in 2.13.

The contrast in conventional bright and dark field images is attributed to the change of the *amplitude* of either the transmitted beam or diffracted beam, due to absorption and dynamic scattering in the specimens. This image contrast is called the *amplitude contrast*. It is suited to study *mesoscopic* microstructures.

For *high resolution transmission electron microscopy* (HRTEM), several beams on the back focal plane are selected, by using a large objective aperture. The image results from multiple beam interference and is based on the *phase* difference between the transmitted and diffracted beams. It is therefore called the *phase contrast* image [120], [121]. HRTEM can be used to determine structural models, which should however be refined by other high-resolution diffraction techniques by X-ray or neutrons. However, the strength of HRTEM lies in determining disordered and defect structures, which are often difficult to determine by other methods.

In the last few years, there has been increasing interest in the use of the *scanned* electron beams in the *transmission* microscopes (STEM). Scanning coils are present below the condenser lenses (see below) to scan the spot across the specimen on a suitable raster of small size. Where conventional TEM mode works with a parallel, coherent beam, STEM mode uses a convergent (incoherent) beam. This convergent beam acts as a probe, which can be used to localize the signals coming from the specimen, as e.g. in micro-analysis. Resolution in the case of scanning systems is mainly governed by the size of the electron spot and the current in the spot which, together with the production and detection efficiencies, determines the length of time the spot must stay in one place for the signal-to-noise ratio to be acceptably high. In thin samples, some of the electrons are transmitted with little energy loss, and it are these electrons that are usually detected in the STEM. However, the specimen emits a wide spectrum of electromagnetic waves, ranging from optical wavelengths to the characteristic X-rays, described in section 2.3.3.1, which are used in scanning X-ray micro-analysis [120].

3. *Elastic scattering: Diffraction.*

When no aperture is placed in the *back focal plane* of the objective lens, the diffraction pattern itself can be observed and recorded. By inserting an aperture at the *image plane* of the objective lens, the field from which the diffracted information is obtained is limited, which is referred to as selected area electron diffraction (SAED). The use of such an aperture makes it possible to obtain diffraction from small portions of the specimen. In this way, a direct correlation can be made between the morphological infor-

mation obtained by imaging and the crystallographic information obtained by diffraction of very small areas: typical intermediate aperture sizes range from 50 to 5 μm.

As explained already for diffraction by X-rays (section 2.3.2.1), the necessary condition to be fulfilled to obtain (any type of) diffraction is represented by Bragg's law (Eq. (2.15)). Due to the high energy of the electrons in a TEM (small values for λ), the scattering angles that fulfill Bragg's law are very small (order of mrad) and Bragg's law can be simplified to $\lambda = 2d\theta$. In practice, planes that are parallel (within a few degrees) to the incident beam will be represented in the diffraction pattern by a diffraction spot located along the normal of the crystallographic plane it represents and at a distance $\frac{\lambda L}{d_{hkl}}$ from the center of the diffraction pattern. λL is the *camera constant* (L is the camera length) (Fig. 2.14). The angle between the diffraction vectors remains equal to the angle between the normal to the crystallographic planes in the real crystal. The value of the camera constant is determined by a standard with known d-spacings.

Since a set of planes that are parallel to a single direction constitute a zone, the direction of the incident beam is parallel to the zone axis. Once a zone direction $[uvw]$ can be attributed to the direction of the incident beam, the spots in the diffraction pattern can be indexed by hkl indices since they are related to the indices of the zone-axis by the so-called *Weiss zone law* or *zone equation*:

$$hu + kv + lw = 0. \tag{2.29}$$

Eq. (2.29) summarizes in fact all planes complying with Bragg's law for in the special case of electron diffraction [122].

A convenient way to visualize the poles that will be visible for a beam parallel to a certain direction $[uvw]$, is by making the stereographic projection with $[uvw]$ in the center: the vectors $\overline{g}$ or the poles of the planes $\{hkl\}$ satisfying eq. (2.29), will lie on the great circle at 90° of [uvw] [120]. A more detailed explanation on the construction of such a stereographic projection is given in appendix B.

4. *Inelastic scattering: Micro-analysis and damage*

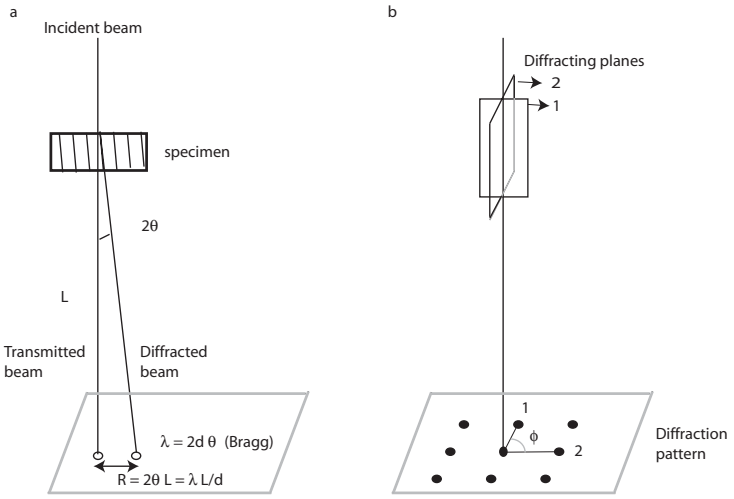

Fig. 2.14: (a) Schematic diagram showing the geometry of the formation of an electron diffraction pattern and illustrating the parameter camera length. (b) Schematic diagram of the formation of a diffraction pattern from a single crystal in the electron microscope. The beam is parallel to a zone axis, with two planes of that zone shown. Note that the angle ϕ between the spots is equal to the angle between the normals to the planes themselves [122].

Historically in TEM, only forward elastically coherent scattered electrons were used (small angle), for imaging and diffraction. However, similarly like in the SEM, signals related to inelastic scattering like secondary electrons, characteristic X-rays, Auger electrons...are generated. Inelastic scattering produces a range of scattering angles, but there is no relationship between the energy lost and the scattering angle.

Modern transmission electron microscopes provide a number of complementary capabilities, known as *analytical electron microscopy*.

(a) EDX

The way characteristic X-rays are generated and why they are characteristic has been discussed in detail in section 2.3.3.1. The cross section for ionization, which expresses the probability of ionization, is a function of the overvoltage, $U = E_0/E_c$, with E_0 the electron energy and E_c the characteristic binding energy ($E_c < 20kV$). Thus, unlike in SEM where the applied voltage should be at least 20kV, we can expect X-rays to be generated in each TEM, regardless their accelerating

voltage [115].

(b) Electron Energy Loss Spectrosopy (EELS)

Besides secondary, backscatterd and Auger electrons, and characteristic X-rays generated in a SEM, an extra signal can be measured in a TEM, which is the result of the ionisation of atoms by the primary electrons (Fig. 2.15 a). The electron that ionized the atom is deviated only through a small angle, since its loss in energy is quite small ($\leq$ 10 mrad), and is likely to pass through the sample. These inelastically scattered electrons with a characteristic energy of $E = E_0 - E_{binding}$ are being measured in EELS microanalysis.

The technique is especially useful for the analysis of light-weight elements, since they are difficult to detect by EDX, due to the nearly complete absorption of their characteristic energy at the detector [116].

The electron spectrometer which is usually mounted at the bottom of a (S)TEM is a magnetic sector in which electrons with the same mass are deflected in a $\overline{\mathbf{B}}$ field, perpendicular to the direction of their velocity, $\overline{\mathbf{v}}$, by means of the Lorentz force, given by $-e(\overline{\mathbf{v}}x\overline{\mathbf{B}})$. They follow a circular pathway, of which the radius depends on their velocity, i.e. their energy. The higher the energy of the electron, the least it will be deflected [116]. Specimen thickness is very crucial for EELS analysis and should be $<$ 50 nm.

Although inelastic scatter transfers energy to the specimen, generating a lot of useful signals about chemistry and electronic structure of the sample, the same processes transfer heat to the specimen which, unfortunately, can be disastrous, in particular for low-conductive materials. To minimize heat transfer, higher voltages can be used, but this on the other hand, might increase the possibility of so-called knock-on damage. This process occurs by the direct transfer of the beam energy to atoms in the solid, *knocking* them out of their atomic site and creating a combination of vacancy and interstitial. Such a displacement damage manifests itself as small vacancy clusters, which appears as black-white lobe contrast or dot contrast. Vacancies caused by this displacement damage can enhance diffusion processes (and diffusional transformation), when studied *in-situ*, especially at higher

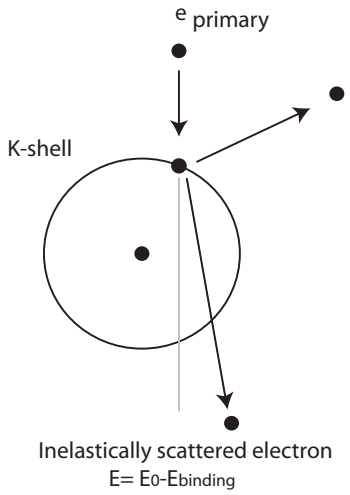

Fig. 2.15: (Schematic representation of the generation of the electron signal used in EELS micro-analysis.

voltages [115].

2.3.3.3 Components and architecture of standard electron microscopes

1. *Electron source* All microscopes need a source to illuminate the specimen. The electron source has to produce a *monoenergetic* electron beam. Generally, two types of sources can be distinguished: a) thermo-ionic emission and b) field emission.

   In the first case, a beam of electrons is produced upon heating electrically. In fact, if one heats any material to a high enough temperature, one can give the electrons sufficiently energy to overcome its *work function* Φ, the natural barrier that prevents them from leaking out of the material. Unfortunately, most materials will melt/vaporize providing them with the necessary amount of energy. Materials for thermoionic sources are typically refractory, like tungsten, or have an exceptionally low value for Φ, e.g. LaB_6.

   The electrons emitted from the thermoionic source are accelerated away from the filament under application of a high voltage between the cathode (the filament itself) and an anode. In between these electrodes a so-called "Wehnelt-cup" is usually present with a negative bias, shaping the beam electrostatically, i.e. reducing the *cross over* of the diameter of the beam,

optimizing its brightness. It is obvious that a good vacuum system is required to remove gas molecules that would lead to scattering of the electrons.

The emission of electrons with a field emission gun is based on quantummechanical tunneling between the sharp tip of the cathode, and a first anode. A second anode determines the final energy of the electron beam. With this type of source, a higher quality beam is obtained than in the case of the filament, however, a high quality vacuum is required. Since the tip suffers large mechanical shocks and stresses, a high strength material should be used. Typically, this is a W single crystal, since this can also be easily shaped in a tip with a radius $< 0.1\mu$m.

The important parameters of the electron source are the 1) energy - depending on the voltage at the anode and the degree of monochromatism ΔE, 2) the initial diameter (cross-over) d_c, 3) the angle of divergence α, 4) the current density J_0 and 5) the gun brightness β. A comparison of some important characteristics is given in Table 2.1 for both types of electron sources.

Tab. 2.1: Comparison of the characteristics of electron sources: thermo-ionic (W-filament), thermo-ionic (LaB_6) and W field emission gun (FEG) [116].

	W-filament	LaB_6	W FEG
Current density, J_0 Acm^{-2}	1-3	25	$10^4 - 10^6$
Brightness - 10-20 keV	$5x10^4$	$3x10^5$	$5x10^7 - 5x10^8$
β - 100 keV	$1 - 5x10^5$		$2x10^8 - 2x10^9$
Diameter cross-over, d_c (μm)	20-50	10-20	0.005-0.010
Energy range, ΔE (eV)	1-2	0.5-2	0.2-0.4
Required vacuum (Pa)	$10^{-2} - 10^{-3}$	$10^{-3} - 10^{-4}$	$10^{-7} - 10^{-8}$

The gun brightness expresses the current density per unit solid angle of the electron source, given by

$$\beta = \frac{J_0}{\pi\alpha^2}. \tag{2.30}$$

It is a constant through the whole electro-optical system, which means that current and aperture cannot be changed independently from each other.

2. *Optics*

   - Lenses

Electron lenses are the magnetic equivalent of glass lenses in an optical microscope. Almost any operation carried out in an electron microscope involves basically changing magnification or focussing of a parallel beam. Magnification can involve demagnification of the electron source (beam diameter) and magnification of the formed image afterwards. Where in an optical microscope magnification is changed by physically changing the lens to one with a stronger curvature, magnification in an electron microscope is changed by varying the strength of the magnetic field, without changing the lens itself.

A typical electron lens consists of two parts: a cylindrically symmetrical core of soft magnetic material (polepiece) with a hole drilled through it (bore), an a coil of Cu wire which surrounds each polepiece. When a current is passed through the coil, a magnetic field is created in the bore. Since electrons have a net charge, they experience a Lorentz force by the generation of this magnetic field, resulting in convergent spiraling around the optic axis of the electrons, reducing further the beam diameter [115].

The final electron beam diameter that is used in a SEM or TEM is formed by focussing the cross over by means of 1 to 3 lenses.

In a typical SEM with a thermoionic source, the primary cross over beam diameter is typically on the order of 30 μm. If we want to reduce the beam diameter to around 30 nm on the sample surface, this would require a reduction of 1/1000, which is not easily obtained with one lens only. Therefore, the beam passes through *two condenser lenses* to demagnify the cross over diameters, before their final pass through the *objective lens*, that controls the final focus of the electron beam by varying the magnetic field: the higher the current through the coils of the objective lens, the stronger the electromagnetic field and thus, the stronger the focussing of the electrons.

The first part of the electronic optics in a TEM is quite similar to the optics in an SEM: it exists of condensor lenses and the objective lens. However, the latter is located *underneath* the sample. In fact, there are two objective lenses in a TEM, with the lower one the most important

one: diffraction spectra are formed in its back focal plane, while the images are formed in the image plane of the lower objective lens. This objective lens is in fact the most important lens of the electro-optic system in the TEM [116]. The upper objective lens plays an important role in STEM mode.

Afterwards, the transmitted and/or diffracted beam pass through a number of *imaging* lenses, which magnify the image/diffraction pattern to the desired magnification. This is also a multilens system, placed in tandem set-up, like the case of condenser and objective lenses. Typically, the imaging lenses consist of an intermediate lens and 1 or 2 projector lenses, depending on the desired magnification [119].

- Apertures

  Apertures and diaphragms are used in TEM to limit the collection angle of the lens. The aperture of the objective lens allows the control of resolution, the image contrast, the depth of focus, the degree of convergence (important in STEM),... Apertures are circular holes in metal disks (diaphragm), usually made of a refractory metal like, Pt or Mo [115].

- Scanning coils

  The principle to scan a beam over a sample (in SEM and/or STEM), an oscillating magnetic field is generated. In a SEM, two *scanning* coils are present inside the objective lens. During scanning, the electron beam has a fixed pivot point in the lens [116].

  In a (S)TEM, the use of two sets of deflection coils, located between the second condenser lens and the upper objective (which is in STEM used as a third condenser) enables us to translate (scan) the beam across the specimen without apparently changing the angle of incidence (the beam is tilted twice in order to keep it parallel to the optic axis) or to tilt the beam without changing its position on the specimen. It is important in a TEM to be able to translate the beam without tilting it, since tilting reduces resolution, due to the presence of spherical aberration [119].

3. *Other components*

Other important components of the architecture of electron microscopes, are different types of *detectors*, to detect and record all different types of signals generated in SEM and TEM, e.g. the EDX detectors. The different detectors for each signal are described in detail in [116]. In the past, images were typically recorded by an analogue camera. Nowadays, typically, CCD cameras are used to record images and diffraction in electron microscopy.

Furthermore, a high level of vacuum is indispensable in order not to degrade the quality of the information generated, a good *vacuum system* is essential in the architecture of an electron microscope.

2.3.3.4 Aberrations and resolution

In the ideal case, the image of a circular object would be circular as well. However, in practice, this is usually not achieved due to several aberrations, with important consequences and limits of resolution, both in SEM and TEM. Four aberrations have an important influence [116], [115]:

1. *Diffraction* of the rays occurs at the lenses due to their finite size. This results in a point being imaged as a disk (called the Airy disk), with a diameter of $d_d = 1.22\frac{\lambda}{\alpha}$. α is the beam divergence angle or the semiangle of collection of a lens aperture, if one is being used. Note that, even if the electron source was a perfect single point source and no other aberrations were present, a point would not be imaged as a point, due to this diffraction. This is in fact the Rayleigh criterion, mentioned in section 2.3.3.2, that gives a first approximation of the resolution, if no other aberrations were present.

2. *Spherical aberration* is caused by the lens field acting inhomogeneously on the off-axis rays, i.e. the electron rays that are not parallel to the central optical axis. The further off axis the electron is, the more strongly it is bent back toward the axis. Curved wavefronts are curved even further by spherical aberration, what explains the terminology used. A point object P is imaged as an intense central bright region with a surrounding halo in the Gaussian image plane P' (Fig. 2.16). This defect is the main resolution limiting factor in electron microscopes. The smallest diameter of the cone of rays formed does not occur at the Gaussian image plane. It is called the

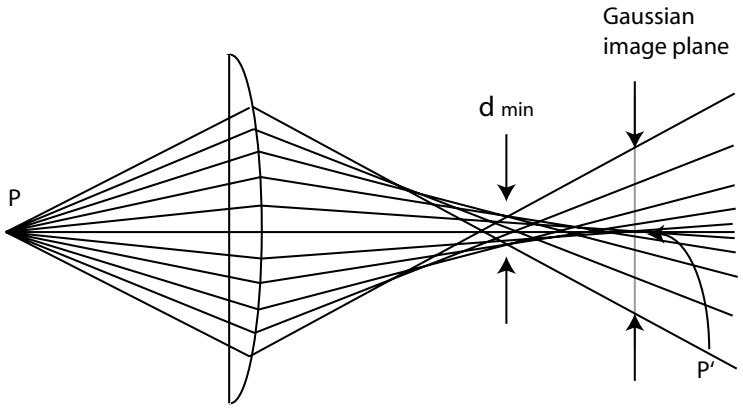

Fig. 2.16: Spherical aberration in the lens causes wavefronts from a point object P to be spherically distorted. The point is imaged as a disk with a minimum radius in the plane of least confusion, and as a larger disk in the Gaussian image plane.

disk of least confusion and has a diameter of of $d_s = C_s * \alpha^3$, with C_s the coefficient of spherical aberration for a particular lens.

Correction of this spherical aberration is typically done by multipole (typically hexapoles) lenses, which have six polepieces instead of two as typical in the magnifying lenses in the optic system of a TEM [115], [123].

3. *Chromatic aberration* is a consequence of the fact that the electrons possess small inaccuracies in energy due to the instability of the voltage at the anode in the electron source. In TEMs however, variations at the electron source are usually very small and could be ignored. On the other hand, a much more important source of chromatic aberration results from inelastic interaction occurring in the sample itself. Electrons with a lower energy $(E - \Delta E)$ are stronger deflected by the objective lens, leading to a *chromatic* broadening of a point to a disk with a diameter given by $d_c = 2C_c\frac{\Delta E}{E}\alpha$, with C_c the chromatic aberration coefficient of the lens. Chromatic aberration in TEM can be minimized for very thin samples.

4. *Astigmatism* is a consequence of the fact that the magnetic field inside the electron lens is not perfectly homogeneous. Astigmatism distorts the beam to an elliptical shape on either side of focus and prevents the beam from being fully focused. It is corrected by applying two orthogonal correction

fields in the x and y directions. This defect can have various causes (imperfect symmetry, inhomogeneities in the pole material or contamination, imperfectly placed apertures..).

Resolution (or strictly resolving power) is defined as the closest spacing of two points which can be resolved by the microscope to be separate entities. The actual beam diameter results from the diameter of the original beam leaving the electron gun, $d_g = \frac{C_0}{\alpha} = \frac{2}{\pi}\sqrt{\frac{I_{beam}}{\beta}}\frac{1}{\alpha}$ broadened mainly by the effect of spherical aberration in the lenses d_s and diffraction at the aperture d_d. This actual beam diameter can be calculated as:

$$d_{tot} = \sqrt{d_g^2 + d_s^2 + d_d^2}. \tag{2.31}$$

In all factors contributing to d_{tot} α plays a crucial role, e.g. a larger value for α is unfavorable for the spherical (and chromatic) aberration, where it improves the initial beam diameter and diffraction. It is clear that there exists an optimum value for α, where the beam diameter is minimum, and the resolution is maximum. This leads to a *practical* expression for the resolution of an electron microscope [119]:

$$d_{min} \quad \sim \quad (C_s(C_0\lambda)^3)^{\frac{1}{4}}. \tag{2.32}$$

Since $C_0 = (\frac{4I_{beam}}{\pi^2\beta})^{\frac{1}{2}}$ and β, the gun brightness β is a constant for the whole electro-optical system of a microscope as mentioned above, there is only one beam current I_{beam} at the optimum resolution. This involves that it is not possible to increase the beam current, e.g. to increase brightness or for micro-analysis, without a loss of resolution [116].

Note that in this definition, chromatic aberration, which is usually small in both SEM and conventional TEM, was ignored. However, chromatic aberration can become important in modern C_s-corrected TEMs, especially if the sample is relatively thick ($> 30 - 50$ nm). If the sample is too thick, chromatic aberration will become the resolution limiting factor, and it does not really matter how low C_s is. The "thickest" thickness allowed does depend however on the voltage applied [115].

2.3.3.5 Use of TEM in this work

1. Indexing of electron diffraction

   Electron diffraction of amorphous samples results in a typical diffuse ring pattern. The positions of the diffuse rings roughly correspond to the (reciprocal of the) average nearest (short-range order) and next-nearest (medium-range order) atomic spacings in the material [122].

   The diffraction pattern of a crystal consists of a lattice of spots that bears a reciprocal relationship to the real lattice of the crystal and is therefore referred to the *reciprocal lattice*. This reciprocal lattice is a mathematical concept, defined as a lattice of spots, each of which represents a set of planes (hkl) of spacing d in the real lattice. Together with the Ewald sphere construction, it provides us with a manner to express Bragg's law as a vector equation More details concerning these mathematical concepts are described in App. A. One of the advantages of the use of the reciprocal lattice is that any 2-D section of a reciprocal lattice can be defined by two vectors $\overline{g_{hkl}}$ so we only need to index 2 spots. All others can be deduced by vector addition [119].

   The intensity of a given diffraction spot is related to the shape, volume and perfection of the crystal and the *structure factor* F_{hkl} for the unit cell. This structure factor is a measure of the amplitude scattered by all the atoms in a unit cell into the reflection hkl. F_{hkl} is not a simple sum of all the values of f_j (Eq. (2.27)) because the phase difference between the waves scattered by the different atoms has to be taken into account. The calculation of the structure factor is done in App. A. The intensity diffracted by the unit cell into the hkl reflection, I_{hkl} is the square of the amplitude F_{hkl}:$I_{hkl} = F_{hkl}F^*_{hkl}$ with F^*_{hkl} known as the complex conjugate of F_{hkl}. From this definition, it is clear that diffraction will only occur for these points for which $F_{hkl} \neq 0$.

   It can be shown that for certain lattice types or symmetry elements, this structure factor becomes zero, leading to systematic absences or *forbidden* reflections [120], [122]. On the other hand, each diffracted beam behaves to some extent as an incident beam and can diffract electrons to a point on the diffraction pattern which was actually forbidden by the structure factor

rules. This can complicate to some extend the indexing of the diffraction pattern of systems with low symmetry. In fcc or bcc crystals, double diffraction does not introduce extra spots since the combination of any two diffracted beams generates only allowed reflections. Presence of *twins* can introduce extra spots by double diffraction, even in cubic systems [120].

2. Imaging by *incoherently* scattered electrons: High Angle Annular Dark Field(HAADF)

   Imaging in conventional TEM uses typically elastically coherently scattered electrons. However, interpretation of these images can be sometimes difficult due to e.g. thickness variations [124].

   Incoherently scattered electrons, i.e. scattered at larger angles, can also be used for imaging in the scanning transmission electron microscope (STEM). It relies on the use of a high angle annular detector to average phase correlations between diffracted beams, as illustrated in Fig. 2.17. These electrons provide enhanced image resolution, comparable to the resolution in HRTEM and a wealth of composition information, because the intensity increases according to a Z^2 dependence, as suggested by the Rutherford cross section for elastic scattering [115], [126]:

$$\frac{d\sigma(\theta)}{d\Omega} = \frac{e^4 Z^2}{16(E_0)^2 \sin^4 \frac{\theta}{2}}, \tag{2.33}$$

   with e the electron charge, E_0 the electron energy (in keV) and θ the scattering angle. This Rutherford cross section is mathematically equivalent to $|f(\theta)|^2$, described in Eq. (2.27). In fact, both approaches are complementary, where the atomic scattering factor is useful for describing low-angle (coherent) elastic scattering, where the Rutherford differential cross section is inappropriate.

   Maxima in intensity are accurately correlated with the locations of atomic colums, making possible the direct inversion to the projected structure without the need for simulation or models. The Z-contrast image also provides a convenient, high intensity, *reference image* for atomic resolution EELS or EDX, since both signals may be measured simultaneously. As the Z-contrast image is obtained with an annular detector, a large fraction of the inelasti-

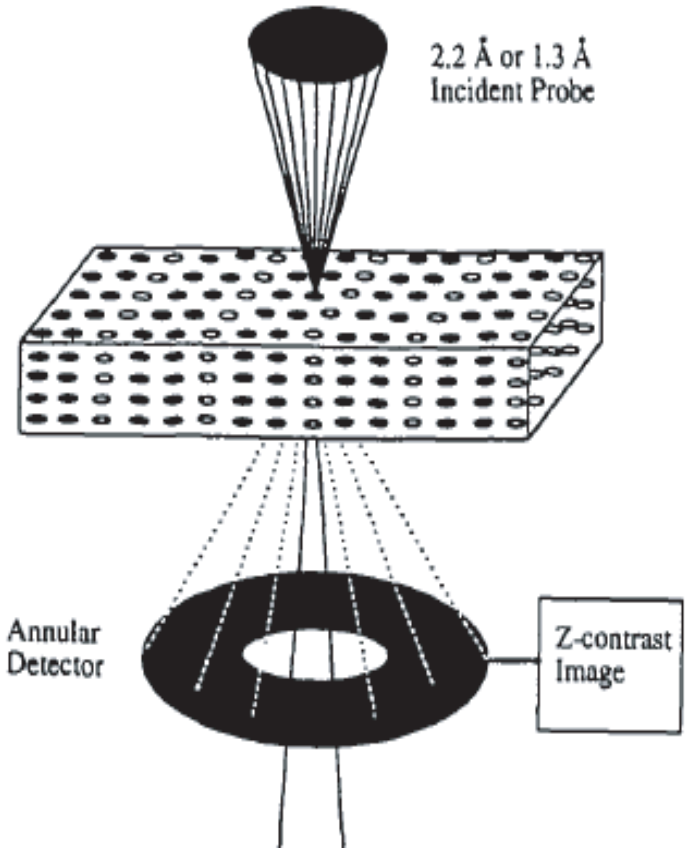

Fig. 2.17: Schematic illustration of the detector set-up in a STEM equipped with a high angle annular detector [125].

cally scattered electrons used in EELS can simultaneously be collected with an axial spectrometer [125]. The images formed are almost independent of sample thickness and defocus [126], [127].

3. Use of C_s-corrected TEM - imaging of medium-range order

   High-resolution electron microscopy is now readily available for direct observation of local structures almost down to the atomic scale. Attempts at high-resolution imaging of glassy structures started in the 1970s [128]. However, a direct clear imaging of the local structures by this technique has not been possible, even for very thin amorphous structures. This is mainly because of the important negative influence of spherical aberration of the objective lens on the resolution, which causes the information in the image to be blurred.

   One of the ways to improve the quality of the image or to reduce the problem, is typically done by post-processing via a series of through-focus images [123]. The principle is that by slightly defocusing the image, the disk of least confusion, where the beam diameter is minimum, can be brought closer to the Gaussian image plane (Fig. 2.16).

   By this defocusing technique, it has been possible to image selectively atomic clusters in an amorphous matrix as high-contrast lattice fringes, when periodic atomic planes of the cluster are aligned parallel to the electron beam. Under suitable defocus, bcc atomic clusters in an amorphous $Fe_{84}B_{16}$ [37] and fcc-clusters in amorphous $Pd_{77.5}Cu_6Si_{16.5}$ [38] and $Pd_{82}Si_{18}$ [39] were observed. Typical defocus distances were on the order of 100-150nm from the Gaussian focus. However, even under these defocus conditions, a fine-grained background contrast could not be avoided, which disturbs the clear lattice imaging of clusters.

   Very recently, Hirata and coworkers [129] demonstrated by simulations and experiments, that the locally ordered clusters in metallic glasses could be directly imaged, i.e. without the need of (large) defocus values, by correcting the spherical aberration constant C_s. This is illustrated in Fig. 2.18, where high resolution images are compared, respectively made with a TEM without (left) and with the spherical aberration corrected. When no corrector is

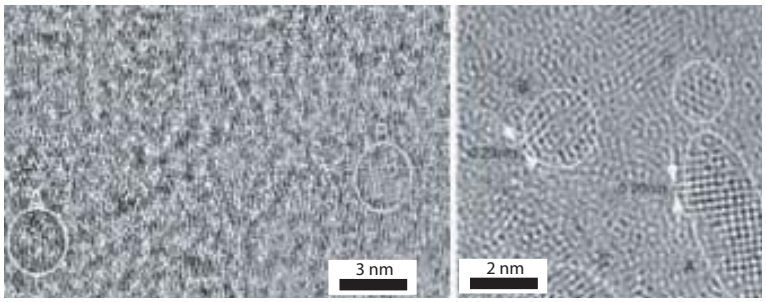

Fig. 2.18: Comparison of HRTEM images without (left) and with C_s correction (right). The left image was made with a 300kV FEG TEM, without C_s correction. MRO clusters can be observed at a defocus value of 150nm. When C_s is corrected for, a clearer contrast between matrix and clusters is obtained, near the Gaussian focus, with a 200kV FEG TEM. [129]

present, large underfocus values are necessary and the contrast is poor.

Nowadays, C_s can effectively be reduced to (values nearly) zero, so other aberration become the limiting factor, mainly chromatic aberration becomes the new challenge to overcome, in order to improve resolution to the sub-Angström level [123].

2.3.3.6 Practical conditions

Microstructural observation and analysis by SEM were performed at the Servei de Microscòpia at the Universitat Autònoma de Barcelona. A Jeol JSM-6300 scanning electron microscope, equipped with an energy dispersive x-ray spectrometer (EDX, Link ISIS-200) was used for microstructure observation and phase identification.

Samples were mechanically polished to mirror finish with 1 μm diamond paste, followed by a final polishing step with a colloidal silica suspension. To enhance contrast, the sample was chemically etched by dipping it in a fresh-made, aqueous solution containing 10% HNO_3 and 2% HF for 5 to 10 seconds.

TEM studies were performed at 4 different locations.

Conventional imaging and diffraction were performed mainly with a 200kV JEOL JEM-2011, located at the Servei de Microscòpia at the Universitat Autònoma de Barcelona (Bellaterra) or with a 200 kV Hitachi 600AB TEM, located at the Serveis Cientificotècnics at the Universitat de Barcelona (Barcelona), both

equipped with a LaB_6 thermo-ionic source.

HAADF images and EDX in scanning mode were obtained by the aid of Dr. Jürgen Thomas at the IFW Dresden (Germany) with a a 300kV Tecnai F30 with field emission.

In-situ heat treatments, described and analyzed in chapter 4, were performed by Dr. Frédéric Mompiou at the CEMES in Toulouse (France) with a 200kV JEOL JEM-2011. The sample holder, designed by Gatan, had a special design to minimize thermal drift during the experiments.

EELS experiments and HRTEM images finally were made by ing. Florent Houdellier, using a 200 kV F20-SACTEM Tecnai TEM fitted with an energy filter GIF-Tridiem, located at the CEMES in Toulouse (France). The correction for spherical aberration in the latter microscope results in an increased resolution, permitted the visualization of medium range order in amorphous samples, according to the principle above. Due to thermal drift of the samples it was not possible to make whole series at different defocus values, as was done in [129]. Furthermore, in practical situations, the Gaussian focus is set were the contrast is maximum, i.e. were the amorphous background is minimum.

2.3.3.7 Sample preparation for TEM and possible artifacts

In order to observe and analyze a sample by TEM, it should be *electron transparent*. This means that it should be thin enough to transmit sufficient electrons such that enough intensity falls on the screen or photographic film to give an interpretable image in a reasonable time.

In fact, this requirement for thin specimens is probably one of the major limitations for TEM, since all existing preparation techniques involve a great risk of changing both structure and/or chemistry of a specimen - even for conventional/stable materials. For metastable materials like metallic glasses and nanocrystalline materials, an extremely careful control of sample preparation should be taken [124], [130].

In general, we can divide the specimens into two groups: self-supporting specimens and specimens that require the use of a supporting grid (usually Cu). The samples investigated in this work all belong to the first group and have the advantage for example during X-ray analysis that there is no signal coming from the supporting grid. The thinning process for this group of specimens involves three

steps, which on their turn can be done by various techniques [115]:

- Flat thinning to make a (flat) slice of material, usually up to 100 μm thick (and perfectly parallel faces to avoid stresses). After flattening, a disk of 3 mm should be cut from this slice.

- Dimpling: thinning of the central region from one or both faces of the disk to a few micrometers

- Final thinning to perforation

The method used for each step depends on what you want to study and on the physical characteristics of the material.

In this work, all samples were obtained with diameter of 3 mm directly upon casting. Therefore, the first step was done by simply cutting disks of approximately 300 μm with a diamond bladed saw of the type Struers Accutom (IFW Dresden) or Struers Minitom (Servei de Microscòpia at UAB) and mechanically polishing them, using a Gatan Disc Grinder and SiC paper, down to 120-130 μm, with the final polishing step with 4000-grid paper. The final thickness of this step should not be below 100 μm in order to obtain good positioning during the final thinning process.

The aim of the second step is to thin the center of the disk while minimizing damage to the surface of the sample. This step can be performed mechanically or chemically. Most commercial mechanical dimplers consist of two rotating systems with different diameter and with perpendicular rotating axes. A wheel with a small radius rotates on the center of the sample to grind and polish it to a fixed radius. Both load, speed of rotation and the precise depth of the dimple are controlled. On the small-radius tool, diamond paste is applied while at the same time, the sample is cooled with a refrigerant.

An alternative, which combines step 1 and 2 is the so-called tripod polisher with which the sample can be immediately thinned to less than 5μm on a regular polishing wheel. By adhering a Si monocrystal, which changes color when thinned below 5 μm, next to the specimen, thickness is controlled during the process. This tool has had a major impact on TEM sample preparation, particularly in semiconductor industry [115].

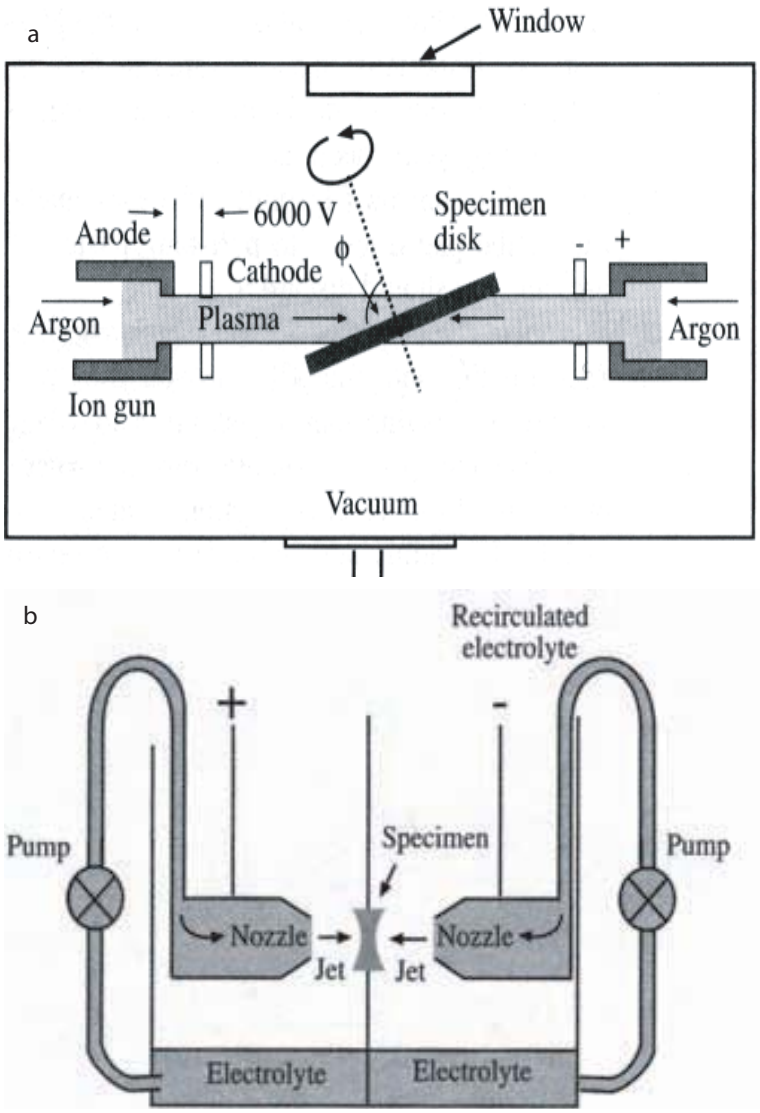

Fig. 2.19: Schematic representation of (a) ion beam milling and (b) electropolishing (twin jet) [115].

In this work, samples were pre-thinned by mechanical dimpling at one side with a Gatan Dimple Grinder 656. Final thickness was around 20-25 μm.

Final thinning of the disk can generally be done by *ion beam milling* or by *electropolishing*. Both techniques were tested in this work and there principles are illustrated schematically in Fig. 2.19.

Ion milling involves bombarding the delicate thin specimen with energetic

ions (usually Ar) in order to sputter the material from the sample until it is thin enough to be studied in the TEM. The parameters to control are the voltage, the nature of the ion (Ar, He or a reactive ion) and the geometry (angle of incidence, attack from bottom or top part). Some devices also offer the possibility of cold milling with liquid nitrogen. The specimen is usually rotated at a few rpm during thinning to avoid the development of surface structure under the form of grooves which run in certain directions.

To avoid penetration of ions into the sample, the angle of incidence of the ion beam should be minimized. Preferential (compositional) thinning has also been proven to be avoided by low inclination angles ($< 5°$). However, in this way, the energy of the ion beam will be deposited in a region close to the surface, leading to implantation and thus change of the chemistry of this near-surface region. Physical damage of this zone can also occur, e.g. amorphization of this region in (stable) crystalline samples. Lowering the beam energy or using ions with a lower atomic number might decrease the damage level, but increase the milling time. Finally, the last drawback of ion thinning is that there is a rather large possibility that material removed from one part of the sample is redeposited elsewhere on the sample.

Fig. 2.20 illustrates three possible problems encountered during this work. First of all, complete amorphization of a nanostructured eutectic alloy, based on TiFe(Sn). For comparison, the XRD pattern is shown next to it, revealing the initially (nano-)crystalline structure. Secondly, an initially nanocrystalline Zr-based sample, shows an amorphous matrix with a homogeneous distribution of nanocrystals of around 10 nm. However, the electron diffraction pattern does not coincide with the interplanar distances measured from X-ray diffraction. This could be the results from amorphization and (partial) recrystallization or partial amorphization only. Finally, Fig. 2.20 c shows an initially amorphous Zr-based BMG, as can be seen from the typical amorphous broad halo in the XRD spectrum, that (nano-)crystallized completely during TEM sample preparation. All samples were prepared with a Gatan precision ion polishing system (PIPS 691) a voltage of 5 keV and inclination angles of 8°. The device does not have the possibility to cool with liquid nitrogen.

Even with a procedure for polishing heat-sensitive samples without liquid-nitrogen cooling, described by Gatan itself, crystallization could not be avoided.

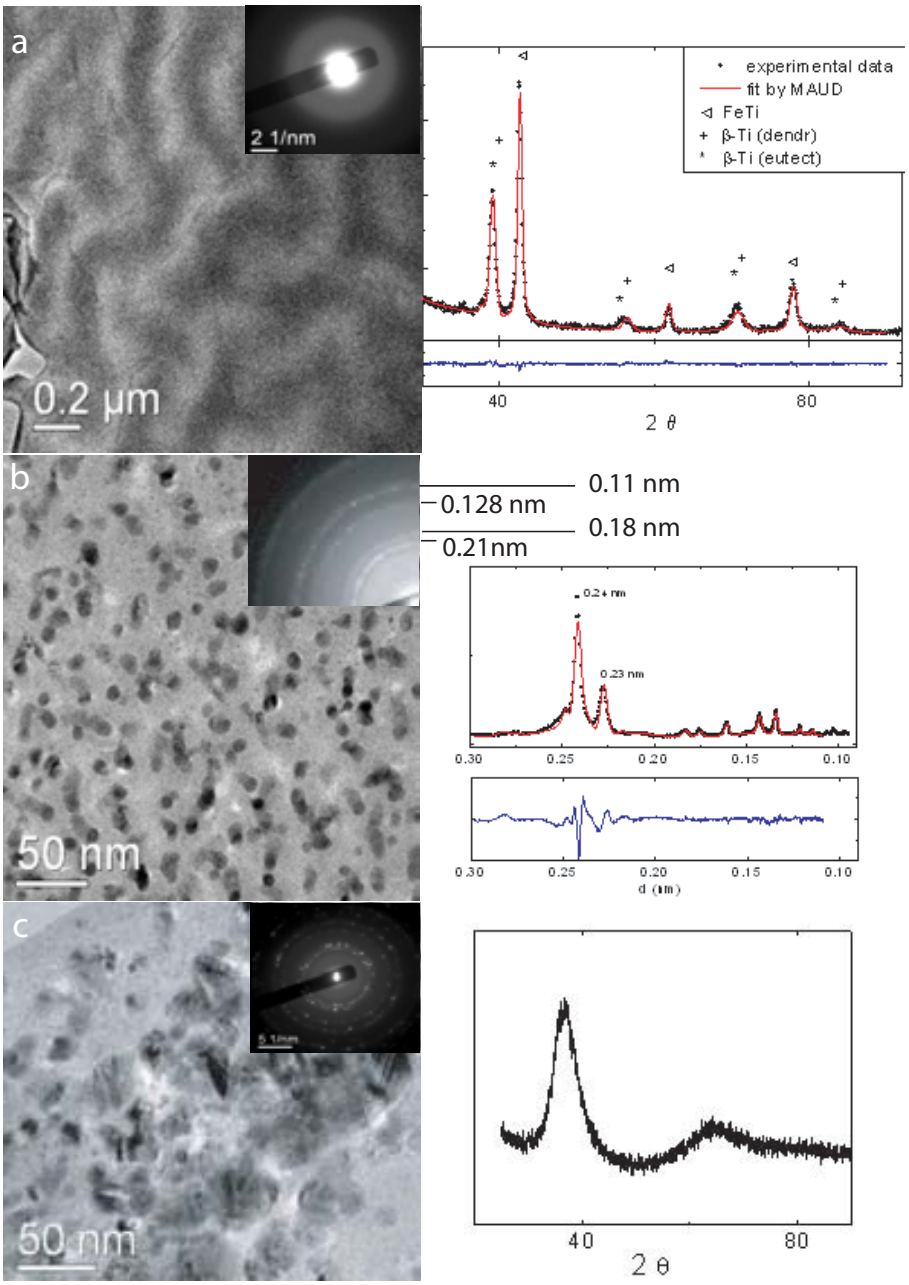

Fig. 2.20: Possible artifacts encountered during TEM sample preparation. a) Amorphization of a nanocrystalline TiFeSn-sample b) Partial amorphization/partial recrystallization of a nanocrystalline Zr-based sample. c) Nanocrystallization of an initially amorphous Zr-based BMG.

Furthermore, this procedure requires the use of a Cu supporting grid, since it consists of a mechanical polishing step down to 30 to 50 μm, followed by a dimpling step down to 10 or even 5 μm. Ion beam milling should be performed by gradually decreasing the ion beam energy from 4 to 2 keV, as perforation approaches with inclination angles of 4° on top (dimpled surface) and 2° on the bottom (flat) side. Such low values led often to milling times over 40 hours, resulting in the attack (and diffusion) of Cu inside the sample and/or crystallization could not be avoided.

The fact that no mechanical damage is introduced and the relatively fast production of samples (few minutes per sample) are the great advantages of *electropolishing*. On the other, it can change the surface chemistry of the sample and it can be a hazardous method for the health of the person preparing the samples.

The basic principle of this technique is that there is a certain voltage applied at which the current induced creates a polished surface, due to anodic dissolution of the specimen. When the voltage and concomitantly the current are too low, etching (oxidation) occurs while on the other hand, if they are too high, pitting (non-uniform) dissolution appears. In practice, the suited voltage lies within a range where increasing or decreasing the voltage leads to a more or less constant current, as shown schematically in Fig. 2.21. Ideal conditions for obtaining a polished surface require the formation of a viscous film between the electrolyte and the specimen surface.

In the twin-jet apparatus (as shown in Fig. 2.19b), a jet of electrolyte is pumped onto both sides of the dimpled disk. The sample itself is being used as a conductor. A laser beam or light sensor detects transparency after which the voltage is switched off automatically. To avoid any chemical etching, the disk must be rapidly extracted from the electrolyte and carefully washed and dried afterwards.

Electropolishing can still be considered as a black art when it comes to control of working conditions and reproducibility. However, where in the past a lot of the process parameters as voltage, electrolyte flux, temperature, electrolyte solution chemistry... were determined by trial and error, currently, modern equipments are accommodating some of these needs for better reproducibility by offering programmed functions e.g. to determine voltage, temperature control, ...

In this work, a Struers Tenupol-5 device was used for electropolishing. As

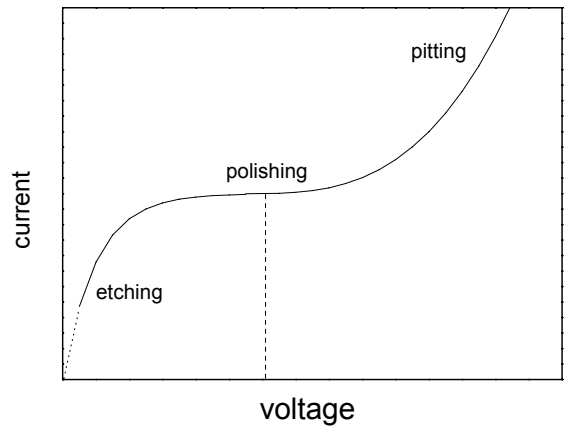

Fig. 2.21: Electropolishing curve showing the increase in current between anode and cathode as the applied voltage is increased. Polishing occurs on the plateau, etching at low voltages and pitting at high voltages.

electrolyte, a solution of nitric acid in methanol (3/7) was chosen, after literature data for a similar composition ($Zr_{54}Cu_{46}$) [131]. The polishing voltage of 10.5 V was determined automatically by this device by running a full scan from 0 to 20 V on an unpolished test sample of 300 μm thick. Some 20 test samples were prepared to investigate further the influence of several parameters, like temperature, flow rate, sample thickness before electropolishing and shape of the dimple. In the first place, microstructural changes should be avoided at all times of course. Secondly, the quality of the polishing, i.e. the final thickness and the amount of observable area.

Operation *temperature* should be kept around -25°C, to avoid microstructural changes (nanocrystallization) induced during preparation at higher temperatures (> -20°C). Cooling was achieved by circulating a refrigerant of 50% ethylenglycol and 50% distilled water inside the coil by means of a separate cooling device. If necessary, extra cooling could be obtained by adding liquid nitrogen directly into the electrolyte. Temperature was recorded continuously. Too low temperatures on the other hand (< -30°C) increase too much the viscosity of the electrolyte and might result in contaminated surfaces afterwards, which make unambiguous analysis afterwards very difficult.

The *flow rate* of the electrolyte should be high enough in order to attack in the center of the dimple and in order to remove the polished material away from

the sample during the process. On the other hand, if the flow rate is too high, this results in a too high impact on the thinnest region around the perforation and "blows" it away, leaving the sample without sufficient thin area for observation.

Concerning the thickness of the dimple (before final thinning), there was little influence on the quality of the observable area after electropolishing. The shape of the dimple on the other hand, seems to have a more important influence. For example, dimpling from 90 to 20 μm resulted afterwards in a worse observable (thicker) area than dimpling from 120 to 20 μm, whereas dimpling from 140 to 40 μm did not give necessarily worse results. Since it is difficult to polish (flatly) always until exactly the same thickness, we choose to remove by dimpling always 100 μm (to a final thickness between 20 and 35 μm), which gave very satisfying and reproducible results.

2.3.4 Mechanical characterization

The application of a force to a material is known as loading. The reaction of the material to such an applied load are related to the load by its mechanical properties. Materials can be subjected to different loading schemes, and the materials (mechanical) properties and thus its performance are dependent on these loading conditions. There exist five fundamental loading conditions: tension, compression, torsion, bending and shear. The most common properties to classify and/or characterize a material are strength, ductility, impact (resistance) and toughness. Besides the type of loading, the rate of loading, temperature,... can have their influence on the mechanical properties measured: they are often not intrinsic properties of the material. Often, multiple tests should be conducted to determine mechanical properties.

In this work, (uni-axial) compression tests, acoustic measurements and (tri-axial) nano-indentation and were applied to measure mechanical properties. By compression tests, yield stress and fracture stress, as well as the Young's modulus can be determined (for compressive load). Acoustic measurements are a relatively fast, non-destructive technique to determine elastic properties, like Young's modulus, shear modulus, bulk modulus, Poisson ratio...

Indentation experiments were historically performed to measure the hardness of a material, which on its turn can be related to the (uni-axial) yield stress, as explained below. Nowadays, it is also possible to determine the elastic modulus

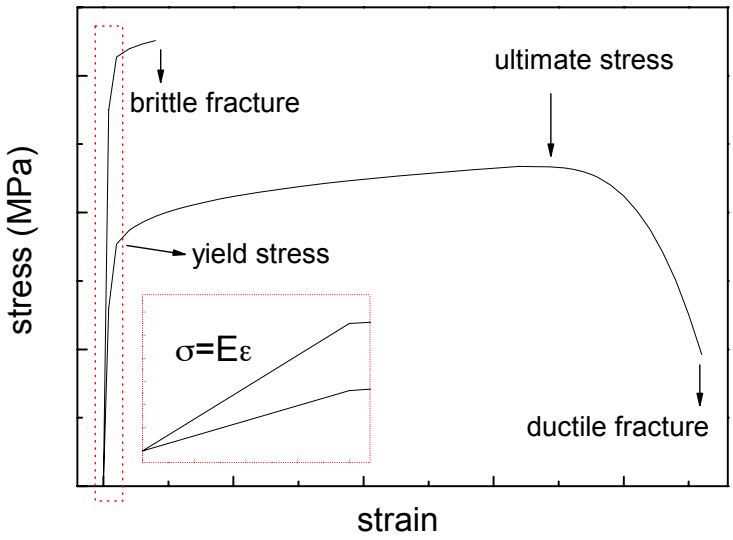

Fig. 2.22: Engineering stress-strain curve of a brittle and a ductile material.

from the unloading curve. Besides the measurement of mechanical properties, nano-indentation proved its merit in the study of local deformation behavior, e.g. shear banding in metallic glasses.

2.3.4.1 Uni-axial compression

In compression testing, a specimen is subjected to a continuously increasing uni-axial compressive force until it fractures. Load (F) and displacement (l) are carefully recorded. The outcome of a compression test is a load-displacement curve, which on its turn is usually converted into a (compressive) stress-strain curve by:

$$\begin{aligned} \sigma_{eng} &= \frac{F}{A_0} \\ \epsilon_{compr,eng} &= \frac{l_0 - l}{l_0} \end{aligned}$$

with A_0 the (initial) cross section area on which the load is applied and l_0 the initial length of the test specimen. Note that in this case, the compressive strain, although in theory negative, is expressed in such a way to represent it on the positive axis. Typical stress-strain curve is shown in Fig. 2.22. Up to certain loads, a solid will recover its original dimensions when the load is removed, which is known as *elastic* behavior. The limiting load beyond which the material no

longer behaves elastically is the elastic limit. If the elastic limit is exceeded, the body will show a permanent deformation after the load is removed. The specimen has undergone *plastic deformation*. For most materials, as long as the load does not exceed the elastic limit, the deformation (strain) is proportional to the load (stress), known as Hooke's law: $\sigma = E\epsilon$. The constant E is called the *Young's modulus*. A detail of the (usually small) elastic region, the initial linear region of the stress-strain curve, is shown in the inset of Fig. 2.22 (marked by the dotted rectangular).

The determination of the exact elastic limit is quite tedious and depends strongly on the sensitivity of the instrument measuring the displacement. For engineering purposes, the limit of elastic behavior is therefore described by the *yield strength*. This yield strength is defined as the stress which will produce a small amount of permanent deformation, generally equal to 0.0002 or 0.2%.

Once plastic deformation has set in in conventional (crystalline) metals/metallic alloys, they become stronger and load has to increase to deform the specimen further (strain hardening). Eventually, load reaches a maximum value. This maximum load divided by the original area of the specimen is the ultimate strength. Beyond that value, the diameter of the specimen begins to decrease rapidly and the load required drops off. Since the definition of the average stress (Eq. (2.34)) is based on the original area of the specimen, it also decreases from maximum load to fracture. In true stress-strain curves, which take into account the instantaneous surface area and length, stresses increase continuously up to fracture. They are calculated similarly as the engineering stress-strain curve, but using the instantaneous surface area instead of the initial one for the true stress. True strain is calculated as $\epsilon_{true} = \ln(\epsilon_{eng} + 1)$.

The general behavior of materials under load can be classified as ductile or brittle, depending upon whether or not the material exhibits the ability to undergo plastic deformation. A brittle material fractures almost at the elastic limit with only a few degrees of plasticity before fracture, as shown in Fig. 2.22. Adequate ductility is an important engineering parameter, because it allows the material to redistribute stress concentrations [52].

Note that brittleness is not an absolute property of a material. Metallic glasses for example usually behave brittle in tension, but can show a rather ductile behavior in compression.

Macroscopic compression tests in this study were done at room temperature by an Instron 8562 testing machine, located at the IFW Dresden, with an initial strain rate of $1x10^{-4}s^{-1}$. The compression test samples were prepared according to ASTM standards to a perfectly orthogonal geometry with an aspect ratio of 2:1.

2.3.4.2 Ultrasonic spectroscopy

Ultrasonic spectroscopy typically measures the relationship between material's properties and acoustical characteristics in a non-destructive way. It is a spectroscopy technique based on the use of sound waves instead of the typical electromagnetic waves in most known spectroscopy techniques.

In particular, a high-frequency acoustical wave probes intermolecular/interatomic forces in materials. Oscillating compression and decompression in the wave cause oscillations in the material, i.e. vibrations in the atomic arrangements in the sample, which responds with interatomic attraction or repulsion. However, these (amplitudes of) deformation are extremely small, giving the non-destructive character to this technique.

The two main parameters measured by high-resolution ultrasonic spectroscopy are the attenuation and the velocity of the waves. Attenuation is determined by the energy losses in compression and decompression in the wave, which include absorption and scattering. Ultrasonic velocity depends on the density and elasticity of the material. This is extremely sensitive to the atomic arrangement and interactions in the material and can be exploited in the analysis of a broad range of processes, e.g. accurate determination of elastic properties.

In this method, an electronic signal is transferred into longitudinal and transversal ultrasonic waves by a piezotransducer, and these waves are sent through the sample whose width is larger than the respective wavelengths. Another piezotransducer transfers the received ultrasonic wave into an electronic signal for subsequent analysis [132].

From the two resulting velocities of these waves the elastic constants can be calculated as following [133]:

$$E = \rho \frac{3V_L^2 - 4V_T^2}{(\frac{V_L}{V_T})^2 - 1} \quad (2.34)$$

$$\nu = \frac{3V_L^2 - 4V_T^2}{2(V_L^2 - V_T^2)} - 1 \quad (2.35)$$

with E the elastic modulus, ν Poisson's ratio, V_L and V_T are the longitudinal and transverse wave velocities respectively and ρ is the sample density.

Samples with a length of 3 and 6 mm were tested, after polishing them to perfect orthogonal geometry (perfectly parallel planes). Their density had been determined by the Archimedes method, using CCl_4, with an average value of 6.75±0.07 g/cm^3.

2.3.4.3 Nanoindentation

1. General concepts of indentation

   Indentation testing is a simple method that consists essentially of touching the material of interest, whose mechanical properties such as elastic modulus and hardness are unknown, with another material whose properties are known.

   In a typical indentation test - whether on the macroscopic, microscopic or nanometric scale - load is applied to an indenter that is in contact with the surface of a specimen. While in a conventional micro- or macrohardness test, penetration depths h of the order of 10^1-10^3 μm and forces P in the range 10^{-2}-10^2 N are used, in a nanohardness test, both h and P can be as small as 10μm and 10 mN respectively [134].

   In any indentation experiment, evaluation of hardness is done by dividing the applied force F by the contact area A between the indenter and the sample surface. However different *shapes* can be used for the indenter, and if A is taken as the curved surface area under the indenter, the shape of the indenter clearly will have a strong impact on the hardness values obtained , [134], [135]. Therefore, a more physical meaning is assigned to H, when A is taken as the projection of the area of contact, A_p, between indenter and

surface onto the specimen surface:

$$H = \frac{P_{tot}}{A_p}. \tag{2.36}$$

This definition has become known as Meyer hardness H_{meyer} [136], the physical meaning of which is the mean pressure p over the surface of the indentation, if the friction between the surface of the indenter and the sample can be neglected.

In conventional macro- and microhardness tests, the projected contact area is calculated *after unloading* from the residual impression left in the surface of the specimen by optical means. For sub-micron testing, the size of the residual impression is too small to be measured accurately with optical techniques. Therefore, load and depth of penetration are recorded during the whole experiment - both during loading and unloading. The depth of penetration together with the known geometry of the indenter provides an indirect measure of the area of contact *at full load*, from which the mean contact pressure, and thus hardness, may be estimated. For this reason, nanoindentation testing is often referred to as depth-sensing indentation testing.

When load is removed from the indenter, there is some degree of recovery due to the relaxation of elastic strains within the material. An analysis of the initial portion of this elastic unloading response can be used to estimate the elastic modulus of the indented material. By analyzing the initial (linear) portion of the elastic unloading response, also referred to as the stiffness, $S = \frac{dP}{dh}$, and the area of contact A, the elastic modulus E^* is calculated as:

$$E^* = \frac{\sqrt{\pi}}{2\beta\sqrt{A}} \frac{dP}{dh}. \tag{2.37}$$

The value of β can be set to 1 in a first approximation. However, when very accurate values of the mechanical properties are required, a more accurate value of β should be determined, which is usually done by simulations [137]. The contact area is determined from the value of h_p and the known geometry of the indenter. The value of h_p is found by analysis of the load-displacement data, as explained below.

Analysis of the elastic modulus by the method described above is only valid in the part where there is only elastic recovery. Note that the elastic modulus measured by depth-sensing indentation techniques does not have the same meaning as the term "Young's modulus". The "indentation" or "reduced" modulus contains contributions of both the material and the indenter, since the elastic displacements occur both in the specimen and the indenter. The reduced modulus is related to the Young's modulus of the material by:

$$\frac{1}{E^*} = \frac{1-\nu^2}{E} + \frac{1-\nu_i^2}{E_i} \tag{2.38}$$

with E and ν the Young's modulus and the Poisson's ratio of the sample and E_i and ν_i the corresponding properties of the indenter respectively.

The value of the indentation modulus may be affected greatly by the material behavior, e.g. pile-up around the indenter, which is not always accounted for in the analysis of the load-displacement data. For this reason, care has to be taken when comparing the modulus for materials generated by different testing techniques and on different types of specimens. Similarly, in materials that are able to recover a large amount of the elastic deformation during unloading (e.g. rubbers), hardness values measured by conventional methods after unloading can differ quite a lot from the results from nanoindentation tests, since the latter ones are calculated at the moment of maximum load, before unloading.

Finally, besides the conventional hardness and elastic modulus measurements, the shape of the load-displacement curve, e.g. appearance of pop-ins, is often found to be a rich source of information: the identification of non-linear events such as strain-hardening, cracking, phase-transformations and creep [134].

2. Determining the area of contact from depth measurements

   The determination of the contact area is of crucial importance for the values of H and E.

   The methods of determining the area of contact from depth measurements are founded upon the elastic equations of contact of Hertz [134]. The mean contact pressure is usually determined from a measure of "plastic" depth,

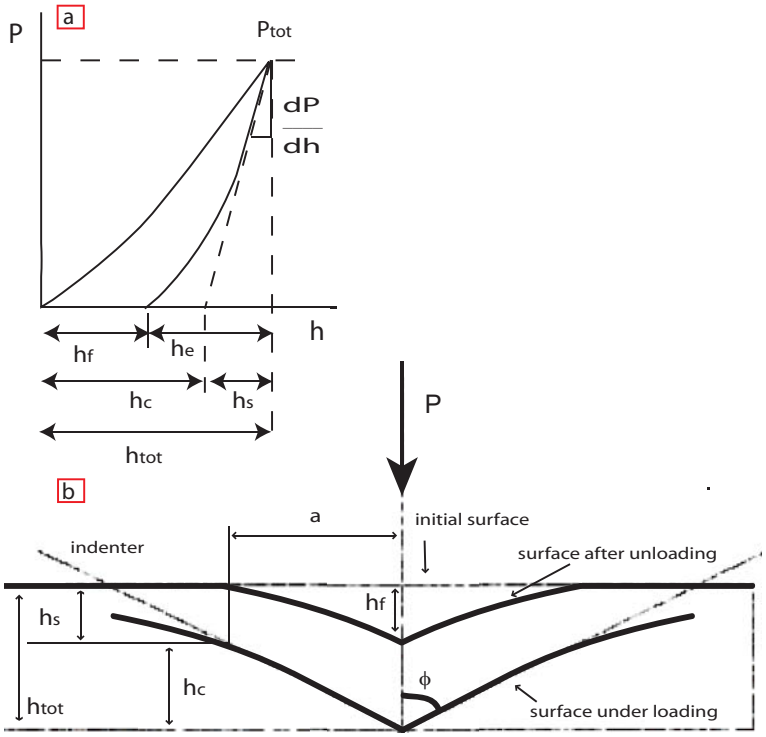

Fig. 2.23: (a)Load versus displacement for elastic-plastic loading followed by elastic unloading from a typical nanoindentation experiment [134]. (b) Schematic illustration of the indenter and specimen surface at full load and unload and the parameters characterizing the contact geometry: h_{tot} is the total depth at full load P_t from the original specimen surface. The depth of the contact circle h_c and slope of the elastic unloading $\frac{dP}{dh}$ allow specimen modulus and hardness to be calculated. h_f is the depth of the residual impression and h_e is the displacement associated with the elastic recovery during unloading. h_s is the distance from the edge of the contact to the specimen surface at full load [138]

.

i.e. the depth along which contact is made with the indenter, h_c, as shown in Fig. 2.23.

The validity of the results for hardness and modulus depends largely upon the analysis procedure used to process the raw data. Such procedures are concerned not only with the extraction of modulus and hardness, but also correcting the raw data for various systematic errors that have been identified for this type of testing, e.g. the rounding of the tip. To determine the area, the shape of the indenter and the compliance of the whole system must be known. Moreover, the shape and the compliance

are linked [134], [137], [139].

The compliance of the system, $C = C_f + C_s$, is made up of the load frame compliance C_f and the specimen compliance $C_s = \frac{1}{S}$, which is the inverse of the stiffness as defined above. Therefore, system calibrations are based on the relation:

$$C = C_f + \frac{\sqrt{\pi}}{2E^*\sqrt{A_p}}. \tag{2.39}$$

Once $A_p(h_c)$ is known, Eq. (2.39) can be plotted as C vs $A_p^{-\frac{1}{2}}$, and the intercept will give the load frame compliance.

In a first approximation, the projected area of contact can be put equal to the one for a perfect indenter, which is for a perfect Berkovich (the tip used in this work) given by:

$$A_p = 3\sqrt{3}h_c^2 \tan^2\theta, \tag{2.40}$$

which results in $A_p = 24.49h_c^2$ with $\theta = 65.27°$.

In reality, a certain amount of blunting of the tip occurs and the tip is not perfect. To account for this non-ideal geometry of the indenter, it is necessary to apply a correction factor to Eq. (2.40) to determine the real area of contact at a depth h_c. This correction factor can be found by making a series of indentations for a range of loads and plotting the contact areas against the corresponding values of h_c.

A first way to obtain these contact areas is the *direct* method: direct measurements of the indents using either atomic force or scanning electron microscopy. Regression analysis of the appropriate order may provide an analytical function that gives the actual projected area for a given value of h_c. This function is commonly called the "area function" for the particular indenter being characterized.

However, this direct measurement approach is particularly inconvenient, especially at very low loads where the area correction is the most important and where direct imaging is the most difficult to perform. Alternatively, *indirect* methods for determining area functions are available, e.g. the method of *Oliver and Pharr*.

Oliver and Pharr developed a mathematical form to fit the data of the

projected area as a function of the contact depth given by [138]:

$$A_p = \sum_{n=0}^{8} C_n h_c^{2-n} = C_0 h^2 + C_1 h + C_2 h^{1/2} + ... + C_8 h^{1/128}. \quad (2.41)$$

They calculated the "plastic depth", h_c, from the measured value of h_{tot} and h_s as shown in Fig. 2.23, where the latter value is calculated from the slope of the initial portion of the unloading curve [139]:

$$h_c = h_{tot} - h_s \quad (2.42)$$

$$h_c = h_{tot} - \epsilon \frac{P_t}{\frac{dP}{dh}}. \quad (2.43)$$

The parameter ϵ depends again on the shape of the indenter, which is 0.75 for a spherical indenter and should be 0.72 for a conical one. However, experimental results showed that in practice $\epsilon = 0.75$ better accounts for the material behavior under a Berkovich tip, due to the inevitable rounding of the tip [138].

The constants $C_0...C_8$ are constants determined by performing a series of indentations with varying maximum loads on a standard test specimen whose elastic modulus and Poisson's ratio are known, e.g. fused quartz. Knowing these parameters of both the reference material and the indenter tip material (usually diamond), the projected contact area can be calculated from the measured stiffness, by combining Eq. (2.37) and Eq. (2.38). A least square fit of the data of the contact area for each maximum load and its corresponding value of h_c to Eq. (2.41) gives a set of values of the constants C_i.

These new values for the contact areas will influence the total compliance and thus the load frame compliance and reduced modulus values in Eq. (2.39). During the calibration process, these new values are then filled in into this equation and new values for the load frame compliance can be calculated. This process is iterated until convergence, i.e. $C - C_f = 0$ is achieved.

The function given in Eq. (2.41) does not have any physical significance. It has been selected strictly because of its ability to fit data over a wide range of

depths [137]. A perfect pyramid would be described by the first term alone with $C_0 = 24.5$ [134]. The first two terms describe a hyperboloid of revolution, a very reasonable shape for a tip-rounded pyramid that approaches a fixed angle at large distances from the tip. The higher order terms in Eq. (2.41) are generally useful in describing deviations from perfect geometry near the indenter tip and provide the flexibility in developing an area function that is accurate over several orders of magnitude in depth [137].

3. Possible measurement errors

   When using indentation in general, a few possible errors should be taken into account.

   First of all, the method developed by Oliver and Pharr takes all measurements of height from the surface. However, some materials *pile up* around the indenter, increasing the actual contact height. This means that some of the area supporting the load would not be accounted for, giving rise to an overestimation of the hardness.

   However, simulation results showed that the amount of pile-up/sink-in behavior can be represented by the ratio of the final indentation depth h_f to the depth of the indentation at peak load h_{max}. h_f can be deduced by fitting the unloading curve to the power law relation $P = \alpha(h - h_f)^m$, with α and m power law fitting constants.

   When $h_f/h_{max} < 0.7$, the method of Oliver and Pharr can be applied without any problem, independent whether the material shows any work-hardening behavior or not. However, if pile-up is large, accurate measurements of H and E cannot be obtained using the contact area deduced from the load-displacement data; rather, the area measured from the image should be used to compute H and E.

   Another method that does not involve imaging is based on the work of indentation, which can be measured from the areas under indentation loading (W_{tot}) and unloading curves W_{unload}. The ratio of the irreversible work to the total amount was found by simulations to be a unique function of $E*/H$:

$$\frac{W_{tot} - W_{unload}}{W_{tot}} \cong 1 - 5\frac{H}{E*}. \tag{2.44}$$

Furthermore, combining eq. (2.36) and eq. (2.37) leads to another equation involving $E*$ and H:

$$\frac{4P_{max}}{\pi S^2} = \frac{H}{E*^2}. \tag{2.45}$$

Because W_{tot}, W_{unload}, P_{max} and S can be calculated from load-displacement data, Eqs. (2.44) and (2.45) represent two independent relations that can be solved for H and $E*$ in a manner that does not involve the contact area [137]. However, the values obtained by this method for the elastic constants depend very strongly on the accuracy of extracting the above described parameters from load-displacement curves and can induce a significant error as well.

A second possible error can result from the blunting of the tip when (very) small indents are made. In all theory considering pyramidal indenters, the tips are assumed to be sharp even when their shape deviates from a perfect Berkovich (or Vickers) pyramid. However, these tips always show some rounding at a certain scale, leading to indentations being carried out with a spherical tip. These spherical tips are known to deform introduce a certain amount of elastic deformation before plastic deformation starts, whereas in the case of sharp tips, deformation is immediately plastic. This could mean, in the extreme case, that a perfectly elastic indent would be formed, giving rise to a material with an infinite hardness.

Accurate determination of height and therefore precise detection of the surface of the sample is important for the determination of H and E^*: especially for small indents, where the total depth is around 50 nm, inaccuracies in surface detection of even a few nanometer will lead to significant errors.

Finally, in crystalline materials, the occurrence of a so-called indentation size effect is a well known phenomenon. This means that hardness measured by indentation techniques is not a constant, but increases for smaller loads applied, due to the production of extra "geometrically necessary" dislocations, which are in fact necessary to accommodate the increased strain gradient at lower loads. The results part of this thesis starts with a chapter dedicated to the study of a similar effect in metallic glasses. It will be shown that indeed such an effect exists in metallic glasses. However, instead of a hardening, it is attributed to the typical softening occurring upon deformation and thus at higher loads.

4. Experimental conditions

   Nanoindentation experiments were carried out with an MTS Nano indenter XP, at MATGAS in Bellaterra and at the CTM (Centre Tecnologic) in Manresa. All experiments were performed at room temperature, in load control mode using a Berkovich indenter tip. This indenter has a resolution of 50nN in load determination, 0.02 nm in displacement and an accuracy of 0.5 μm in positioning the tip on the specimen surface.

   The indentation function consisted of a loading segment of 40 s, followed by a load holding segment of 30 s and an unloading segment of 13 s. The maximum applied loads, P_{max}, ranged from 4 to 500 mN.

   The thermal drift was set to stay below ± 0.05 nm s^{-1}. In principle, the hardness and modulus values were evaluated at the end of the load holding segments using the model of Oliver and Pharr. The contact area between the diamond indenter and the specimen was calculated from a calibration on a fused-quartz standard material. However, in certain cases, the model based on the work of indentation or even calculation of hardness, based on the ratio of P_{max} and the residual area obtained by imaging by SEM have been applied for comparison and/or confirmation.

   Prior to nanoindentation, the samples were carefully polished to mirror-like appearance using diamond paste.

3. INDENTATION SIZE EFFECT

This first chapter of the result part is dedicated to the study of an indentation size effect in metallic glasses, in accordance with the well known effect in crystalline materials. It will be shown that indeed such an effect exists in metallic glasses. However, instead of a hardening, it is attributed to the typical softening occurring upon deformation and thus at higher loads. Although it is in fact a part that could go with *structural changes upon deformation*, which is the topic of chapter 6, it is put here separately since indentation techniques have been used all through this thesis and thus one should be aware of the existence of this effect.

3.1 Introduction

Depth-sensing nanoindentation techniques have become widely used for the mechanical characterization of solid materials since they allow the evaluation of the mechanical properties from a relatively small volume of material [140], [141]. In addition, these techniques do not require complicated sample preparation and they also allow testing brittle materials, which may exhibit premature failure during macroscopic tensile tests. In particular, indentation techniques permitted the determination of the mechanical properties of thin ribbons of metallic glasses. Furthermore, extensive indentation studies on various types of bulk metallic glasses have been pursued in order to explore their structural applications. In the load displacement indentation curve, many interesting features in the form of serrations, ripples, displacement bursts, discontinuities, pop-ins (all these features are identical but differ in terms of scaling) have been reported. The importance of shear bands for plastic deformation are emphasized [135].

The variation of hardness with load/depth of indentation, as often found in crystalline materials, has led to difficulties in using hardness as a fundamental or characteristic mechanical property of materials [135], [142]. This phenomenon, often referred to as indentation size effect (ISE), can be particularly pronounced

in single-crystalline materials and has been ascribed to a variety of factors, such as surface effects [143], friction between the indenter and the sample [144] or, more recently, strain gradient hardening [145]. This latter model considers that, as a result of the shear field created by the indenter, the crystal lattice becomes distorted and (extra) geometrically necessary dislocations have to be created, besides the statistically stored dislocations present in crystalline materials, to account for these large shear strains. For large indentations, the strain variation between two extremes is more gradual and the statistically stored dislocations can easily accommodate the shear stress without the need of geometrically necessary dislocations, thus reducing strain gradient effects.

In spite of the lack of dislocations in metallic glasses, the ISE has also been occasionally reported in these systems [142], [146], [147], [148], [149]. The origin of this effect in amorphous solids is however not well understood. One possible explanation claimed that, by analogy to crystalline materials, strain-induced distortions in metallic glasses are accommodated by formation of geometrically necessary clusters [146]. More recently, Yang et al. used the concept of "geometrically necessary excess free volume" [150], next to the statistically amount of excess free volume typically trapped in the material upon quenching.

This trapped in free volume plays a role in the deformation of this class of materials. Furthermore, flow events in metallic glasses are accompanied by dilatation [44], [45], [50], which induces strain softening in amorphous metals [151] [152], mainly due to a local reduction of viscosity in shear bands [44], [50]. These shear bands have a similar role as dislocations in crystalline materials, i.e. they both allow the accommodation of shear stresses during nanoindentation experiments. However, this accommodation is not instantaneous and thus, the system will show a dynamical response during deformation [50], [78], [151], [152], [153].

On the one hand, the glass attempts to annihilate this excess free volume to reach its equilibrium value c_e, a process that is enhanced at higher temperatures and can be described by:

$$\frac{dc_f}{dt} = -k_r c_f (c_f - c_e), \tag{3.1}$$

with c_f as defined in section 1.3.3. On the other hand, dilatation during plastic

deformation under high stresses is typically represented by [154], [155]:

$$P \approx a_x \dot{\epsilon} c_f \ln^2 c_f, \tag{3.2}$$

where $\dot{\epsilon}$ is the strain rate (in this work during nanoindentation) and a_x is a proportionality factor depending on temperature, average atomic volume and the stiffness of the material [155]. Note that this dilatation corresponds to the "geometrically necessary excess free volume" above-mentioned.

Yang and co-workers used the theory of geometrical similarities to model an indentation size effect, observed/investigated up to 2 mN. In this work, we used the (modified) theory of Spaepen on inhomogeneous deformation to investigate *qualitatively* the possible role of dilatation/free volume on the existence of a size effect in BMGs. It has been studied in two Zr-based BMGs ($Zr_{58.5}Ti_{8.2}Cu_{14.2}Ni_{11.4}Al_{7.7}$ and $Zr_{55}Cu_{30}Al_{10}Ni_5$(both compositions are in at. %)) upon casting and after various heat treatments. An indentation size effect is observed for loads even up to 500 mN. The results of the first composition are presented in this chapter, the second alloy is studied extensively in the next chapter and the indentation results will be presented over there.

3.2 Experimental conditions

Samples with nominal composition $Zr_{58.5}Ti_{8.2}Cu_{14.2}Ni_{11.4}Al_{7.7}$ were studied in the as-cast and structurally relaxed state. For the latter, the sample had been annealed to 623K at a rate of 40K/min. Nanoindentations with maximum loads 4, 10, 25, 50, 100, 250 and 500 mN were made with a Berkovich tip. The indentation function consisted of a loading segment of 40 s, followed by a load holding segment of 30 s and an unloading segment of 13 s for all loads applied. For each load, 10 indents for each load were made. From the load-displacement curves, the hardness values were evaluated at the end of the load holding segments using the model of Oliver and Pharr [138]. The contact area between the diamond indenter and the specimen was calculated from a calibration on a fused-quartz standard material.

3.3 Thermal characterization

The glassy state of both the as-cast and relaxed sample are evidenced by the DSC scans (Fig 3.1), which show a clear glass transition at 678±2 K (onset at 660±1 K).

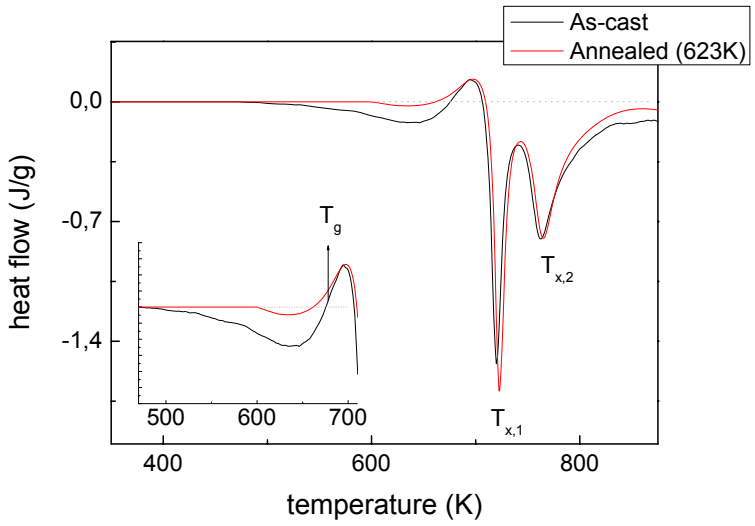

Fig. 3.1: DSC spectrum for the as-cast and annealed sample made at 40 K/min.

The samples crystallize in two steps ($T_{x,1} = 725 \pm 1$ and $T_{x,2} = 766 \pm 2$ K) with a total crystallization enthalpy of -30 ± 2 Jg^{-1}. All values were determined at a heating rate of 40 Kmin^{-1}. The DSC scans for the as-cast and relaxed samples are very similar, except for the broad exothermic peak at low temperatures, which is more pronounced for the as-cast sample. This peak corresponds to the enthalpy release during structural relaxation. The change in enthalpy of 10.7 Jg^{-1} or 79.7 kJmol^{-1}, calculated as described in section 2.3.1.5, can be expected to result in a decrease of average free volume per atomic volume ($\Delta\nu_f \sim \gamma\Delta x$) (density increase) around 0.0015-0.002 based on data given in literature for α ($(\Delta H)_{fv} = \alpha\Delta\nu_f$, Eq. (2.3)) [47].

3.4 Nanoindentation results

Plastic flow in metallic glasses below the glass transition temperature is typically inhomogeneous [153], correlated with the nucleation and/or propagation of a few shear bands [152], [140]. This inhomogeneous flow gives rise to a serrated flow, which causes the appearance of pop-in events in the indentation load-displacement curves (Fig. 3.2). This serrated flow is in fact the product of rapid strain accommodation by individual shear bands emitted discretely in sequence. These pop-in events are less clearly seen when the maximum applied load is exceedingly large

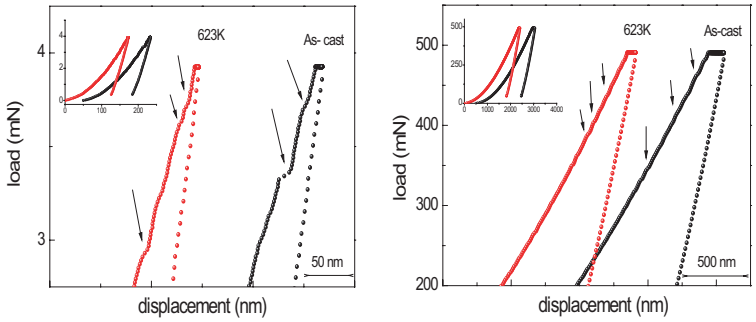

Fig. 3.2: Load-displacement curves with maximum loads applied 4 mN (left) and 500 mN for as-cast and annealed samples. The arrows mark the presence of pop-ins, related to the nucleation/propagation of shear bands.

(e.g. 500 mN), mainly because of lack of resolution of the experimental setup: pop-in events represent discontinuous displacements of the order of 1-25 nm [140], [156].

Fig. 3.3 shows the hardness, calculated at maximum load at the end of the holding segments, in function of the maximum displacement reached at that moment. In the inset, hardness is presented as a function of the (logarithm of) load. The dependence of the hardness on the maximum penetration depth, evidences the existence of an ISE in both as cast and structurally relaxed samples. Annealing-induced structural relaxation causes an overall mechanical hardening of the glass. Similar effects have been reported in other structurally relaxed metallic glasses [157], [158], [159]. Furthermore, the difference in hardness between the two samples becomes more pronounced as the maximum load applied during nanoindentation increases, resulting in a more manifested ISE in the as-cast sample.

One significant problem with the method described originally by Oliver and Pharr [138] is that it does not account for pile-up of material around the contact impression, which is observed in many elastic-plastic materials. When pile-up occurs, the contact area is greater than the one predicted by the method, and both hardness and the modulus estimated from eq. (2.36) and eq. (2.37) respectively are overestimated, sometimes by as much as 50%. The opposite effect of pile-up is sink-in, in which case the real area will be smaller than the experimentally measured one and thus leads to underestimation of the mechanical properties.

The fundamental material properties affecting pile-up are the ratio of the ef-

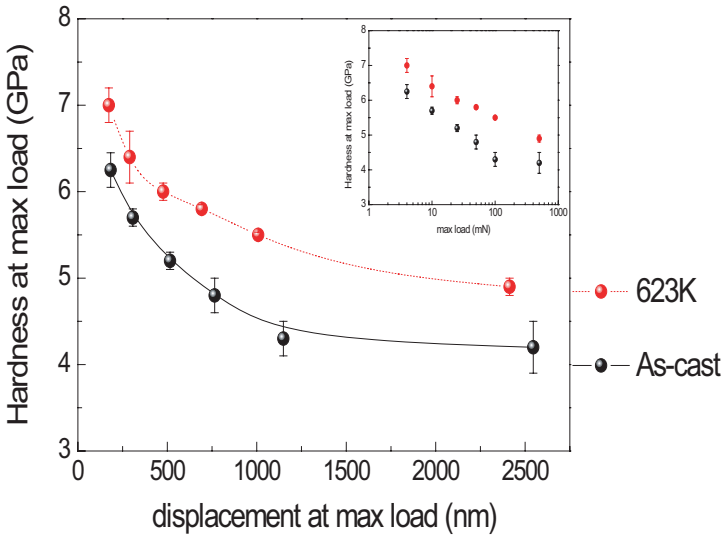

Fig. 3.3: Hardness at maximum load in function of the displacement at maximum load (in function of the applied maximum load in the inset on a logarithmic scale), showing a decrease of hardness in function of an increasing load, thus a so-called size-effect. The lines are not a fit, and have only the intention to guide the eye.

fective modulus to the yield stress, E^*/σ_y, and the work-hardening behavior. In general, pile-up is greatest in materials with large E^*/σ_y and little or no capacity for work-hardening. The ability to work harden inhibits pile-up because as material at the surface adjacent to the indenter hardens during deformation, it constrains the upward flow of material to the surface.

Piled-up material can be observed around the indents when observing them in the SEM, as illustrated in Fig. 3.4. Although metallic glasses have in fact rather low values of E^*/σ_y, these material can be considered in a first approximation as being elastic-perfectly plastic.

The pile-up in Fig. 3.4 is shown for the largest load applied, since the smaller ones are difficult to observe by SEM. Atomic force microscopy would be necessary for the lower loads. On the other hand, if pile-up occurs around the smaller indents, it may have its influence on the size effect described above. The application of the method of Oliver and Pharr might have been erroneous, in particular for the lowest loads. Therefore, hardness and modulus values have been calculated by the method described in section 2.3.4.3 by Eqs. (2.44) and (2.45) for the smallest and largest loads. The results are summarized in Table 3.1. To calcu-

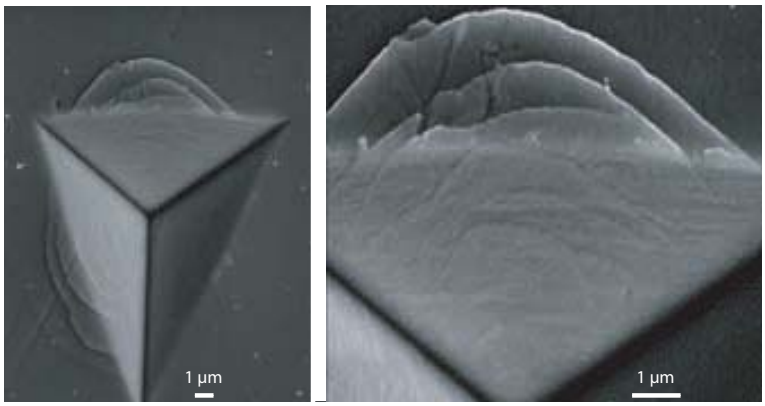

Fig. 3.4: Typical pile-up observed by SEM for the sample under investigation.

late the Young's modulus from the reduced modulus E^*, 0.18 was used as Poisson ratio of the diamond indenter and 1200 GPa for its modulus. The Poisson ratio of the samples was roughly set to 0.3, in accordance with the value used during the measurements. For comparison, the values obtained by the method of Oliver and Pharr are given in italic underneath each value.

These results are in very good agreement with the results obtained by the method of Oliver and Pharr. The error of the method by the work of indentation is estimated around 15%. The results obtained by this method lie all within this range of error compared to the values obtained by the method of Oliver and Pharr. This confirms that pile-up is not the cause for the observed size effect.

3.5 Discussion

1. Strain rate in the free volume model

   To explain the observed indentation size effect, we will have recourse to one of the original mechanistic models of glass deformation, originally developed by Spaepen [44]. Although this model only assumed single atom jumps, while currently glass deformation is known to occur as a collective effect arising from the operation of many small atomic-scale shear events, in which a few atoms collectively shuffle in a shear mode under the combined action of stress and temperature, the phenomenology of both models is essentially identical and physical predictions made with either model are equivalent. Recently, the initial model developed by Spaepen has been modified to take

Tab. 3.1: Values of the Young's modulus and hardness as determined by the method of the work of indentation. For comparison, the values obtained for these samples by the method of Oliver and Pharr are given in *italic* font. The ratio of the values obtained by both methods is shown as well.

	As-cast	623 K
4 mN - E(GPa)	100	114
	94	*105*
ratio (%)	94	92
500 mN - E(GPa)	78	81
	72	*75*
ratio (%)	95	92
4 mN - H(GPa)	7.1	8.4
	6.3	*7*
ratio (%)	85	83
500 mN - H(GPa)	4.7	5.4
	4.2	*4.9*
ratio (%)	89	91

into account this chain-like deformation behavior [155].

For a metallic glass subjected to a shear stress τ, the shear strain rate resulting from the superposition of many individual STZ operations is given as:

$$\dot{\gamma} = \alpha_0 c_f k_{f,0} \frac{\epsilon_0 \nu_0}{\Omega} \exp(-\frac{\Delta F_0}{kT}) \sinh(\frac{\epsilon_0 \nu_0 \tau}{kT}) \tag{3.3}$$

with Ω the atomic volume, $\epsilon_0 \nu_0$ the activation volume for a flow event **($\sim$10Ω)**, τ is the shear stress, k is the Boltzmann constant and ΔF_0 is the activation barrier energy for defect migration. The term $k_{f,0} \exp(-\frac{\Delta F_0}{kT})$ is the rate constant for plastic flow, with $k_{f,0}$ related to the Debye frequency. α_0 is a constant incorporating the amount of material capable of undergoing shear transformation.

Equation 3.3 was initially developed to describe *high temperature* viscous flow, in which STZs are roughly spherical and there is no spatial correlation between them [50]. However, as proposed by Argon, at lower temperatures (where shear banding occurs) the STZ might change character somewhat, with a somewhat different value for ΔF_0. If we assume however that STZs have roughly the same character at any rate and temperature, then the main difference in Eq. (3.3) when shear localization occurs will be in the

parameter α_0, as suggested by Spaepen [44]. These assumptions have also been made by other groups and this model has been applied to describe deformation behavior in metallic glasses [160], [161].

2. Correlation between hardness, yield stress and shear stress

   The shear stress present in Eq. (3.3) can be correlated to the hardness, since, on one hand, hardness is correlated to the yield stress through the Tabor relation $H = K\sigma_y$ [153], with K a parameter dependent on the indenter shape as well as on the mechanical properties of the material. On the other hand, the correlation between the yield stress and shear stress is given by various yield criteria.

   In conventional, crystalline materials, such a correlation between the shear stress and yield stress is usually presented by the Von Mises criterion $\sqrt{3}\tau_y = \sigma_y$. Although some early works reported on the validity of this model for metallic glasses as well, more recent work revealed that the glassy material is pressure-sensitive and the normal stress on a shear plane plays an important role. This normal stress delays the yielding under compression and thus under indentation, compared to that predicted by the Von Mises criterion. Therefore the MohrCoulomb criterion, typically used for granular materials, appears to be more applicable for the glassy material. This can be expressed as $\tau_y = k - \alpha\sigma_n$, with τ the shear stress on the slip plane at yield, σ_n is the normal stress acting on the shear plane, k is the intrinsic shear resistance of the material and α is a friction coefficient that dictates the strength of the normal-stress dependence. Metallic glasses are stronger in compression than in tension, since pressure can delay yielding. This signifies that BMGs will show higher hardness values than polycrystalline material with the same tensile yield strength. Theoretical calculations of the constraint factor K in the Tabor relationship, based on elastic-plastic behavior, suggest values between 2 and 3, whereas experimental results point more towards this upper limit value. This can be due to the fact that the pressure-sensitivity, that is particularly important in indentation experiments, was not taken into account in the former calculations [135], [140], [162].

   Although it is not completely correct to apply the Von Mises criterion, in a

first approximation, $H \cong 3\sqrt{3}\tau$, and thus Eq. (3.3) can be rewritten as:

$$H \approx A \sinh^{-1}\left(\frac{\dot{\gamma}\Omega}{\alpha_0 c_f k_{f,0} \epsilon_0 \nu_0} \exp\left(\frac{\Delta F_0}{kT}\right)\right), \tag{3.4}$$

with $A = \frac{6\sqrt{3}kT}{\epsilon_0 \nu_0}$.

This equation predicts that, for a given shear strain rate, the hardness will decrease when increasing the flow defect concentration associated with free volume and will also depend on the activation barrier energy for flow event. Furthermore, this free volume also influences (lowers) ΔF_0 for consecutive STZ and shear band formation. In other words, this equation envisages that accumulation of free volume during deformation will cause a mechanical softening of the metallic glass.

3. Strain rate in nanoindention experiments - load control mode

During nanoindentation with a constant loading rate, the displacement rate ($\frac{dh}{dt}$) is a non-linear function of time t, as is the indentation strain rate defined by $\dot{\epsilon} = \frac{1}{h}\frac{dh}{dt}$. This nanoindentation strain rate $\dot{\epsilon_i}$ is in fact multiaxial, but is directly proportional to the uniaxial strain rate $\dot{\epsilon_u}$ by [153]:

$$\dot{\epsilon_u} = C\dot{\epsilon_i} \tag{3.5}$$

with $C = 0.09$. Indentation rates are thus about one order of magnitude larger than their equivalent uniaxial strain rates. Between this uniaxial strain and the corresponding shear strain another proportionality of $\sqrt{3}$ exists, which results in $\dot{\gamma} = 0.16\dot{\epsilon_i}$. Strain rates ($\dot{\epsilon_i}$) have been calculated for each sample and each load and are presented in Fig. 3.5.

At the beginning of each experiment, the strain rate is very high but decreases with depth as h^{-1} approaches an approximately constant value at large depths. The trends in strain rate are not smooth and monotonic but exhibit many short peaks that appear to increase in size as the indentation proceeds. These short bursts of rapid displacement correspond to the pop-in events exhibited in the Ph curve.

Since $\dot{\epsilon_i}$ is found to level off to very similar values (about 1.1 x 10^{-2} s^{-1}) in all cases, according to Eq. (3.4), variations in hardness essentially depend on the amount of free volume created in each sample during loading. As

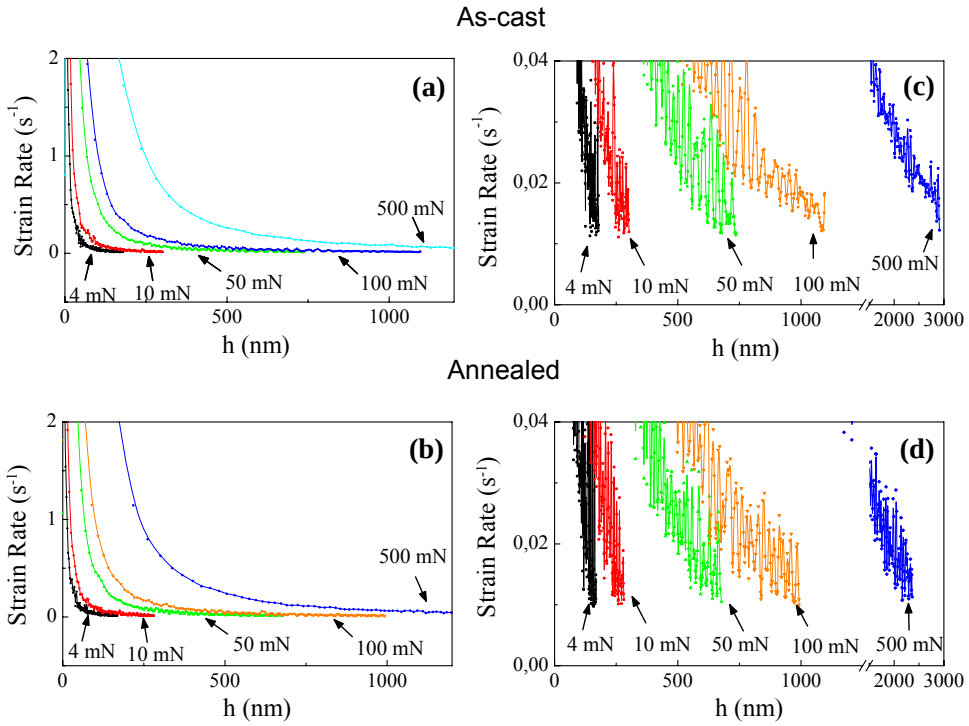

Fig. 3.5: Dependence of the strain rate, $\dot{\epsilon}$, on the penetration depth, h, for the as-cast (a-c) and structurally relaxed (d) samples. The values of maximum loads applied in each case are indicated.

the instanteneous strain rate is higher for larger maximum loads for a given h, the production of free volume is more pronounced for larger maximum applied loads at this indentation depth (Eq. (3.2)). This increased free volume reduces the viscosity of the propagating shear bands in which it is created, resulting in a mechanical softening [44], [50], [151], [152], [163]. Furthermore, consecutive activation of STZs and shear bands requires each time a lower stress to form due to the presence of local strain fields and free volume creation, since the latter lowers the value of ΔF_0 [153].

Since the amount of generated free volume increases with the maximum load applied, this yields the observed ISE.

4. Instantaneous hardness - dynamic softening

The mechanical softening associated with deformation-induced dilatation is not necessarily instantaneous. In fact, anelastic deformation has been

reported during nanoindentation of a metallic glass [164].

To investigate this time-effect on the correlation between mechanical softening and the ISE, the dynamic hardness, H_d, was calculated dividing the *instantaneous* force by the projected contact area, following the method of Oliver and Pharr [138], [152]. The area function, determined by indenting a fused quartz reference material, is given by:

$$\begin{aligned} A_c &= 24.4574 * h_C^2 + 442.0989 * h_C + 533.2619 * h_C^{\frac{1}{2}} - 234.9924 * h_C^{\frac{1}{4}} \\ &\quad -321.3878 * h_C^{\frac{1}{8}} - 343,7284 * h_C^{\frac{1}{16}} - 351,1737 * h_C^{\frac{1}{32}} \\ &\quad -354,095 * h_C^{\frac{1}{64}} - 355,3694 * h_C^{\frac{1}{128}}. \end{aligned} \tag{3.6}$$

The results are shown in Fig. 3.6.

At a given h, the dynamical hardness is smaller for smaller values of maximum load, although the deformation-induced production of free volume (and the expected mechanical softening) should be larger for larger maximum loads. However, indentations with larger maximum loads continue to soften with time and at the end of the load holding segments, H_d is indeed smaller for these larger final loads, in agreement with the ISE reported in Fig. 3.3. Furthermore, the displacement of the indenter into the sample during the load *holding* segments is more pronounced for indentations with larger maximum loads, as can be seen from Fig. 3.2. This is the consequence of the larger amount of dilatation occurring at higher loading rates. Since successive shear transformation zones can each time be easier activated, in particular for the higher loads, but the time available during the loading segment is insufficient to accommodate the applied strain rate, deformation continues during the load-holding segment, resulting in the observed creep.

Therefore, the mechanical softening of a metallic glass depends not only on the flow defect concentration but also on its ability to accommodate the applied strain rate and the excess free volume over the duration of the experiment.

5. Verification of the model

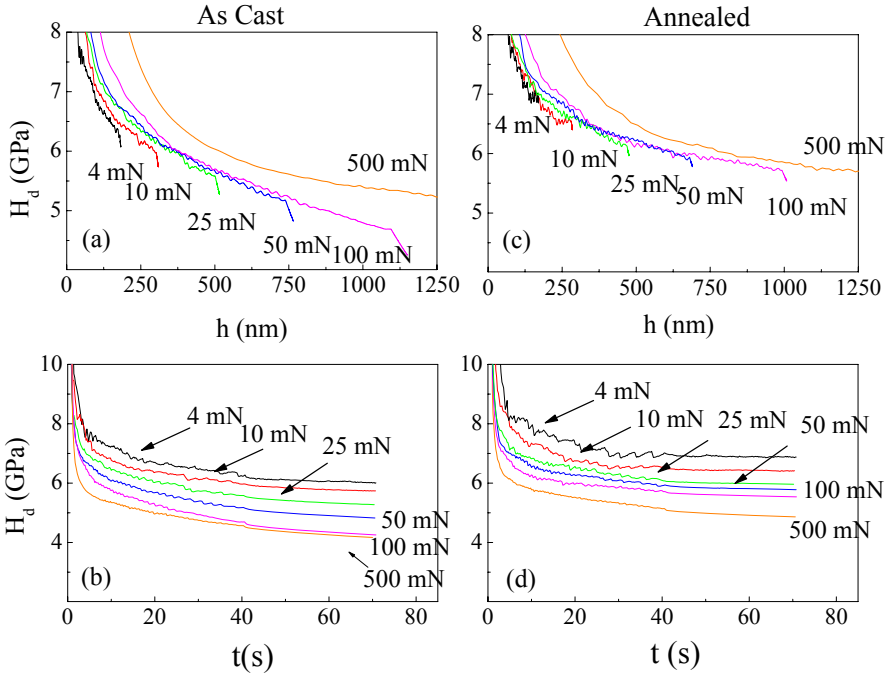

Fig. 3.6: Dependence of the dynamic hardness, H_d on the displacement into the sample, h [(a) and (c)] and time, t [(b) and (d)], corresponding to the loading plus load holding segments, for the as-cast [(a) and (b)] and annealed [(c) and (d)] samples. The values of maximum applied loads applied are indicated.

To estimate the role of free volume on the observed size effect, some calculations were made to obtain orders of magnitude of free volume changes, predicted by the current model and compare them with expected values from literature.

First of all, the final amount of free volume present after deformation in the samples deformed with a maximum load of 4 and 500 mN was calculated based on measured parameters. For the other parameters in the model, data available in literature were used. The latter parameters are summarized in Table 3.2, together with the obtained results.

Tab. 3.2: Parameters used to calculate the final free volume content after deformation from Eq. (3.4). The values obtained for the reduced free volume ($-(\ln(c_f))^{-1}$) are given in the second part of this table.

Parameter	Value	Reference
$\dot{\gamma}$	$0.16\ 10^{-2}\ s^{-1}$	Calculated
ϵ_0	0.125	[153]
ν_0	$4.8\ 10^{-28}\ m^3$	[153]
Ω	$13\ 10^{-30}\ m^3$	[155]
T	300 K	-
ΔF_0	1.3 eV	Calculated
k_f	$10^2 4\ s^{-1}$	[165]
τ	$\frac{H(h)}{2\sqrt{(3)}}$	Calculated
$-(\ln(c_f))^{-1}$	4 mN	500 mN
As-cast	0.0227	0.0284
623 K	0.0213	0.0262

Typical changes of this reduced free volume upon deformation reported were on the order of 4-5%, with deformations up to 30% [48]. Note that this is averaged over the whole volume of the sample, while local changes (within the shear bands) will be much larger. Shear strains can easily be 40 times larger inside the shear transformation zone than in the surrounding matrix [153].

For indentations with the lowest loads, the change in free volume was set fixed to 4 %. However, the values obtained here would indicate that, a maximum load of 500 mN would have to induce a change up to 25%, since the initial amount of free volume has to be the same for indentations made

Tab. 3.3: Overview of the second series of free volume values with adjusted parameters. These new parameters, ΔF_0 (in eV) and τ_{MC} (in GPa), are given as well. The original value of the shear stress used, obtained by the Von Mises criterion is given for comparison (τ_{VM} in GPa). 'AC' indicates as-cast; 'Ann' refers to the annealed sample.

Sample	ΔF_0	τ_{MC}	τ_{VM}	$-(\ln(c_f))^{-1}$	$-(\ln(c_{f,ini}))^{-1}$
AC - 4 mN	1.45	1.82	1.38	0.031	0.0298
AC - 500 mN	1.3	1.21	0.92	0.0323	0.0307
Ann - 4 mN	1.45	2.02	1.53	0.0293	0.0279
Ann - 500 mN	1.3	1.41	1.07	0.0301	0.0286

in the same sample, independently of the maximum load applied. It is clear that these values are not realistic.

If we take into account that dilatation and existing STZs can trigger the activation of more STZ and facilitate the successive formation of shear bands, a lower value of ΔF_0 can be expected for the higher loads. Furthermore, the use of the Mohr-Coulomb criterium instead of the Von Mises yield criterium improves the obtained results to an acceptable level. Application of the Mohr-Coulomb criterion was done based on the simulation results by Vaidyanathan et al. [166], who showed that:

$$\begin{aligned} \tau &= \sigma \sin\theta \cos\theta - \alpha\sigma(\sin\theta)^2 \\ &= \frac{H}{K}\sin\theta\cos\theta - \alpha\frac{H}{K}(\sin\theta)^2 \end{aligned} \tag{3.7}$$

with α=0.13 and $\theta = 41.3°$ typical values for nanoindentation.

These new parameters and the resulting values for the final $-(\ln(c_f))^{-1}$ and initial free volume, $-(\ln(c_f))^{-1}$, calculated as 95% of the final value, are summarized in Table 3.3. Note finally, that the change in initial level of free volume between the as-cast and the relaxed samples agrees very well with the change expected based on the DSC results (0.0015-0.002).

While temperature has additional effects on the kinetics flow, this first order of magnitude estimate indicates that indeed a deformation-induced increase of free volume causes the observed mechanical softening.

In the model of Yang and coworkers, the free volume produced during deformation under indentation (referred to as geometrically necessary excess free volume) was calculated based on the theory of geometrical similarities,

in analogy with the model for crystalline materials. This means that this excessive free volume is represented as equally distributed loops, approximated by equilateral triangles for a Berkovich indenter. This resulted in the following formula [150]:

$$\Delta V_G = \frac{9\sqrt{(}3)\tan^2\theta}{16\pi\lambda h}, \tag{3.8}$$

with θ the angle between the surface of the material and the side surface of the indenter, h is the indentation depth, λ is the characteristic spacing between the triangular loops of geometrically necessary excessive free volume. Note that Eq. (3.8) gives a change in *concentration* of free volume per unit area, based on a dimensional analysis. According to the work of Ramamurty and co-workers [167], this λ is not a constant, but depends on the distance from the center of the indent, and thus depends on the applied load. However, for the low load values used in the work of Yang, this parameter should be around 1 μm (upper limit). θ is 25° for a Berkovich tip, h for our smallest load of 4 mN is around 100nm. Substituting these values in Eq. (3.8) yields a value of $0.67/(\mu\text{m})^2$ for ΔV_G. For a contact area of $0.3\mu\text{m}^2$, this would mean a change in free volume concentration of 0.2, which is in fact a factor of 10 to 100 (depending on the value of γ, which lies between 0.1 to 1 (Eq. (1.8))) too large compared to experimentally measured free volume changes per atomic volume unit [47]. Note that values for γ in literature are around unity [44]. Our model shows that the observed ISE is indeed correlated with free volume changes and free volume production upon deformation, which can be reasonably explained with the generally accepted (modified) theory of Spaepen and Argon [44], [50].

The softening effect observed here can also be interpreted in the other approach, discussed in section 1.3.3. Activation of shear transformation zones leads to a destruction of the clusters that form the short/medium range order in metallic glasses, which on its turn leads to a softening of the model. More deformation requires the activation of more shear transformation zones, destroying further the short-range order, leading to softening. This is in fact the idea of the model of Lam on "geometrically necessary clusters". However, instead of explaining the observed softening at large loads, they suggest

that more clusters should be generated at low loads to account for the higher strain gradient [146].

3.6 Summary

In summary, this chapter demonstrates that the indentation size effect in metallic glasses is related to the dynamic mechanical softening that occurs in these materials when being plastically deformed. The influence of free volume on this effect has been evidenced by comparing the mechanical response of a metallic glass in as-cast and structurally relaxed states. Larger free volume concentrations result in enhanced mechanical softening and, concomitantly, more pronounced indentation size effects.

4. CHARACTERIZATION OF $ZR_{55}CU_{30}AL_{10}NI_5$ AFTER ANNEALING TREATMENTS

4.1 Introduction

Since glasses are in metastable equilibrium, they traverse a series of lower energy states within the potential energy landscape when they are annealed at a temperature high enough for atomic motion, but insufficient for crystallization. This process is common to all glasses and is know as structural relaxation; the lowest energy state that is non-crystalline is referred to as the ideal glass.

The atomic scale phenomena associated with structural relaxation can be broadly classified as either topological or compositional (or chemical) short-range ordering. *Topological* short-range ordering (TSRO) refers to changes in the structure of the glass, particularly with regard to the arrangement of atomic sites. One of the major consequences of irreversible structural relaxation of metallic glasses is annihilation of free volume due to densification.

Changing the topological short-range order requires significant atomic mobility and is usually associated with irreversible structural relaxation due to annealing near the glass transition. *Compositional* short range order (CSRO) refers to how atoms of different elements are arranged on these atomic sites and is associated with reversible structural relaxation, often at temperatures well below the glass transition.

On one hand, relaxation upon annealing has been reported even for short annealing times [168], but are usually classified as TSRO.

Studies of the thermal behavior and heat effects registered by DSC experiments suggested that heat effects observed in DSC traces are probably a combination of topological and chemical ordering, in particular in the low temperature range, i.e. in the initial stages of relaxation [107], [169], [47]. In fact, changes in the CSRO have been observed upon annealing, especially at low annealing temperatures for Co-based [170] and Pd-based BMGs [171]. Chemical-short range order can further

lead to clustering or phase separation [111], [172], [173]. Anomalous viscosity results for the current composition after pre-annealing treatments were attributed to the occurrence of such phase separation or clustering during a preceding heat treatment at low temperatures [174].

However, a systematic study of the occurrence of this changes has not been done so far, especially, concerning the influence of CSRO on the mechanical behavior. This is the scope of this chapter, where a large variety of complementary, experimental techniques was applied for this purpose. Samples were annealed to 623 and 723K, which are below and above T_g respectively for the given treatment. Details of the annealing treatment were given in section 2.2.1.

The chapter starts with the thermal characterization by DSC, in the as-cast state and after annealing. Microstructural characterization before and after annealing were done by XRD (conventional and synchrotron radiation), TEM and in-situ heat treatments in the TEM. Finally, the mechanical behavior was investigated by uni-axial compression tests, nanoindentation tests and measurement of the elastic properties by acoustic measurements.

4.2 Thermal characterization of $Zr_{55}Cu_{30}Al_{10}Ni_5$

Thermal analysis confirms the general preservation of the amorphous nature upon annealing (Fig. 4.1). The transition from glass to supercooled liquid occurs at 702 ± 4 K while the width of the supercooled liquid region (SLR) is 79 ± 2 K, for a heating rate of 0.667 K/s. Comparison of the top and the bottom parts of the as-cast rods revealed very good homogeneity along the length of the rod.

Upon annealing, the samples relaxed to a more thermodynamically stable state, resulting in a lower enthalpy release during the exothermic event preceding the glass transition. Following the procedure described in section 2.3.1.5 and using the data given in [47], an enthalpy change of 4.73 J/g for the sample annealed below T_g would result in a free volume change (per atomic volume) of $0.6{*}10^{-3} \pm 1.8 * 10^{-5}$ approximately as compared to the as-cast sample. For the sample annealed above T_g, an enthalpy change of 9.15 J/g was calculated what would correspond to a free volume change of $1.2{*}10^{-3} \pm 3.6 * 10^{-5}$.

Slipenyuk and Eckert found a proportionality constant of 7.375±0.2 between the enthalpy changes upon annealing as compared to the as-cast state and the free

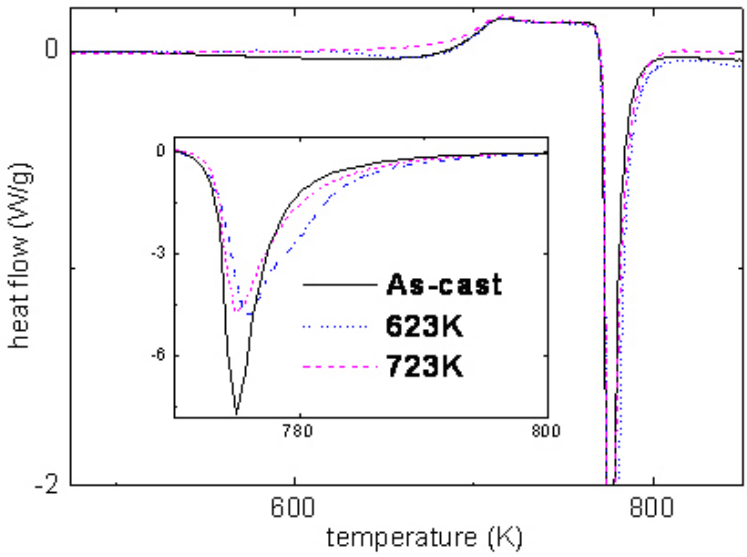

Fig. 4.1: Effect of annealing treatments on thermal stability and crystallization behavior of the respective samples, compared to the as-cast sample, measured by DSC. No change in glass transition temperature neither in width of the supercooled region is observed. After annealing below T_g, a double crystallization peak is observed (see inset).

volume changes. This constant was interpreted as the energy to form a vacancy with the magnitude of one atomic volume. However, since this value is in fact 2.5 times larger than the activation energy for vacancy formation in crystalline Zr, it was thought that CSRO and TSRO occur simultaneously at low temperatures, where CSRO probably gives an additional contribution to the enthalpy change during structure relaxation.

Integration of the crystallization peak area gives values of -52 ± 2J/g, -54 ± 2J/g and -48 ± 2 J/g calculated respectively for the as-cast sample, the sample annealed below and above T_g respectively.

All values of temperatures (T_g, T_x) and crystallization enthalpies are in good agreement with literature data [175], [176]. The small decrease in crystallization enthalpy after annealing to 723K might indicate that some nanocrystals have nucleated ($vol\% \simeq \frac{\Delta H_{AC} - \Delta H_{723}}{\Delta H_{AC}} * 100 = 7 - 8\%$), although similar variations were already reported from the as-cast material [176]. Anyway, the influence of possible (nano)crystals should be minor, since they only appear in a very small volume fraction.

Although the overall crystallization at first glance did not change significantly

Tab. 4.1: Parameters obtained by fitting the regular XRD spectra of the respective samples to a pseudo-Voight function (Eq. (2.18)). Γ_{fG} represents the width from the Gaussian part, $\Gamma_f L$ indicates the width from the Lorentzian part.

	Γ_{fG}	Γ_{fL}	δ_{hkl} (nm)
As-cast	5.4	6.1	1.65
623K	5.3	6.1	1.65
723K	4.96	6.0	1.67

upon annealing, a closer look to the shape of the crystallization peak does indicate some changes induced by the pre-annealing treatments: a shorter, but broadened peak is observed for the annealed samples, with a clear second shoulder in case of the sample annealed below T_g (inset of Fig. 4.1).

Such a change in shape has been attributed in literature to the occurrence of phase separation preceding the crystallization process [177], formation of clusters upon a preceding deformation treatment [178] as well as to the presence of oxygen [25].

However, the latter possibility can be ruled out since the oxygen content was measured to be around 0.0005 at% both before and after annealing treatment. The results of thermal characterization indicate that some changes on the CSRO might have occurred during the pre-annealing treatments.

4.3 Microstructural characterization of $Zr_{55}Cu_{30}Al_{10}Ni_5$

4.3.1 X-ray diffraction

Investigation by conventional XRD reveals the 'Bragg amorphous' nature of the samples: two broad diffuse halos are observed, without any sharp diffraction peaks typical for the presence of crystalline phases (Fig. 4.2 a). The main halos were fitted to a pseudo-Voight function, as described by Eq. (2.18) in section 2.3.2.1. The fit parameters and the calculated size of 'coherent diffraction domains' are given in Table 4.1. The size of this domain comes mainly from the medium range order present in metallic glasses (order scale of 1 nm). However, no significant differences can be observed by conventional X-ray diffraction.

By the use of high-energy synchrotron radiation, large values for the scattering vector $q = \frac{4\pi \sin\theta}{\lambda} = \frac{2\pi}{d_{hkl}}$ can be reached, increasing significantly the resolution and allowing structure characterization at smaller $d_{hkl}-$values. This allows the

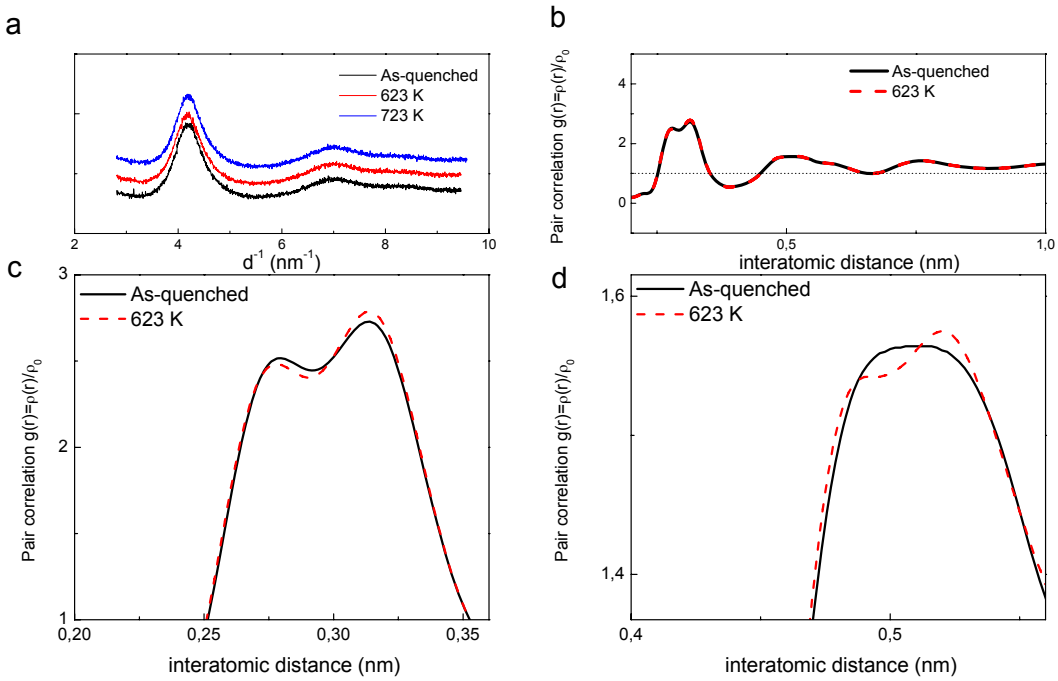

Fig. 4.2: Effect of the heat treatment on the short-medium range order. (a) The conventional X-ray diffraction spectrum of the as-cast sample compared to the spectra of the annealed samples shows the typical "Bragg amorphous" structure. (b) Pair correlation function $\rho(r) = \rho_0$ of the as-cast and the sample, annealed below T_g. Details of the first (c) and second (d) "peak" in (b) show small but significant changes in short- medium range order.

direct measurement of the structure factor $S(q)$. Once $S(q)$ is determined for all scattering vectors, the pair correlation function $g_(r)$ can be calculated from the Fourier transform of the structure factor by Eq. (2.22).

Calculation of the pair correlation function $\rho(r)$ (Fig. 4.2 b-d) for the as-cast and the sample annealed below T_g shows small but significant changes in the peak profile of this annealed sample compared to the as-cast sample. The main peaks at interatomic distances of 0.275 and 0.312 nm can be attributed to the pair between Cu-Zr and Zr-Zr respectively, based on literature data for binary Zr-Cu-based alloys [36], [179], and ZrCuNiTiBe-type BMG [180]. Upon annealing, the intensity of Cu-Zr pair decreases, while the peak for Zr-Zr pair intensifies. The interatomic distance between Cu and Zr on the other hand decreases slightly, visible in the small shift to the left of the first peak, in accordance with the expected structural relaxation and annihilation of free volume, leading to densification of the sample.

Furthermore, changes in the second peak around 0.5 nm indicate a change in medium range order in the glassy phase. The initially flat peak for the as-cast sample starts to split after annealing. Based on the partial pair correlation functions for Cu-Cu-, Zr-Cu and Zr-Zr-interactions, the intensity of Zr-Cu-pairs decreases, while there is a slight increase in probability for the other two pairs to occur.

The changes observed here are small, but yet too large to be caused by experimental error. Furthermore, these observations are in good agreement with the observations after low-temperature annealing of a Zr-based BMG, as made by neutron diffraction [181]. These authors revealed that the first step during structural relaxation cannot be correlated to annihilation of free volume, but should involve subtle structural changes. The changes observed in this work occurred on an even smaller time-scale. This could be due to the fact that here a quaternary alloy is investigated while in Ref. [181], a quinary alloy was studied, where atomic mobility is even further reduced (cfr. section 1.2.5).

4.3.2 Transmission electron microscopy

Observation of the microstructure of the as-cast and annealed samples should clarify more the changes that occurred upon annealing. In a first step, the samples, as-cast and annealed, were observed by conventional TEM with high contrast. Compositional changes were studied by HAADF and EDX in STEM mode.

To rule out possible influences of preparation and to gain insight in the process occurring upon heating, the heat process was simulated *in-situ* in the TEM. These heat treated samples were further analyzed by HRTEM and EELS.

4.3.2.1 Ex-situ *heat treatments*

1. Conventional TEM

   Observation by TEM reveals a clear difference in the microstructures of the as-cast and annealed samples (Fig. 4.3). While the as-cast sample (a) shows a homogeneous, featureless microstructure, the microstructure of the annealed samples (b-c) consists of a bright matrix with darker regions. These regions are in the order of 2-5 nm for the sample annealed below T_g and around 10 nm for the sample annealed above T_g. This contrast was observed

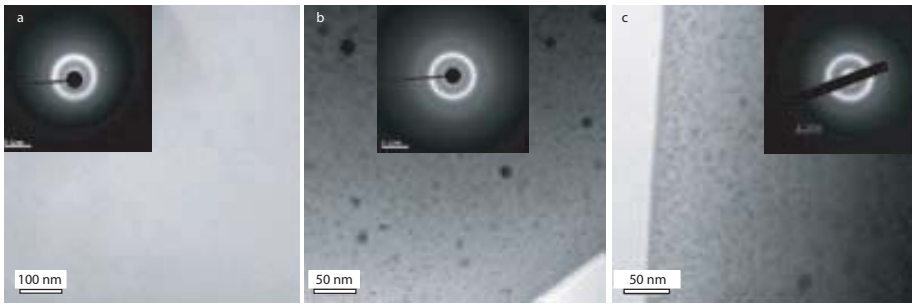

Fig. 4.3: Microstructural features in the as-cast (a) and annealed (623 K - b, 723K - c) samples, observed by TEM, revealing the change of a homogeneous microstructure to a heterogeneous one upon annealing, even below T_g. The respective SAED patterns are shown in the insets.

all over the sample. The SAED patterns shown in the respective insets show the conservation of an overall amorphous structure, although the outer rings become each time a bit sharper upon annealing, pointing towards increased ordering, but probably below 2nm [66], [85].

2. HAADF/STEM

   Preparation of samples for TEM sometimes leads to inhomogeneous thinning, which might be interpreted erroneously as compositional contrast [124]. To rule out this possibility, one of the annealed samples, annealed below T_g, was checked by HAADF, where contrast is based mainly on the atomic number, and depends less on thickness.

   HAADF-STEM imaging of this annealed sample confirms that the observed contrast in Fig. 4.3 b is due to compositional fluctuations (Fig. 4.4 a) and is not the result of an inhomogeneous thickness. Mapping by EDX in scanning transmission mode reveals further that the dark zones in Fig. 4.3 b (bright zones in STEM image) are enriched in Cu (Fig. 4.4 b-c), while no distinct variations of the other elements were observed (Fig. 4.4 d-f).

3. High resolution TEM

   High resolution TEM images of the annealed samples revealed the presence of lattice fringes of nano-crystals in the range of 2-5 nm in some of the darker regions (not shown here). However, it is not clear at this moment whether these nano-crystals were formed during TEM sample preparation,

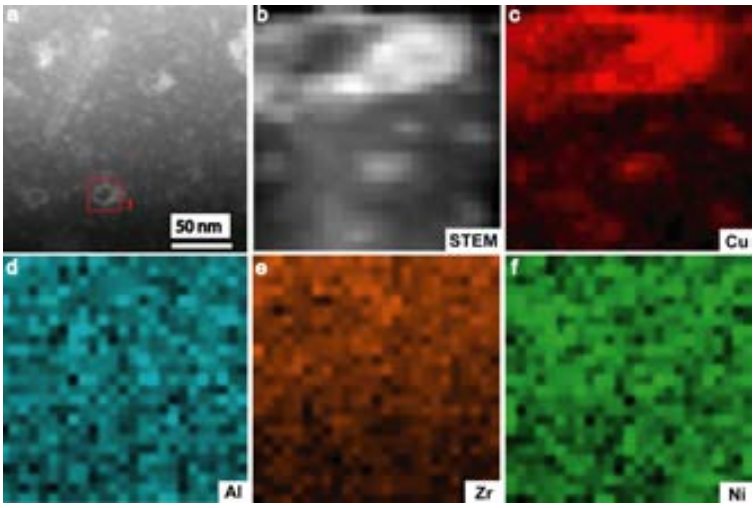

Fig. 4.4: Compositional analysis by scanning transmission electron microscopy and high angle annular dark field of the low-temperature annealed sample. By high angle annular dark field imaging, an overall compositional contrast is observed (a). When a mapping of the energies is made of a detail of one of the bright areas (b), indicated by the square in (a), of the respective elements (c-f), a clear enrichment in Cu is observed in the bright regions of (a), while the amount of the other elements, Zr, Ni, Al, does not seem to vary significantly.

in particular during the final step by ion-beam milling, or whether they crystallized during the preceding heat treatment. No clear indication towards nano-crystallization was obtained by the other techniques, in particular for the low-temperature annealed sample. Note that it has been shown that ion beam milling has a higher probability to alter the microstructure and in particular medium range order compared to electropolishing [40].

4.3.2.2 In-situ *heat treatments*

A first objective of the study presented in this section was to rule out possible influences of preparation by simulating the heat treatment *in-situ* inside the TEM. In this way, the micro-structural changes upon annealing can be investigated. Furthermore, the recording of the changes of the microstructure during the in-situ treatment would provide an insight on the time-scale of the process occurring during annealing.

Annealing treatments to 623 and 723 K were performed, as well as to 793 K to allow full crystallization. The temperature reading of the heater of the TEM was

Tab. 4.2: Overview of the in-situ heat treatments performed and the observations made. T was the maximum set temperature (in K), β the heating rate applied (in K/min) and *time* the holding time at maximum temperature (in minutes).

Sample	T	β	*time*	Observations
K 260-3 a + K 260-9 (*)	623	60	10	appearance (and disappearance) of unstable "entities"/double diffraction ring
K 260-11 + K 260-14 (*)	623	20	35	phase segregation + double diffraction ring/ nanocrystals but no (full) crystallization (Fig. 4.5)
K 260-4 (*)	723	60		stable nanocrystals from 673K - but too fast heating to be able to record at time repeated with a 2-step heating
K 260-5 (*)	723	60	10	phase segregation (1 min) + full crystallization (10 min)
K 260-7	723	20		oxidation/evaporation
K 260-12 (*)	723	20		phase segragation/oxidation?
K 260-3 b	793	60		full crystallization

"calibrated" by allowing a sample to fully crystallize. Accuracy of temperature reading can be expected within 10 K. For the applied heating rates, an equilibrium had to be found between high enough heating rate, to be representative of the ex-situ heat treatments, and to avoid too much evaporation and oxidation. High heating rates involve on the other hand the risk to show a temperature overshoot. Also observation is difficult: note that only a small area is under observation and possible changes do not necessarily initiate at the zone of observation.

Table 4.2 gives an overview of the parameters predetermined during the in-situ heat treatment experiments together with the observations. To avoid beam induced damage (as described in section 2.3.3.2), some experiments were repeated with a defocussed beam, while maintaining the magnification low, during the heating part. Recording started then at 50K below the set temperature. These experiments are marked by (*) in Table 4.2. If necessary, the heating was performed in two steps, using two set temperatures. The experiment was then stopped at the first temperature to search for the initially observed area (which might have changed due to thermal drift) and switch on the recording. Afterwards, heating to the second temperature was started.

Figure 4.5 shows the evolution of an as-cast homogeneous structure (a) to-

wards an inhomogeneous microstructure with brighter regions and darker borders upon annealing to 623K. The SAED spectra of the respective samples show clearly a change in the diffraction pattern: the initially broad diffuse halo changes into two sharper rings, pointing towards the development of a more ordered structure upon annealing. The position of the diffraction ring splits and shifts from 2.89 $\mathring{A}$ in the as-cast condition to two rings at 2.55 $\mathring{A}$ and 3.18 $\mathring{A}$ upon annealing.

EELS measurements in these in-situ annealed samples is in agreement with the EDX-STEM results, showing an enrichment of Cu in the darker zones (Fig 4.5).

Since it is not possible to observe a large area during the recording of the in-situ experiments, the first image of such inhomogeneous microstructure was observed after holding for 10 minutes and was located above the initial region of observation. However, based on the size of the bright regions, already arisen in such a short period of time, it is most likely to assume that chemical fluctuations occur earlier on a smaller scale, which might have been too small to be detected with the magnification and microscope set-up used for these experiments. In the darker 'edges' nanocrystals started to appear after annealing for 20 minutes, which could be observed in dark field mode.

Note that this inhomogeneous microstructure remained stable during the course of the whole experiment (35 minutes of holding). The amorphous nature of the microstructure was confirmed by tilting the sample, as well as by in-situ diffraction. For illustration, Figures 4.6 and 4.7 show the process of crystallization. This starts with the formation of these white areas. When the sample is annealed directly to high temperature (T_x), these white areas form almost immediately crystals as can be seen from Fig. 4.6b and c. Time was too short during the experiment to confirm if these areas were amorphous in the very beginning. Note however, that the diffraction pattern shows also the *double* halos of the remaining amorphous matrix, similar to the diffraction shown in Fig. 4.5 upon annealing. However, annealing in the supercooled liquid region (723K), shows the formation of amorphous regions, that crystallize in a later stage. Note the difference in contrast between the white amorphous and white crystalline zones. In the borders of the white areas (amorphous and crystalline), an increasing amount of nanocrystals appear.

Although damage induced by the beam during the in-situ treatments can be excluded, since the experiment was performed both with a focused and a

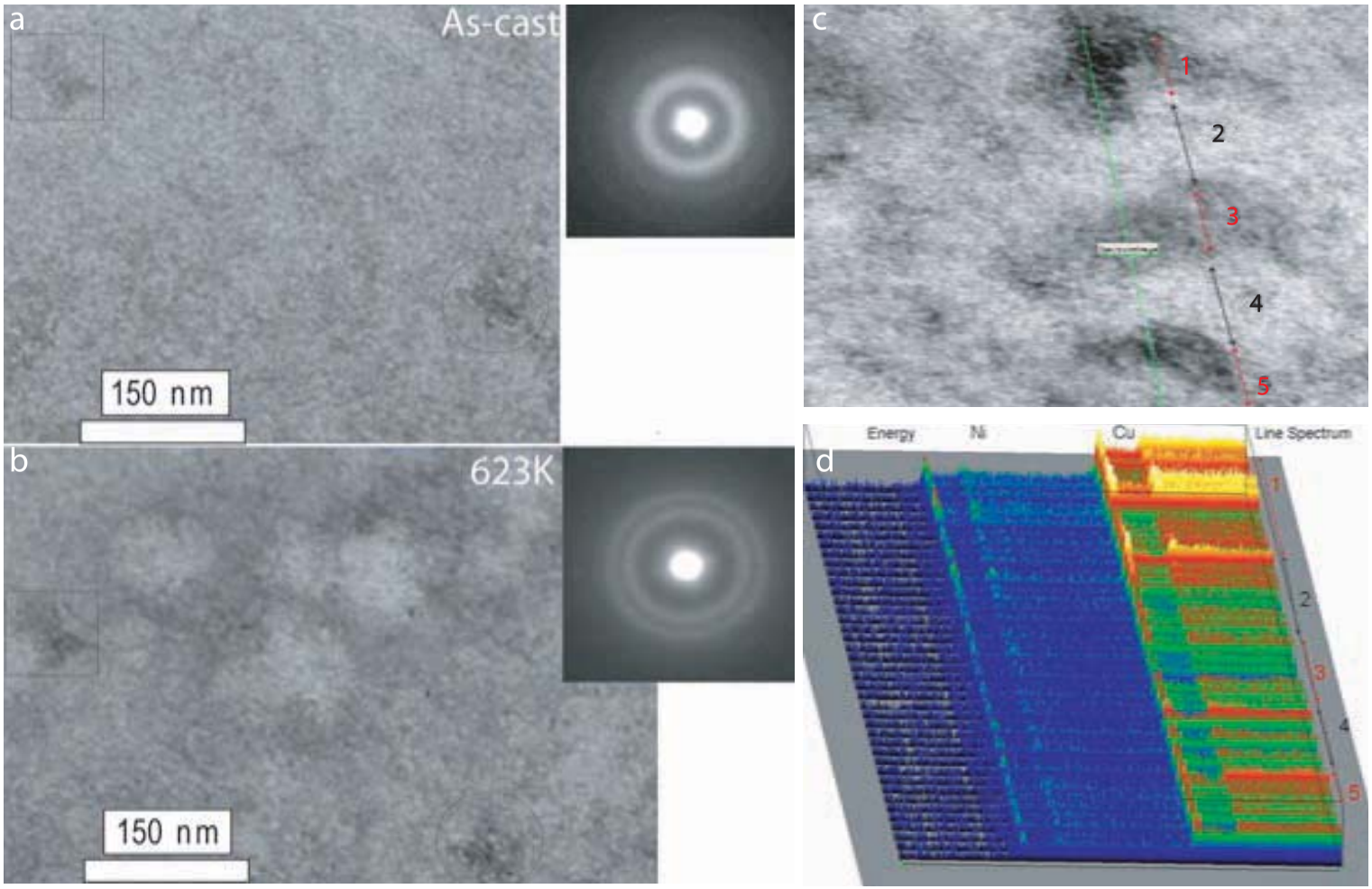

Fig. 4.5: Microstructural features in the as-cast (a) and annealed (623 K) sample (b), observed by TEM, revealing the change of a homogeneous microstructure to a heterogeneous one upon annealing. The respective SAED patterns are shown in the insets. (c) and (d) are the STEM/EELS results, with (c) the bright-field STEM image and (d) the EELS-energy spectrum, showing an enrichment of Cu in the darker regions, while Ni remained homogeneously distributed upon annealing.

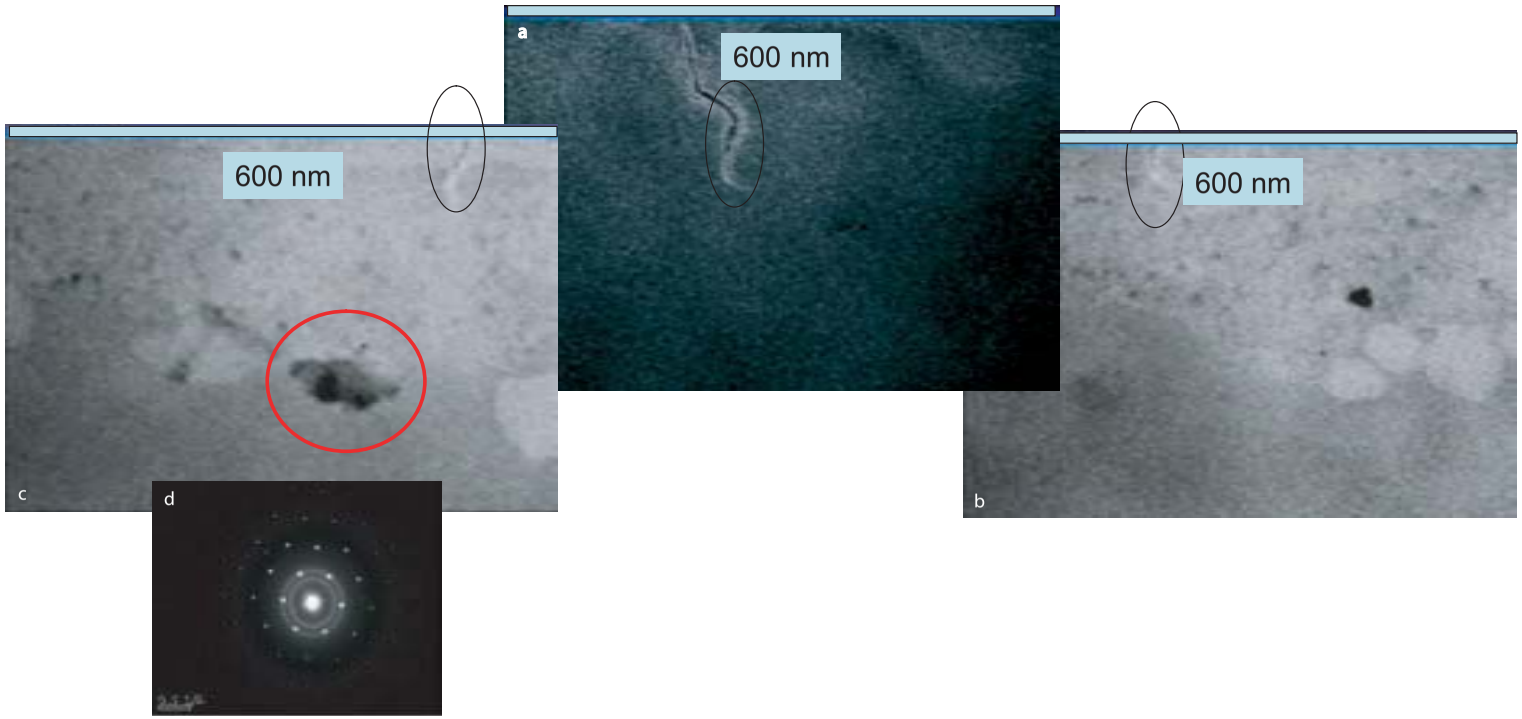

Fig. 4.6: Illustration of crystallization behavior in-situ - annealing up to crystallization temperature (K 260-3b): (a) is the initial microstructure, before annealing; (b) is taken at 793K during the first minute; (c) is taken 2 minutes after at the same temperature; (d) diffraction pattern of the crystal indicated by the circle in (c). The tip of the crack, marked with the ellips was used as a reference point during the observation.

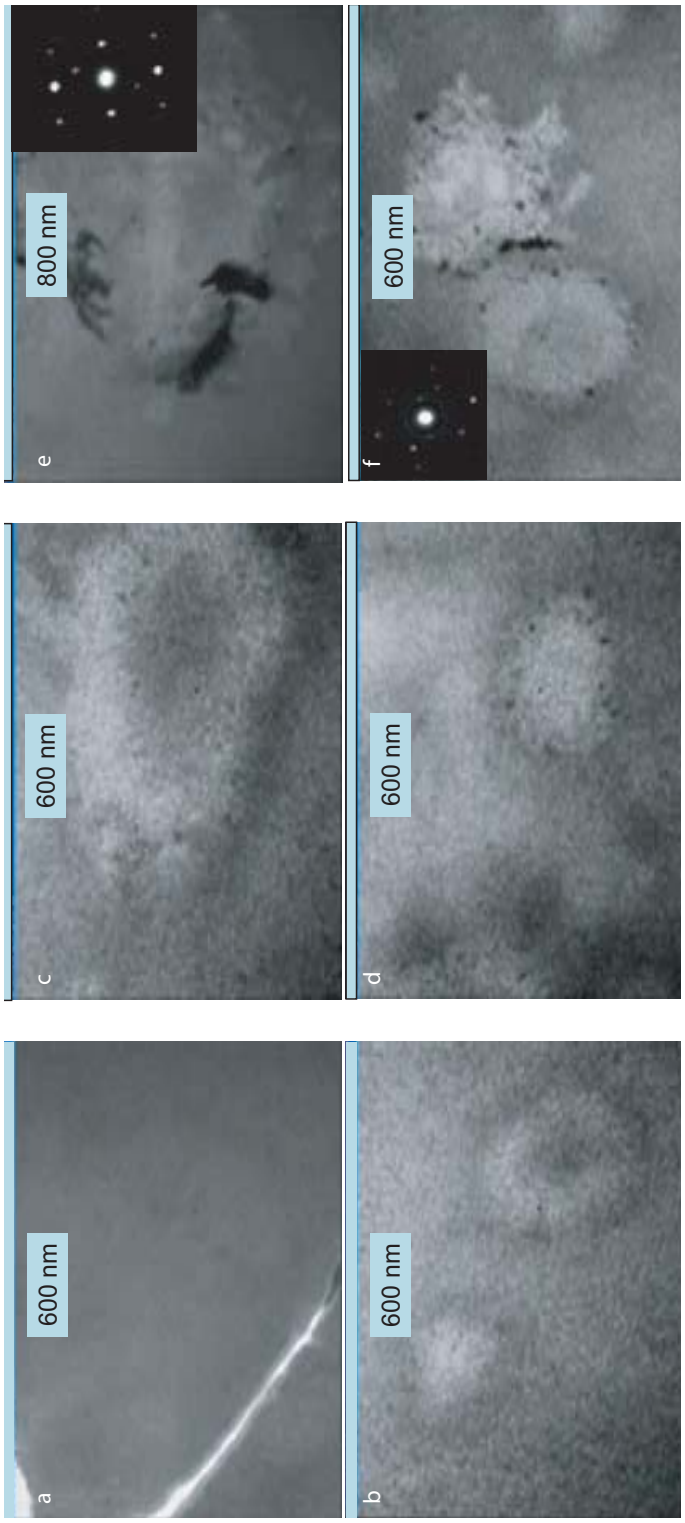

Fig. 4.7: Illustration of crystallization behavior in-situ - annealing in the supercooled liquid region (723K) (K 260-5): (a) is the initial microstructure, before annealing; (b)-(c)-(d) phase segregation observed during minute 1; (e)-(f) crystals formed out of the white areas after 10 minutes of holding with their respective diffraction patterns given in the insets.

defocussed beam at low magnification, diffusion during the in-situ experiments was probably enhanced by an increased amount of surface defects as compared to bulky samples, which might also explain the large size of the bright areas observed. Furthermore, presence of cracks due to sample preparation can even enhance further this diffusion effect.

This enhanced diffusion prevented the second goal of this study to be achieved: no characteristic time scale could be deduced from the experiments. Therefore, the time scales given should not be interpreted as actual time scales. Nonetheless, the important information obtained here is that this system shows a tendency to form Cu-rich zones as a first step towards structural ordering.

4.3.3 Discussion

This observation is in accordance with the reduced probability for Zr-Cu interactions observed by synchrotron radiation X-ray diffraction experiments. Note further that the change in position of the diffraction ring(s) agrees well with reported values of probability of appearance of Zr-Cu (2.9 Å) [179], Cu-Cu (2.6 Å) [179] (or Cu-Al 2.5 Å [182]) and Zr-Zr pairs (3.21 Å) [180], [183].

Systems based on Zr-Cu have been reported several times in literature to show a strong tendency for decomposition into Cu- and Zr-rich regions, although it might not be expected based on the available data of their heat of mixing [67]. For example, such decomposition has been reported in the binary system over the whole composition range of Cu-25-65 at% Zr during synthesis by vapour-quenching [184]. Formation of Cu-rich clusters in similar compositions have further been observed upon (high temperature) deformation [178] and after hydrogenation experiments [185]. This leads to the conclusion that this clustered state must be more thermodynamically stable than the monolithic glass, independent whether the alloy is in its glassy state or is a (supercooled) liquid.

In fact, the formation of these Cu-rich clusters and changes in chemical short and medium range order can be seen as the very first step towards crystallization: they can be considered as subcritical particles in the process towards the creation of *stable* nuclei which further might grow out to crystalline phases, similar to the crystallization scenario suggested by Wang and co-workers [186]. This will be further investigated in the next chapter.

4.4 Mechanical characterization

Several authors observed embrittlement induced upon annealing, which is usually attributed to a reduction of free volume [157], [158], [159], [187], [188], [189].

Reduction in free volume due to structural relaxation contributes to embrittlement in two ways. First, a loss of free volume increases the viscosity of the metallic glass, which implies a reduction of atomic mobility. This on its turn makes stress relaxation by means of viscoplastic flow more difficult and thus reduces toughness. Secondly, shear banding susceptibility was observed to be suppressed in annealed glasses by the reduced density of shear bands in annealed glasses [54].

4.4.1 Compression tests

Figure 4.8 shows the engineering stress-strain curve after uni-axial compression of the as-cast and heat-treated samples. A detail of the true stress-strain curve is given in the inset. In all cases, an average yield stress of around 1805 ± 52 MPa and an elastic strain of 2.1% were obtained. Elastic moduli measured by this technique were 99.7 ± 1.7, 90.7 ± 2.5 and 96 ± 4 for the as-cast sample and the samples annealed to 623 and 723K respectively.

However, unlike the reported embrittlement upon annealing, an increase of the total strain from $2.7 \pm 0.5\%$ for the as-cast sample up to $10 \pm 3\%$ for the samples annealed below T_g is observed. After annealing at 723K, plasticity started to decrease again; an average total strain of $3.3 \pm 0.4\%$ was measured which is still higher than the average total strain for the as-cast sample. Furthermore, the annealed samples show initially a weak increase of the flow stress upon deformation, before the typical softening sets in (inset of Fig. 4.8), caused by the decrease of medium range order/increase in free volume typically accompanying deformation of metallic glasses.

Deformation at room temperature is typically inhomogeneous and localized in a few shear bands. In compression tests, this deformation behavior manifests itself in a serrated flow curve (inset of Fig. 4.8), where stress drops occur and each drop corresponds typically with a single shear event. Improvement of the plasticity must have been provoked by a multiplication of shear bands in the glassy phase. Indeed, the serrations in the stress-strain curves in Fig. 4.8 increase in number with an increase in plasticity level, whereas the size of stress drops decreases. This

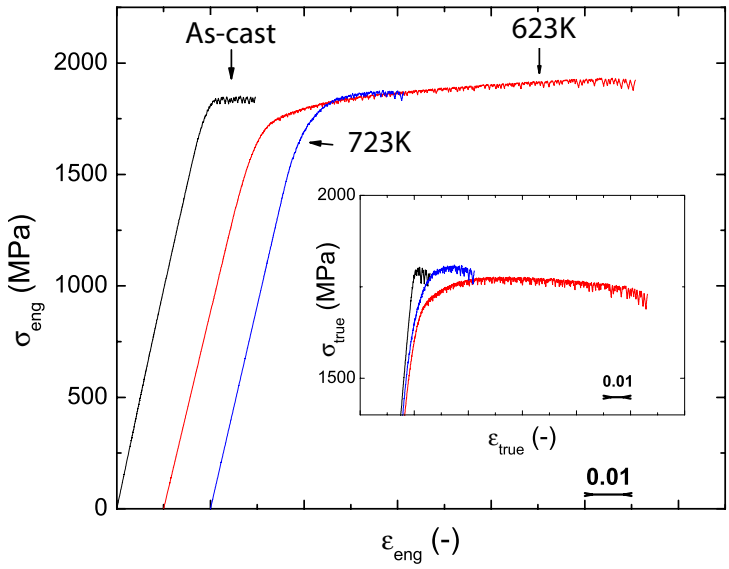

Fig. 4.8: Comparison of behavior in uni-axial compression of an as-cast sample and two samples, heat treated respectively below and above the glass transition temperature, revealing an increase in plasticity upon (sub-T_g) annealing.

decrease in stress drops points towards a more homogeneous deformation, similar as observed e.g. at high strain rates [160], [190].

Furthermore, the outer surfaces of the compressed annealed samples show an increased amount of shear bands (with the highest amount observed in the sample annealed below T_g, in accordance with the plasticity level), whereas the as-cast samples shows only one or two principal shear bands that are crossing over the specimen, (Fig. 4.9). Moreover, strong branching, deflection and interaction took place between the shear bands developed in the annealed samples.

The behavior of these shear events has been studied further by nanoindentation testing and will be discussed below.

Further insight in the mechanisms of strain localization, crack initiation and fracture can be obtained from studying the fracture surface after deformation. In literature, the fracture surfaces from tension [191], compression [192], toughness and fatigue tests [193] have been studied. Different features can be observed, depending on the fracture mode. Mainly, three distinct patterns were described: vein-like, river-like and smooth featureless surfaces. The first one is typically ob-

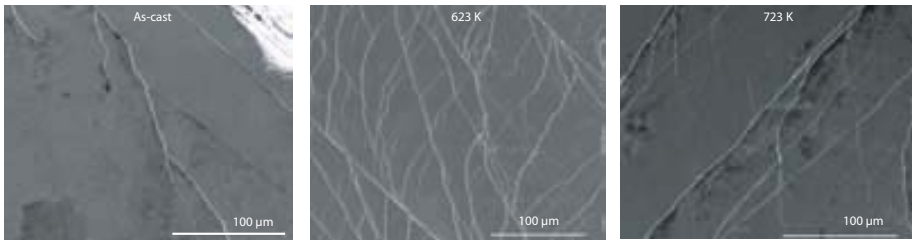

Fig. 4.9: SEM images of the outer surfaces of the compressed samples after failure show an increase of the amount of branched shear bands on the outer surfaces in accordance with the increase in plasticity for the respective samples.

served on the fracture surfaces of compression test samples. River-like is common on tensile fracture surfaces and smooth featureless surfaces have been attributed to fast crack propagation.

In fact, Kusy [192] and Concustell [15] showed that typical fracture surfaces under compression show a *mixed* morphology: river-like patterns as well as intermittent smooth regions cover isolated regions of the fracture surface, surrounded by a dominating vein-like pattern. The river like pattern forms on transversal shear planes, i.e. planes of secondary shear bands, which act as bridging ligaments and strain accommodation. Possibly sub-critical crack nucleation starts from sites covered with the river-like pattern. Crack propagation in its turn causes the formation of the intermittent smooth regions. The vein like pattern develops during the ultimate failure of the compression specimens in the regions of the softened shear bands [15].

Figure 4.10 a shows the fracture surface of the compressed as-cast sample, with a mixture of mainly vein and river pattern, as indicated on the figure. Figure 4.10 b shows a detail of a transversal step with river pattern, followed by the smooth region and surrounded by the typical vein pattern, as described above. However, this river pattern plays a more important role than generally observed and does not occur only in isolated regions but occupies important parts of the total fracture (Fig. 4.10 a and c).

Figure 4.11a shows a mixed morphology as well on the fracture surface the sample annealed below T_g. However, other zones with rather different features are observed as well (Fig. 4.11b-d). In general, the vein pattern is much finer than in case of the as-cast sample and is not homogeneously distributed over the fracture

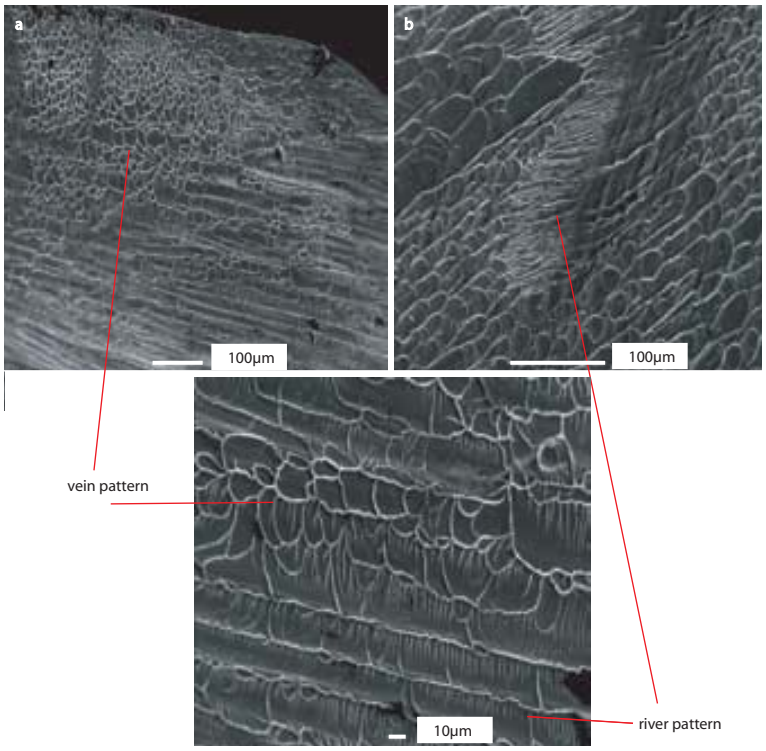

Fig. 4.10: Observation of the fracture surface after compression of the as-cast sample. An overall view is given in (a), showing a region with the typical vein pattern, and a rather large region with the river pattern, typical for brittle fracture. Details of this vein and river pattern are given in (b) and (c) respectively.

surface. Figure 4.11c shows a mixture of a such very fine vein pattern surrounded by a very rough zones, with a granular structure.

Xi and co-workers investigated the fracture surface of brittle materials into detail by atomic force microscopy and found that even the river-like patterns are in fact built up of a nanometer size dimple-structure [194]. They found further a correlation between the size of the plastic zones (dimples/veins) and the toughness of various BMGs, with a decreasing size (transition vein to river-like) indicating a decreased toughness.

On the other hand, a refinement of the vein pattern itself, as observed in this work in the samples with increased plasticity level, was also observed on the fracture surface of a BMG composite in the neighborhood of the reinforcing crystalline particles [195] and an increasing amount of reinforcing particles showed to lead to a gradual reduction of the sizes of the veins together with a gradual increase of

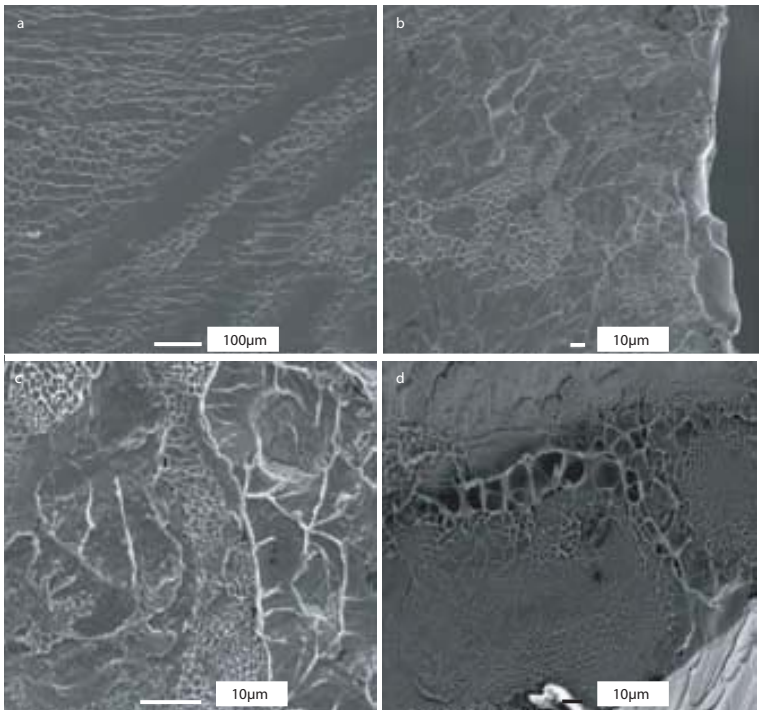

Fig. 4.11: Fracture surface of the sample annealed to 623K ($< T_g$). The overall view given in (a) is similar to the one of the as-cast sample. However, regions with very fine vein patterns are observed and irregular zones in between (not smooth river patterns) (c-d).

plasticity [42]. This reduced vein size in front of the particle was attributed to a slowed down flow of material in front of the particle [195]. Furthermore, during fatigue testing of a monolithic BMG, a refined vein pattern was observed in the region of (slow) crack propagation, where it was attributed to the relatively low fracture velocity (as compared to the region of fast crack propagation at the end of fatigue failure) [196].

Thus, this fracture morphology seems to be typical for reduced crack propagation and thus is a result of the increased plasticity observed for these samples.

The fracture surface of the sample annealed above T_g is similar to the one of the as-cast sample (Fig. 4.12a), but with relatively large river-like and smooth regions (Fig. 4.12b).

Finally, to better understand the role of the Cu-rich nano-clusters on the enhancement of plasticity observed after low-temperature annealing, the compression test of one of these low-temperature annealed samples was stopped before

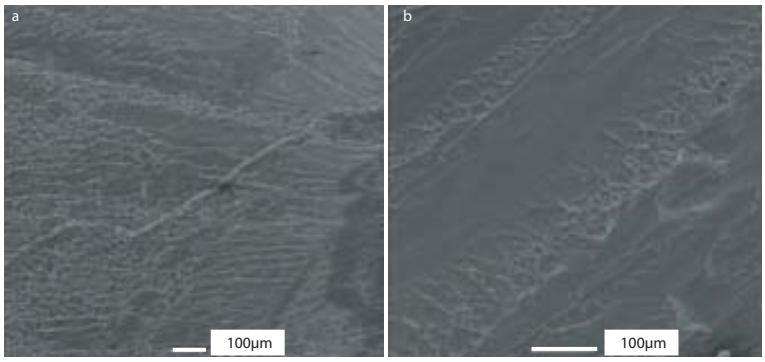

Fig. 4.12: Fracture surface of the sample annealed to 723K ($> T_g$). The overall view given in (a) is similar to the one of the as-cast sample, although again the vein pattern seems finer. Also in this sample, regions with river pattern are present (b).

failure and its microstructure containing a certain amount of shear bands was investigated by TEM. Several shear bands with a wavy shape could be observed of which an example is shown in Fig. 4.13. This high amount of deflections is typical for a shear band that has difficulties to propagate straight on and thus, was forced to deviate locally into zones of easy deformation [66]. Furthermore, the shear band mainly propagates through the bright zones and deflects around the darker Cu-rich zones, as indicated by the arrows in Fig. 4.13.

4.4.2 Nanoindentation

4.4.2.1 Shear band behavior upon casting and annealing

As discussed in the previous chapter for $Zr_{58.5}Ti_{8.2}Cu_{14.2}Ni_{11.4}Al_{7.7}$ and above for the current alloy under investigation, single shear events during inhomogeneous deformation manifest themselves as serrated flow in stress-strain or load-displacement curves. Figure 4.14 shows the load-displacement curves of nanoindentation experiments on $Zr_{55}Cu_{30}Al_{10}Ni_5$ in as-cast and annealed conditions (annealed below and above T_g, and up to T_x). Although the compression test results for these samples showed a clear difference in shear band behavior, the nanoindentation curves do not reveal large differences for the various samples: pop-ins with a moderate increase in displacement during the release of a shear band seem to have occurred for all samples. Note that the curves for 4mN are shown, where the highest resolution can be expected [156]. On the other hand, Liu and coworkers observed a similar modest pop-in behavior for the same alloy

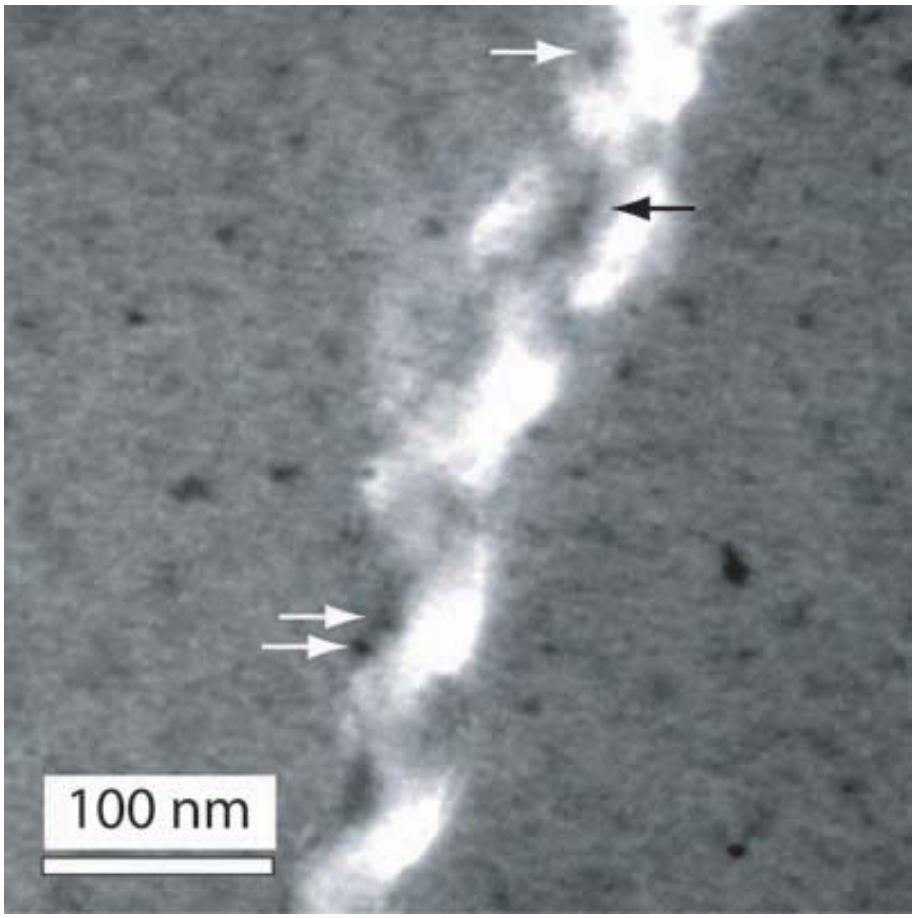

Fig. 4.13: Effect of the presence of Cu-rich nanoclusters on the plasticity and propagation of shear bands.

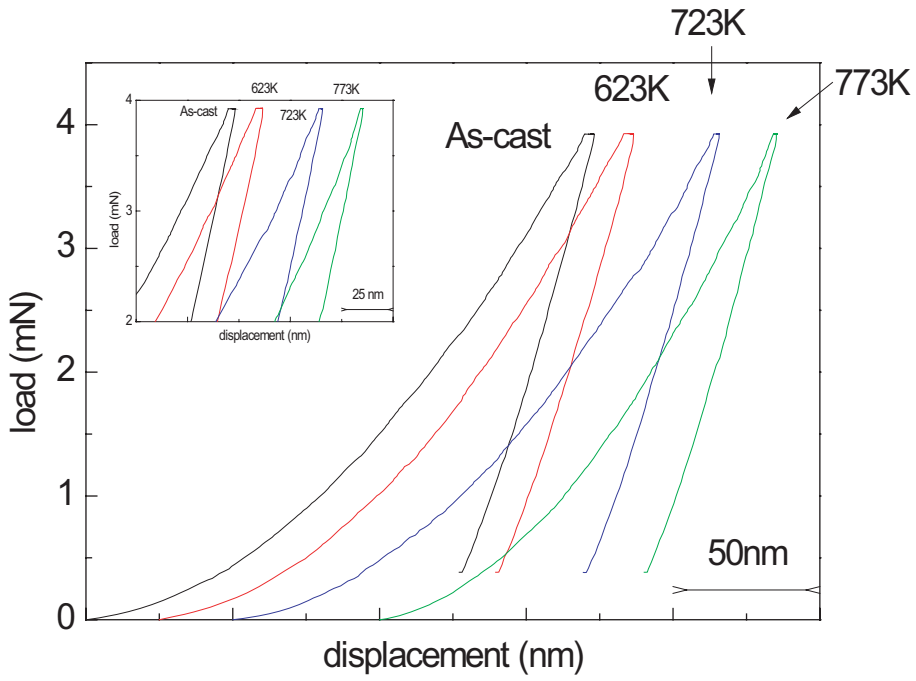

Fig. 4.14: Load-displacement curves with maximum load applied 4mN for as-cast and annealed samples. The inset shows a detail to make the observation of pop-ins more easy. Starting points of the curves have been shifted for

as compared to other Zr-based BMGs [197].

However, if the respective indents are investigated by SEM, some clear difference can be observed. Figure 4.15 shows several SEM images of indents made in the as-cast and annealed samples. They all show semi-circular surface steps, produced by shear bands propagating to the unconstrained free surface. In agreement with the compression test samples, a larger amount of shear bands surrounding and inside the indent are observed in the sample annealed to 623K upon nanoindentation, as compared to the other samples. These shear bands can be observed for all loads that could be observed by SEM.

Multiplication of shear bands during nanoindentation has been attributed in literature to various causes. Li et al [198] observed such a multiplication of shear bands during nanoindentation at cryogenic temperature. They concluded that due to the reduced propagation possibilities of the shear bands, the multiplication was necessary in order to accommodate the applied strain during nanoindentation. Jiang and Atzmon [199] attributed the increased amount of shear bands to a

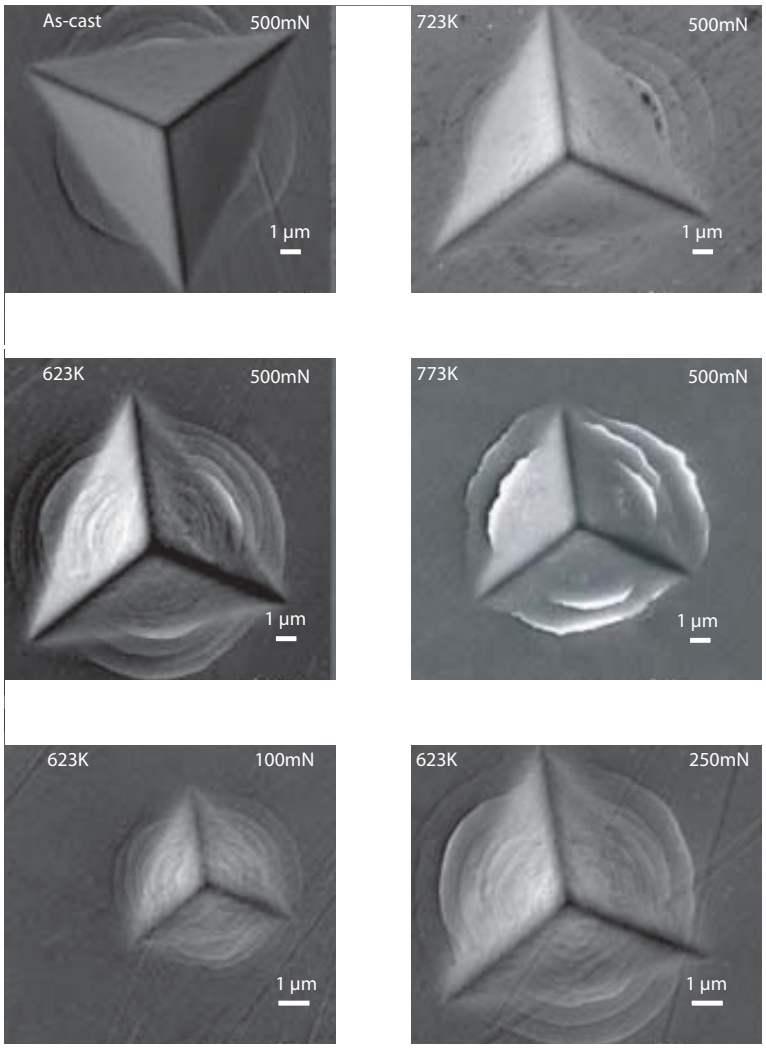

Fig. 4.15: Shear band formation in as-cast and annealed samples. In particular, for the sample annealed at 623K, a large amount of shear bands in and around the indents can be observed, for all loads observable by SEM.

required increase in nucleation rate, due to a reduction of free volume upon annealing. Besides reduction of free volume, we believe that the presence of structural changes upon annealing might have contributed to the observed multiplication, both by reducing the propagation possibilities and/or by acting like nucleation sites for new shear bands due to the presence of strain fields (see below).

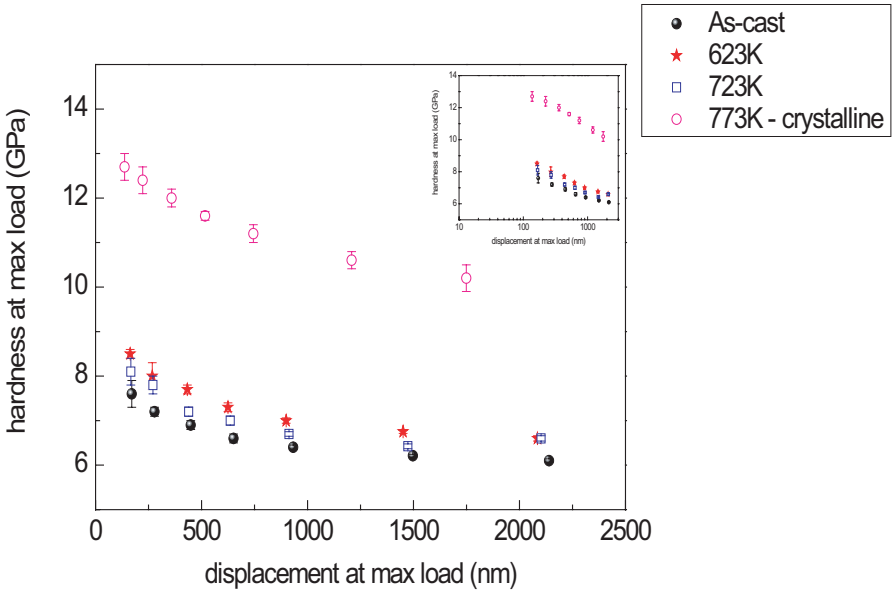

Fig. 4.16: Hardness at maximum load in function of the displacement at maximum load for the as-cast and various annealed samples of $Zr_{55}Cu_{30}Al_{10}Ni_5$. Inset shows the same graph on a logarithmic scale.

4.4.2.2 Indentation size effect

Figure 4.16 shows the hardness, calculated at maximum load at the end of the holding segments, in function of the maximum displacement reached at that moment. In the inset, hardness is presented on a logarithmic scale, which evidences the size effect more clearly. A similar trend is observed for the modulus. The obtained values of hardness and modulus, calculated by the method of Oliver and Pharr, are summarized in Table in function of the maximum applied load. The obtained values for the hardness and modulus of the as-cast are in agreement with literature data for similar loads and loading rates applied [200], [197].

Around all indents of each sample, a large amount of pile up can be observed (larger than what was observed for the sample presented in chapter 3), as can be seen from Fig. 4.15. Nonetheless, the ratios h_f/h_{max} for 4mN and 500mN lie around 0.7 (Table 4.4), which would indicate that little pile-up should be expected (and thus the method of Oliver and Pharr should be possible to be applied without a problem), whereas the images show the opposite. So care should be taken by using this ratio as a parameter to investigate the validity of the method of Oliver

Tab. 4.3: Values of the hardness (H), Young's modulus (E) as determined by the method of Oliver and Pharr for the as-cast (AC) and annealed samples (indicated by their respective temperatures). The upper line gives the values corrected for thermal drift, the uncorrected values are given underneath. Finally, for illustration, the values of the measured drift are given in the third part of this table. Too large values for the drift are emphasized in *italic* font.

H (GPa)	AC	623K	723K	773K
4 mN	7.6 ± 0.3	8.5 ± 0.1	8.1 ± 0.3	12.7 ± 0.3
	7.8 ± 0.3	8.5 ± 0.1	*9.4 ± 0.4*	12.7 ± 0.3
10 mN	7.2 ± 0.1	8.0 ± 0.3	7.8 ± 0.2	12.4 ± 0.3
	7.2 ± 0.1	8.0 ± 0.3	*8.4 ± 0.2*	12.0 ± 0.9
25 mN	6.9 ± 0.1	7.7 ± 0.1	7.2 ± 0.1	12.0 ± 0.2
	6.9 ± 0.1	7.7 ± 0.1	7.5 ± 0.1	12.7 ± 0.2
50 mN	6.6 ± 0.1	7.3 ± 0.1	7.0 ± 0.1	11.6 ± 0.1
	6.6 ± 0.1	7.3 ± 0.1	7.1 ± 0.1	12.0 ± 0.1
100 mN	6.4 ± 0.05	7.0 ± 0.1	6.7 ± 0.05	11.2 ± 0.2
	6.3 ± 0.07	6.9 ± 0.1	6.8 ± 0.05	11.3 ± 0.2
500 mN	6.1 ± 0.04	6.6 ± 0.06	6.6 ± 0.06	10.2 ± 0.3
	6.0 ± 0.04	6.5 ± 0.06	6.6 ± 0.06	10.2 ± 0.3

E (GPa)	AC	623K	723K	773K
4 mN	112 ± 3	119 ± 4	118 ± 4	157 ± 5
	112 ± 3	118 ± 4	123 ± 4	157 ± 5
10 mN	109 ± 2	115 ± 2	113 ± 3	152 ± 2
	109 ± 2	115 ± 2	116 ± 3	149 ± 3
25 mN	107 ± 1	111 ± 1	112 ± 4	147 ± 2
	107 ± 1	111 ± 1	113 ± 4	150 ± 2
50 mN	102 ± 1	107 ± 1	107 ± 1	143 ± 1
	102 ± 1	107 ± 1	107 ± 1	145 ± 1
100 mN	100 ± 1	104 ± 1	104 ± 1	139 ± 1
	100 ± 1	104 ± 1	105 ± 1	138 ± 1
500 mN	93 ± 0.3	95 ± 0.5	100 ± 1	122 ± 2
	93 ± 0.3	95 ± 0.5	100 ± 1	123 ± 2

drift	AC	623K	723K	773K
4 mN	-0.02	0.01	*-0.13*	0.01
10 mN	-0.009	0.007	*-0.1*	0.04
25 mN	-0.001	0.006	*-0.09*	*-0.09*
50 mN	0.009	0.024	-0.05	*-0.08*
100 mN	*0.097*	*0.118*	-0.045	-0.055
500 mN	*0.17*	*0.129*	-0.036	*-0.063*

and Pharr and the presence/absence of pile-up.

Tab. 4.4: Values of the ratio of the final indentation depth h_f to the depth of the indentation at peak load h_{max}, which is normally applied to control validity of the application of the method of Oliver and Pharr [137].

	As-cast	623 K	723 K	773 K
4 mN	0.69	0.67	0.68	0.61
500 mN	0.71	0.69	0.71	0.62

Especially for the lowest loads, the possibility that pile-up might have occurred and thus the fact that the application of the method of Oliver and Pharr might be erroneous should at least be considered. Therefore, hardness and modulus values have been calculated by the method described in section 2.3.4.3 by Eqs. (2.44) and (2.45). The results for the various samples are summarized in Table 4.5. To calculate the Young's modulus from the reduced modulus, 0.18 was used as Poisson ratio of the diamond indenter and 1200 GPa for its modulus. The Poisson ratio of the samples was roughly set to 0.3, in accordance with the value used during the measurements. For comparison, the values obtained by the method of Oliver and Pharr are given in italic underneath each value.

Although the results obtained are somewhat higher than the ones obtained

Tab. 4.5: Values of the Young's modulus (E) and hardness (H) as determined by the method of the work of indentation. For comparison, the values obtained for these samples by the method of Oliver and Pharr are given in *italic* font.

E (GPa)	As-cast	623 K	723 K	773 K
4 mN	126	125	128	166
	111	*119*	*118*	*157*
50 mN	116	120	121	
	102	*107*	*107*	*143*
500 mN	109	108	113	130
	93	*95*	*100*	*122*
H (GPa)				
4 mN	9.2	9.3	9.4	14.4
	7.6	*8.5*	*8.1*	*12.7*
50 mN	8.2	8.7	8.5	
	6.6	*7.3*	*7*	*11.6*
500 mN	7.8	8	8	11.3
	6.1	*6.6*	*6.6*	*10.2*

Tab. 4.6: Hardness values (after unloading) based on the measurement of the residual areas by SEM for the indents made at 500mN.

	AC	623K	723K
H (GPa)	6.6 ± 0.1	7.8 ± 0.1	6.5 ± 0.1

through the method of Oliver and Pharr, a size-effect is still observed, i.e. larger hardness values at lower loads. The discrepancy between both results might be caused by the 15% error, typically reported for the method of work of indentation [201], rather than that it would be caused by sink-in.

Note that although the observed indentation size effect is most likely not caused by an erroneous calculation of hardness based on the method of Oliver and Pharr, the absolute values obtained by this technique might still be overestimated to a certain extent, as will be discussed in the following section.

Surprisingly, the sample annealed to 723K which lies in the supercooled liquid region appears softer than the sample annealed below the glass transition temperature (623K).

The former suffered a large amount of thermal drift, in particular during the measurements at low loads, as can be seen in Table 4.3, so the values of these measurements should in fact not be taken into account. Note that for low loads, minimization of thermal drift is the most crucial, in particular for hardness measurements. For the loads of 500mN, values of thermal drift up to 0.17 nm/s have been measured, which is more than 3 times the recommended value (0.05 nm/s). Their influence however at high loads is moderate, as can be seen in Table 4.3.

On the other hand, calculation of the residual areas observed by SEM suggests the same trend as measured directly by the method of Oliver and Pharr. The values of final hardness (after unloading) for the indents made at 500mN are summarized in Table 4.6. The other values have not been calculated due to the lack of resolution in the imaging technique and thus due to the too large error expected in the measurements. Remarkably, Ramamurty and co-workers observed a similar trend in a Pd-based BMG in function of the annealing time [167].

Besides, work hardening upon nanoindentation has been reported in metallic glasses [202]. Similarly, work hardening was observed for the annealed samples, in particular for the sample annealed at low temperature, which might explain the trend observed.

Tab. 4.7: Overview of the elastic constants (E, ν, μ and K) measured by acoustic measurements. They are compared with the results of compression tests (E).

	E (GPa)	ν	μ (GPa)	K (GPa)	E_{comp}
As-cast	83.9 ± 1.6	0.3680 ± 0.0006	30.7 ± 0.6	105.9 ± 1.6	99.7 ± 1.7
623K	76.6 ± 0.3	0.3776 ± 0.0007	27.8 ± 0.1	104.3 ± 0.6	90.7 ± 2.5

Finally, note that in agreement with the discussion in the previous chapter, less free volume creation is expected in more relaxed samples, as for example the sample annealed to 723K. This decreased amount of excess free volume created requires less accommodation during the holding segment (and thus less creep during the holding), which is indeed seen in the inset of Fig. 4.14. So the reason for the observed softening during the loading segment requires still further investigation.

4.4.3 Acoustic measurements of elastic constants

From acoustic measurements, the elastic constants - the elastic modulus E, the Poisson ratio ν, the shear modulus μ and the bulk modulus K can be calculated based on the velocity of ultrasonic waves passing through the sample. The results for the as-cast and annealed samples are summarized in Table 4.7 and compared with the results obtained from uni-axial compression tests and tri-axial nanoindentation.

Although there is a difference in the absolute values of the elastic modulus measured by acoustic measurements and compression test results, both results show the same trend in change of the elastic modulus upon annealing. There is a decrease of 10% of this constant upon annealing. The discrepancy in absolute values could be attributed to the typical measurement error of 20 to 50 GPa by uni-axial compression tests, which is in fact not such an accurate technique to measure elastic properties. Furthermore, there is also a decrease in shear modulus, while the bulk modulus remains more or less unchanged.

The difference with the value of E measured by nanoindentation might be due to a difference in Poisson's modulus applied, or an influence of pile-up that might affect the absolute values, as mentioned above, or a consequence of the observed work hardening. Furthermore, the fact that nanoindentation is a dynamic technique, while the acoustic measurements are quasi-static might influence the obtained values as well.

The decreasing trend is on one hand surprising, since usually an increase of the elastic modulus and/or shear modulus is reported upon annealing [200], [203]. On the other hand, it is in agreement with the increased plasticity observed upon annealing here, and confirms that the observed result is not due to preparation artifacts but is indeed due to the structure of the material itself.

As mentioned in the introduction, annealing of a metallic glass produces structural relaxation wich can involve changes in the topological and compositional short-range order, which affect the elastic (and plastic) behavior. Although it is difficult to characterize the structural changes precisely, irreversible relaxation is often associated with changes to the *topological* short-range order. These result in an increase in density and a corresponding increase in elastic modulus, due to both the decreased interatomic spacing and topological changes which make internal rearrangements as described in section 1.4.3, more difficult.

Changes in the *compositional* short-range order can influence the room temperature elastic modulus as well. A decrease in unlike atomic near-neighbor bonds will decrease the elastic modulus, since it can be assumed that unlike bonds are stiffer on average than bonds between equal near-neighbors [54].

The observed decrease in elastic modulus in this work is thus very likely the result of the change in *compositional* short-range order, i.e. it is due to the decrease of the unlike Cu-Zr pairs and the increase of the like Zr-Zr and Cu-Cu-pairs, in agreement with the observations by synchrotron X-ray diffraction and TEM analysis.

Most likely, both compositional and topological relaxation occur during the short annealing treatment below T_g. However, the changes resulting from the latter are still minor and did not influence negatively elastic properties and plasticity, whereas the reduced amount of plasticity upon high temperature annealing is probably provoked due to the higher amount of topological relaxation.

4.4.4 Discussion

The model for yielding of metallic glasses below T_g of Johnson and Samwer [57], described by Eq. (1.12), foresees that the barrier height for shear flow for a given glass is proportional to its shear modulus μ. The results of the acoustic measurements are at this point in agreement with the compression test results, i.e. a slightly lower yield stress can be seen from Fig. 4.8 for the sample annealed below

T_g, although the difference is minor, as pointed out before.

The evolution of compositional fluctuations upon annealing under the form of Cu-clusters must result not only in an overall change in elastic properties, but also in (even stronger) *local* fluctuations. Recent simulations predict further a decrease of μ with decreasing Cu-content in Cu-Zr-alloys [204]. The Zr-based matrix, depleted to a certain extent with Cu and with an increased amount of Zr-Zr interactions, can thus be considered as less stiff with a lower barrier for shear flow.

Furthermore, the ability of the Zr-based matrix and in particular the nucleating STZs to accommodate strain and strain rate differences plays an important role in shear band nucleation, as pointed out by Schuh [160]. In the very initial stage of deformation, a very local region of the glass (a cluster of STZs) deforms more quickly than the rest of the matrix and a strain rate mismatch exists between such a shear band embryo $\dot{\gamma_n}$ and the surrounding matrix $\dot{\gamma}$. The ratio of these two strain rates is given by:

$$\dot{\Gamma} = \frac{\dot{\gamma_n}}{\dot{\gamma}} = \exp(\frac{\phi \Delta F_0}{kT}), \tag{4.1}$$

with ϕ the fraction of the transformation strain energy stored in each STZ-sized volume, typically on the order of 0.08, ΔF_0 is the free energy required to operate a single STZ and is a function of the elastic properties of the glass, k is the Boltzmann constant and T is temperature. At the point where a legitimate shear band has formed and is carrying all of the deformation, $\dot{\Gamma}$ diverges quickly to infinity. The influence of the elastic properties on shear band nucleation is present through ΔF_0 (Eq. (1.11)), where reducing the latter reduces the strain rate ratio, leading to a more homogeneous (less inhomogeneous) character of the deformation. Using the values measured by the acoustic measurements for μ and ν and representative values for the other parameters given in [160], values of 1.42 eV and 1.26 eV are obtained for ΔF_0 the as-cast and the samples annealed to 623K, suggesting a more homogeneous deformation (lower value of $\dot{\Gamma}$) for the annealed samples. This shows indeed that the nucleating shear bands in the Cu-depleted, Zr-rich matrix are capable of accommodating more the strain rate, postponing the moment for fast shear band propagation, than in case of the as-cast, homogeneous sample.

Finally, the Cu-rich clusters show a higher degree of order and can be con-

sidered to be solid-like, therefore forming a barrier for rapid shear *propagation*, by increasing viscosity inside the soft, propagating shear band. Note that these suggestions concerning nucleation and propagation of shear bands are in fact in agreement with the observed propagating shear band in the low-temperature annealed sample, which was presented in Fig. 4.13.

4.5 Summary

Thermal and microstructural characterization through calorimetry, diffraction with synchrotron radiation and transmission electron microscopy, combined with several spectroscopy techniques, reveal the possibility to induce subtle microstructural changes, even upon annealing below the glass transition temperature. These changes involve a demixing of the Cu and Zr atoms (the main components of the alloy under investigation) and the formation of Cu-rich clusters in a Cu-depleted, Zr-rich matrix, in agreement with several literature data. Heat treatments in-situ in the TEM suggest that this segregation process might be the first step towards crystallization. This will be investigated further in the next chapter.

Although the (compositional) changes observed were moderate, their influence on the mechanical behavior, and in particular plasticity under compression, is great, when the topological changes are still moderate (low temperature annealing). The samples with the inhomogeneous matrix show higher levels of plasticity and thus an increased amount of shear bands, both after compression and nanoindentation. Acoustic measurements of the elastic properties finally are in agreement with the observed change in chemical short range order. A too large increase in topological short range order (free volume decrease) counterbalances the effect induced by the chemical short range order upon high temperature annealing.

Finally, nanoindentation results confirm the existence/appearance of a so-called indentation size effect in bulk metallic glasses, which is not caused by the typically observed pile-up for these sample. Care should be taken when applying this technique to measure the elastic properties, in particular with low loads. Discrepancy with other techniques can be large in those cases.

5. CHARACTERIZATION OF $ZR_{55}CU_{30+X}AL_{10}NI_{5-X}$ (X=-2, 0, 2)

In the previous chapter, the possibility to obtain a heterogeneous microstructure upon low-temperature annealing with important influence on the plasticity, was discussed. Before this annealing technique can be made more technologically applicable, a more fundamental study of the influencing parameters is necessary.

The formation of a composite structure with Cu-clusters in a more Cu-depleted matrix seemed to alter the thermal (crystallization) behavior. The crystallization behavior and crystallization products are investigated in this chapter, with special emphasis on the influence of the heating rate (and thus the time effect). It will be shown that in function of the applied heating rate, the thermal behavior of the alloy can be altered in a similar way as after a preceding heat treatment.

Secondly, three compositions with varying Cu/Ni-ratio are studied in order to get a deeper insight in the role of Cu itself, again with a special emphasis on the thermal/crystallization behavior. This crystallization behavior was investigated by DSC (conventional and modulated), XRD and TEM.

The chapter is concluded with a brief discussion on the role of the Cu-content on the mechanical and thermomechanical behavior of the different alloy compositions.

5.1 Thermal characterization

Changing the composition, even in small amounts, can have an important influence on the glass forming ability. Therefore, first of all, the influence of composition on thermal stability was investigated by DSC and mt-DSC. Furthermore, by varying the heating rate, the activation energy for crystallization can be determined by the Kissinger method, as explained in section 2.3.1.5.

Table 5.1 summarizes the thermal characteristics as glass transition temperature, crystallization temperature (peak temperature) and the enthalpies for crystallization for the various compositions. Based on these numbers, there is no

significant decrease of stability of the glass, as can be seen from the difference $T_x - T_g$. However, the absolute values of glass transition and crystallization temperatures of the most Cu-rich alloy (x=+2) shift to slightly lower temperatures.

While the values for crystallization enthalpy (peak area) do not indicate large differences between the various compositions, an important change in crystallization peak shape occurs, as shown in Fig. 5.1 a1-a3. This change in shape depends further on the heating rate. For the alloy with the lowest amount of Cu (x=-2), only one peak is observed for all heating rates. However, at low heating rates, this peak is very sharp, whereas from 40K/min on, it loses its sharpness and becomes spread out towards high temperatures. For x=0, the main composition, one crystallization peak splits into two clear distinguishable peaks upon lower heating rates, with the second one less deep than the first one. At higher heating rates, no distinction can be observed, which could indicate that the two temperatures lie closer to each other and/or the size of the second peak becomes too small. This crystallization behavior is similar to what was observed after the heat treatment described in the previous chapter, although then, the high temperature shoulder in the annealed sample was clearly observed for a heating rate as high as 40K/min. Adding more Cu (x=2) leads to two overlapping peaks with more or less the same depth. Note that, although the peaks seem to be smaller for higher Cu contents, the total enthalpy calculated remains the same (Table 5.1).

By superposing a modulating signal on the conventional linear heating, the resolution of the outcoming signal can be improved significantly. By mt-DSC, a distinct separation of the crystallization events could be observed (Fig. 5.1 b1-b3). In addition, a very clear glass transition region can be seen for all compositions, confirming the glassy nature of all compositions, as shown in the inset of the respective figures.

Figure 5.1 c1-c3 shows the Kissinger plots for the three compositions from which slope the activation energy for crystallization can be determined. The values are summarized in Table 5.2. As will be shown later, the peak for the Cu-poor alloy should be compared with the second peak of the base alloy.

A small decrease in activation energies can be observed by increasing the Cu-content of the overall composition. For the x=0, a decrease in activation energy is observed between the two peaks.

The values are somewhat higher than the ones reported in literature [175] for

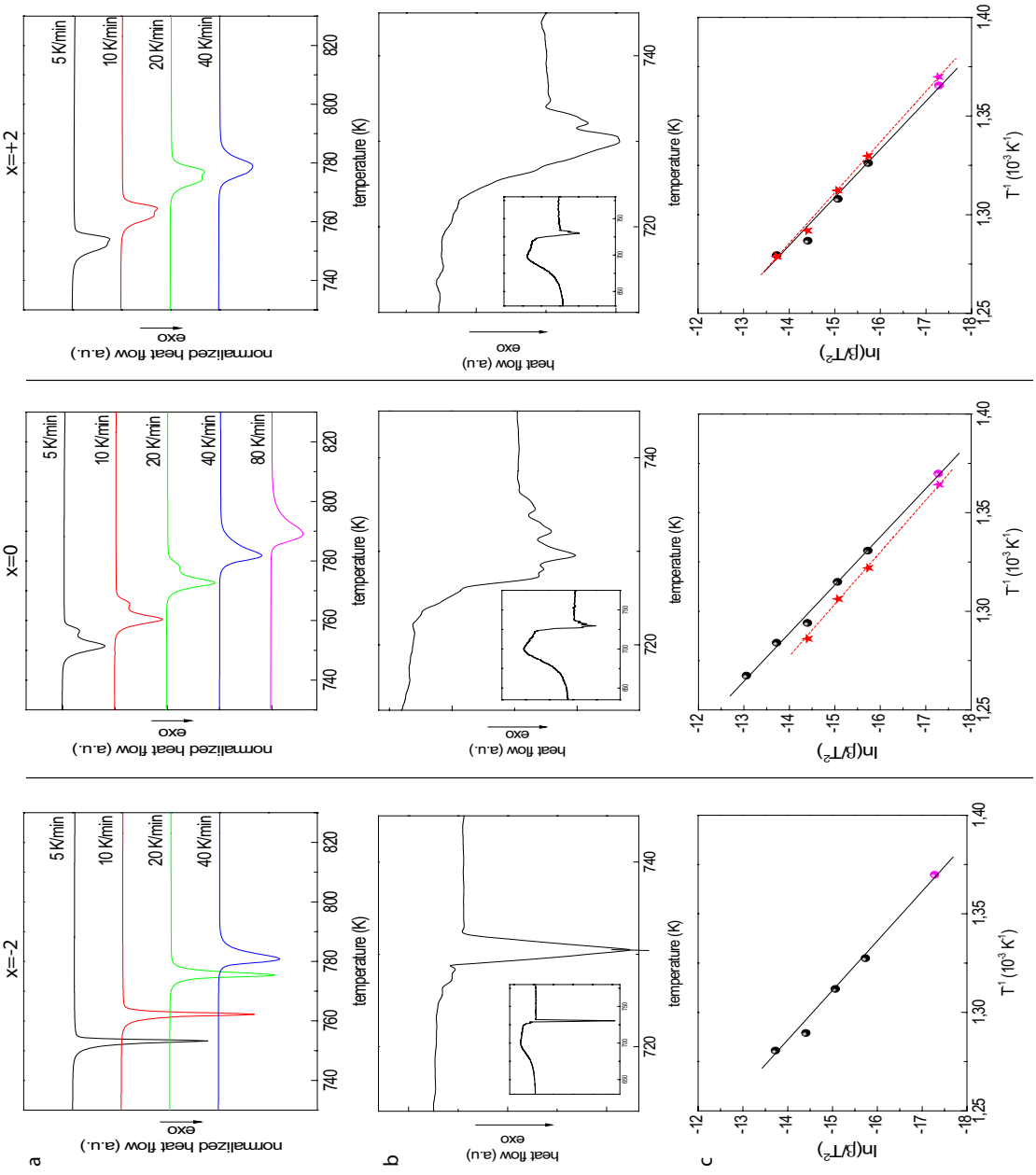

Fig. 5.1: Overview of the DSC (upper row) and mt-DSC scans (center row) obtained at various heating rates, showing change in crystallization peak shape. The lowest row shows the respective Kissinger plots for the various compositions.

Tab. 5.1: Characteristics of thermal stability of $Zr_{55}Cu_{30-x}Al_{10}Ni_{5+x}$ alloys. All temperatures are in Kelvin; enthalpies are in J/g and β, the heating rate is in K min^{-1}. Errors are on the order of 2 K and 3 J/g respectively. Two values for the crystallization peak are given if clearly observed by DSC (or mt-DSC); values replaced by * could not be determined accurately.

	β	T_g	$T_{x,peak1}$	$T_{x,peak2}$	ΔH_x
x=-2	1 (mt-DSC)	682		730	*
x=-2	5	684.5		753	-51
x=-2	10	690		762	-51
x=-2	20	697		776	-52
x=-2	40	701		781	-54
x=0	1 (mt-DSC)	681	730	733	*
x=0	5	685	751	756	-49
x=0	10	690	761	766	-50
x=0	20	699	773	778	-51
x=0	40	701	779	*	-52
x=0	80	709	789	*	-56
x= 2	1 (mt-DSC)	675	725	732	*
x= 2	5	677	747	749	-47
x= 2	10	684	757	760	-49
x= 2	20	691	769	772	-51
x= 2	40	694	*	777	-52

Tab. 5.2: Activation energies for crystallization calculated by the Kissinger method. Units are kJ/mol. Errors are on the order of $2 - 2.5\%$

sample	$E_a(T_{x,peak1})$	$E_a(T_{x,peak2})$
x=-2	-	330
x=0	340	315
x=2	322	313

continuous heating. They are on the same order of the activation energy during isothermal annealing in the low temperature range of the supercooled liquid region, reported by the same author [176]. Generally, the activation energy is considered as the extra energy needed to surmount short-range barriers coming from neighbor atoms during local atomic structure evolution. A large value suggests that the local structural units involving the neighboring atoms may be rather different for the supercooled liquid and the first crystallization phases [205].

5.2 Microstructural characterization - Crystallization products

5.2.1 Introduction - literature review

The basic alloy $Zr_{55}Cu_{30}Al_{10}Ni_5$ has been studied widely in the past: mainly due to its high glass-forming ability, it was considered as a 'model' BMG to study general aspects of metallic glasses. However, its crystallization behavior and its products remains quite ambiguous, as can be seen from Table 5.3, where several literature data are summarized. Table 5.4 gives an overview of Zr-Cu-based metallic glasses with a composition close to the alloy under investigation, with varying Zr, Cu and Al contents. Most authors report on the formation of $CuZr_2$ and an intermetallic between Al and Zr, possibly accompanied by an unknown metastable and/or unknown stable phase.

This $CuZr_2$ is an equilibrium phase and is sometimes reported to form only in a second stage, upon transformation from another phase, typically a so-called "big-cube" phase [25], [206]. Usually, the fcc structure $NiZr_2$ with lattice parameter a=12.27 $\AA$ is reported, which is oxygen stabilized. When the oxygen content is low, $Ni_{42}Zr_{58}$ has been reported [25], which is cubic, probably primitive [207], with lattice parameter slightly smaller: a=12.1Å.

Variations in the Zr and Cu content (Table 5.4) lead usually to the formation of $CuZr_2$ (Zr-rich phase), $Cu_{10}Zr_7$ (Cu-rich phase) and/or ZrCu (high temperature phase), with possible solid solution of Al and/or Ni, which is in agreement with the thermodynamic binary phase diagram of Cu-Zr in the composition range under consideration.

In some cases, quasicrystals have been reported, especially at higher Zr-contents [208] or due to the presence of oxygen [209].

Suggestions for the observed ambiguity in crystallization products of $Zr_{55}Cu_{30}Al_{10}Ni_5$ include the variation in heating mode applied: differences have been reported between isothermal annealing, continuous heat treatments and cycling annealing treatments, as observed e.g. by Ref. [200]. Besides the heat treatment, the heating rate might lead to different crystallization products. Yavari and coworkers noted that a metastable tetragonal phase [113] formed upon fast heating to melting but not upon (slower) cooling from the melt. As mentioned above, oxygen is also known to play an important role in the crystallization behavior [25], [206], [209]. Furthermore, often only one method, usually X-ray

Tab. 5.3: Overview of literature data on crystallization products of $Zr_{55}Cu_{30}Al_{10}Ni_5$, determined by various methods and various heat treatments. (s) indicates that synchrotron radiation was used as X-ray source.

composition ref.	products	heating/ cooling rate	method
$Zr_{55}Cu_{30}Al_{10}Ni_5$ [113], [210], [211]	$CuZr_2$ metastable (tetragonal) phase	10-60K/s	in-situ XRD (s)
$Zr_{55}Cu_{30}Al_{10}Ni_5$ [209]	$CuZr_2$ Al_3Zr_4 metastable (tetragonal) phase	20K/min	XRD
$Zr_{55}Cu_{30}Al_{10}Ni_5$ [212]	$CuZr_2$	40K/min	XRD
$Zr_{55}Cu_{30}Al_{10}Ni_5$ [175]	$NiZr_2$ $Al_{1.7}Ni_{0.3}Zr$ unknown phase	isotherm - SQL	XRD
$Zr_{55}Cu_{30}Al_{10}Ni_5$ [200]	$CuZr_2$ $AlCu_2Zr$	10K/min	XRD
$Zr_{55}Cu_{30}Al_{10}Ni_5$ [206]	$NiZr_2$	solidification (ingot) 40K/min	XRD
$Zr_{55}Cu_{30}Al_{10}Ni_5$ [25]	$NiZr_2$/ $Ni_{42}Zr_{58}$ $CuZr_2$	20K/min	XRD XRD

diffraction, was used to analyze the crystallization products, usually without a refinement technique. Finally, casting conditions have been reported to cause differences in the thermal/crystallization behavior of Zr-Cu-Ni-based alloys [207].

5.2.2 Results

In this section, a study of the crystallization products was performed, as a function of the Cu-content and the heating rate. Both slowly cooled ingots (crystallized upon cooling from the melt) and reheated rods (rapid cooling) have been investigated. The rods were annealed in the DSC up to the various crystallization peaks by slow heating rates ($\beta = 5Kmin^{-1}$) or to $T_{p,1}$ and $T_{p,1} + 10$ in case no two distinct peaks can be observed by DSC, as is the case for x=-2 or for high heating rates $\beta = 80Kmin^{-1}$. After XRD measurements, one sample of each group was prepared for TEM observation. In particular, the use of TEM is complementary to the use of XRD since it gives information on larger inter-planar distances than XRD.

Tab. 5.4: Overview of literature data on crystallization products of Zr-Cu -based metallic glasses, with a composition close to $Zr_{55}Cu_{30}Al_{10}Ni_5$.

composition ref.	products	heating/ cooling rate	method
$Zr_{65}Cu_{35}$ [213]	ZrCu Zr_7Cu_{10} $CuZr_2$ Cu_5Zr	cooling - ingot	XRD/ SEM
$Zr_{65}Cu_{35}$ [213]	ZrCu $CuZr_2$	cooling Cu-mould	XRD/ SEM
$Zr_{65}Cu_{35}$ [213]	Zr_7Cu_{10} $CuZr_2$	splat- cooling	XRD/ SEM
$Zr_{65}Cu_{27.5}Al_{7.5}$ [213]	$\beta-Zr$ $Zr_{73}Cu_{14}Al_{13}$ $CuZr_2$	cooling - ingot	XRD/ SEM
$Zr_{65}Cu_{27.5}Al_{7.5}$ [213]	Zr(Cu,Al) $Zr_7(Cu,Al)_{10}$ $(Cu,Al)Zr_2$	cooling Cu-mould	XRD/ SEM
$Zr_{65}Cu_{27}Al_8$ [214]	$CuZr_2$ metastable fcc-phase unknown fcc phase	5-80K/min	XRD
$Zr_{65}Cu_{17.5}Al_{7.5}Ni_{10}$ [213]	Zr(Cu,Al,Ni) $(Cu,Al,Ni)Zr_2$ + additional phases from undissolved components	cooling Cu-mould	XRD/ SEM
$Zr_{69}Cu_{12}Al_{7.5}Ni_{11}$ [208]	quasi- crystals		XRD/ TEM
$Zr_{48.5}Cu_{46.5}Al_5$ [76]	CuZr $Cu_{10}Zr_7$ $CuZr_2$		XRD/ TEM
$Cu_{50}Zr_{45}Al_5$ [215]	Zr_7Cu_{10} $CuZr_2$		in-situ synchrotron
$Zr_{51}Cu_{20.7}Al_{16.3}Ni_{12}$ [216]	$NiZr_2$-type Al_2Zr_3-type $Al_{1.7}Ni_{0.3}Zr$ rhombohedral phase monoclinic phase	10 K/s	TEM

Due to the complexity of the crystal structure (space group) of the possible phases (non-cubic, orthogonal, hexagonal..), the analysis of the (electron) diffraction spectra is not trivial. Therefore, a rough selection of possible candidates was obtained by means of Philips X'Pert Highscore software, which provides a first profile match, combined with the literature data, given in table 5.3. The candidates based on the XRD spectra were further compared with the TEM results and electron diffraction patterns obtained.

Sometimes, the longest interplanar distances had to be calculated, since they are not always provided in diffraction databases. These distances were compared with the experimentally measured ones. For each set of planes $(h_i k_i l_i)$, the zone-axis $[uvw]$ along which the diffraction was made could be calculated by means of the zone law: $h_i u + k_i v + l_i w = 0$. Once the possible zone-axis was known, the stereographic projection (App. B) along this zone-axis $[uvw]$ could be calculated by means of WinWulff 1.0.7 software [217]. In this way, the measured angle can be compared with the angle to be expected. Furthermore, the 3-dimensional reciprocal lattice can be calculated which can be compared with the 2-dimensional one measured by electron diffraction.

5.2.2.1 Ingots

Figure 5.2 shows the XRD spectra of the respective slowly cooled ingots. A match to the profiles of each possible crystalline phase separately is given as well for the respective alloys. Generally, $CuZr_2$ is found in all the alloys, together with a cubic or tetragonal phase with large lattice parameters, but in different quantities. Generally, a certain amount of an Al-Zr-intermetallic is observed. Note that the profile match has only been done qualitatively and is still to be confirmed by a refinement technique. Some peaks could not be unambiguously linked to the phases available in the database used.

In the ingot of $Zr_{55}Cu_{28}Al_{10}Ni_7$, a mixture of the big cube $NiZr_2$ (main phase) and $CuZr_2$ (I4/mmm - a=3.22 Å; c=11.18 Å) is clearly formed. Some big cube $Ni_{42}Zr_{58}$ (cubic; a=12.1 Å) might also be present. The remaining peak is probably originating from an Al-Zr intermetallic (most likely Al_4Zr_5 - P63/mcm, a=8.44 Å; c=5.8 Å).

Slowly cooled $Zr_{55}Cu_{30}Al_{10}Ni_5$ is built up of big cube $Ni_{42}Zr_{58}$ (main phase), $CuZr_2$, Al_4Zr_5 and $Ni_{11}Zr_9$ (I4/m - a=9.88 Å; c=6.61 Å).

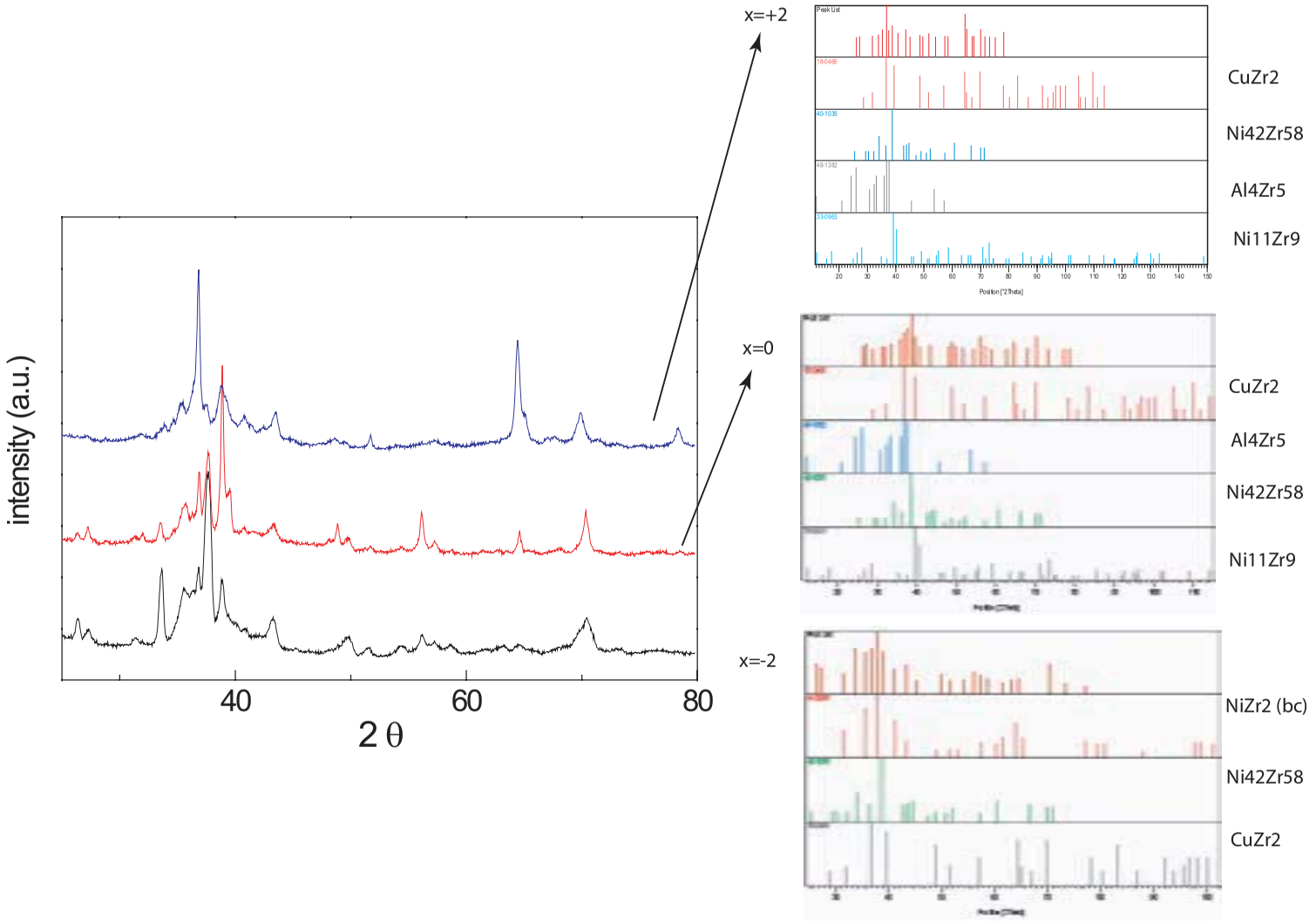

Fig. 5.2: XRD patterns of the slowly cooled ingots for the three compositions and a match of the respective peaks of the possible candidates for each alloy. x in the figure indicates the Cu-content of each alloy.

The most Cu-rich alloy, $Zr_{55}Cu_{32}Al_{10}Ni_3$, shows a mixture of $CuZr_2$ (main phase), the big cube $Ni_{42}Zr_{58}$, $Ni_{11}Zr_9$ and Al_4Zr_5.

It should be noted that instead of (or together with) the big cube phase $Ni_{42}Zr_{58}$, $Cu_{10}Zr_7$ (C2ca - a=12.675 Å, b=9.313 Å, c=9.347 Å) could be present. This is an orthorombic phase with a complex diffraction pattern and it is difficult to judge its presence without a refinement technique. However, it should be taken into account, as will be further discussed below with the electron microscopy data.

Figures 5.3, 5.4 and 5.5 show an overview of the microstructures of the different ingots (master alloys) of the three compositions, made by scanning electron microscopy.

Generally, the microstructures consist of a (rather) fine eutectic with one or two types of other phases: dendrites and/or lath type structure. However, the respective microstructures are rather inhomogeneous, i.e., differences in coarse-grained structure are clearly observed between different parts (top, center, bottom) of each master alloy. These results are similar as what was observed by Baricco et al. [206] . Furthermore, the Cu-content has also its influence on the coarseness of each composition separately: for x=-2, the finest microstructure is observed, with possible amorphous regions, while x=+2 has the coarsest microstructure. This can be understood based on the principle of confusion: increasing the amount of the fourth element makes the alloy a 'stronger' quaternary alloy, frustrating the overall alloy and limiting kinetics. Increasing the amount of Cu to the detriment of the amount of Ni gives the alloy more a ternary character and faster kinetics upon solidification can be expected.

Point analysis of EDX in the coarsest regions of the master alloy x=+2 suggests that the (darker) lath structure is $Zr_2(Cu, Al, Ni)$ (Fig. 5.5). The eutectic matrix shows an enrichment in Al and depletion in Cu, which might coincide with the observed Al-Zr intermetallic by XRD. The white dendrites show an enrichment in Cu and a decreased amount of Zr, which could indicate towards the presence of $Cu_{10}Zr_7$ or $(Ni, Cu)_{11}Zr_9$ rather than the big cube phase $Ni_{42}Zr_{58}$, indicated by XRD.

Note that the values given in Fig. 5.5 are only qualitative, not absolute due to the uncertainty due to overlap in the EDX signal. However, for comparison, the overall composition measured by EDX was 57% of Zr, 31% of Cu, 3% of Ni and 9% of Al, which is rather close to the nominal expected composition. For

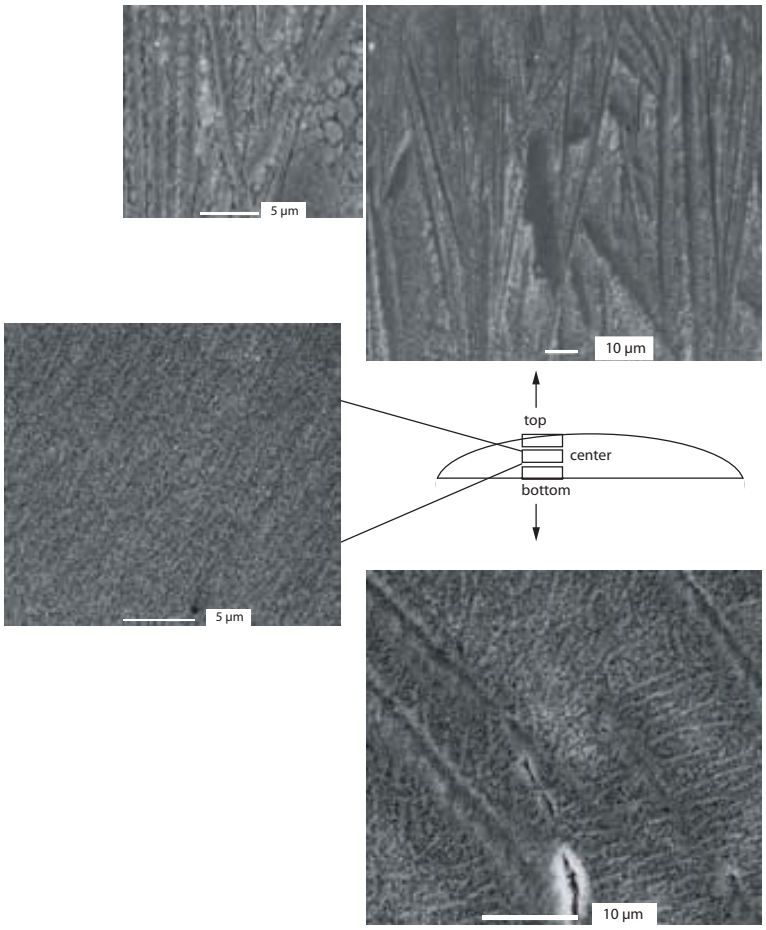

Fig. 5.3: Overview of the microstructures at top, center and bottom (see scheme) of the master alloy ingot for x=0, made by scanning electron microscopy.

the other alloys, the expected error is even larger due to the finer structure, in particular for the Cu-poor alloy. However, where possible to measure (mainly the lath structure and dendrites), the EDX results were more or less similar for the other alloys.

5.2.2.2 Rapidly cooled rods - X-ray diffraction

Figure 5.6 shows the X-ray diffraction spectra of $Zr_{55}Cu_{30}Al_{10}Ni_5$ in the as-cast (amorphous) state and after crystallization with varying heating rates. During the second peak at low heating rates, new peaks clearly arise (indicated by the * in Fig. 5.6). Upon fast annealing, only traces of this phase are present (marked

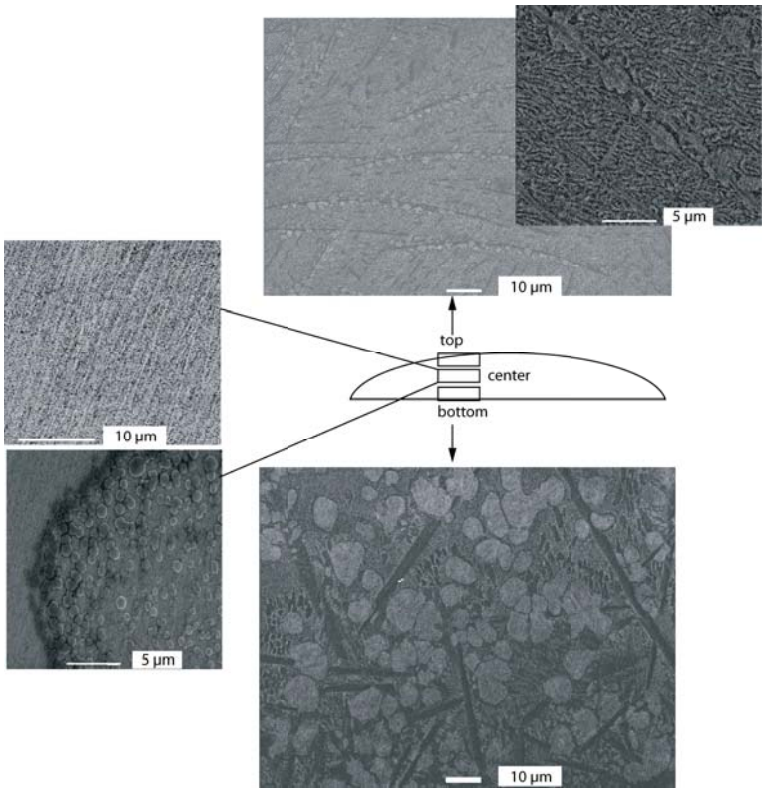

Fig. 5.4: Overview of the microstructures at top, center and bottom (see scheme) of the master alloy ingot for x=-2, made by scanning electron microscopy.

by the arrow). However, these traces are already present from the first annealing step (but remain unchanged during the second annealing), indicating that the nucleation occurred more easily than during annealing with a slow heating rate, but growth is more limited than in the first case.

Analysis of the respective diffraction spectra shows unambiguously that this phase can be attributed to $CuZr_2$. Thus, this phase, which is usually reported in literature data for this composition (see Table 5.3) and which is largely found in the master alloy, is only formed in a second step. Study of the spectrum taken after annealing to the first peak reveals a mixture of a big cube (probably $Ni_{42}Zr_{58}$) and $Cu_{10}Zr_7$. The fact that this Cu-rich phase $Cu_{10}Zr_7$ forms is quite surprising. In literature, it is never mentioned for this alloy, although on the other hand it is the Cu-rich phase to form, based on the binary Cu-Zr phase diagram in the current compositional range. The big cube formed is most likely $Ni_{42}Zr_{58}$ since it shows

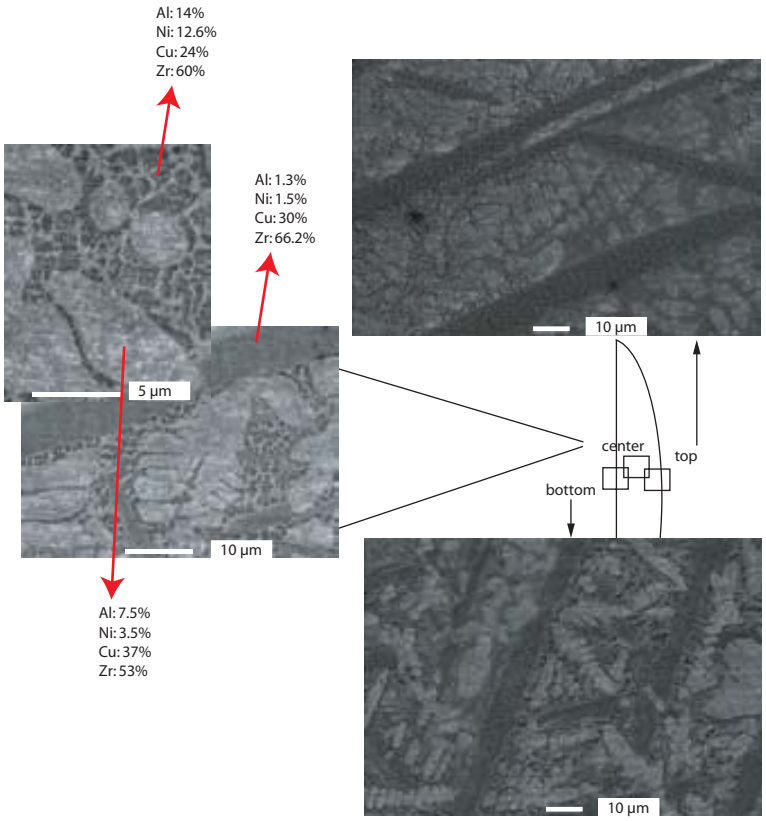

Fig. 5.5: Overview of the microstructures at top, center and bottom (see scheme) of the master alloy ingot for x=2, made by scanning electron microscopy.

resemblance with all measured peaks, although the intensity is not always similar. On the other hand, this agreement in peak position was not always fulfilled for all strong lines of the other big cube phase $NiZr_2$.

Besides $Ni_{11}Zr_9$ might be expected. Some peaks remain unidentified - a possibility could be Al_3Zr but this should be further investigated to confirm, since this phase would not be expected since its composition lies very far from the nominal composition of the overall alloy.

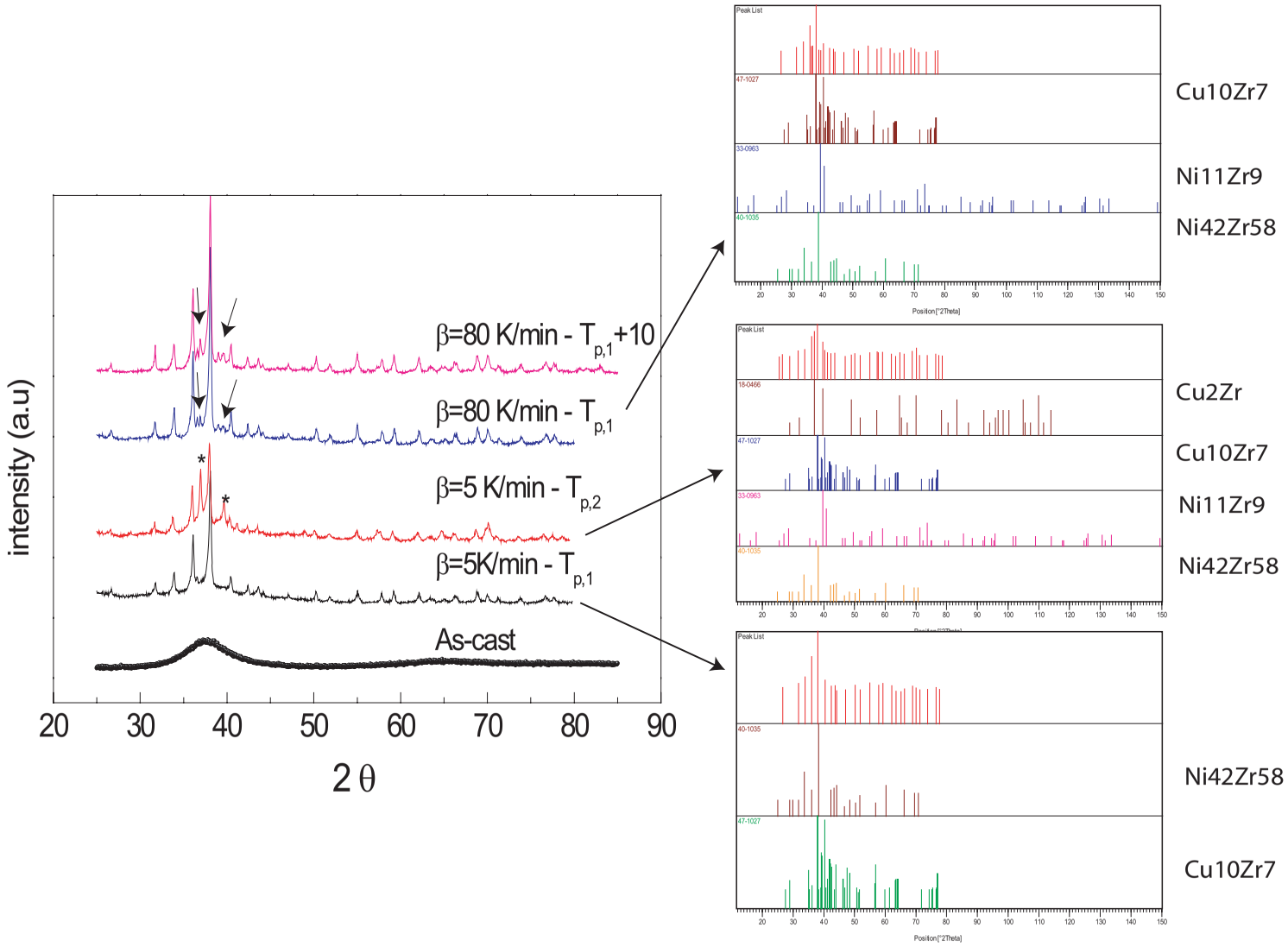

Fig. 5.6: XRD patterns of $Zr_{55}Cu_{30}Al_{10}Ni_5$ of the as-cast state and after the first crystallization and second crystallization step, occurring upon slow heating (5K/min). Upon fast heating (80K/min), only one peak was visible in the DSC scan, but two runs were made anyway, the first to T_p and the second to $T_p + 10$. No large difference is observed between these two runs upon fast heating. The different peaks are compared to the peak patterns of the respective matching candidates.

Figure 5.7 shows the XRD spectra of the alloys with slightly varied Cu/Ni ratios, in the as-cast state, annealed at a slow heating rate and their respective master alloys.

Note that, in general, the spectra upon annealing to crystallization temperature differ greatly from the spectra of the master alloys. This can be understood if we assume that these master alloys are already in a further state towards thermal equilibrium, despite the relatively high cooling rates that can be expected also in the preparation of ingots.

The XRD spectrum of slowly heated $Zr_{55}Cu_{28}Al_{10}Ni_7$ is much less complicated than for the more Cu-rich alloys, in agreement with the crystallization sequence observed by mt-DSC. Mainly big cube $NiZr_2$ and $CuZr_2$ are formed. Annealing to $T_p + 10$ shows an increase of peak that can be attributed to $CuZr_2$ (inset of Fig. 5.7 (top)), and thus reveals that also here, this phase is formed in a second step. The first phase that forms, is the big cube $NiZr_2$.

The Cu-rich alloy $Zr_{55}Cu_{32}Al_{10}Ni_3$ crystallizes most likely into $Ni_{42}Zr_{58}$, $Cu_{10}Zr_7$ and $Ni_{11}Zr_9$. Some Al_3Zr might also be formed. The splitting of one of the peaks (marked by the arrow in the inset Fig. 5.7) indicates the development of some $CuZr_2$, probably still under the form of small crystallites. Similarly, a small amount of Al_4Cu_9 can be expected, although their number and their size should be very small, based on the intensity and shape of the matching peaks (not shown).

5.2.2.3 Rapidly cooled rods - Transmission electron microscopy

The crystallization behavior of the Cu-poor alloy (x=-2) was rather different than for the other two alloys, as indicated by XRD. Not only the phases formed, but also the morphology of the crystals is different, as can be seen from Fig. 5.8. For the Cu-poor alloy, a rather star-shaped morphology can be found. Further, hardly any residual amorphous phase can be detected, whereas for the Cu-rich alloys, more spherical morphologies are detected, with clearly a crystallization in two steps: annealing to the first peak reveals a composite structure of an amorphous matrix with crystals of around 50 nm in size. The observed structure for the intermediate alloy was similar to the latter one.

Furthermore, in the Cu-poor alloy, mainly big cube $NiZr_2$ is formed in agreement with the XRD results. An example of this phase is shown in Fig. 5.9 with zone-axis [-1 1 2] (crystal at the bottom on the right). A second phase is present

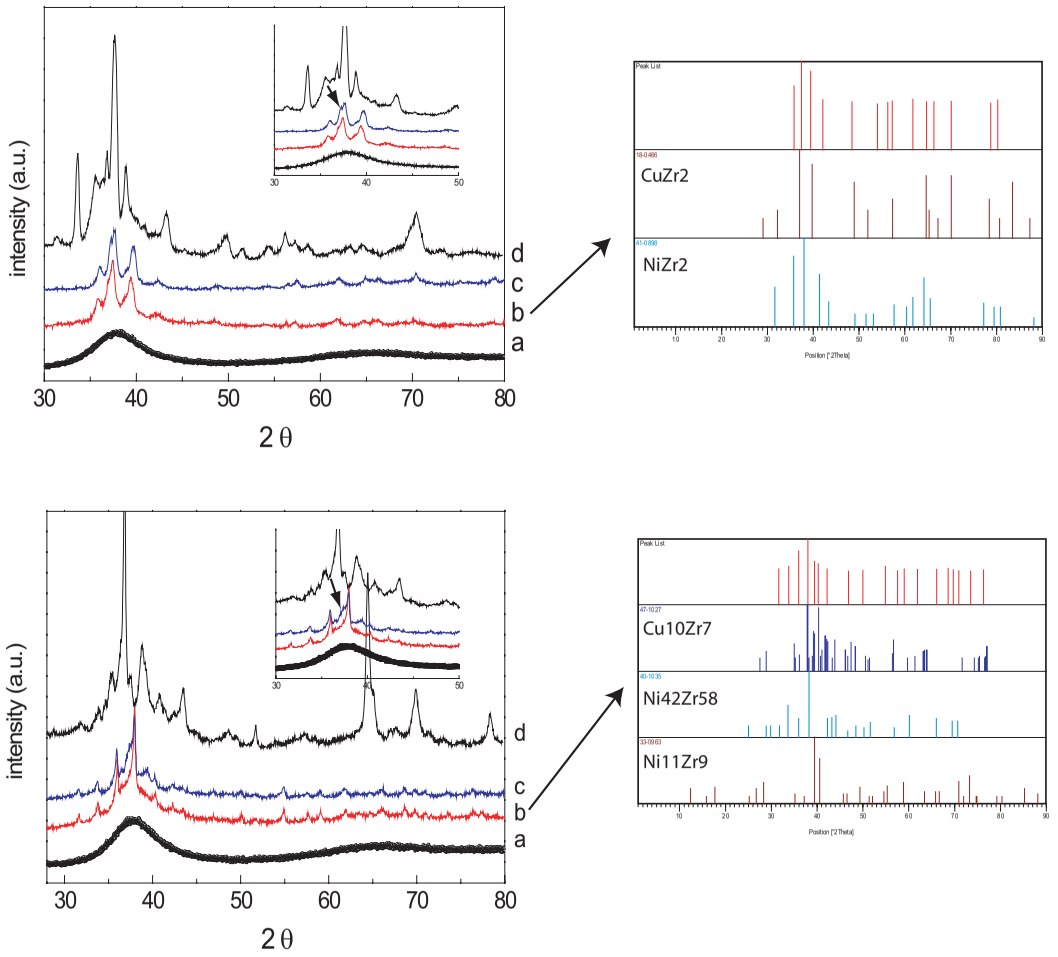

Fig. 5.7: (top) XRD patterns of $Zr_{55}Cu_{28}Al_{10}Ni_7$ of the as-cast state (a), upon slow heating (5K/min - T_p) (b), upon slow heating (5K/min - $T_p + 10$) (c), compared with the XRD pattern of the slowly cooled ingot (d). (bottom) XRD patterns of $Zr_{55}Cu_{32}Al_{10}Ni_3$ of the as-cast state (a), upon slow heating (5K/min - $T_{p,1}$) (b), upon slow heating (5K/min - $T_{p,2}$) (c), compared with the XRD pattern of the slowly cooled ingot (d).

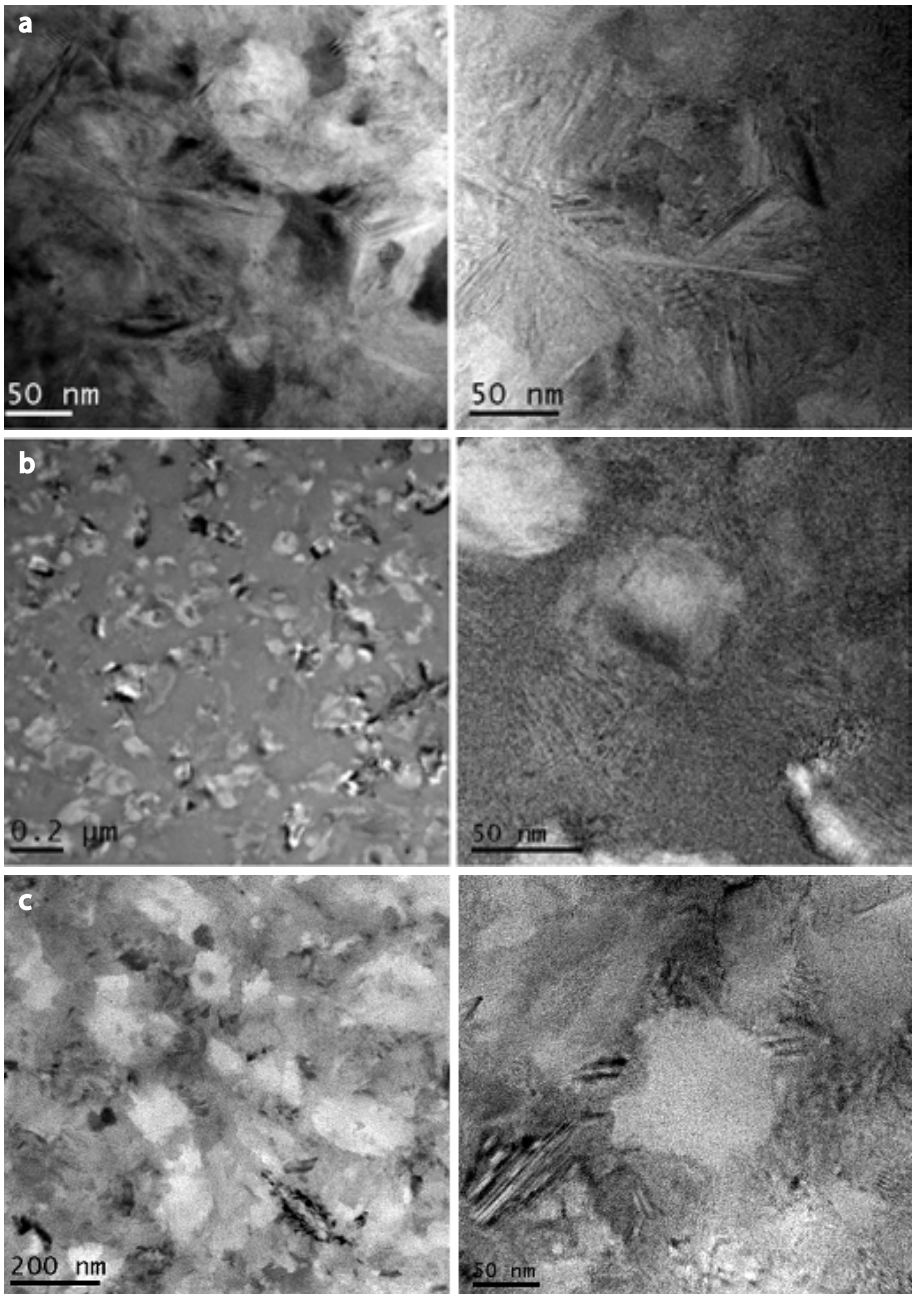

Fig. 5.8: Comparison of the crystal morphology formed for (a) x=-2 and (b) x=+2, annealed to the first crystallization peak and (c) x=+2 to the second crystallization peak, all upon slow heating.

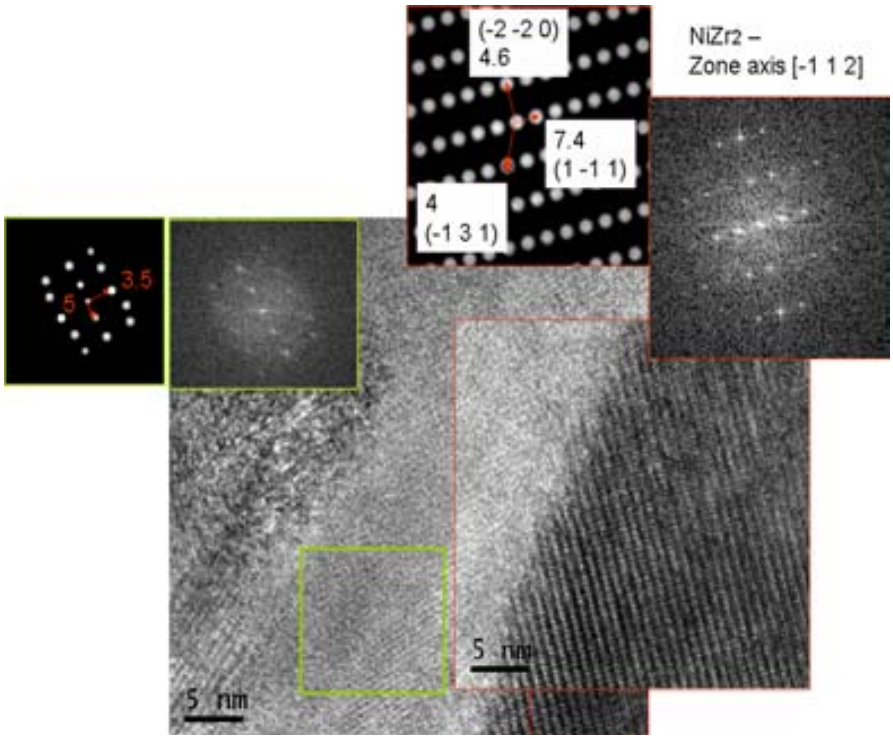

Fig. 5.9: High resolution TEM images and Fourier transformations of the selected areas of $Zr_{55}Cu_{28}Al_{10}Ni_7$ (x=-2), slowly annealed to crystallization. The large crystal in the bottom on the right can be analyzed as the big cube $NiZr_2$ with zone-axis [-1 1 2].

in a long fine shape of around 10 nm, which could be $CuZr_2$, along zone-axis [0 1 1]. However, the weak spots (lines - d=3.5 $\AA$ for example) are in fact forbidden reflections for this body-centered structure.

In the Cu-rich alloys (x=0 and x=2), the presence of $Cu_{10}Zr_7$ and $Ni_{11}Zr_9$ is confirmed by TEM imaging and diffraction.

Figure 5.10 gives an overview of the images captured of $Cu_{10}Zr_7$ and their respective Fourier transforms, observed under different zone-axes in both alloys and for varying heating rates. For faster heating rates, the observed crystals are distorted, i.e. $\alpha = 95°$ instead of $\alpha = 90°$ in Fig. 5.10 e. Note that the images in Fig. 5.10 b and c could be also from a primitive cubic phase, with zone-axis along [110]. However, the measured values would suggest a lattice parameter of 12.8 $\AA$ which is 0.7 $\AA$ larger than the lattice parameter of $Ni_{42}Zr_{58}$. The other big cube phase, $NiZr_2$, can be ruled out due to its face-centered symmetry and thus are the reflections (1 0 0) and (1 1 0) forbidden ones. $Cu_{10}Zr_7$ on the other hand has an

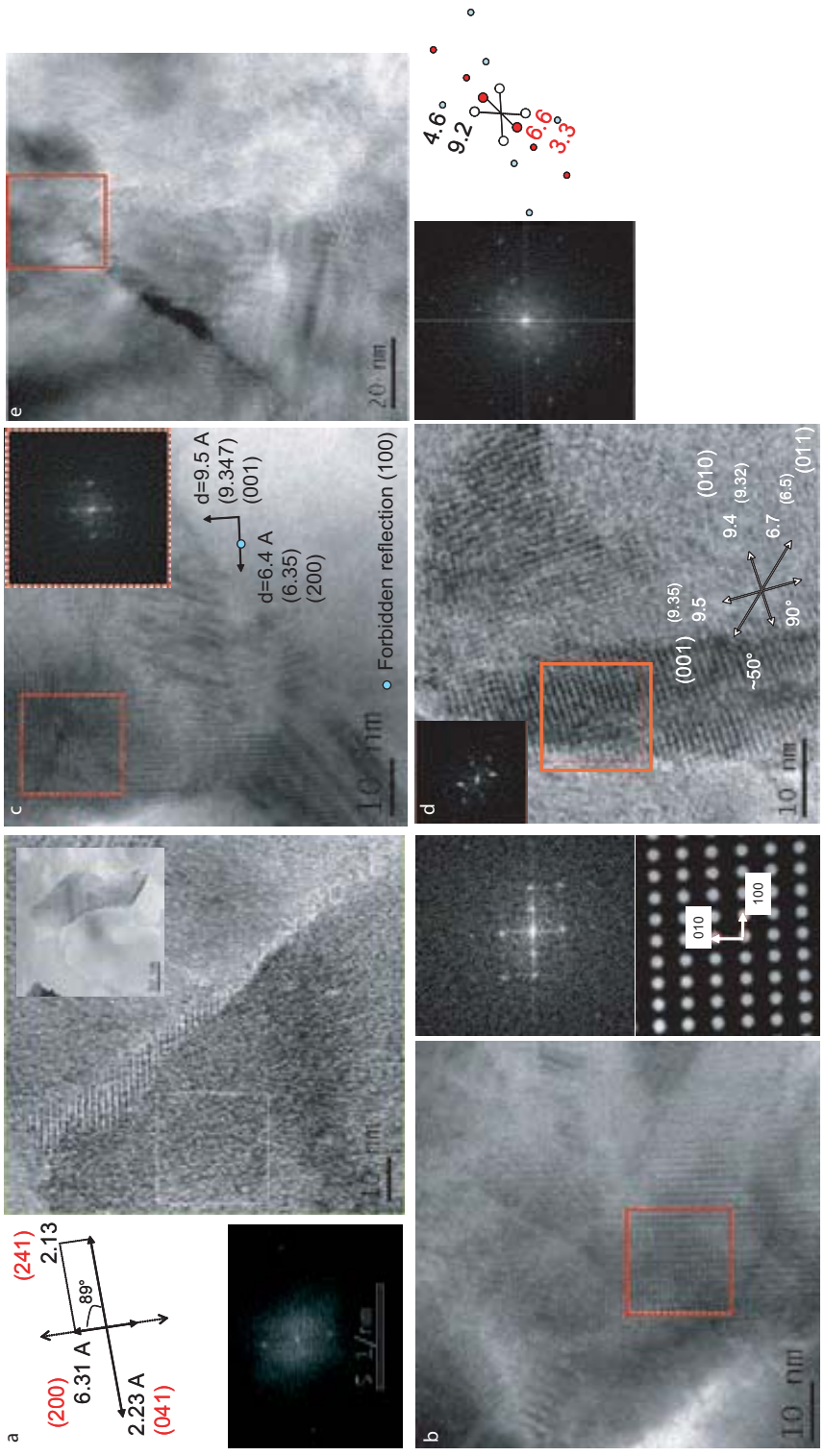

Fig. 5.10: Overview of the TEM images and the respective Fourier transformations of Cu(Al, Ni)$_{10}$Zr$_7$, observed in variously treated samples: (a)x=0, annealed at 5K/min to peak 1; zone-axis [01 – 4]; (b)x=0, annealed at 5K/min to peak 2; zone-axis [010]; (c)x=0, annealed at 5K/min to peak 2; zone-axis [001]; (d)x=+2, annealed at 5K/min; zone-axis [100]; (e) x=0, annealed at 80K/min; zone-axis [001]

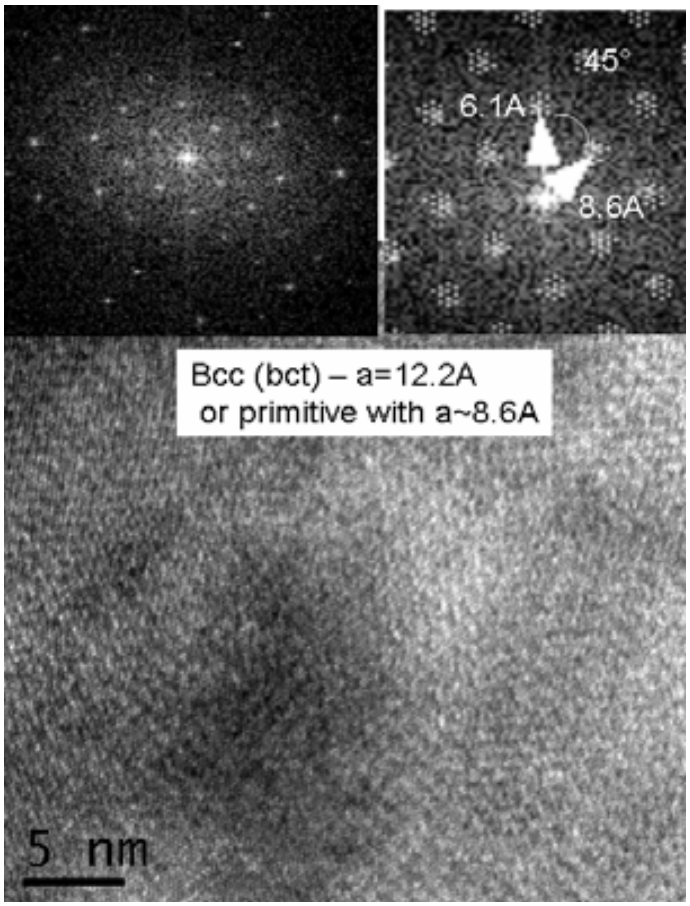

Fig. 5.11: Example of the electron diffraction pattern of a body-centered (cubic or tetragonal) structure with lattice parameter 12.2 $\AA$, similar to the one of $Ni_{42}Zr_{58}$.

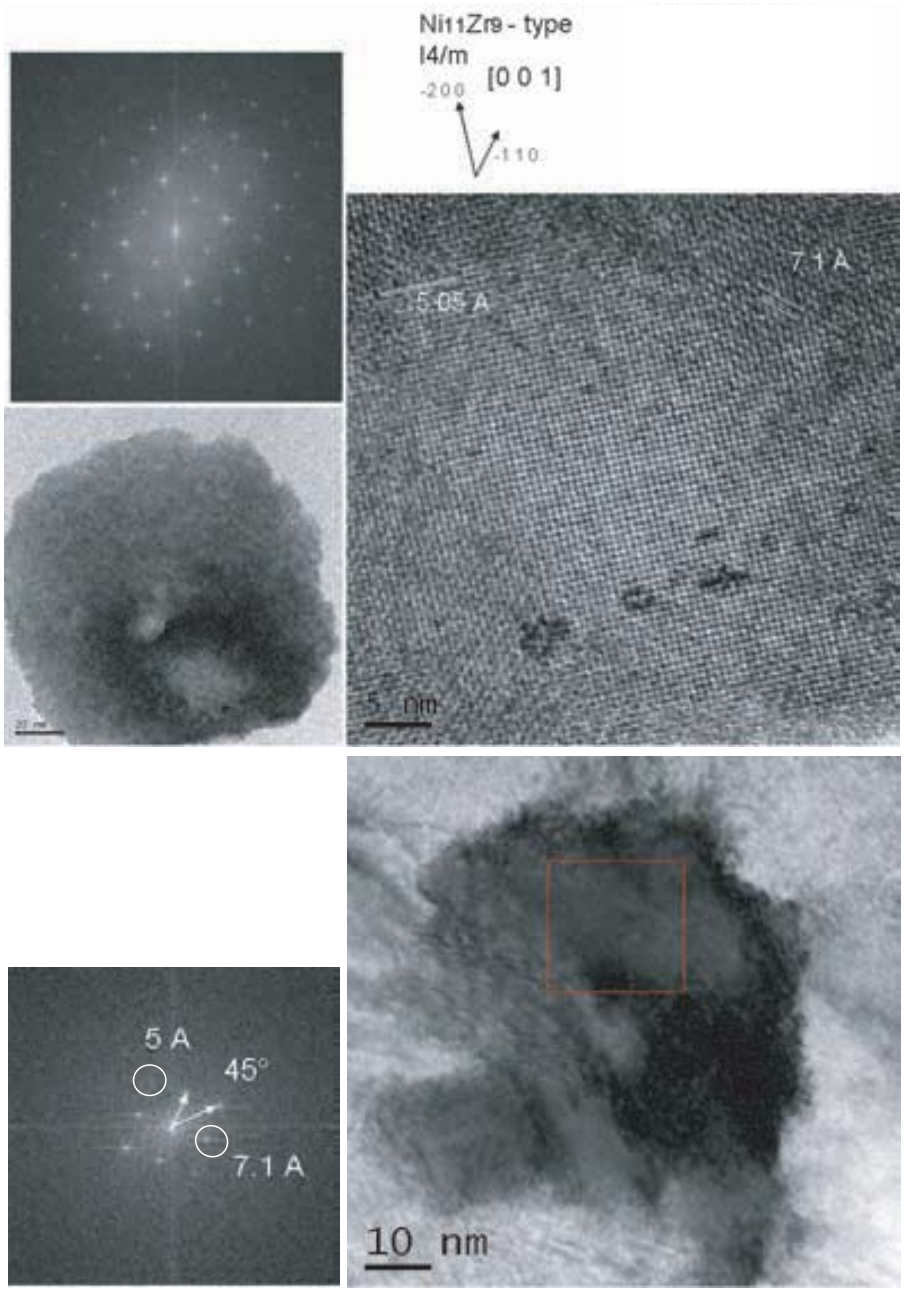

Fig. 5.12: (HR)TEM images of $Ni_{11}Zr_9$. (up)$Zr_{55}Cu_{30}Al_{10}Ni_5$ (x=0), annealed at 5K/min (under) $Zr_{55}Cu_{32}Al_{10}Ni_3$ (x=2) annealed at 5K/min.

end-centered lattice (centered in C) for which the reflections $h + k = 2n + 1$ are forbidden [115]. However, due to the lower degree of symmetry, double reflections can be expected, giving rise to the appearance of forbidden reflections [115]. Note

further that, for example in Fig. 5.10 a (inset), d and e, these Cu-rich phases have an enlarged irregular shape, and are formed *around* other big crystals. These crystals could be $Ni_{42}Zr_{58}$.

However, the analysis of the latter phase remains quite ambiguous. Several electron diffraction spectra with interplanar distances equal to the ones for this phase were found, but the spectra could only be attributed to a body-centered (cubic/tetragonal) space group (Fig. 5.11). Note that this rules out again $NiZr_2$ which is well-known as a face-centered cubic structure for which only the planes (hkl) that fulfill h, k, l, all odd or all even, will be visible in the electron diffraction pattern. The space group of $Ni_{42}Zr_{58}$ is not so well established, although some works suggest that it would be primitive [207].

Finally, some very large crystals were observed by TEM under different conditions, as shown in Fig. 5.12. This crystals are cubic (or tetragonal) in space group: either body-centered with a=10 $\mathring{A}$ or primitive with a=7 $\mathring{A}$. The former coincides with $Ni_{11}Zr_9$ (bct (I4/m) - a=9.88 $\mathring{A}$, c=6.61 $\mathring{A}$).

In addition, some very small crystals of around 20 nm were found after annealing to the second step (x=0). They could be analyzed as Cu_9Al_4 and are located in the border of large crystals (Fig. 5.13). Although the interplanar distances measured fit very well the theoretical ones, the angles measured are not perfectly 60° between (110) and (211) (zone-axis $[-111]$) or 45° between (100) and (111) in case the diffraction was made along zone-axis $[01-1]$. This means that the unit cell is not perfectly cubic, i.e. $\alpha, \beta, \gamma \neq 90°$. However, the lattice parameter is close to the theoretical one. Note further that this phase was also found in the Cu-rich master alloys, although its volume fraction and size had to be small, based on the relative intensity of the peaks.

On the other hand, Zr_2Cu was not found for these alloys. However, based on the results of SEM/EDX for the master alloys, this phase is expected to grow in "lath-shape". These laths are on one hand rather coarse but they are not finely dispersed in the sample. Therefore, it is likely that the area investigated by TEM lies in between these lath structures.

5.2.3 Discussion

When a double crystallization step for $Zr_{55}Cu_{30}Al_{10}Ni_5$ is reported in literature [25], [206], the first step consists of the formation of a so-called big cube phase.

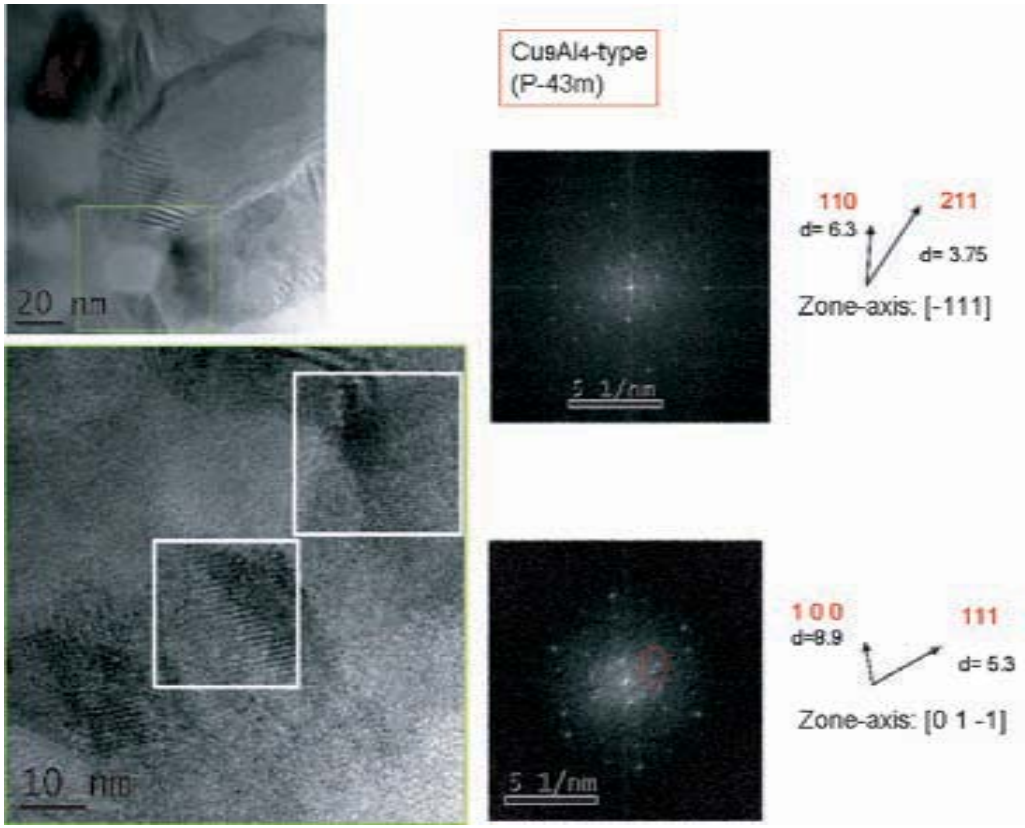

Fig. 5.13: High resolution image and its Fast Fourier Transform (electron diffraction pattern) of one type of crystals formed during annealing up to the second peak in the DSC scan. The crystal can be identified as (distorted) Cu_9Zr_{Al}.

As mentioned in the introductory notes of this section, two different big cube phases have been reported, the fcc structure $NiZr_2$, which is oxygen-stabilized and $Ni_{42}Zr_{58}$, which typically forms when the oxygen content is low and is expected to be cubic primitive [207]. In these phases, Ni is replaced to a certain extent by Cu [206] and probably also by Al [213]. Note that the latter phase has in fact a composition rather close to the overall composition, regarding the Zr/(Cu,Ni,Al) ratio. Although it is slightly enriched in Zr, it might indeed be expected to crystallize more easily from the complex amorphous alloy. XRD suggested indeed this phase, although it is certainly not the only phase that formed, based on the relative intensities. On the other hand, the TEM imaging suggests presence of a body-centered phase with lattice parameter similar to $Ni_{42}Zr_{58}$.

In fact, both analysis by Philips X'pert software of the XRD spectra and TEM point towards the formation of the orthorombic Cu-rich phase $Cu_{10}Zr_7$ during the first peak of the DSC scan of $Zr_{55}Cu_{30}Al_{10}Ni_5$ and $Zr_{55}Cu_{32}Al_{10}Ni_3$. This phase is also formed upon fast heating, but angular distortions are present.

The higher temperature peak in the DSC scan coincides with the formation of $CuZr_2$, as indicated by XRD. Although this second peak cannot easily be distinguished upon fast heating, some nuclei of this phase are still formed even when this higher heating rate is applied.

Oxygen contamination during annealing in the DSC is probably not of influence. During slow heating, the longest time for oxidation is available. This oxygen would lead to the formation of $NiZr_2$ rather than $Ni_{42}Zr_{58}$ and stabilize the former to the detriment of $CuZr_2$ [25]. This is not the case here: the largest amount of $CuZr_2$ is formed upon slow heating while exactly under these conditions, more time is available for oxygen contamination upon annealing than upon fast heating.

The results obtained here can be interpreted in the following way. Crystallization requires clearly chemical fluctuations and diffusion. These chemical fluctuations lead to the development of a more Cu-rich and a more Cu-poor part in the amorphous alloy. This is in agreement with the observations during in-situ heat treatments in the TEM, discussed in the previous chapter. These Cu-rich regions will lead to the formation of $(Cu, Al, Ni)_{10}Zr_7$ while the Cu-poor regions will crystallize into $(Ni, Cu, Al)_{42}Zr_{55}$ (slightly Cu-depleted) and $CuZr_2$. Formation of the latter phase requires not only rejection of Cu from the matrix, but

most likely also of Al as compared to the overall composition, can be expected. These rejected elements form on their turn Al_4Cu_9 (Fig.5.13).

In the same context, the formation of the Cu-rich clusters in the previous chapter can now be further interpreted. The formation of these clusters can be seen as the very first step towards crystallization similar to the crystallization scenario suggested by Wang and co-workers [186].

Atomic diffusion in BMGs proceeds via two parallel processes: single atom hopping and collective chain-like motions of groups of atoms. The former dominates below T_g whereas the latter dominates above T_g [218], [219]. Tracer diffusion studies in several BMG materials have consistently demonstrated that large atoms such as Zr and Al are slow. By contrast, atoms like Ni and Cu remain mobile even at temperatures below T_g [220], even though the viscosity increased by several orders of magnitude. Besides, experiments with Zr-Al-Cu-Ni diffusion couples combined with thermodynamic calculations [221] showed that Cu has no tendency to mix with Zr(Al, Ni) upon annealing (or has a tendency to separate from this Zr-rich matrix).

The homogeneous formation of Cu-rich clusters is due to the local exchange of atoms. This is a fast interface controlled process involving only neighboring atoms (short range diffusion of mobile atoms). On the longer term, the formation of these clusters also creates depleted zones, which might overlap in case of a high density of clusters. Finally, continued chemical fluctuations move the composition of these subcritical particles and/or depleted zones closer to that of the developing crystalline phases, which eventually triggers the amorphous-to-crystalline phase transformation [186]. In this case, the depleted zones form $CuZr_2$ (and $Ni_{42}Cu_{58}$, the Cu-rich clusters lead mainly to the generation of $Cu_{10}Zr_7$.

Note that in case of a lower amount of Cu (x=-2) coincides in fact with the second peak for the base alloy, and leads to the direct formation of $CuZr_2$, without formation of $Cu_{10}Zr_7$.

5.3 Mechanical and thermo-mechanical characterization

This final section sheds light on the influence of the Cu-content of the overall alloy on its mechanical behavior. Influence of annealing and heating rates has not been investigated yet. However, since both slow and fast heating show the development of the same crystallite structures, but different amounts and crystallite sizes can be expected, this interesting fact should be investigated into greater detail in future work, with special emphasis on the influence of this heating rate on the resulting mechanical properties.

5.3.1 Viscosity measurements

Viscosity is a key parameter to describe the kinetic slowdown when a melt is undercooled below its liquidus temperature. It can also be used to monitor the glass transition and crystallization of a metallic glass upon heating.

The increase of viscosity with undercooling reflects the increasingly longer time scale for structural rearrangements in the supercooled liquid state. If the viscosity reaches a value of 10^{12}Pa s upon undercooling, the intrinsic time scale for maintaining metastable equilibrium becomes comparable to the laboratory time scales for the cooling time. The liquid freezes to a glass.

On the other hand, when a metallic glass is heated, viscosity will decrease again near the glass transition because the mobility of the atoms increases. Once crystallization starts however, the atoms will be trapped in a crystalline net and from a critical volume fraction of crystals, the material cannot flow any longer, leading to a steep increase in viscosity again. This can be seen in Fig. 5.14, where viscosity measurements are represented together with DSC curves, both recorded at a heating rate of 10 K min^{-1}.

5.3.2 Compression tests

The mechanical properties of $Zr_{55}Cu_{30+x}Al_{10}Ni_{5+x}$ have been studied in the as-cast state by means of compression tests. Inhomogeneities, even on the atomic scale/change of medium range order, have been reported to have a significant influence on the plasticity [40], [41]. The Cu-clusters discussed in the previous chapter can be classified into this group.

Increasing the amount of Cu (x=2) is expected to give rise to a higher amount

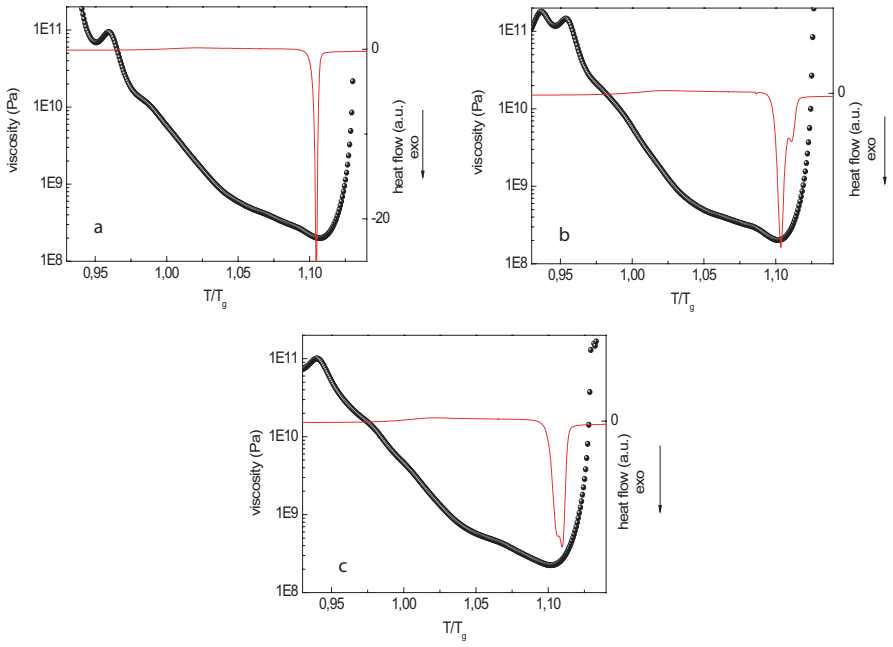

Fig. 5.14: Viscosity (symbol) and heat flow (continuous line), both measured at a heating rate of 10 K min^{-1}, in function of (the reduced) temperature (T/T$_g$), for the different compositions: (a)x=-2, (b) x=0 and (c) x=2.

of such clusters, even upon casting, what might be expected based on the shape of the crystallization peak.

However, very recently, questions are rising whether it is the presence of the inhomogeneities itself that is responsible for the improved plasticity or whether it could be due simply to the change in composition or short/medium-range order of the remaining glassy phase. Similarly, Liu et al. [64], reported that when the composition of a $Zr_{65}Cu_{15}Ni_{10}Al_{10}$ is adjusted in such a way to maximize the Poisson number, the resulting BMGs can sustain extremely high deformation (up to 170%) without fracture both in compression and in bending, without the presence of a second phase. In this context, the behavior of the alloy with reduced amount of Cu (x=-2) could give some more information on this aspect.

Fig. 5.15 shows the compressive engineering stress-strain curves for the three studied compositions. To facilitate comparison, the starting points of the curves are displaced. The average values (and standard deviations) for the Young's modulus, the yield strength (σ_Y), the strain at yield (ϵ_Y), the ultimate stress

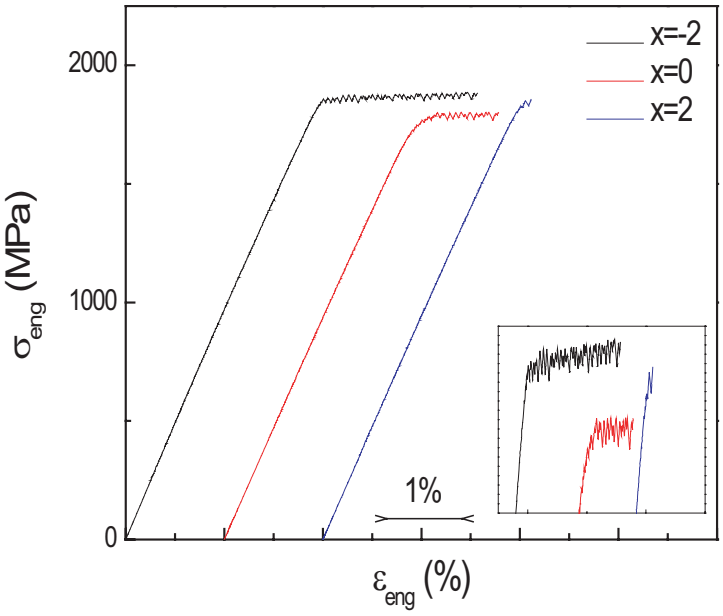

Fig. 5.15: Engineering stress-strain curves from uni-axial compression tests for $Zr_{55}Cu30 + xAl_{10}Ni_{5+x}$ in the as-cast state. Starting points of the curves are displaced for visibility.

σ_{US} and the total strain (ϵ_{tot}) are summarized in Table 5.5. All the compositions show a high yield strength (around 1850MPa) and similar modulus (around 98 GPa). The elastic strain is typically very high (around 2%) in comparison with conventional crystalline material, which have an elastic limit of 0.2%.

Tab. 5.5: Overview of the mechanical properties determined by uni-axial compression tests in function of the Cu/Ni-content.

	E (GPa)	σ_Y (MPa)	ϵ_Y (%)	σ_{US} (MPa)	ϵ_{tot} (%)
x=-2	98 ± 1	1851±10	2.1	1891±10	3.3±0.5
x=0	99±2	1816±23	2.1	1850±22	2.7±0.6
x=2	95±1	1850±10	2.1	1850±10	2.1±0.2

However, the plasticity is generally quite low: the alloy with x=2 does not show plasticity and breaks almost immediately after yielding. A lower amount of Cu on the other hand does lead to a reasonable increase of plasticity.

As discussed in section 1.4.5, Lewandowski and Greer established that metallic glasses show a brittle behavior in toughness for certain ratios of shear to bulk

Tab. 5.6: Summary of scaled ratios of shear and bulk modulus, calculated according to Eqs. (5.1), for the various compositions.

alloy	$0.78\frac{\mu_c}{K_c}$
x=-2	0.298
x=0	0.296
x=+2	0.295

modulus, i.e. $\mu/K > 0.41 - 0.43$, or equivalently expressed by the Poisson's modulus $\nu < 0.31 - 0.32$ [62]. Based on this correlation, Yang and Greer presented a formula to predict plasticity of metallic glasses, based on the weighted average of the constituent elements [222]. Each modulus is calculated according to two models, a uniform strain and a uniform stress model, and the final value is the average of the two values resulting from these two models. The two formulas to calculate the weighted average of each model are:

$$\begin{aligned} \overline{X_c} &= \sum_i \frac{X_i c_i V_i}{\overline{V_m}} \\ \overline{X_c} &= \sum_i \left(\frac{c_i V_i}{X_i \overline{V_m}}\right)^{-1}, \end{aligned} \tag{5.1}$$

for the uniform strain and stress model respectively. X_i, c_i and V_i are the modulus (μ or K), the atomic fraction and the volume fraction of the i-th constituent element respectively. $\overline{V_m}$ and $\overline{X_c}$ are the measured average atomic volume and the calculated modulus of the metallic glass.

In this way, the ratio of shear and bulk modulus can be calculated, which should however be scaled with a factor 0.78 [222].

On the basis of this calculation, the scaled ratio for the three alloys was calculated (Table 5.6) to predict the plasticity level expected and to compare it with the compression test results.

The calculated elastic properties cannot explain the observed trend in plasticity, since the highest plasticity level observed agrees with the highest value for the scaled ratio of shear and bulk modulus.

This indicates that calculation only of elastic properties does not predict the behavior of metallic glasses in all cases. A similar discrepancy between calculated and measured properties was also reported for Fe-based amorphous alloys [223]. This discrepancy was attributed to the influence of interatomic interactions. This

is in fact in agreement also with the observations in the current work for one single composition in the as-cast and annealed condition, where the appearance of like bondings was thought to be the reason for the observed increase in Poisson's ratio.

These results imply that the Cu-poor matrix (with a decreased amount of Cu-Zr unlike bonds) is the pre-dominant factor, responsible for the observed plasticity and multiplication of shear bands. The Cu-rich clusters can be seen as a second factor, mainly limiting propagation by increasing viscosity in the propagating shear band [66], which could explain the different behavior upon thermomechanical testing (viscosity measurements) for the two Cu-rich alloys compared to the Cu-poor one, discussed above. However, acoustic measurements are required to measure accurately the elastic properties of the various alloys. In this way, influences from the structure of the glass can be taken further into account. Advanced TEM techniques might help to visualize changes on the medium range order [129], as explained in section 2.3.3.5 and illustrated in the next chapter, and could help to confirm the suggestions made here about the differences that can be expected between the different alloys.

6. CHARACTERIZATION OF $ZR_{55}CU_{30}AL_{10}NI_5$ AFTER SEVERE DEFORMATION

This chapter deals, in a preliminary way, with the influence of heavy deformation, induced by high pressure torsion, on the thermal stability and (micro)structure of a metallic glass. A correlation between microstructural changes and (local) mechanical properties will be made.

6.1 Introduction

Severe plastic deformation techniques (SPD) are used mainly to refine the microstructure of crystalline materials, yielding a significant increase in hardness in accordance with the well-known Hall-Petch correlation [52]. One of the most frequently used SPD techniques for producing bulk nanocrystalline samples is high-pressure torsion. For example, experiments on pure Ni resulted in an increase of the hardness from 1.4 to > 3 GPa while the grain size was reduced from 100 μm to 170 nm [102]. In particular, the HPT method results in porosity and impurity-free specimens.

The use of SPD and HPT in the processing of metallic glass is rather limited. So far, it has been mainly applied as a compacting method for amorphous ribbons, in order to obtain a homogeneous bulk (nanocrystalline) material [224], possibly with improved properties compared to the initial ribbons [225]. Very recently, a study was performed in order to produce an impurity-free bulk metallic glass from a (crystalline) ingot, avoiding the size-limiting cooling techniques [226]. Work from the same group showed that when applying HPT directly to a (Zr-based) bulk metallic glass the glass remains in its amorphous state, but a large structural anisotropy was introduced [227].

The effect of (severe) deformation in general on the microstructure and properties of bulk metallic glasses is in fact still under discussion. Deformation by rolling, bending, nanoindentation, compression,... has been reported several times before,

but with different effects on the (micro)structure and different explanations.

On the one hand, deformation leads to dilatation, often referred to as excess free volume, which has been characterized by different experimental techniques, like DSC, density measurements, synchrotron radiation and positron annihilation [45], [46], [47], [48], [49], [108]. Besides dilatation, nanovoids are often observed inside shear bands which are correlated to the excess free volume that coalescence into these more stable voids [199], [224], [228], [163].

Upon extensive inhomogeneous deformation, density decreases typically on the order of 0.1-0.2%. These density changes are large compared with those experienced by crystalline alloys, which usually show only around 0.01% dilatation due to plastic deformation, but small in comparison to polymers. Based on the number of shear bands and the fact that dilatation is restricted to these shear bands, this leads easily to the conclusion that the dilatation inside the shear bands themselves must be quite large ($> 10\%$) [54]. Nonetheless, this dilatation can cause a *softening* effect [152], [229]. Note that the observed size effect upon nanoindentation in metallic glasses in chapter 3 was attributed to excess free volume creation and its concomitant softening.

On the other hand, microstructural changes as nanocrystallization [78], [90], [230], [228], [231], [232], phase separation [79] and phase transitions [75] have been reported upon deformation. The works cited above all deal with room temperature deformation. Similar changes have been reported at deformation at high temperatures [178], [233] and even at cryogenic temperatures [234]. In certain cases, these "in-situ" microstructural changes like nanocrystallization occurring upon deformation [78] or phase separation [79] were thought to be the reason for the observed improved mechanical behavior.

Furthermore, deformation techniques and HPT in particular introduce a(n) (inhomogeneous) stress state. These residual stresses have their influence as well on the mechanical response of metallic glasses [88].

The observed nanocrystallization in particular has been topic of investigation and discussion during the last years. Several explanations have been considered to it, such as temperature rise due to localized heating at shear bands, enhanced diffusion induced by the higher amount of defects (dilatation), presence and growth of nanocrystalline nuclei during deformation.

Although it is well known that *temperature* can rise significantly within shear

bands [59], elevated temperatures alone are probably not a sufficient explanation, because the driving force for nucleation decreases with increasing temperature [235]. So, if there are no pre-existing nuclei to grow, it is not clear that the rapid heating and cooling inside a shear band allow sufficient time for nucleation and thus crystallization. Furthermore, the *strain state* itself appears to be important as well (compression versus tension), whereas the temperature rise is expected to be independent of this strain state [230]. Lee and co-workers correlated it to a decreased energy barrier for crystallization by the stresses applied during deformation (uniaxial compression). These stress states can not only reduce the energy barrier for overall crystallization but can also lower the energy barrier for diffusion. Therefore, uniaxial compression can enhance the nucleation rate, which promotes crystallization [90]. Another possibility is that shearing affects not only the kinetics but also the thermodynamics of glass-forming alloys. Short-range chemical ordering might be altered by the non-equilibrium conditions associated with strong shear flow. Since a large portion of the activation barrier for homogeneous nucleation in glass-forming liquids comes from the need to establish compositional fluctuations, chemical ordering may significantly lower the activation barrier for crystallization [54].

In this work, we took advantage of the constraint geometry of high pressure torsion, which offers the possibility to apply a large amount of deformation, without failure, even in brittle materials. This allows a more systematical and controlled study of the effect of deformation on microstructural changes, which were investigated by DSC, XRD and (HR)TEM, with special attention to chemical fluctuations . The mechanical response after strong deformation was investigated by nanoindentation, described at the end of this chapter.

6.2 Thermal characterization: DSC

Thermal analysis shows the general preservation of the amorphous nature upon deformation for both treatments (Fig. 6.1). For all samples, a clear glass transition occurs at 701 ± 1 K, for a heating rate of 0.667 K/s, similar to the temperature observed for the untreated as-cast samples (702 ± 3 K). At this heating rate, crystallization occurs at 779 ± 3 K for the deformed samples, where undeformed it was slightly higher in average (781 K). A slight decrease of $\leq 4\%$ in crystallization enthalpy (49 ± 1 J/g) is observed as compared to the as-cast sample.

Although changes in crystallization enthalpy seem negligible, a clear change in the shape of the crystallization peak is observed, similar to the one observed after heat treatments.

Deformation by HPT can typically be inhomogeneous, with a larger amount of deformation occurring at the edge than in the center, especially when a low amount of revolutions is applied [102]. Negligible differences are observed between center and edge of each sample. An increase from two to five whole revolutions does not alter the thermal behavior either.

Both dilatation and residual stresses give rise to relaxation at low temperature, which was expected to increase the exothermic signal before the glass transition to a supercooled liquid occur. However, the relaxation exotherm only increases slightly or remains more or less unchanged, as compared to the as-cast, undeformed state. However, it has been reported several times that free volume increases significantly at the onset of deformation but at a certain moment, the excess free volume saturates (equilibrium between creation and annihilation) [79] or even seems to decrease, due to the formation of more stable nanovoids [48], [49]. This could explain why in fact in the sample with the lower amount of deformation we see indeed an increase in the relaxation exotherm, while at higher amounts of deformation, the saturation level was reached and nanovoids might have formed.

Anyway, the interesting point is that it seems possible to introduce similar changes by deformation as by low-temperature annealing, as indicated by the shape of the DSC scan, without the competing adverse effect of topological relaxation, which leads to embrittlement.

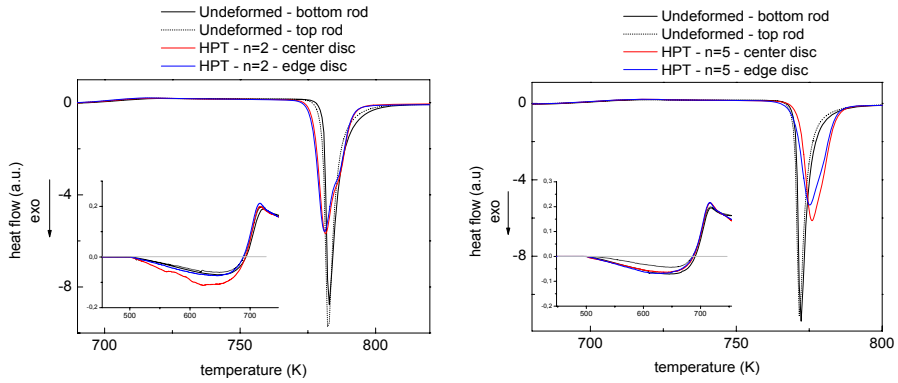

Fig. 6.1: Comparison of the DSC spectra before and after deformation after (a) 2 and (b) 5 whole revolutions, showing a broadening of the crystallization peak upon deformation. Edge and center region of the deformed sample are compared, while comparison of top and bottom region of the undeformed sample reveals good initial homogeneity. The insets show the glass transition region.

6.3 Microstructural characterization

6.3.1 X-ray diffraction

Investigation by conventional XRD shows the 'Bragg amorphous' nature of the samples: two broad diffuse halos are observed, without any sharp diffraction peaks typical for the presence of crystalline phases (Fig. 6.2).

The main halos were fit to a pseudo-Voight function, as described by Eq. (2.18) in section 2.3.2.1. The fit parameters and the calculated microstrains are given in Table 6.1. These results show that the strains accumulated inside the material increase slightly after deformation, as expected.

Tab. 6.1: Parameters obtained by fitting the regular XRD spectra of the respective samples to a pseudo-Voight function (Eq. (2.18)). Γ_{fG} represents the width from the Gaussian part, Γ_{fL} indicates the width from the Lorentzian part, $\langle e \rangle$ is the maximum microstrain, calculated from Γ_{fG}.

	Γ_{fG}	Γ_{fL}	$\langle e \rangle$
Undeformed	5.4	6.1	0.030
HPT - n=2	6.1	6.1	0.035
HPT - n=5	6.6	6.1	0.038

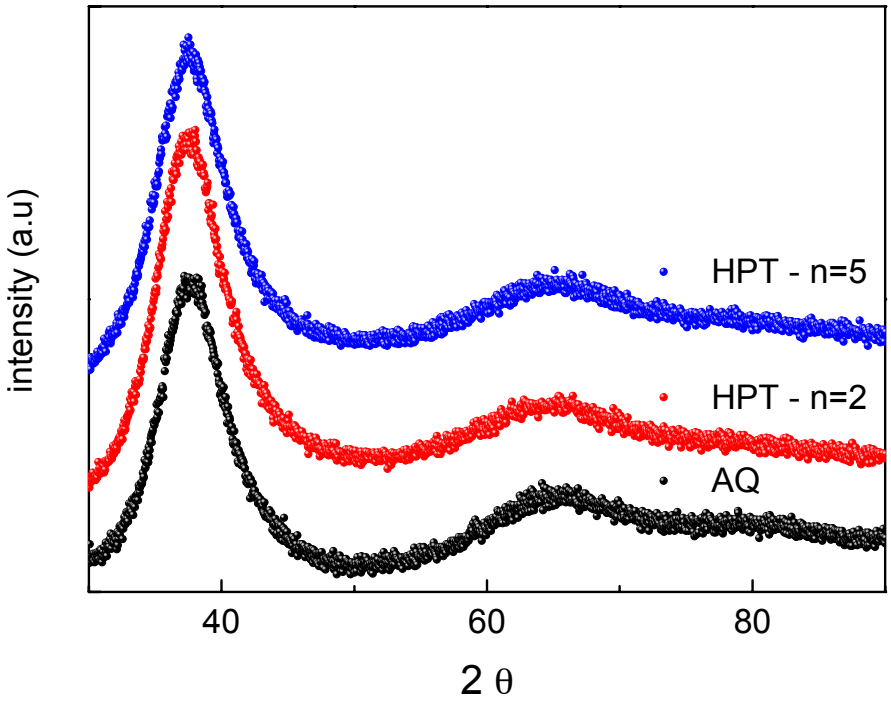

Fig. 6.2: X-ray diffraction pattern of the deformed sample compared to the untreated as-cast sample. The Bragg-amorphous nature is retained after deformation.

6.3.2 Transmission electron microscopy

6.3.2.1 Conventional TEM

Although the DSC scans look very similar for the deformed samples as compared to the samples after heat treatments investigated in the previous chapters, the TEM does not show immediately any observable changes. However, it should be mentioned that it was not possible to investigate these deformed samples in the same microscope as in which the images of Fig. 4.3 were made due to problems with the camera at that time, and that microscope showed a higher contrast due to the different settings of the lenses and camera.

At a first glance, the overall image, shown in Fig. 6.3, appears homogeneous and amorphous. However, looking into further detail shows the presence of some variations within the microstructure. First of all, there seem to be zones with different "orientation" (Fig. 6.3 b), repetitively found throughout the whole sample. This could be caused by thickness variations, but note that they are on the

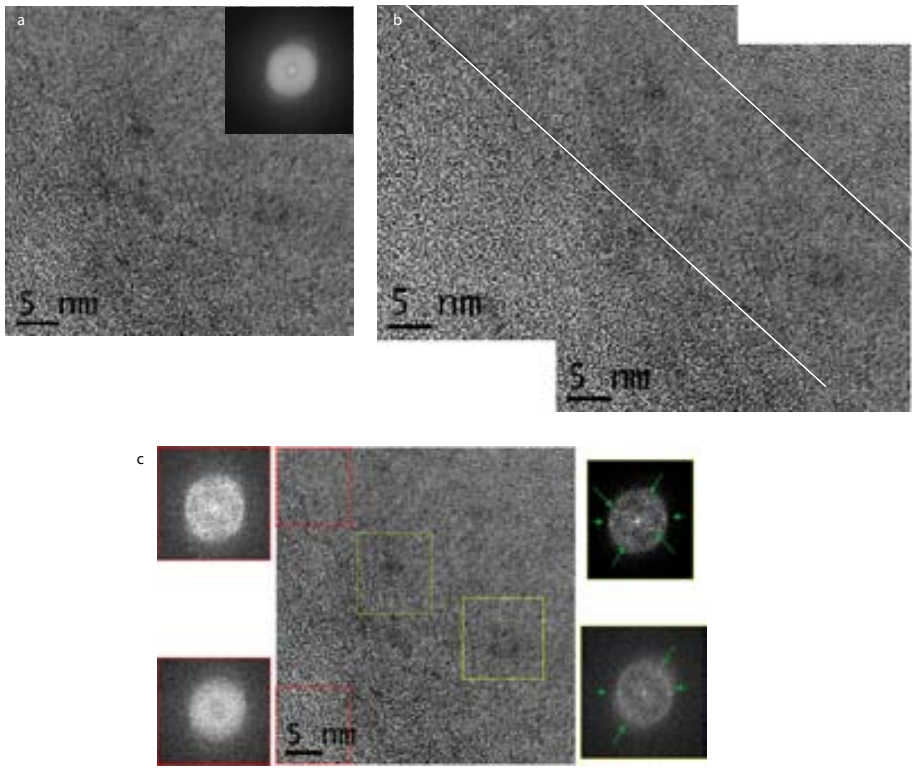

Fig. 6.3: TEM images of the sample deformed by HPT - two whole revolutions. General image and its Fourier transform (a) appear amorphous and rather homogeneous. However, variations in the structure of around 15-20nm can be observed (b) and local Fourier transforms show presence of more ordered structures (marked by arrows) (c).

order of 15-20 nm which is unlikely to be caused by sample preparation. Most likely they are caused by the deformation treatment and related to shear band formation upon deformation. Typical shear band thickness is on the order of 20 to 30 nm [84]. Furthermore, spots in the Fourier transform of local areas inside such a zone show presence of ordered clusters or nuclei (Fig. 6.3). The images here are shown for the sample with 2 turns, but the sample with 5 turns gave similar images.

6.3.2.2 C_s-corrected HRTEM

In a second step, the sample was investigated in a high resolution TEM, equipped with a corrector for astigmatism. This increases resolution significantly [123], and is even capable of revealing medium range order of metallic glasses [129].

Analysis of the deformed sample reveals presence of two main types of clusters/nanocrystals: both are face-centered cubic, but with different lattice parameters (Fig. 6.4). The first type has a lattice parameter of 3.6 $\mathring{A}$ and are most likely (pure) Cu-clusters. This might indicate that the observed changes are similar to the structures induced by low temperature annealing.

The second type of cluster has a lattice parameter of 5-5.2 $\mathring{A}$. This could be ZrO_2 (Fm3m - a=5.07 $\mathring{A}$), but by EELS, no increase in the oxygen signal could be detected as compared to the matrix. Another possibility could be that these clusters are the building blocks of the medium range order of the amorphous material in general [236]. 2.9 $\mathring{A}$ is on one hand the closest packed direction in these fcc-clusters and is also the distance where the main halo appears in the electron diffraction pattern of the amorphous material. The latter clusters have also been detected by the same technique in the undeformed material (Fig. 6.5).

6.4 Mechanical characterization - Nanoindentation

6.4.1 Introduction

1. Indentations in function of radius

   In crystalline materials deformed/processed by HPT can show quite inhomogeneous microstructures and a gradient in mechanical properties in function of the position along the radius, with the finest microstructure, and the highest hardness, observed at the edge.

   Although initially a highly inhomogeneous stress state is provoked (see section 2.2.2.1), it was shown recently that HPT may be used effectively to develop an essentially *homogeneous* microstructure throughout crystalline samples, provided the applied pressure and the torsional strain (as measured in terms of number of rotations) are sufficiently high. Deformation starts initially in regions where the shear strain is the highest, i.e. close to the edge. However, at the same time, this shear leads to work hardening and consequently to a transfer of shear to adjacent zones, until the central region deforms the same amount. For pure Ni, a homogeneous microstructure of equiaxed grains may be achieved if the applied pressure is at or above 6 GPa and the sample is subjected to at least 5 whole revolutions.

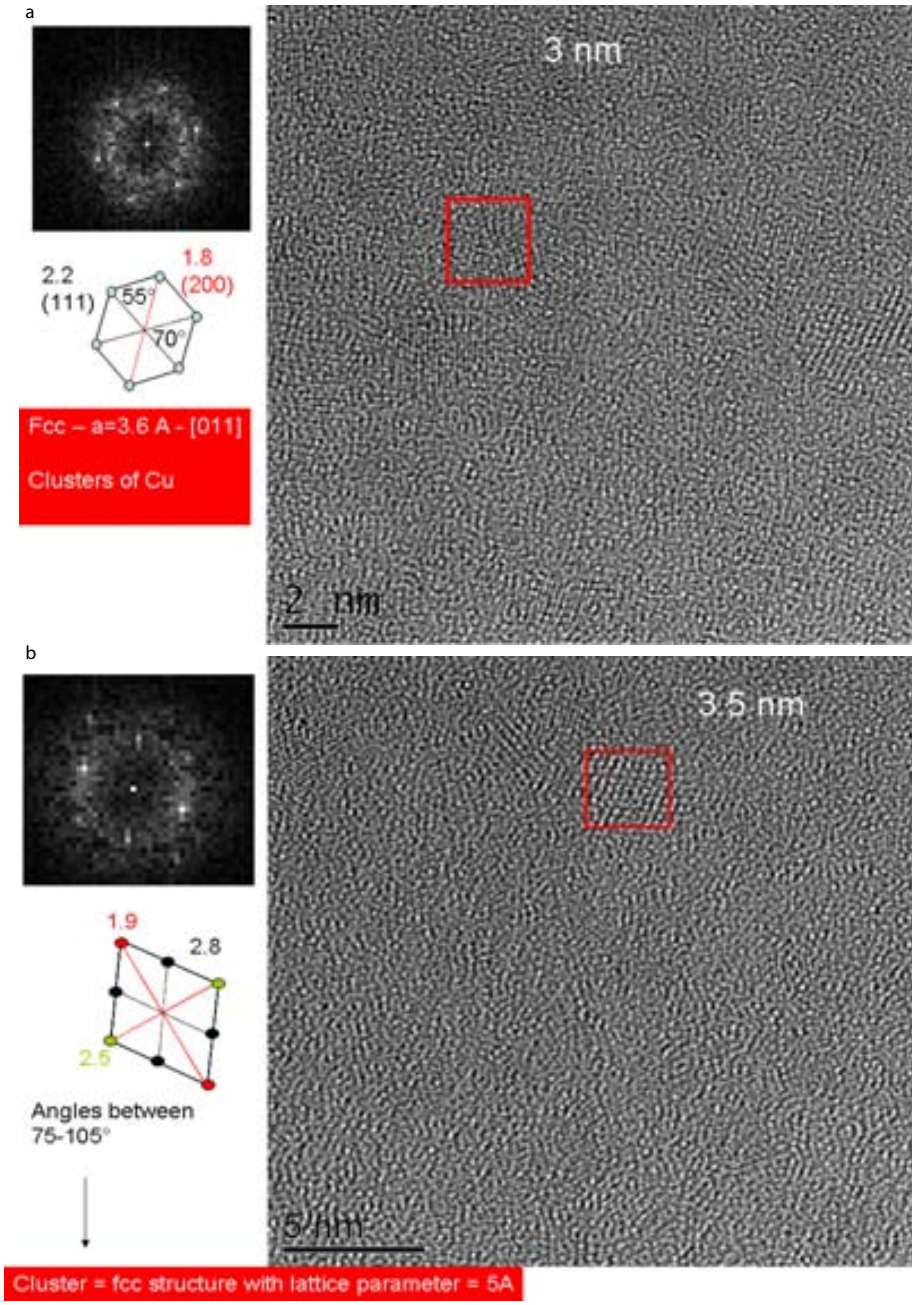

Fig. 6.4: Analysis of clusters/nanocrystals in the deformed sample (2 turns) by high resolution TEM with C_s corrector. Two main types of clusters have been analyzed:(a) pure Cu-clusters and (b) an fcc-type with lattice parameter around 5-5.2 $\AA$.

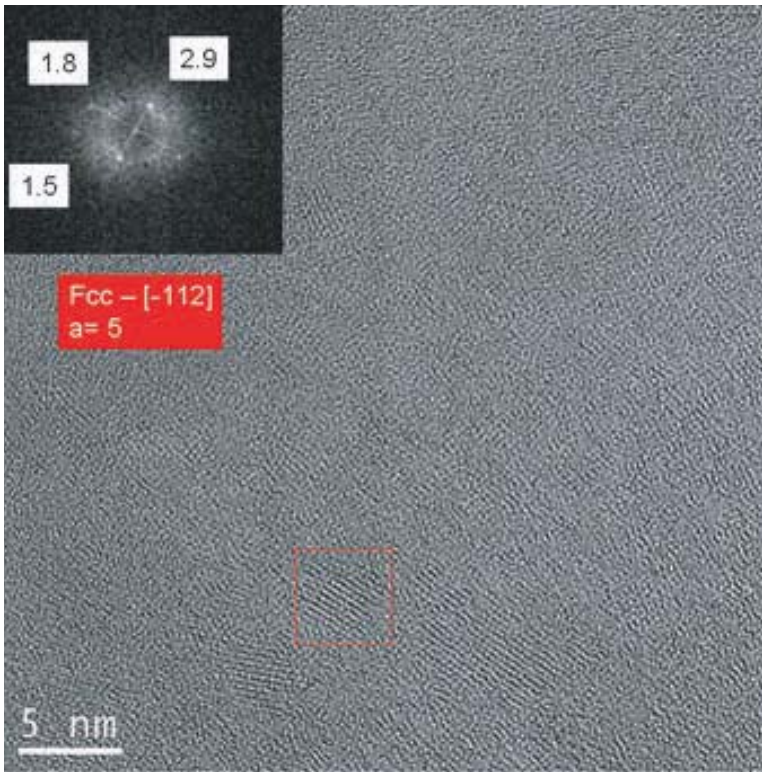

Fig. 6.5: Analysis of clusters/nanocrystals in the undeformed sample. The same fcc-type cluster with lattice parameter around 5-5.2 $\AA$ has been detected several times.

To study the effect of a possible inhomogeneous stress distribution along the radius of the rod, indentations were made along the diameter. Three indentations were made for each position; at the edge where the surface was rougher, this number was increased up to 5 to reduce statistical error.

2. Indentations in the cross section

   Finite element modeling predicts that a different stress distribution can be expected during HPT processing, not only along the radius, but also as a function of thickness. The central inner part is in a compressive state of stress, with pressure decreasing with the radius, while the outer part is even under tensile stress. Stress and strain fields caused by e.g. indentation will interact strongly with pre-existing fields, which in turn affects hardness and stiffness values measured. Compressive stresses lead to an increase in the observed hardness, while tensile stresses decrease it [88], [237].

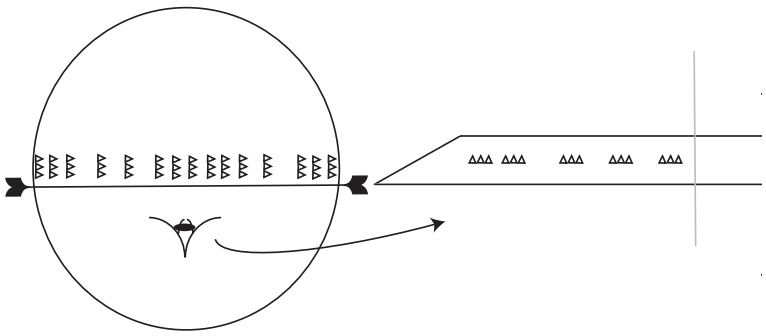

Fig. 6.6: Schematic representation of the indents made in the surface (left) of the discs, formed by HPT, and in the cross section (right).

Finally, synchrotron measurements showed that a different interatomic spacings (anisotropy) can be expected, when comparing surface and cross section measurements [227]. To investigate the influence of this anisotropy and different stress states, indentations were also performed in the cross section of the sample.

6.4.2 Experimental conditions nanoindentation

To be able to compare with the untreated as-cast sample and heat-treated samples, indentations were made with a maximum force of 250 mN, with a loading time of 40 sec, holding time 30 seconds and unloading 40/3, equal to the conditions applied for the nanoindentation studies discussed in chapter 3.

Figure 6.6 gives an overview of the indentations made in the surface and the cross section of the discs.

6.4.3 Results and discussion

Figure 6.7 and 6.8 show the results for the modulus and hardness, calculated by the method of Oliver and Pharr, as a function of the position along the radius of the disc. A moderate softening occurred upon deformation, as compared to the undeformed sample, in accordance with the expected increase in free volume. A similar decrease is observed in Young's modulus, which could be dedicated on one hand to an increase in free volume and concomitantly an increase in interatomic spacing. However, the altered medium range order, with formation of Cu-clusters, and thus a decrease in un-like bonds might be a second effect to cause this observed

decrease.

In agreement with the thermal behavior, no large differences are seen between edge and center of each sample, especially in the sample deformed by only two revolutions. This is interesting since it might indicate that the deformation in the whole disc was more or less homogeneous, even at low deformation, which is necessary to be able to apply HPT as a method to produce bulky samples. Although anisotropy in atomic bonds was reported for surface versus cross section measurements [227], its influence on the mechanical properties seems to remain minimal after two revolutions, i.e. no difference between surface and cross section indentations is observed.

A higher number of revolutions might lead to a more inhomogeneous deformation, in contrast as what is observed for crystalline materials - although the observed change in properties is still moderate. Note that the observed increase in inhomogeneous deformation coincides with the increased anisotropic structure observed by synchrotron radiation diffraction [227].

Figure 6.9 compares the SEM images of the indentations in the undeformed sample and the sample deformed by HPT by 2 whole turns. The indentation shown was made in the cross section. The other indents were similar, in agreement with the similarity in properties measured but are not shown here. The main difference is that the deformed sample shows hardly no pile up, which contain shear bands.

A corresponding decrease in pop-ins/serrations is also observed in the load-displacement curve after deformation. Note that the number of serrations was already rather low in the as-cast sample, as discussed in chapter 4. Figure 6.10 shows the load displacement curves for the undeformed and deformed sample (2 revolutions), for maximum indentation loads of 250 mN and 5mN. The latter experiment was performed to circumvent the lack of resolution at higher loads.

These results are in agreement with the results reported by Jiang and Atzmon [199] and Tang [229], who also observed a reduced amount of shear banding/pile-up and/or a reduced amount of serrations in the load-displacement curve upon deformation.

These observations have been explained by considering the different effects of nucleation of new shear bands and propagation of exisiting shear bands. Modelling by Vaidyanathan et al. [166] predicted that the location of the local maximum effective stresses in the sample are located along disconnected arcs surrounding

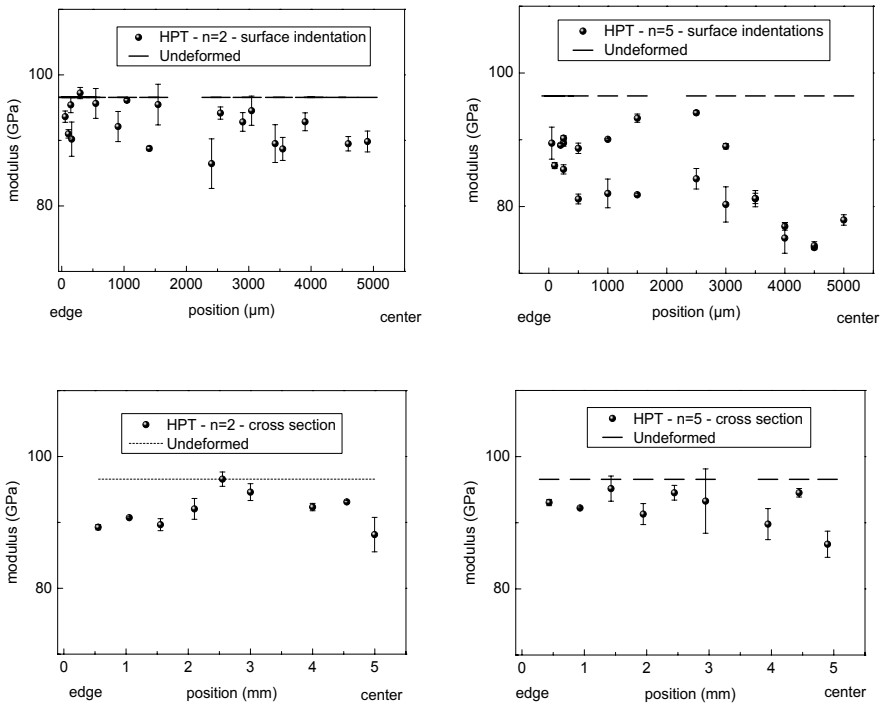

Fig. 6.7: Overview of nanoindentation results from which the elastic modulus was calculated.

the indent. Shear bands are expected to *nucleate* along these arcs of maximum stresses, which is in agreement with the typical shape of surface steps observed experimentally around indents. The *nucleation* of shear bands in an amorphous alloy results in serrations during plastic flow. New, concentric, shear bands form outside the indent as the indenter moves deeper into the sample, resulting in surface steps [199].

The pile-ups around the indents in the undeformed sample (Fig. 6.9) indicate that during nanoindentation, inhomogeneous deformation occurred, and the deformation mechanism is the nucleation and propagation of new shear bands. In the deformed sample, small pile-ups around the indents indicate that few new shear bands were generated during nanoindentation, and the predominant deformation mechanism is the *propagation* of pre-existing shear bands, developed during high pressure torsion.

Note that in chapter 4, in the annealed sample with similar structure, a multiplication in shear bands was observed, dedicated to a combination of reduced

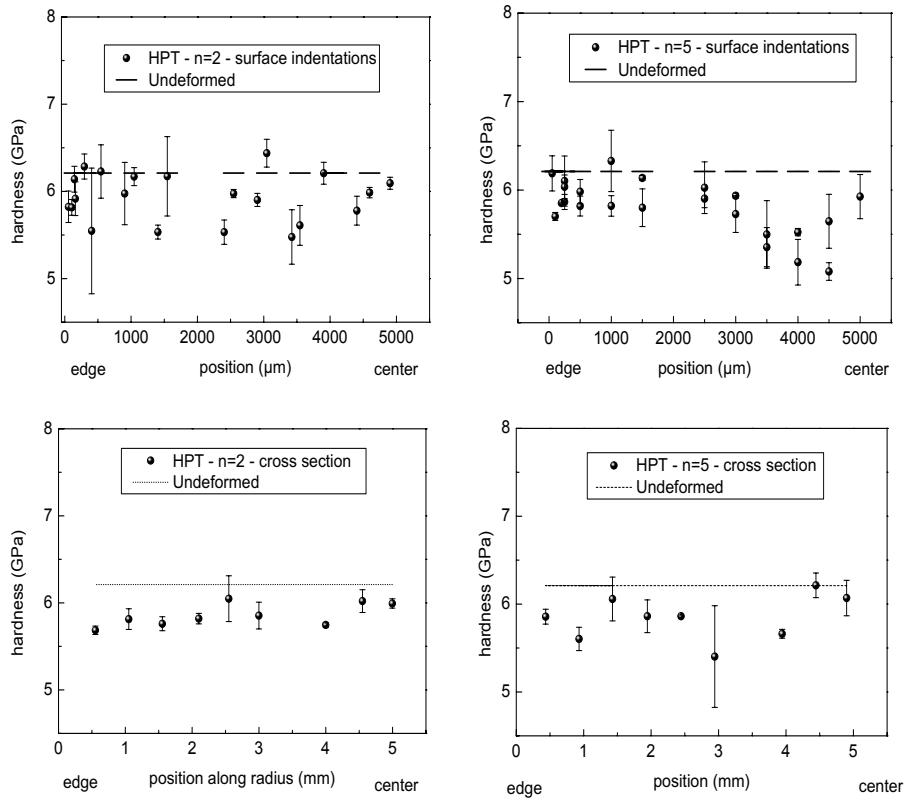

Fig. 6.8: Overview of nanoindentation results from which the hardness was calculated.

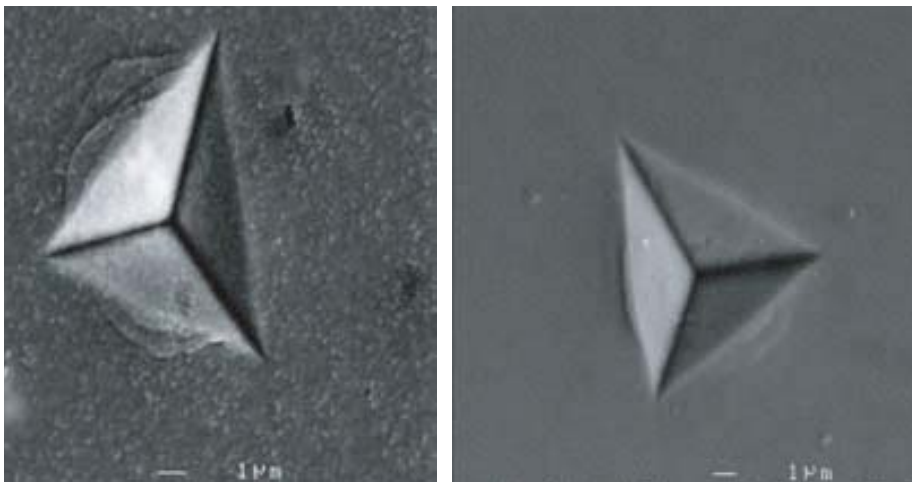

Fig. 6.9: Comparison of the indents of the undeformed sample (left) and the sample deformed by HPT by 2 whole turns (right) observed by SEM.

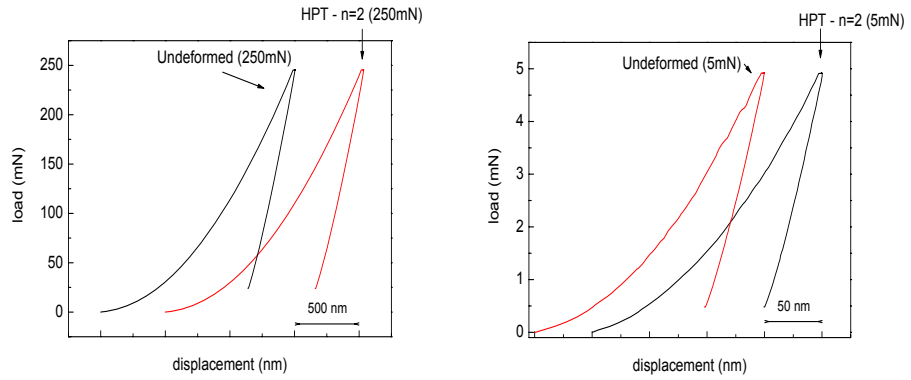

Fig. 6.10: Load-displacement curves for the undeformed sample and deformed by HPT (2 turns). The curves on the left side represent the curves made with a maximum load of 250mN, on the right hand side are the curves with higher resolution, made with a maximum load of 5mN, showing clearly the serrations in the undeformed sample.

free volume and presence of Cu-clusters. Here it seems that the pre-existing excess free volume and/or shear bands are sufficient and no multiplication of shear bands is required, despite the presence of Cu-clusters. Therefore, the role of Cu-clusters, formed upon deformation, on the resulting mechanical properties should be investigated in more detail and compared with the observed properties after low-temperature annealing.

6.5 Summary

Thermal and microstructural analysis suggest that (heavy) deformation can introduce changes in the medium range order of a bulk metallic glass, similar to the changes observed upon (low temperature) annealing that were beneficial for the mechanical behavior of this glass.

The mechanical response in nanoindentation tests is very similar to the undeformed sample under the same loading conditions. Only a moderate softening is observed.

Furthermore, HPT is capable of producing samples in bulk with a fairly homogeneous overall structure: no large difference were observed between edge and center, neither in thermal behavior, nor in mechanical response during nanoindentation. In contrast to crystalline materials, a higher number of revolutions might start to induce inhomogeneous behavior again, although this should be looked

into with further detail.

7. CONCLUSIONS

Structural changes, both topological and chemical, of Zr-based bulk metallic glasses have been characterized in this work, upon annealing and deformation, by calorimetry, X-ray diffraction and electron microscopy. The influence of these changes on the mechanical behavior of these glasses was investigated through compression tests and nanoindentation tests.

7.1 Indentation size effect

Application of (nano)indentation techniques should be done with care, due to the existence of a so-called size effect, which is exactly one of the consequences of structural changes occurring during deformation.

A decrease of hardness and elastic modulus on the maximum penetration depth, was found, evidencing the existence of a so-called indentation size effect in BMGs, similar as what is typically observed for crystalline materials.

A first structural characteristic of metallic glasses is its so-called free volume, which typically decreases upon thermal relaxation and increases upon deformation, resulting in hardening and softening respectively. Due to its increase upon deformation, free volume will influence the response of the material during nanoindentation testing, in particular a dynamic softening is observed when being plastically deformed at higher loads. The influence of free volume on this effect has been further demonstrated by comparing the mechanical response of a metallic glass in as-cast and structurally relaxed states. Larger free volume concentrations in the as-cast state result in enhanced mechanical softening and, concomitantly, more pronounced indentation size effects.

The existence of this size effect in metallic glasses has an important technological consequence, i.e. one should be aware of it when using indentation techniques to characterize properties like hardness and/or elastic moduli and comparing them with other data and/or sources.

7.2 Study of changes on medium range order upon annealing

Upon annealing, the metastable metallic glass relaxes to more stable states. One well-known consequence is the decrease of the quenched-in (excess) free volume, to which typically an embrittlement is ascribed. Besides these so-called topological changes however, changes on the chemical short-range order have been reported, in particular at low temperatures in the early stages of relaxation. Although inhomogeneities in the microstructure of metallic glasses down to the nanometer-scale (or below) can influence their (mechanical) behavior, the influence of these chemical short/medium range order have not been investigated in a systematic way.

The first goal therefore was to perform such a study on changes on the short and medium range order upon *annealing*, in particular at *low temperatures* - i.e. the possibility to induce such structural changes at low temperatures. By means of various characterization techniques, important changes in *chemical ordering* were found, with the formation of Cu-clusters in a more Cu-depleted matrix, already upon low temperature annealing for a short time, with an important influence on thermal and mechanical behavior.

A more detailed study of the thermal behavior with varying heating rates shows that crystallization occurs in a two-step process through the formation of the Cu-rich $Cu_{10}Zr_7$ phase and the more Cu-poor phase $CuZr_2$. Variations in overall Cu-content confirm these results: lower Cu-contents favor the formation of $CuZr_2$ while increasing the Cu-content leads to the crystallization into $Cu_{10}Zr_7$. The origin of the Cu-rich clusters upon annealing can thus be understood as a very embryonic phase towards crystallization. Importantly, DSC, which is a relatively accessible technique with few demands on sample preparation, proves its usefulness as a first indication of changes on the short/medium range order.

Although the (compositional) changes observed are moderate, their influence on the mechanical behavior, and in particular plasticity under compression, is great, when the topological changes are still moderate (low temperature annealing). The samples with the inhomogeneous matrix show higher levels of plasticity, in large contrast to the generally assumed embrittlement upon annealing. Acoustic measurements of the elastic properties as-cast and after annealing finally are in agreement with the observed change in chemical short range order,

i.e. an increased amount of like-like (Cu/Cu and/or Zr/Zr) instead of the initial unlike Cu/Zr bonds, lead to a decrease in elastic constants and higher plasticity can indeed be expected, with a lower barrier for shear band nucleation in the Cu-depleted matrix. A too large increase in topological short range order (free volume decrease) counterbalances the effect induced by the chemical short range order upon high temperature annealing. The mechanical behavior of alloys in the as-cast state with varying content of Cu suggests further that in fact the reduced probability for Cu/Zr bonds to be present is the key factor to improved plasticity and shear band nucleation, rather than the Cu-clusters themselves, although the latter may play a role in reducing the capacities of a propagating shear band by increasing its viscosity.

7.3 Study of changes on medium range order upon deformation

Upon annealing, topological (densification) and chemical ordering occur simultaneously, but these processes have a contradictory effect on plasticity. It might be difficult to control these two effects.

Therefore, it is interesting that the beneficial changes in chemical ordering can be achieved also upon high-deformation treatments, e.g. by high-pressure torsion. Deformation does not lead the adverse reduction of free volume but even produces some more, before this free volume transforms to more stable nanovoids. The observed softening on the other hand is rather moderate, indicating that deformation is certainly a treatment with promising capacities.

The technique high-pressure torsion itself is able to produce a rather homogeneous bulky sample, in particular for a low amount of revolutions - contrary to what is observed in crystalline materials, where more revolutions are necessary to overcome the undesired inhomogeneous microstructure.

7.4 Suggestions for future research

The work presented in this thesis has shed some light on the influence of nanometric and smaller inhomogeneities on the mechanical behavior, in particular the plasticity of metallic glasses, which is up to date still one of the main factors confining their overall application. Most likely, it will motivate further studies in-depth on the subject, both from fundamental and technological point of view.

More concretely, the use of advanced microscopy like TEM, corrected for aberrations, revealed its power in revealing and helping to understand the microstructure down to and even below the nanometer scale. This powerful tool should be further exploited, preferably in combination with diffraction techniques with synchrotron sources, e.g. in the study of the influence of the overall Cu-content on microstructure and its changes upon annealing and link them further to the changes in mechanical behavior.

From technological point of view, the results here indicate that care should be taken to manufacture metallic glasses in the most reproducible way, with a strict control of temperatures and pressure. A systematic study of casting parameters, e.g. with special emphasis on the amount of overheating, could be performed to investigate the (chemical) short-range order already present in the melt and concomitantly the influence thereof on the mechanical behavior. Finally, optimization of the ductilization by low-temperature annealing should be studied in function of the applied heating rate, as the latter was found to clearly alter the thermal behavior.

Deformation treatments, producing large-scaled samples, should be performed to confirm the observed results and test the influence of the inhomogeneous matrix on the plasticity.

7.5 Articles

An overview of papers directly or indirectly related to the present work and published in international journals are summarized below:

- *"Influence of annealing on the microstructure and hardness of Ti67.79Fe28.36Sn3.85 nanocomposite rods"*, N. Van Steenberge, J. Das, A. Concustell, J. Sort, S. Suriñach, J. Eckert and M.D. Baró, **Scripta Mater. 55 (2006)** pp. 1087-1090

- *"Dynamic Softening and Indentation Size Effect in a Zr-Based Bulk Glass-Forming Alloy: Free Volume Considerations"* N. Van Steenberge, J. Sort, A. Concustell, J. Das, S. Scudino, S. Suriñach, J. Eckert and M.D. Baró, **Scripta Mater. 56 (2007)** pp. 605-608

- *"Microstructural changes in a Zr-based BMG induced by low-temperature an-*

nealing" N. Van Steenberge, A. Concustell, J. Sort, N. Mattern, A. Gebert, J. Das, S. Suriñach, J. Eckert and M.D. Baró, **Mater. Sci. Eng. A** doi:10.1016/j.msea.2008.01.083

- *"Study of the Mechanical Behaviour of a Zr-Based Metallic Glass Rod Using Micro- and Nano-Indentation"*, J. Sort, N. Van Steenberge, A. Gimazov, A. Concustell, S. Suriñach, A. Gebert, J. Eckert and M.D. Baró, **The Open Materials Science Journal 2 (2008)**pp. 1-5

BIBLIOGRAPHY

[1] Klement W., Willens, and Duwez P. *Nature*, 187:869, 1960.

[2] Inoue A., Kato A., Zhang T., and Kim S.G. *Mater. Trans. JIM*, 32:609, 1991.

[3] Zhang T, Inoue A., and Masumoto T. *Mater. Trans. JIM*, 32:1005, 1991.

[4] Peker A. and Johnson W.L. *Appl. Phys. Lett.*, 63:2342, 1993.

[5] Greer A.L. and Ma E. *MRS Bulletin*, 32:611, 2007.

[6] Loffler J. F. *Z. Metallkd.*, 97:3, 2006.

[7] van den Beukel A. and Radelaar S. *Acta Metall.*, 31:419, 1983.

[8] Bossuyt S. *Microstructure and Crystallization Behavior in Bulk Glass Forming Alloys*. PhD thesis, California Institute of Technology, 2001.

[9] Brown M. E. *Introduction to Thermal Analysis - Techniques and Applications*. Kluwer Academic Publishers, 2 edition, 2004.

[10] American Society of Metals, editor. *Metallic Glasses*. Metals Park, Ohio, 1976.

[11] Boettinger W.J. and Perepezko J.H. In Das S.K., Kear B.H., and Adam C.M., editors, *Rapidly solidified crystalline alloys*, page 21. The Metallurgical Society, Inc., 1985.

[12] Christian J.W. *Theory of Transformations in Metals and Alloys*. Oxford, 1975.

[13] Iqbal N., van Dijk N.H., Offerman S.E., Moret M.P., Katgerman L., and Kearley G.J. *Acta Mater.*, 53:2875, 2005.

[14] Vreeswijk J.C.A., Gossink R.G., and Stevels J.M. *J. Non-Cryst. Solids*, 16:15, 1974.

[15] Concustell i Fargass A. *Deformation Behavior and Strengthening of Bulk Metallic Glasses and Nanocomposites.* PhD thesis, Universitat Autònoma de Barcelona, 2007.

[16] Mukherjee S., Schroers J., Johnson W.L., and Rhim W.-K. *Phys. Rev. Lett.*, 94:245501, 2005.

[17] Schober H.R. *Physica*, 201 A:14, 1993.

[18] Masuhr A., Waniuk T.A., Busch R., and Johnson W.L. *Phys. Rev. Lett.*, 82:2290, 1999.

[19] Li Y., Poon S.J., Shiflet G.J., Xu J., Kim D.H., and Löffler J.F. *MRS Bulletin*, 32:624, 2007.

[20] Johnson W.L. *MRS Bulletin*, 24:42, 1999.

[21] Ramachandrarao P. *Z. Metallkde*, 71:172, 1980.

[22] Concustell A., Mattern N., Wendrock H., Kuehn U., Gebert A., Eckert J., Greer A.L., Sort J., and Baró M.D. *Scripta Mater.*, 56:85, 2007.

[23] Mattern N. *J. Non-Cryst. Solids*, 353:1723, 2007.

[24] Stoica M., Hajlaoui K., Lemoulec A., and Yavari A. R. *Phil. Mag. Lett.*, 86:267, 2006.

[25] Castellero A., Bossuyt S., Stoica M., Deledda S., Eckert J., Chen G.Z., Fray D.J., and Greer A.L. *Scripta Mater.*, 55:87, 2006.

[26] Bernal J.D. *Nature*, 185:68, 1960.

[27] Gaskell P.H. *J. Non-Cryst. Solids*, 32:207, 1979.

[28] Miracle D., Egami T., Flores K.M., and Kelton K.F. *MRS Bulletin*, 32:629, 2007.

[29] Yavari A.R. *Nature*, 439:405, 2006.

[30] Busch R. *JOM*, 52:39, 2000.

[31] Inoue A. *Mater. Sci. Eng. A*, 267:171, 1999.

[32] Miracle D.B. *Acta Mater.*, 54:4317, 2006.

[33] Wang A. P., Wang J. Q., and Ma E. *Appl. Phys. Lett.*, 90:121912, 2007.

[34] Xing L.Q., Mukhopadhyay A., Buhro W.E., and Kelton K.F. *Philos. Mag. Lett.*, 84:293, 2004.

[35] Sheng H.W., Luo W.K., Alamgir F.M., Bai J.M., and Ma E. *Nature*, 439:405, 2006.

[36] Mattern N., Kühn U., Concustell A., Schöps A., Baró M.D., and Eckert J. *Mater. Trans.*, 48:1639, 2007.

[37] Hirotsu Y. and Akada R. *Jp. J. Appl. Phys.*, 23:L479, 1984.

[38] Hirotsu Y., Uehara M., and Ueno M. *J. Appl. Phys.*, 59:3081, 1986.

[39] Anazawa K., Hirotsu Y., and Inoue Y. *Acta Metall. Mater.*, 42:1997, 1994.

[40] Li J., Xu X., and Hufnagel T.C. *Microsci. Microanal.*, 9:509, 2003.

[41] Xing L.-Q., Li Y., Ramesh K. T., Li J., and Hufnagel T. C. *Phys. Rev. B*, 64:180201, 2001.

[42] Liu L., Chan K.C., Sun M., and Chen Q. *Mater. Sci. Eng. A*, 445-446:697, 2007.

[43] Cohen M. H. and Turnbull D. *J. Chem. Phys.*, 31:1164, 1959.

[44] Spaepen F. *Acta Met.*, 25:407, 1977.

[45] Hajlaoui K., Benameur T., Vaughan G., and Yavari A.R. *Scripta Mater.*, 51:843, 2004.

[46] Louzguine D.V., Yavari A.R., Ota K., Vaughan G., and Inoue A. *J. Non-Cryst. Solids.*, 351:1639, 2005.

[47] Slipenyuk A. and Eckert J. *Scripta Mater.*, 50:39, 2004.

[48] Flores K.M. *Scripta Mater.*, 54:327, 2006.

[49] Flores K.M., Sherer E., Bharathula A., Chen H., and Jean Y.C. *Acta Mater.*, 55:3403, 2007.

[50] Argon A.S. *Acta Metall.*, 27:47, 1979.

[51] www.arcelormittal.com.

[52] Dieter G. E. *Mechanical Metallurgy.* McGraw-Hill Book Company, 1986.

[53] Egami T. *Intermetallics*, 14:882, 2006.

[54] Schuh C.A., Hufnagel T.C., and Ramamurty U. *Acta Mater.*, 55:4067, 2007.

[55] Zink M., Samwer K., Johnson W.L., and Mayr S.G. *Phys. Rev. B*, 73:172203, 2006.

[56] Shi Y. and Falk M. L. *Phys. Rev. Lett.*, 95:095502, 2005.

[57] Johnson W.L. and Samwer K. *Phys. Rev. Lett.*, 95:195501, 2005.

[58] Eckert J., Das J., Pauly S., Duhamel C., Kim K.B., Yi S., and Wang W.H. *Mater. Trans.*, 48:1806, 2007.

[59] Lewandowski J.J. and Greer A.L. *Nature Mater.*, 5:15, 2006.

[60] Eckert J., Das J., Pauly S., and Duhamel C. *Adv. Eng. Mater.*, 9:443, 2007.

[61] Schroers J. and Johnson W.L. *Phys. Rev. Lett.*, 93:255506, 2004.

[62] Lewandowski J.J., Wang W.H., and Greer A.L. *Philos. Mag. Lett.*, 85:77, 2005.

[63] Gu X.J., McDermott A.G., Poon S.J., and Shiflet G.J. *Appl. Phys. Lett.*, 88:211905, 2006.

[64] Liu Y.H., Wang G., Wang R.J., Zhao D.Q, Pan M.X., and Wang W.H. *Science*, 315:1385, 2007.

[65] Kűhn U., Eckert J., Mattern N., and Schultz L. *Mat. Sci. Eng. A*, 375-377:322, 2004.

[66] Hajlaoui K., Yavari A.R. Doisneau B., Le Moulec A., Vaughan G., Greer A.L., Botta W.J., Inoue A., Zhang W., and Kvick A. *Scripta Mater.*, 54:1829, 2006.

[67] Park E.S. and Kim D.H. *Acta Mater.*, 54:2597, 2006.

[68] Choi-Yim H., Conner R. D., Szuecs F., and Johnson W. L. *Acta Mater.*, 50:2737, 2002.

[69] Choi-Yim H., Schroers J., and Johnson W.L. *Appl. Phys. Lett.*, 80:1906, 2002.

[70] Siegrist M. and Löffler J. F. *Scripta Mater.*, 56:1079, 2007.

[71] Kato H., Hirano T., Matsuo A., Kawamura Y., and Inoue A. *Scripta Mater.*, 43:503, 2000.

[72] Hays C. C., Kim C. P., and Johnson W. L. *Phys. Rev. Lett.*, 84:2901, 2000.

[73] Oh J.C., Ohkubo T., Kim Y.C., Fleury E., and Hono K. *Scripta Mater.*, 53:165, 2005.

[74] Kim K.B., Das J., Baier F., Tang M.B., Wang W.H., and Eckert J. *Appl. Phys. Lett.*, 88:051911, 2006.

[75] Das J., Kim K.B., Xu W., Wei B.C., Zhang Z.F., Wang W.H., Yi S., and Eckert J. *Mater. Trans.*, 47:2606, 2006.

[76] Sun Y. F., Wei B. C., Wang Y. R., Li W. H., Cheung T. L., and Shek C. H. *Applied Physics Letters*, 87:051905, 2005.

[77] Fan C. and Inoue A. *Appl. Phys. Lett.*, 77:46, 2000.

[78] Chen M., Inoue A., Zhang W., and Sakurai T. *Phys. Rev. Lett.*, 96:245502, 2006.

[79] Cao Q., Li J., Zhou Y., and Jiang J. *Appl. Phys. Lett.*, 86:081913, 2005.

[80] Kim K.B., Das J., Baier F., Tang M.B., Wang W.H., and Eckert J. *Appl. Phys. Lett.*, 88:051911, 2006.

[81] Choi-Yim H., Xu D.H., Lind M.L., Löffler J.F., and Johnson W.L. *Scripta Mater.*, 54:187, 2006.

[82] Yavari A.R., Lewandowski J.J., and Eckert J. *MRS Bulletin*, 32:635, 2007.

[83] Ott R. T., Sansoz F., Molinari J.F., Ramesh K.T., and Hufnagel T.C. *Acta Mater.*, 53:1883, 2005.

[84] Zhang Y. and Greer A.L. *Appl. Phys. Lett.*, 89:281633, 2006.

[85] Hajlaoui K., Yavari A.R., LeMoulec A., Botta W.J., Vaughan F.G., Das J., Greer A.L., and Kvick A. *J. Non-Cryst. Solids*, 353:327, 2007.

[86] Sergueeva A.V., Mara N.A., Kuntz J.D., Lavernia E.J., and Mukherjee A.K. *Philos. Mag.*, 85:2671, 2005.

[87] Ashby M.F. and Greer A.L. *Scripta Mater.*, 54:321, 2006.

[88] Zhang Y., Wang W.H., and Greer A.L. *Nature Mater.*, 5:857, 2006.

[89] Das J., Tang M. B., Kim K. B., Theissmann R., Baier F., Wang W.H., and Eckert J. *Phys. Rev. Lett.*, 94:205501, 2005.

[90] Lee S.W., Huh M.Y., Fleury E., and Lee J.C. *Acta Mater.*, 54:349, 2006.

[91] Kim K. B., Das J., Venkataraman S., Yi S., and Eckert J. *Appl. Phys. Lett.*, 89:071908, 2006.

[92] Li Q.K. and Li M. *Intermetallics*, 14:1005, 2006.

[93] Yang B., Riester L., and Nieh T.G. *Scripta Mater.*, 54:1277, 2006.

[94] Inoue A. and Nishiyama N. *MRS Bulletin*, 32:651, 2007.

[95] Gebert A., Buchholz K., Leonhard A., Mummert K., and Eckert J. *Mater. Sci. Eng. A*, 267:294, 1999.

[96] Drozdz D., Wunderlich R.K., and Fecht H.J. *Wear*, 262:176, 2007.

[97] Experimental techniques applied to materials science. Lecture notes Universitat Autònoma de Barcelona, 2006.

[98] International Iron & Steel institute & MATTER, editor. *steeluniversity.org*. University of Liverpool, 2007.

[99] Blackburn M.J. and Malley D.R. *Materials and Design*, 14:19, 1993.

[100] Das J., Roy S.K., Löser W., Eckert J., and Schultz L. *Mater. Manuf. Process.*, 19:423, 2004.

[101] Das J., Güth A., KlaußH.-J., Mickel C., Löser W., Eckert J., Roy S.K., and Schultz L. *Scripta Mater.*, 49:1189, 2003.

[102] Zhilyaev A.P., Nurislamova G.V., Kim B.-K., Baró M.D., Szpunqr J.A., and Langdon T.G. *Acta Mater.*, 51:753, 2003.

[103] Kim H.S. *J. Mater. Proc. Techn.*, 113:617, 2001.

[104] Valiev R.Z., Ivanisenko Yu. V., Rauch E.F., and Baudelet B. *Acta Mater.*, 44:4705, 1996.

[105] Inczedy J., Lengyel T., and Ure A.M. *Compendium of Analytical Nomenclature: definitive rules 1997*. Blackwell, Oxford, 1998.

[106] Craig D.Q.M., Barsnes M., Royall P.G., and Kett V.L. *Pharmaceutical Research*, 17:696, 2000.

[107] van den Beukel A. and Sietsma J. *Acta Metall. Mater.*, 38:383, 1990.

[108] Kanungo B.P., Glade S.C., Asoka-Kumar P., and Flores K.M. *Intermetallics*, 12:1073, 2004.

[109] Kissinger H.E. *Anal. Chem.*, 29:1702, 1957.

[110] He Z and Courtney T.H. *Mater. Sci. Eng. A*, 346:141, 2003.

[111] Busch R., Bakke E., and Johnson W. L. *Acta Mater.*, 46:4725, 1998.

[112] Bragg W.L. *Proc. Camb. Phil. Soc.*, 17:43, 1912.

[113] Yavari A.R., Le Moulec A., Botta W.J., Inoue A., Rejmankova P., and Kvick A. *J. Non-Cryst. Solids*, 247:31, 1999.

[114] Eisenberger P., Marra W. C., and Brown G. S. *Phys. Rev. Lett.*, 45:1439, 1980.

[115] Williams D.B. and Carter C.B. *Transmission Electron Microscopy - A Textbook for Materials Science - Basics.* Plenum Press - New York and London, 1996.

[116] De Cooman B. C. Observation techniques in materials science. Lecture notes Ghent University, 2000.

[117] Reimer L. *Scanning Electron Microscopy.* Springer Verlag, 1985.

[118] Lawes G. *Scanning Electron Microscopy and X-Ray Microanalysis.* John Wiley & Sons, 1987.

[119] Goodhew P., Brook D., Tanovic B., Green A., and Jones I. www.matter.org.uk.

[120] Thomas G. and Goringe M.J. *Transmission Electron Microscopy of Materials.* John Wiley and Sons, 1979.

[121] Bendersky L. A. and Gayle F.W. *Journal of Research of the National Institute of Standards and Technology*, 2001.

[122] Champness P.E. *Electron diffraction in the Transmission Electron Microscope.* BIOS Scientific Publishers Limited, 2001.

[123] Freitag B., Kujawa S., Mul P.M., Ringalda J., and Tiemeijer P.C. *Ultramicroscopy*, 102:209, 2005.

[124] Sun B.B., Wang Y.B., Wen J., Yang H., Sui M.L., Wang J.Q., and Ma E. *Scripta Mater.*, 53:805, 2005.

[125] Pennycook S. J., Jesson D. E., McGibbon A.J., and Nellist P.D. *J. Electron Microsc*, 45:36, 1996.

[126] Yamazaki T., Watanabe K., Kikuchi Y., Kawasaki M., Hashimoto I., and Shiojiri M. *Phys. Rev. B*, 61:13833, 2000.

[127] Pennycook S. J. and Jesson D. E. *Phys. Rev. Lett.*, 64:938, 1990.

[128] Krivanek O. L., Gaskell P. H., and Howie A. *Nature*, 262:454, 1976.

[129] Hirata A., Hirotsua Y., Nieh T.G., Ohkuboc T., and Tanaka N. *Ultramicroscopy*, 107:116, 2007.

[130] Chang H.J., Park E.S., Kim Y.C., and Kim D.H. *Mater. Sci. Eng. A*, 406:119, 2005.

[131] Hofmann D.C., Duan G., and Johnson W.L. *Scripta Mater.*, 54:1117, 2006.

[132] Buckin V., O'Driscoll B., and Smyth C. *Spectroscopy Europe*, 15:19, 2003.

[133] Keryvin V., Vaillant M.-L., Rouxel T., Huger M., Gloriant T., and Kawamura Y. *Intermetallics*, 10:1289, 2002.

[134] Fischer-Cripps A.C. *Nanoindentation.* Springer-Verlag New York, 2004.

[135] Mukhopadhay N. K. and Paufler P. *International Materials Review*, 51:209, 2006.

[136] Meyer E. *Phys. Z.*, 9:66, 1908.

[137] Oliver W.C. and Pharr G.M. *J. Mat. Res*, 19:3, 2004.

[138] Oliver W.C. and Pharr G.M. *J. Mat. Res*, 7:1564, 1992.

[139] Fischer-Cripps A.C. *Vacuum*, 58:569, 2000.

[140] Schuh C.A. and Nieh T.G. *J. Mater. Res.*, 19:46, 2004.

[141] Chinh N. Q., Gubicza J., Kovács Zs., and Lendvai J. *J. Mater. Res.*, 19:31, 2004.

[142] Manika I. and Maniks J. *Acta Mater.*, 54:2049, 2006.

[143] Gerberich W. W., Tymiak N. I., Grunlan J. C., Horstemeyer M. F., and Baskes M. I. *J. Appl. Mech.*, 69:433, 2002.

[144] Li H., Ghosh A., Han Y. N., and Bradt R. C. *J. Mater. Res.*, 8:1028, 1993.

[145] Nix W.D. and Gao H. *J. Mech. Phys. Sol.*, 46:411, 1998.

[146] Lam D. C. C. and Chong A. C. M. *Mater. Sci. Eng. A*, 318:313, 2001.

[147] Jana S., Ramamurty U., Chattopadhyay K., and Kawamura Y. *Mater. Sci. Eng. A*, 375-377:1191, 2004.

[148] Zhang B., Wang W., and Zhang G.P. *Mater. Sci. Tech.*, 22:734, 2006.

[149] Zhang H., Jing X., Subhash G., Kecskes L.J., and Dowding R.J. *Acta Mater.*, 53:3849, 2005.

[150] Yang F., Geng K., Liaw P.K., Fan G., and Choo H. *Acta Mater.*, 55:321, 2007.

[151] Bei H., Xie X., and George E.P. *Phys. Rev. Lett.*, 96:105503, 2006.

[152] Concustell A., Sort J., Alcalá G., Mato S., Gebert A., Eckert J., and Baró M.D. *J. Mater. Res.*, 20:2719, 2005.

[153] Schuh C.A., Lund A.C., and Nieh T.G. *Acta Mater.*, 52:5879, 2004.

[154] De Hey P., Sietsma J., and Van Den Beukel A. *Acta Mater.*, 46:5873, 1998.

[155] Heggen M., Spaepen F., and Feuerbacher M. *J. Appl. Phys.*, 97:033506, 2005.

[156] Greer A.L., Castellero A., Madge S.V., Walker I.T., and Wilde J.R. *Mater. Sci. Eng. A*, 375-377:1182, 2004.

[157] Murali P. and Ramamurty U. *Acta Mater.*, 53:1467, 2005.

[158] Van Aken B., de Hey P., and Sietsma J. *Mater. Sci. Eng. A*, 278:247, 2000.

[159] Zhang Z. and Xie J. *Mater. Sci. Eng. A*, 407:161, 2005.

[160] Schuh C.A. and Nieh T.G. *Acta Mater.*, 51:87, 2003.

[161] Huang R., Suo Z., Prevost J.H., and Nix W.D. *J. Mech. Phys. Solids*, 50:1011, 2002.

[162] Dao M., Chollacoop N., Van Vliet K.J., Venkatesh T.A., and Suresh S. *Acta Mater.*, 49:3899, 2001.

[163] Wright W.J., Hufnagel T.C., and Nix W. D. *J. Appl. Phys.*, 93:1432, 2003.

[164] Wang W.H. *J. Appl. Phys.*, 99:093506, 2006.

[165] Daniel B.S.S., Reger-Leonhard A., Heilmaier M., Eckert J., and Schultz L. *Mech. Time-Depend. Mater.*, 6:193, 2002.

[166] Vaidyanathan R., Dao M., Ravichandran G., and Suresh S. *Acta Mater.*, 49:3781, 2001.

[167] Ramamurty U., Jana S., Kawamura Y., and Chattopadhyay K. *Acta Mater.*, 53:705, 2005.

[168] Jiang W.H., Liu F.X., Choo H., and Liaw P.K. *Mater. Trans.*, 48:1781, 2007.

[169] Tuinstra P., Duine P.A., Sietsma J., and van den Beukel A. *Acta Metall. Mater.*, 43:2815, 1995.

[170] Kane S.N., Gupta A., Sarabhai S.D., Kuzminski M., and Lachowicz H.K. *J. Magn. Magn. Mater.*, 280:84, 2004.

[171] Haruyama O., Tando M., Kimura H.M., Nishiyama N., and Inoue A. *J. Non-Cryst. Solids*, 312-314:603, 2002.

[172] Miller M.K., Russell K.F., Martin P.M., Busch R., and Johnson W.L. *J. Physique IV*, 6(C5):217, 1996.

[173] Schneider S., Thiyagarajan P., and Johnson W. L. *Appl. Phys. Lett.*, 68:493, 1996.

[174] Yamasaki T., Maeda S., Fukami T., Yokoyama Y., Kimura H.M., and Inoue A. *Mater. Trans.*, 47:1834, 2007.

[175] Liu L., Wu Z.F., and Zhang J. *J. Alloys Compd.*, 339:90, 2002.

[176] Liu L., Chan K.C., and Zhang T. *J. Alloys Compd.*, 396:114, 2005.

[177] Hays C.C., Kim C.P., and Johnson W.L. *Appl. Phys. Lett.*, 75:1089, 1999.

[178] Liu L., Chen Q., Chan K.C., Wang J.F., and Pang G.K.H. *Mater. Sci. Eng. A*, 449-451:949, 2007.

[179] Duan G., Xu D., Zhang Q., Zhang G., Cagin T., Johnson W.L., and Goddard W.A. *Phys. Rev. B*, 71:224208, 2005.

[180] Wang W.H., Wei Q., Friedrich S., Macht M.P., Wanderka N., and Wollenberger H. *Appl. Phys. Lett.*, 71:1053, 1997.

[181] Dmowski W., Fan C., Morrison M.L., Liaw P.K., and Egami T. *Mater. Sci. Eng. A*, 471:125, 2007.

[182] Fukunaga T., Sugiura H., Takeichi N., and Mizutani U. *Phys. Rev. B*, 54:3200, 1996.

[183] Inoue A., Makino A., and Mizushima T. *J. Magn. Magn. Mater.*, 215-216:246, 2000.

[184] Barbee T. W., Walmsley R. G., Marshall A. F., Keith D. L., and Stevenson D. A. *Appl. Phys. Lett.*, 38:132, 1981.

[185] Ismail N., Uhlemann M., Gebert A., and Eckert J. *J. Alloys Compd.*, 298:146, 2000.

[186] Wang X.L., Almer J., Liu C.T., Wang Y.D., Zhao J.K., Stoica A.D., Haeffner D.R., and Wang W.H. *Phys. Rev. Lett.*, 91:265501, 2003.

[187] Concustell A., Alcalá G., Mato S., Woodcock T.G., Gebert A., Eckert J., and Baró M.D. *Intermetallics*, 13:1214, 2005.

[188] Murah P. and Ramamurty U. *Acta Mater.*, 53:1467, 2005.

[189] Ramamurty U., Lee M.L., Basu J., and Li Y. *Scripta Mater.*, 47:107, 2002.

[190] Dalla Torre F. H., Dubach A., Nelson A., and Löffler J.F. *Mater. Trans.*, 48:1774, 2007.

[191] Shen J. Wang G., Sun J.F., Lu Z.P., Stachurski Z.H., and Zhou B.D. *Intermetallics*, 13:642, 2005.

[192] Kusy M., Kühn U., Concustell A., Gebert A., Das J., Eckert J., Schultz L., and Baró M.D. *Intermetallics*, 14:982, 2006.

[193] Gilbert C. J., Ritchie R. O., and Johnson W. L. *Appl. Phys. Lett.*, 71:476, 1997.

[194] Xi X. K., Zhao D. Q., Pan M. X., Wang W. H., Wu Y., and Lewandowski J. J. *Phys. Rev. Lett.*, 94:125510, 2005.

[195] Choi-Yim H., Busch R., Köster U., and Johnson W. L. *Acta Mater.*, 47:2455, 1999.

[196] Qiao D., Wang G., Jiang W., Yokoyama Y., Liaw P.K., and Choo H. *Mater. Trans.*, 47:1828, 2007.

[197] Liu L. and Chan K.C. *Mater. Lett.*, 59:3090, 2005.

[198] Li H., Tao K., Fan C., Liaw P.K., and Choo H. *Appl. Phys. Lett.*, 53:041921, 2006.

[199] Jiang W.H., Pinkerton F.E., and Atzmon M. *Acta Mater.*, 53:3469, 2005.

[200] Vaillant M.L., Keryvin V., Rouxel T., and Kawamura Y. *Scripta Mater.*, 47:19, 2002.

[201] Cheng Y.-T. and Cheng C.-M. *Appl. Phys. Lett.*, 73:614, 1998.

[202] Yang B., Riester L., and Nieh T.G. *Scripta Mater.*, 54:1277, 2006.

[203] Harms U., Jin O., and Schwarz R.B. *J. Non-Cryst. Solids*, 217:200, 2003.

[204] Wakeda M., Shibutani Y., Ogata S., and Park J. *Intermetallics*, 15:139, 2007.

[205] M. W. Chen, I. Dutta, T. Zhang, A. Inoue, and T. Sakurai. *Applied Physics Letters*, 79:42, 2001.

[206] Baricco M., Spriano S., Chang I;, Petrzhik M.I., and Battezzati L. *Mater. Sci. Eng. A*, 304-306:305, 2001.

[207] Altounian Z., Batalla E., Strom-Olsen J. O., and Walter J. L. *Journal of Applied Physics*, 61:149, 1987.

[208] Kőster U., Meinhardt J., Roos S., and Busch R. *Mater. Sci. Eng. A*, 226-228:995, 1997.

[209] de Oliveira M.F., Kiminami C.S., and Botta Filho W.J. *Mater. Sci. Eng. A*, 304-306:665, 2001.

[210] Yavari A.R., Inoue A., Zhang T., Botta Filho W.J., and Kvick A. *Scripta Mater.*, 44:1239, 2001.

[211] Uriarte J.L., Zhang T., Deledda S., Vaughan G., Yavari A.R., Inoue A., and Kvick A. *J. Non-Cryst. Solids*, 287:197, 2001.

[212] Fukami T., Okabe K., Okai D., Yamasaki T., Zhang T., and Inoue A. *Mater. Sci. Eng. B*, 111:189, 2004.

[213] Xing L.Q. and Ochin P. *Acta Mater.*, 45:3765, 1997.

[214] Wei. *Mater. Letters*, 37:263, 1998.

[215] Ou X.and Roseker W., Saksl K., Franz H., Gerward L., Xu X., Zhang G.Q., Wang L.N., Liu J.F., and Ziang J.Z. *J. Alloys Compd.*, 441:185, 2007.

[216] Yan M., Zou J., and Shen J. *Sci. Techn. Adv. Mater.*, 7:806, 2006.

[217] Winwulff 1.0.7. http://www.jcrystal.com.

[218] Frank W. *Defect Diff. Forum*, 143-147:695, 1997.

[219] Faupel F., Frank W., Macht M.-P., Mehrer H., Naundorf V., Räzke K., Schober H.R., Sharma S.K., and Teichler H. *Rev. Modern Phys.*, 75:237, 2003.

[220] Wenwer F., Knorr K., Macht M.-P., and Mehrer H. *Defect Diff. Forum*, 143-147:831, 1997.

[221] Busch R., Bakke E., and Johnson W.L. *Appl. Phys. Lett.*, 68:2945, 1996.

[222] Zhang Y. and Greer A.L. *J. Alloys Compd.*, 434-435:2, 2007.

[223] Gu X. J., McDermott A. G., Joseph Poon S., and Shiflet G.J. *Applied Physics Letters*, 88:211905, 2006.

[224] Boucharat N., Hebert R.J., Rösner H., and Wilde G. *Solid State Phenom.*, 114:123, 2006.

[225] Sort J., Ile D.C., Zhilyaev A.P., Concustell A., Czeppe T., Stoica M., Suriñach S., Eckert J., and Baró M.D. *Scripta Mater.*, 50:1221, 2004.

[226] Kovács Zs., Hóbor S., Szabó P.J., Lendvai J., Zhilyaev A.P., and Révész Á. *Mater. Sci. Eng. A*, 449-451:1139, 2007.

[227] Révész Á., Schafler E., and Kovács Zs. *Appl. Phys. Lett.*, 92:011910, 2008.

[228] Deng Y., He L., Zhang Q., Zhang H., and Ye H. *Adv. Eng. Mater.*, 5:738, 2003.

[229] Tang C., Li Y., and Zeng K. *Mater. Sci. Eng. A*, 384:215, 2004.

[230] Jiang W.H. and Atzmon M. *Acta Mater.*, 51:4095, 2003.

[231] Jiang W.H. and Atzmon M. *Intermetallics*, 14:962, 2005.

[232] Kim J.-J., Choi Y., Suresh S., and Argon A.S. *Science*, 295:654, 2002.

[233] Nieh T.G., Wadsworth J., Liu C.T., Ohkubo T., and Hirotsu Y. *Acta Mater.*, 49:2887, 2001.

[234] Cao Q., Li J.F., Hu Y., Horsewell A., Jiang J.Z., and Zhou Y.H. *Mater. Sci. Eng. A*, 457:94, 2006.

[235] Demetriou M.D. and Johnson W.L. *Acta Mater.*, 52:3403, 2004.

[236] Guinier A. *X-ray diffraction in crystals, imperfect crystals and amorphous bodies*. 1994.

[237] Chen X., Yan J., and Karlsson A.M. *Mater. Sci. Eng. A*, 406:139, 2006.

[238] Verhoeven J.D. *Fundamentals of Physical Metallurgy*. John Wiley & Sons, 1975.

[239] Electron diffraction in tem. http://nstg.nevada.edu/TEM/TEM.htm.

APPENDIX

A. ELECTRON DIFFRACTION

A.1 The reciprocal lattice

The reciprocal lattice is a mathematical concept, defined as a lattice of spots, each of which represents a set of planes (hkl) of spacing d in the real lattice. Each spot lies further at a distance $|\overline{g}| = d^{-1}$ from the origin, with $|\overline{g}|$ the modulus of the reciprocal lattice vector. These reciprocal lattice vectors are aligned in the direction perpendicular to the planes they represent.

Although the real or direct lattice and the reciprocal lattice look geometrically similar, there is one vital difference between them. Each node of the real lattice is identical and any node can be taken as the origin; in the reciprocal lattice, however, each node is distinct as it represents a different set of planes. The origin of the reciprocal lattice is 000 and represents the undeviated beam.

If $\overline{a}$, $\overline{b}$ and $\overline{c}$ represent the base of the unit cell of a crystallographic structure, the reciprocal lattice is defined by $\overline{A}$, $\overline{B}$, and $\overline{C}$:

$$\begin{aligned} \overline{A} &= \frac{\overline{b} \times \overline{c}}{V} \\ \overline{B} &= \frac{\overline{c} \times \overline{a}}{V} \\ \overline{C} &= \frac{\overline{a} \times \overline{b}}{V}, \end{aligned}$$

with $V = \overline{a} \cdot (\overline{b} \times \overline{c})$ the volume of the unit cell. An interesting consequence of this definition is that:

$$\overline{A} \cdot \overline{a} = \overline{B} \cdot \overline{b} = \overline{C} \cdot \overline{c} = 1 \tag{A.1}$$

For any crystal system, a reciprocal vector can be found by vector addition:

$$\overline{g_{hkl}} = h\overline{A} + k\overline{B} + l\overline{C}. \tag{A.2}$$

As a consequence, any 2-D section of a reciprocal lattice can be defined by two vectors so we only need to index 2 spots. All others can be deduced by vector

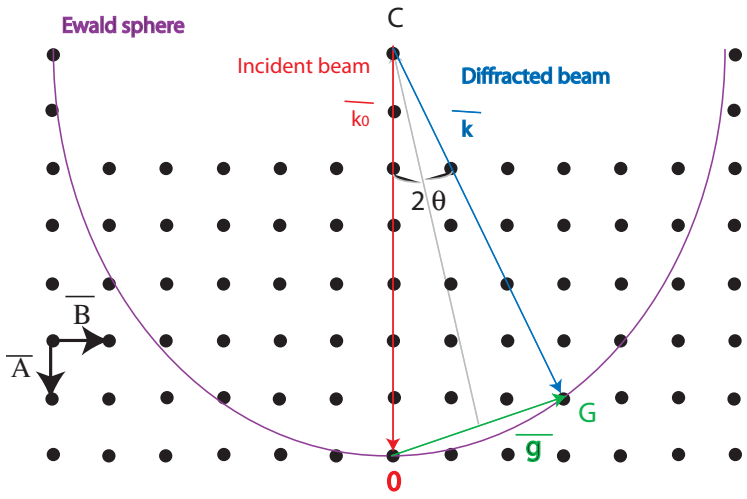

Fig. A.1: The Ewald or reflecting sphere construction. The sphere has a radius of λ^{-1} and the direct beam, parallel to one of the diameters passes through the origin of the reciprocal lattice, 0. If a reciprocal point lies on the surface of the sphere, Bragg's law is satisfied and will appear in an electron diffraction pattern. [119]

addition. [116], [122], [119]

Note that the distances measured in practice on a diffraction pattern are actually magnified reciprocal lattice vectors; the magnification factor for the microscope is the camera constant λL, resulting from the magnifications of the imaging lenses of the microscope.

A.2 The reflecting sphere

The reflecting or Ewald sphere is a concept that connects the concept of the reciprocal lattice to Bragg's law.

This sphere has a radius of $1/\lambda$, where λ is the wavelength of the electrons, it passes through the origin, 000, and one of the diameters is the direction of the direct beam (Fig. A.1). If a reciprocal point lies on this sphere, it represents a set of planes that are at the correct angle θ to the direct beam for diffraction to occur, i.e. Bragg's law is obeyed [120].

The Ewald sphere construction, together with the reciprocal space, allows us to write a vector equation as an alternative to Bragg's law. If the direct beam is a vector $\overline{k_0}$ and the diffracted beam is a vector $\overline{k}$, both with a modulus λ^{-1}, then

$\overline{g} = \overline{k} - \overline{k_0}$.

The fact that we see a large number of reflections in a diffraction pattern, even though the reciprocal lattice point has to be exactly on the reflecting sphere for diffraction to occur, is a consequence of two factors. First of all, the radius of the reflecting sphere is extremely large ($\sim \lambda^{-1} \sim \infty$) in electron diffraction in comparison with the size of the reciprocal lattice, as a consequence of the small wavelength of electrons. Secondly, the diffraction spots are not really spots, but more rod-shaped (relrod or reciprocal lattice rod). If the specimen is of thickness t, hen the reciprocal lattice point is streaked out to a length of t^{-1}. [122]

A.3 The structure factor

The intensity of a given diffraction spot is related to the shape, volume and perfection of the crystal and the structure factor F_{hkl} for the unit cell. This structure factor is a measure of the amplitude scattered by all the atoms in a unit cell into the reflection hkl. It is defined by [120], [122]:

$$F_{hkl} = \sum_j f_j \exp(2\pi \overline{g_{hkl}} \cdot \overline{r_j}), \tag{A.3}$$

where f_j the atomic scattering factor (Eq. (2.27)) of the jth atom at the angle concerned, the atom being at a position $\overline{r_j}$ in the unit cell. The sum is made over the whole unit cell. F_{hkl} is not a simple sum of all the values of f_j because the phase difference between the waves scattered by the different atoms has to be taken into account, which explains the presence of the exponential term in Eq. (A.3).

The (real lattice) vector $\overline{r_j}$ is given by:

$$\overline{r_j} = x\overline{a} + y\overline{b} + z\overline{c}, \tag{A.4}$$

where x, y, z are the coordinates of the atoms in the unit cell with basis vectors $\overline{a}, \overline{b}, \overline{c}$. Therefore:

$$\begin{aligned} \overline{g_{hkl}} \cdot \overline{r_j} &= (h\overline{A} + k\overline{B} + l\overline{C}) \cdot (x\overline{a} + y\overline{b} + z\overline{c}) \\ &= hx + ky + lz \end{aligned}$$

The reciprocal lattice corresponding to diffraction includes only the points for

which $F_{hkl} \neq 0$.

B. STEREOGRAPHIC PROJECTION

Stereographic projections are 2-D maps of the orientation relationships between different crystallographic directions and planes. It is constructed by situating a tiny crystal at the center of a large sphere. The planes of this crystal are represented by their normals, which are projected out to intersect the sphere. The intersections of these normals on the sphere are then mapped onto a plane to obtain the desired projection, along the desired direction (Fig.) [238], [239].

In the high energy electron diffraction, the Bragg angles are so small that the incident electron beam travels nearly parallel to the diffracting planes (zone law). When the electrons travel down the crystal from the north pole of a spherical projection, the diffraction occurs from planes whose poles intersect the equator of the sphere, perhaps within a degree or so. However, when relating stereographic projection to diffraction planes, one should be aware that the former does not contain information about *distances* between the diffraction spots. Neither does it contain information about structure rules, so forbidden reflections do occur on a stereographic projection. Nonetheless, it contains very valuable information on angles between planes belonging to a certain zone. These angles in the stereographic projection are the same as in the diffraction pattern made along the same

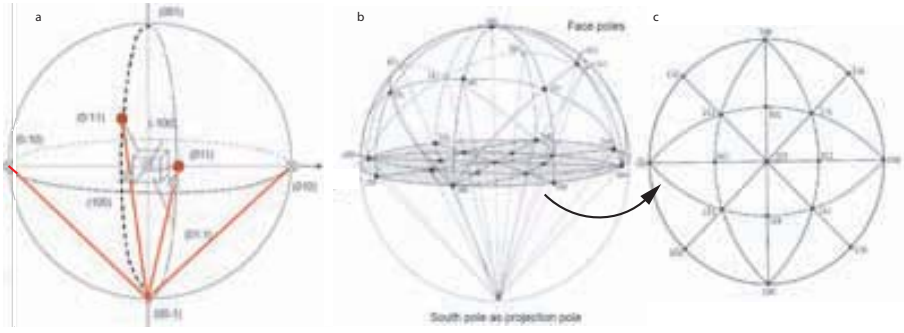

Fig. B.1: (a,b)Construction of a stereographic projection with the horizontal plane through the center as projection plane. (c) Result: the standard [0 0 1] projection. [239]

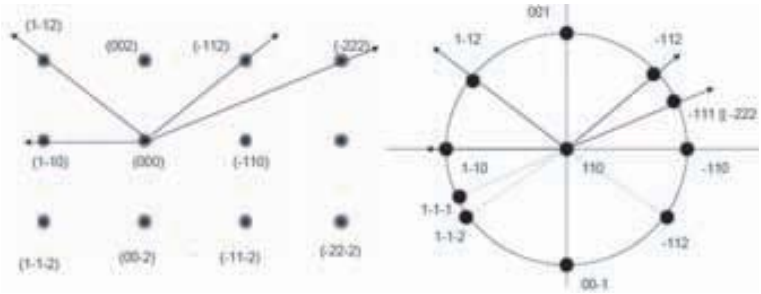

Fig. B.2: Orientation relationship between [110] diffraction pattern (left) and [1 1 0] stereographic projection (right). Angles between the vectors are the same on the left and right sides [239].

zone-axis. This is illustrated in Fig. B.2 for a bcc crystal [239].